INVESTIGATION OF ALD THIN FILMS TO IMPROVE THE RELIABILITY OF ORGANIC ELECTRONIC DEVICES

A Dissertation
Presented to
The Academic Faculty

by

Hyung Chul Kim

In Partial Fulfillment
of the Requirements for the Degree
Doctor of Philosophy in the
School of Mechanical Engineering

Georgia Institute of Technology

December 2015

Copyright © 2015 by Hyung Chul Kim

INVESTIGATION OF ALD THIN FILMS TO IMPROVE THE RELIABILITY OF ORGANIC ELECTRONIC DEVICES

Approved by:

Dr. Samuel Graham, Advisor
School of Mechanical Engineering
Georgia Institute of Technology

Dr. Ting Zhu
School of Mechanical Engineering
Georgia Institute of Technology

Dr. Shannon Yee
School of Mechanical Engineering
Georgia Institute of Technology

Dr. John R. Reynolds
School of Chemistry
Georgia Institute of Technology

Dr. Elsa Reichmanis
School of Chemical & Biomolecular Engineering
Georgia Institute of Technology

Date Approved: Aug. 11, 2015

To my beloved family

ACKNOWLEDGEMENTS

First of all, I would like to express my highest and most profound gratitude to my supervisor Prof. Samuel Graham for his guidance, encouragement, and endless support that he provided me in this research. Whenever I hit a snag during my study, he always suggested me several guides to overcome it, and provided me support. I can never express how much I am thankful to him and how much I respect him. In the future, I wish I hope that I can influence other people in the way he influenced me.

I would also like to thank all of my committee members, Prof. Ting Zhu, Prof. Shannon Yee, Prof. John R. Reynolds, and Prof. Elsa Reichmanis for their advice and participation in the review and evaluation of this work.

I acknowledge Prof. Neal. R. Armstrong at the University of Arizona for his great advice on the research, and want to thank his group members, Dr. Kai-Lin Ou, and Xin Wu for their valuable collaboration work. I also acknowledge Prof. Bernard Kippelen for giving me a chance to use their experimental systems. In particular, I am thankful to Prof. Jaewon Shim, Dr. Amir Dindar, Dr. Talha Kahn, Dr. Dokyung Hwang, Dr. Canek Fuentes-Hernandez, and Prof. Yinhua Zhou for their efforts in fabricating samples and giving time to discuss various research topics with.

I would like to thank many collaborators for their great assistance and support: Dr. Paul F. Ndione, Dr. Joseph Berry, Dr. Bradley A. MacLeod, and Prof. Dana C. Olson at the National Renewable Laboratory; Dr. Philip Schultz and Prof. Anoine Kahn at Princeton University; Dr. Yannick Lambert and Prof. Thierry Mélin at the Institute of Electronics, Microelectronics and Nanotechnology in France; Dr. David Moerman, and

Prof. David Ginger at the University of Washington; and Prof. Michael McGehee at Stanford University.

I also wish to thank all past and current group members for their assistance and support in last few years: Dr. Yongjin Kim, Dr. Anuradha Bulusu, Ankit Kumar Singh, Minseok Ha, Prof. Sukwon Choi, Samuel Haidong Kim, Shweta Natarajan, Anne M. Mallow, Georges Pavlidis, Luke A. Yates, Jason Jones, Wale Odukomaiya, Dr. Jimmy Granstrom, David Samet, and Kyungjin Kim. Especially, I want to say "thank you!" again to Dr. Anuradha Bulusu for her time with advice on various problems that I have faced and her support for my Ph.D. studies. I also thank Regina M. Neequaye for her support as our administrative assistant.

For my friends in Atlanta, I want to thank to Dr. Songkil Kim. I am really glad to have been able to study with him during my entire Ph.D. studies. I also want to thank my coffee mates, Jaeho Oh and Sangbeom Cho. I also wish to thank other fellows at the Georgia Tech: Dr. Sungbum Kang, Dr. Jinsung Hong, Namin Jeong, Dr. Jaemin Shin, Dr. Jane Kang, Myungryul Yoon, Junryul Lim, Dukjoon Kim, Namin Jung, Hongchul Son, Sangin Park, Jungwhon Kim, Seokpum Kim, Jane Kang, Siyuan Zhang.

The main part of this work has been done in The Institute for Electronics and Nanotechnology (IEN), thus I would also like to extend my gratitude to the staff and management of IEN especially Mr. Gary Spinner and Mr. John Pham for all the help and endless support.

I acknowledge financial support from the Center for Interface Science: Solar Electric Materials (CIS:SEM) an Energy Frontier Research Center (EFRC) under U.S. Department of Energy.

Last but not least, I want to thank my family for their support and love during my Ph.D. studies. I would like to acknowledge my wife, Kyung Hee Oh, for her sacrifice and support. Without her support, it would have been much more difficult to finish my Ph.D. studies, and to deal with struggles of the life in the U.S.A. I also want to acknowledge my parents and my in-laws for their endless love that makes me who I am. I am also thankful to big brother, elder sister, for their untiring support and love.

TABLE OF CONTENTS

Page

ACKNOWLEDGEMENTS iv

LIST OF TABLES x

LIST OF FIGURES xi

LIST OF SYMBOLS AND ABBREVIATIONS xxi

SUMMARY xxiv

Chapter 1 Introduction 1

1.1 Overview and Motivation 1

1.2 Objectives and scope of dissertation 6

Chapter 2 Background 10

2.1 Introduction 10

2.2 Device principle of organic photovoltaic 10

2.2.1 Organic Semiconductors 10

2.2.2 Organic Photovoltaics 12

2.3 Device degradation 16

2.4 State of efforts to improve device lifetime 23

2.4.1 Improving the intrinsic material stability 23

2.4.2 Development of Barrier Film Technology 27

2.4.2.1 Gas permeation in a barrier film 28

2.4.2.2 Issue of particles and cracks 34

2.4.2.3 WVTR of recent barrier films 36

2.5 Atomic layer deposition 40

2.5.1 Principle of atomic layer deposition 42

2.5.1.1 Thermal and plasma enhanced ALD 45

2.6 Summary 49

Chapter 3 Chemical Stability of ALD Metal Oxides 50

3.1 Introduction 50

3.2 Experimental 53

3.2.1 Sample fabrication using PEALD 53

3.2.2 Photoluminescence 56

3.2.3 Water soaking test 59

3.2.4 Spectroscopic ellipsometry 60

3.2.5 X-ray photoelectron spectroscopy 62
3.2.6 Scanning electron microscopy 64

3.3 Stability of ultrathin ALD films....................64
3.3.1 PL Emission of ZnO 64
3.3.2 ZnO PL emission with ALD capping layers....................66
3.3.3 Spectroscopic ellipsometry 72

3.4 Investigation of degradation behavior 75
3.4.1 XPS depth profiling 75
3.4.2 SEM 81

3.5 Conclusion 83

Chapter 4 ALD TiO_x as a Stable Electron Selective Layer 85

4.1 Introduction....................85

4.2 Experimental....................88
4.2.1 Sample fabrication 88
4.2.2 Film characterization....................89
4.2.2.1 Angle resolved XPS 89
4.2.2.2 UV photoelectron spectroscopy 90
4.2.2.3 X-ray diffraction 91
4.2.2.4 Transmission electron microscopy 91
4.2.2.5 Atomic force microscopy....................92
4.2.3 Cyclic voltammetry....................93
4.2.4 Si heterojunction diode device fabrication and characterization 95
4.2.5 OPV device fabrication and characterization....................98

4.3 Film properties of ALD TiO_x films 101
4.3.1 Chemical composition 101
4.3.2 Electron band energy structure 103
4.3.3 Structural properties (XRD, TEM) 105
4.3.4 Out-of-plane conductivity....................107

4.4 Investigation of charge selectivity 110
4.4.1 Electrochemical characterization of charge selectivity....................111
4.4.2 Si/TiO_x heterojunction diode characterization....................114

4.5 OPV performance 117

4.6 Conclusion 122

Chapter 5 Structural Issues of ALD Barrier Films 123

5.1 Introduction....................123

5.2 Experimental....................127
5.2.1 Sample fabrication 128
5.2.1.1 Thermal evaporation of the calcium sensor layer 128
5.2.1.2 Spin-coating of a smoothing layer 129
5.2.1.3 ALD of barrier films 130

5.2.2 Optical calcium corrosion test 131
5.2.3 Film stress measurement (curvature method) 133
5.3 Defect-related and mechanical issues of the barrier film fabrication 134
5.3.1 Issue of particles in practical deposition process 134
5.3.2 Issue of film cracking....................139
5.4 Preventing cracks of ALD barrier films 141
5.4.1 Hybrid barrier film fabrication and characterization 142
5.4.2 Effects of hybrid configuration on the barrier film integrity 143
5.5 Conclusion 147
Chapter 6 Improved Measurements of WVTR of ALD Barrier Films....................149
6.1 Introduction....................149
6.2 Optical calcium corrosion test for defect-assisted WVTR measurement 153
6.2.1 Experimental 153
6.2.2 Observation of local degradation spots in optical calcium test....................155
6.2.3 Defect assisted permeation....................158
6.2.4 Intrinsic film permeation....................162
6.2.5 Overall permeation....................164
6.2.6 Section summary....................166
6.3 Electrical calcium corrosion test for the effective WVTR measurement 167
6.3.1 Experimental 170
6.3.1.1 E-beam evaporation 173
6.3.1.2 Calcium sensor layer deposition 174
6.3.1.3 Barrier encapsulation using a side sealant 175
6.3.1.4 WVTR measurement 177
6.3.2 Results of the effective WVTR....................179
6.3.3 Section summary....................182
6.4 Conclusion 183
Chapter 7 Conclusion....................185
7.1 Summary and Conclusion....................185
7.2 Recommendations for future work 190
7.2.1 Stability of a TiO_x OPV device and barrier performance of ESL....................190
7.2.2 Ag NW TiO_x electrode for flexible electrode 191
7.2.3 Indirect encapsulation of complete devices using barrier films and adhesive 191
7.3 List of Publications 199
REFERENCES 201
VITA 223

LIST OF TABLES

Page

Table 1.1 Property comparison of TiO_x and ZnO. Adapted from reference [39, 40]. 5

Table 2.1 Measured defect sizes and defect densities for single-layer inorganic barrier films deposited on polymeric substrates. Adapted from reference [100]. 35

Table 2.2 Summary of performance of PECVD barrier films. Adapted from reference [108]. 37

Table 2.3 Summary of process and performance of ALD barrier films. Adapted from reference [57, 108]. 37

Table 2.4 Theoretical expression for crack onset strain vs. coating thickness. Adapted from reference [129]. 40

Table 3.1 Parameters for metal oxide deposition at 250°C using PEALD. 56

Table 3.2 Parameters for metal oxide deposition at 100°C using PEALD. 56

Table 4.1 List of TiO_x/Si heterojunction test diode devices with various configurations. 97

Table 4.2 List of organic photovoltaic cells. 99

Table 4.3 Ratio of oxide O 1s and hydroxyl O 1s in various thickness of TiO_x layer on ITO. 102

Table 4.4 Summary of *J-V* characteristics for $P_3HT:PC_{61}BM$ photovoltaics with various TiO_x hole-blocking layer thicknesses. 121

Table 5.1 Summary of PECVD deposition conditions for SiN_x film fabrication. 143

Table 6.1 Measured effective WVTR of ALD barrier films prepared on PET substrates. 182

Table 7.1 Summary of PECVD deposition conditions for SiN_x film fabrication. 194

LIST OF FIGURES

Page

Figure 1.1 Architectures of (a) conventional organic photovoltaics which use a highly reactive low workfunction material for electron collection and (b) inverted organic photovoltaics which use a less reactive material for electron collection to improve stability. Adapted from reference [34]... 3

Figure 1.2 Inverted OPV performance over time with sol-gel processed ZnO as an low work function modification layer using different zinc precursors: Zinc acetate (red), diethylzinc (blue), phosphonic acid-modified Zinc acetate (green), and phosphonic acid-modified diethylzinc (gray) electrodes. Adapted from reference [31]. 3

Figure 1.3 Overview of the dissertation objectives.. 7

Figure 2.1 Energy band diagram of an organic semiconductor. The ionization energy (*IE*) is the energy difference between vacuum energy level (E_{vac}) and the highest occupied molecular orbital (HOMO) energy level. Electron affinity is the energy difference between the vacuum energy level (E_{vac}) and lowest unoccupied molecular orbital (LUMO) energy level. 12

Figure 2.2 Four device architectures of conjugated polymer-based photovoltaic cells: (a) single-layer PV cell; (b) bilayer PV cell; (c) disordered bulk heterojunction; (d) ordered bulk heterojunction. Adapted from reference [50]. 13

Figure 2.3 Photovoltaic processes of a conventional bulk-heterojunction OPV device structure illustrated using an energy band diagram: (a) The light absorption and exciton formation process, (b) the charge selection process at the modification electrode interfaces, and (c) charge collection process.. 15

Figure 2.4 Degradation of organic electronic devices with and without encapsulation. (a) OLED devices with various encapusation showing that unencapsulated OLED degraded within 500 h, whereas thin film or glass encapsulated OLED last more than 2000 h,[64] (b) Short-circuit current (Isc) and effeciency of OPV devices (red) with and (black) without a barrier film.[65].. 19

Figure 2.5 Lifetime test of various types of OPV devices from 7 research groups: Institute of Physics, Ilmenau University, German (IAPP), National Renewable Energy Laboratory, USA (NREL), Interuniversity Microelectronics Centre, Belgium (IMEC), Holst Centre, Netherlands (HOLST), Fraunhofer Institute for Solar Energy Systems, German (ISE), Risø National Laboratory for Sustainable Energy, Denmark (Risø). IAPP and ISE devices have glass encapsulation, the devices last more than 1,500 h. NREL, HOLST devices have no encapsulation showing that the power conversion efficiency (PCE) drops rapidly within 100 h. IMEC device is an inverted OPV, Risø devices have thin film encapsulation, and operate up to 1,500 h. Adapted from reference [66]. 20

Figure 2.6 Chemical degradation of OPV devices. (a) Many process that conspire to degrade OPV devices related to ingress of oxygen and water including photo-oxidation effects as well as the diffusion of Al from contacts into the cell,[9] (b) TEM images for (left) freshly prepared and (right) aged ITO/BHJ/Ca/Al OPV devices. The calcium layer oxidized and formed thick calcium oxide (CaO) after operation..[54] Adapted from references. 22

Figure 2.7 General band structure of inverted an OPV using ZnO as an electron selective layer. Adapted from reference [87]. 26

Figure 2.8 Charge recombination (a) in clean bandgap material (b) in the material with sub bandgap states (defect states) at the interface of ZnO and PbS in a QDSC device. The sub bands gap states increase the chance of recombination, resulting in decrease of OPV performance. Adapted from reference [96] 26

Figure 2.9 Schematic diagrams for OLED device encapsulation structures. (a) The first structure shows a traditional package with a metal lid. The second structure (b) laminated shows a barrier-coated lid (indirect encapsulation) sealed onto the device. The third structure (c) shows a monolithic thin film barrier grown onto the device (direct encapsulation). Adapted from reference [64]. 28

Figure 2.10 Different permeation mechanism depending on defects sizes. Lattice permeation is responsible for intrinsic permeation of the material, and nano/macro defects leads to intense gas permeation depending on their size by molecular diffusion. Adapted from reference [99]. 29

Figure 2.11 Conceptual plot of cumulative permeation flux, defining lag-time and steady state regime for a single barrier layer. 30

Figure 2.12 Estimates of barrier film performance requirements for various applications, including organic electronics, along with the reported barrier performance. Adapted from references [58, 101-103]. 31

Figure 2.13 Tortuous pathway by multilayer structures. Adapted from reference [106]. .. 33

Figure 2.14 Cross-sectional image of multilayer barrier structures. (a) inorganic/organic multilayer, (b) inorganic/inorganic ALD multilayer. Adapated from reference (Barix^{TM}, Vitex systems) and [104]. 33

Figure 2.15 Nanoparticles in a barrier film. Adapted from reference [105]. 33

Figure 2.16 SEM images of Hostaphan RD 23 PET-film containing anti-block particles. Adapated from reference [43]. 34

Figure 2.17 SEM images of film defects caused by an antiblock particle and dust particles. Adapted from reference[107] 35

Figure 2.18 Crack formation of SiO_x and Al_2O_3 barrier films after a bending test. Adapted from reference [103]. 36

Figure 2.19 Various methods for WVTR measurement: (a) gravimetric cup method, (b) electrical calcium corrosion test, (c) optical calcium corrosion test, (d) mass spectroscopy, (e) radioactive tracing method, and (f) coulometic sensor method. Adapted from reference [46]. 39

Figure 2.20 crack onset strain of Al_2O_3 films depending on the film thickness. Adapted from reference [130]. 41

Figure 2.21 Cross section TEM images of CVD and ALD films. CVD film shows the grainy feature while the ALD film is uniform. Adapted from reference (Lin Wang, Dupont 2010) 42

Figure 2.22 Schematic representation of ALD using self-limiting surface chemistry and an A-B binary reaction sequence. Adapted from reference [136]. 43

Figure 2.23 Schematic of possible behavior for the ALD growth per cycle versus temperature showing the ALD window. Adapted from reference [38]. 45

Figure 2.24 Schematic representation of thermal ALD and PEALD. Adapted from reference [137]. 47

Figure 2.25 Schematic of various PEALD systems. Adapted from reference [137]. 48

Figure 2.26 Purging time comparison of thermal ALD and PEALD at various processing temperatures. 48

Figure 3.1 Accelerated thioacetamide tarnishing test of ALD coatings on silver coins (ISO 4538). The color of the coin without an ALD coating changes over time due to the thioacetamide exposure. Adapted from reference [139] 51

Figure 3.2 The dual chamber Fiji PEALD system. The right chamber is used for running the PEALD ZnO deposition, and a purple glow is observed due to Ar/O_2 plasma in the window port of the system during the oxidation step. 54

Figure 3.3 Chemical structure of metal precursors used for ALD process. (a) TMA, (b) DEZ, (c) TDMAT, (d) TDMAZ, and (e) TDMAH. 55

Figure 3.4 Schematic diagrams of tested ALD films in this PL study. From the left, an uncapped ZnO sensor sample, an Al_2O_3-coated ZnO sample, a TiO_x coated sample, a ZrO_x-coated sample, and a HfO_x coated sample. 55

Figure 3.5 Energy diagram showing absorption of light and the processes involved in the emission of light as fluorescence and phosphorescence. Adapted from reference [142] 57

Figure 3.6 The LabRAM HR800 Raman system for PL measurment. (a) whole system, (b) a sample under a microscope objective during testing. 59

Figure 3.7 Experimental procedures of water stability testing using photoluminescence spectroscopy. PL emission spectra of samples acquired periodically after water soaking at room temperature condition. 60

Figure 3.8 (a) Typical ellipsometry configuration, where linearly polarized light is reflected from the sample surface and the polarization change is measured to determine the sample response. (www.jawoollam.com) (b) Photograph of M-2000 variable angle SE system. 61

Figure 3.9 (a) Schematic showing the processes that occur during XPS where xray energy ejects a core electron which is picked up by a detector and (b) a Thermo

K-Alpha X-ray photoelectron spectroscope similar to the one used in this study (www.thermoScientific.com).. 63

Figure 3.10 The PL emission from ALD. PL emission of ALD ZnO layer on a Si substrate showed a primary peak near 350 nm and defect band between 450 and 650 nm. The signal was not detectable after water soaking for 24 h.................. 65

Figure 3.11 Integrated area of PL emission spectra of the control sample, N2-stored TiO_x coated ZnO.. 66

Figure 3.12 PL emission spectra of ALD film protected ZnO sensor samples. (a) 5 nm TiO_x, (b) 11 nm TiO_x, (c) 10 nm Al_2O_3, (d) 10 nm HfO_x, and (e) 10 nm ZrO_x capping layer. The ALD capping layers were deposited at 250°C...................... 68

Figure 3.13 PL emission spectra of ALD film protected ZnO sensor samples. (a) 10 nm Al_2O_3 and (b) 6 nm TiO_x. These capping layers were deposited at 100°C 71

Figure 3.14 Normalized peak intensity of ZnO PL emission after water soaking. (a) ALD films that are deposited at 250°C and (b) ALD films that are deposited at 100°C. 72

Figure 3.15 Ellipsometry data of ZnO and ALD protection layer before (solid lines) and after water soaking (dashed line). The light incident angle is 75°. (a) 10 nm thick ZnO layer was not measurable after 19 h water soaking. (b) Optical density and/or thickness changed in Al_2O_3 coated ZnO sample. (c) TiO_x coated ZnO shows almost no change in the ellipsometry data... 74

Figure 3.16 XPS results of Al_2O_3 samples before and after 10 day water soaking. (a) Al 2p spectrum showed no binding energy change, suggesting no chemical state change in Al_2O_3. (b) O 1s peak has more hydroxyl (OH^-) groups after 10 day water soaking due to surface.. 76

Figure 3.17 XPS depth profiling of ALD films, atomic percentage vs. etching time. X=0 corresponds to the surface of samples, and as the etch time increase the percentage represents the composition of the sample in the lower location from the surface. (a) Fresh 10 nm Al_2O_3, (b) Al_2O_3 after water soaking, (c) fresh Al_2O_3 coated ZnO, and (d) Al_2O_3 coated ZnO after 10 day water soaking.................... 78

Figure 3.18 XPS depth profiling of ALD films, atomic percentage vs. etching time. X=0 corresponds to the surface of samples, and as the etch time increase the percentage represents the composition of the sample in the lower location from the surface. (a) Fresh TiO_x coated ZnO, and (b) TiO_x coated ZnO after 10 day water soaking. 80

Figure 3.19 SEM images of ZnO/Al_2O_3 samples before water soaking (a1, a2, a3) and after water soaking for 10 days (b1, b2, b3). (a1, b1) are the top views, (a2, b2) are the tilted views, and (a3, b3) are the cross sectional side views. The Al_2O_3 surface was smooth and uniform before water soaking, but the surface has numerous black spots after water soaking. 82

Figure 4.1 Schematics of common layer structures of OPV devices in (a) conventional and (b) inverted geometries with typical materials noted. Adapted from reference [146]... 85

Figure 4.2 Band energy structure for selected metal oxides showing that TiO_x is the most similar to ZnO in terms of the water stable oxides measured in Chapter 3. Adapted from reference [153, 154] 86

Figure 4.3 Schematic illustration of election transitions in UPS.[169] The distribution of kinetic energy of excited electrons, WF and IE can be evaluated with respect to vacuum energy level. 91

Figure 4.4 (a) Typical excitation signal for cyclic voltammetry, and (b) acquired cyclic voltammogram. Adapted from reference [171]. 94

Figure 4.5 Schematic diagram of the CV measurement. ITO/ALD TiO_x samples were used as a working electrode in the measurement. 95

Figure 4.6 Si/TiO_x heterojunction diode test for charge selectivity test. (a) I-V curves of Al/TiO_x/p-type Si/Ag heterojuntion diode test device, showng retification contact was made with TiO_x and p-type Si. (b) energy band diagram of the TiO_x/Si heterjuntion diode, showng the energy barrier 2.1 eV is built at the interface of TiO_x and Si in their the valence band. Adapted from reference [172]. 96

Figure 4.7 Test structure of metal oxide/Si diode for testing the hole blocking capability of ALD TiO_x films. (a) Schematic illustration of the diode with a patterned top Al electrode, and (b) current-voltage measurement configuration by a 4 point probing method.. 97

Figure 4.8 Heterojunction Si/TiO_x diode devices. (a) Fabricated test sample and (b) custom probing stage, probing the top Al pads using 2 spring pins, and the bottom Ag layer is connected on the bottom copper surface. 98

Figure 4.9 A typical *J-V* curve of a solar device. 100

Figure 4.10 Angled resolved XPS spectrum of normalized O 1s peaks of $TiO_{x,}$ (a) spectrum of normal detection angle, 0°, and (b) spectrum of shallow detection angle, 60°. As the film thicker, the ratio of hydroxyl O1s peak (532.0 eV) to oxide O 1s peak (530.6 eV) decreases in both cases. 102

Figure 4.11 Angled resolved XPS spectrum of normalized Ti 2p peaks of TiO_x (a) at normal detection angle 0°, and (b) a shallow detection angle, 60°. No difference was observed in Ti 2p spectrum... 103

Figure 4.12 Electron band energy structures of ALD TiO_x and ZnO films. (a) UPS spectra of a 3 nm TiO_x film on Si substrate, and (b) band energy diagram from UPS spectra. 105

Figure 4.13 XRD peak analysis of 3 nm, 5 nm and 10 nm TiO_x films on Si substrates. 3 nm and 5 nm film have no peak, suggesting amorphous TiO_x. On the other hand, 10 nm TiO_x film shows XRD peaks corresponding to anatase structure............ 106

Figure 4.14 Cross-sectional TEM images of 10 nm TiO_x film on Si substrate at two locations. (The top right scale bar is 2 nm) At location (a), two crystal phases was observed in 10 nm TiOx film, and at location (b), both amorphous and crystal phase were observed. 107

Figure 4.15 Conductive AFM of the ALD TiO_x films on glass/ITO substrates. Surface morphology images of (a) 1 nm TiO_x, (b) 3 nm, and (c) 10 nm thick TiO_x films on ITO; Current mapping images of (d) 1 nm TiO_x, (e) 3 nm, and (f) 10 nm thick TiO_x films on ITO. The dark spots in the current mapping images show regions of high current. These regions increase with increasing film thickness which act to reduce the shunt resistance of the film in spite of increased film thickness. This is believed to be due to the growth of anatase crystals in the films................... 109

Figure 4.16 Histogram of conductive AFM current distribution for 1 nm, 3 nm, and 10 nm TiO_x films showing that the distribution of current widens as the film thickness increases. Overall, the shunt resistance deteriorates with increasing film thickness.. 110

Figure 4.17 Current-voltage (*I-V*) curves with C-AFM. (a) *I-V* curves of two distinguishable areas of 10 nm TiO_x C-AFM images (inset image). The dark curve comes from the bright areas where current flow is lower and the red curve comes from dark features where current flow through the film is highest. (b) Average *I-V* curves of bright areas with 1, 3, and 10 nm TiO_x films on glass/ITO substrates.. 110

Figure 4.18 Cyclic voltammograms of probe molecules Decamethylferrocene, 1,1-Dimethylforrocene, and TPD(N,N′-Bis(3-methylphenyl)-N,N′-diphenylbenzidine) with (a) bare ITO, (b) ITO/ TiO_x 0.5 nm, (c) ITO/ TiO_x 3 nm, and (d) ITO/ TiO_x 10 nm. Potential showed in graph is referenced to $Ag/AgNO_3$. The data show that current blockage begins with 0.5nm thick films and is sufficiently blocked by 3nm thick films. 113

Figure 4.19 Current density - voltage characteristics of 3 nm TiO_x layers on p-type and n-type silicon wafer ($Ag/Si/TiO_x/Al$) The p-type Si/TiO_x junction shows rectification behavior, whereas n-type Si/TiO_x junction is an Ohmic contact. Without TiO_x, the Si wafer showed a good Ohmic contact for both p-type, and n-type wafer.. 116

Figure 4.20 TiO_x heterojunction diode results in (a) linear scale and (b) log scale. The heterojunction diodes with all 0.5 nm, 1 nm, and 3 nm thick TiO_x films showed noticeable rectification performance. The turn on voltage of the diode decreased with increasing film thickness in this study as well.. 117

Figure 4.21 *J-V* characteristics of fabricated organic photovoltaic cells with various TiO_x hole-blocking layer thicknesses: (a) 0.5 nm TiO_x, (b) 1 nm TiO_x, (c) 3 nm TiO_x, and (d) 10 nm TiO_x. 121

Figure 5.1 Normalized critical strain as a function of the normalized thickness of the organic layer for cracks in inorganic layers. (a) A channel crack in the top inorganic layer, (b) a channel crack in the top inorganic layer and a propagating tunnel crack in the bottom inorganic layer, and (c) a propagating channel crack in the top inorganic layer and a propagating tunnel crack in the bottom inorganic layer sandwiched between organic layers. Adapted from reference [206]............ 126

Figure 5.2 Structures of calcium corrosion test samples ALD barrier film deposited directly on a CYTOP layer. 128

Figure 5.3 Thermal evaporation system (EvoVac, Angstrom Engineering) used for calcium deposition, which is installed in a glove box (MBraun). 129

Figure 5.4 Calcium sensor layer fabricated using the thermal evaporation.................. 129

Figure 5.5 Savannah ALD system (Cambridge Nanotech).. 131

Figure 5.6 (a) A benchtop environmental test chamber (MicroClimate, Cincinatti SubZero, Inc.). (b) Calcium test samples under testing in the environmental chamber.. 133

Figure 5.7 A flatbed photo scanner V800 (Epson). The calcium samples are mounted in a sample frame, and images were scanned while the sample is facing down (toward the image sensor). 133

Figure 5.8 Crack tip stress fields in elastic material. For a crack of length 2a in an infinite plate of unit thickness under uniform tension, the direct stress component is given by $K/2\pi r$, where K is the stress intensity factor. 135

Figure 5.9 (a) Image of Ca films on glass coated with 200 nm of CYTOP polymer and the ALD Al_2O_3/HfO_x nanolaminate. (b) Image of the sample after exposure to 50°C/85% RH for 10 days showing evidence of localized degradation (c) Microscope images showing the presence of a particle and the degradation of the Ca sensor in the vicinity of the particle. (d) SEM image of a particle defect, showing the presence of cracks in the vicinity of the particle. 137

Figure 5.10 Observed degraded calcium spots densities in a ALD films with various CYTOP layer thickness... 138

Figure 5.11 Schematic illustration of the effect of a smoothing layer on particle coverage. (a) With a thin smoothing layer more defects can be caused by poor particle coverage, and (b) With a thick smoothing layer, small particles can be covered by the smoothing layer. 138

Figure 5.12 ALD barrier films on calcium sensors on glass with various thicknesses of CYTOP polymer layers. Images a-d are as-made samples imaged immediately after barrier film deposition. Images e-h are samples imaged after 24 h at 50°C/85% RH where the Ca degradation along the crack defects are clearly visible for CYTOP layers greater than or equal to 780 nm. (It should be noted that samples with 40 nm of CYTOP did not withstand the first 24 h period and are not shown.)... 140

Figure 5.13 (a) ALD barrier films with 1000 nm thick CYTOP coated with an Al_2O_3/HfO_x nanolaminate showing the occurrence of cracks. (b) SEM image of the crack opening due to the residual tensile stress in the film (c) an optical image showing cracks initiating from a particle defect. 141

Figure 5.14 Structures of calcium corrosion test samples for a hybrid (ALD/PECVD) barrier film deposited on a CYTOP layer. 142

Figure 5.15 Oxford PECVD system used to deposit SiN_x films at a low temperature, 100°C. 143

Figure 5.16 (a) Depiction of the tensile stresses acting on a channel crack in an ALD barrier sample where the polymer layer offers little resistance to the crack opening displacement and crack driving force. (b) Depiction of the stiff and compressively stressed SiN_x acting to reduce the overall average stress in the vicinity of the ALD film and reduce the probability of cracking (as well as crack driving force). 144

Figure 5.17 Hybrid (ALD/PECVD) barrier films on calcium sensors showing the lack of crack formation after 500 h of exposure to 50°C/85% RH. In contrast to ALD barrier films which do not have the SiN_x layer, these films are more resistant to cracking and show fewer particle defects than ALD barrier films. 146

Figure 5.18 Degradation of the calcium sensor layers as a function of time for varying CYTOP film thicknesses for ALD and hybrid (PECVD/ALD) barrier films. ... 147

Figure 6.1 Two different approaches of barrier film encapsulation: (a) direct encapsulation where the barrier is grown on the device and (b) indirect encapsulation where the barrier is attached to the device using an adhesive layer. Pathways of the intrinsic film permeation and pinhole-driven permeation are illustrated with arrows. 150

Figure 6.2 Calcium corrosion test cell with a spacer used to improve measurement sensitivity developed by the National Renewable Energy Laboratory. Adapted from reference [128]. 152

Figure 6.3 Schematic diagram of (a) the calcium degradation test sample and (b) the flatbed photo scanner used to scan the image of the Ca sample to determine changes in light transmission through the Ca and regions of localized defects.. 155

Figure 6.4 An example of pinhole local degradation of a Ca sensor due to the existence of particle defects. (a) A scanned image of the full 16 calcium square sample after degradation, (b) a zoomed in image of a local degradation spot, and (c) a cross-sectional diagram of devices showing localized high permeation in regions with defects. 156

Figure 6.5 Calcium sample image of a tested barrier film (CYTOP/100 nm SiN_x/20 nm ALD/20 nm ALD nanolaminate) after 506 h at 50°C/85%RH condition. (a) Fresh calcium sample, (b) a scanned image of the calcium sample after 506 h of degradation, and (c) images showing the growth of selected local degradation spots over time. 158

Figure 6.6 Growth of local degradation spots over time: (a) Local degradation spots chosen from the 16 Ca sensors, (b) Change in the radius of the selected local degradation spots versus time, and (c) Change in area of the selected local degradation spots versus time. 160

Figure 6.7 A 1D axisymmetric diffusion model of water vapor permeation inside the underlying layers: (a) a diffusion model diagram with a quarter symmetry image of a local degradation spot, (b) The concentration contour plot on radius vs. time

plane with a constant concentration boundary condition at the center ($C=C_0$ at $r=0$), and (c) The concentration profile on radius vs. time plane with a constant total flux boundary condition, $Q=Q_0$ at $r=r_0$. 162

Figure 6.8 Uniform degradation of the calcium layer and the evaluation of the degradation. (a) An original sample image after 506 hours at 50°C/85% RH, (b) histogram of the original image with a threshold value (orange vertical line), (c) intact calcium region, selected using the threshold value, and (d) average intensity change of the intact calcium area over time. 164

Figure 6.9 Water vapor permeation test of an indirect barrier by calcium degradation. 168

Figure 6.10 Side permeation test of the sealant material (PVS101, ADCO). Calcium was encapsulated with a glass lid using the sealant, and degradation from the sample boundary was observed due to the side permeation. Adapted from reference [232] 169

Figure 6.11 Calcium corrosion test with barrier films. 'L'-shape calcium marker was embedded under the side sealant, the marker degraded due to the improper edge sealing procedure. 170

Figure 6.12 Design steps to achieve a high sensitive calcium sensor that is resistance to the side permeation: (a) dual calcium sensor layer, (b) 4 wire Au probing, card edge compatible connection pads, (c) side permeation detecting check line, (d) inner side seal, (e) interim desiccant, and (f) outer side seal. 172

Figure 6.13 Schematic of an improved sample design for electrical calcium corrosion test. 173

Figure 6.14 (a) Denton E-beam evaporation system for depositing Ca layers. (b) A shadow mask used to fabricate electrode patterns of Cr/Au layers. 174

Figure 6.15 (a) Spectros thermal evaporation system (Kurt J. Lesker), which is installed in a glove box. (b) Four 38 mm x 38 mm samples mounted on a deposition holder with a shadow mask for calcium deposition. 174

Figure 6.16 Sequence of applying the sealant strips by pieces 176

Figure 6.17 Alignment of the ADCO side sealants using 4 strips. (a) Improper alignment due to overlapping, (b) proper alignment, and (c) recommend sealant preparation. 176

Figure 6.18 Examples of good and bad applications of side sealants. The top sealant strip contacts partially with glass, whereas the bottom sealant strip completely contacts with glass. 177

Figure 6.19 (a) Data acquisition system (34970A, Agilent), (b) a multiplexer module (34901A, Agilent). 178

Figure 6.20 Configuration of the wiring of a single multiplexer module that can measure four calcium samples at a time. Two 4-wire sensing and one 2-wire sensing for each sample. 178

Figure 6.21 Electrical WVTR measurement setup for multiple samples in an environmental chamber. (a) Multiple samples under testing, and (b) a fabricated calcium sample inserted in a card edge for the test. 179

Figure 6.22. Minimum WVTR resolution test using a glass coverted control samples. (a) Schematic of the control samples covered with a glass lid, and (b) measured resistance of calcium sensor over time at two envrionmental conditions: room temperature in a lab, and 50°C/85%RH in a humidity chamber. A WVTR = $6x\ 10^{-5}$ g/m^2/day was observed due to the side permeation. 180

Figure 6.23 A) An SEM image of a nanolaminate Al_2O_3/ZnO barrier film and B) the conductance change of calcium sensors over time for an Al_2O_3, ZnO, and Al_2O_3/ZnO nanolaminate barriers. 181

Figure 7.1 Suggested integrated barrier/ESL in an inverted OPV device fabricated on polymer substrate. 191

Figure 7.2 (a) Unaxis PECVD system used to deposit SiN_x films at low temperature, 110°C. (b) Hybrid (PECVD/PEALD) barrier films prepared on PEN substrates with 50 mm x 75 mm a glass supporting substrate. 193

Figure 7.3 Adhesive lamination procedures on barrier films using a soft rubber roller. 194

Figure 7.4 Indirect encapsulation of devices using a separate barrier film. A barrier film is prepared on a separate substrate and applied on a solar cell device. 195

Figure 7.5 Photovoltaic lifetime test at controlled environmental conditions 60°C/90%RH. The measurements are repeated after exposing devices to environmental conditions. 196

Figure 7.6 Environmental stability test of perovskite solar cells with and with barrier films at room temperature conditions. (a) Devices tested in the laboratory environments and (b) photo images of the devices before and after 36 h. 197

Figure 7.7 PCE vs. time of perovskite solar cells with (red) and without (black) barrier films tested in laboratory condition. The two packaged cells (red) operated with the PCE over 10% up to 35 days, where the two unpackaged cells (dark) degraded rapidly when they exposed to ambient light. 198

LIST OF SYMBOLS AND ABBREVIATIONS

E_G	bandgap energy
I	current
J	current density
J_{SC}	short-circuit current density
R_P	shunt (parallel) resistance
R_s	series resistance
V	voltage
V_{OC}	open-circuit voltage
δ	density
ρ	resistivity
E	Young's modulus
v	Poisson's ratio

AFM	atomic force microscopy
ALD	atomic layer deposition
CTE	coefficient of thermal expansion
CVD	chemical vapor deposition
DEZ	diethyl zinc
DLE	deep level emission
EA	electron affinity
FF	fill factor
GIXRD	grazing incidence X-ray diffraction
HOMO	highest occupied molecular orbital

IE	ionization energy
ITO	indium tin oxide
LUMO	lowest unoccupied molecular orbital
NBE	near band edge
OLED	organic light emitting diode
OPV	organic photovoltaic
OTFT	organic thin film transistor
OTR	oxygen transmission rate
P_3HT	poly(3-hexylthiophene)
PA	phosphonic acid
$PC_{61}BM$	phenyl-C61-butyric acid methyl ester
PCE	power conversion efficiency
PEALD	plasma enhanced atomic layer deposition
PECVD	plasma enhanced chemical vapor deposition
PEDOT:PSS	poly(3,4-ethylenedioxythiophene) polystyrene sulfonate
PEIE	polyethylenimine exothylated
PEN	polyethylene naphthalate
PET	polyethylene terephthalate
PL	photoluminescence
RH	relative humidity
rms	root mean square
sccm	standard cubic centimeters per minute
SE	spectroscopic ellipsometry
SEM	scanning electron microscopy
TDMAH	tetrakis(dimethylamido) hafnium

TDMAT	tetrakis(dimethylamido) titanium
TDMAZ	tetrakis(dimethylamido) zirconium
TEM	tunneling electron microscopy
TMA	trimethylaluminum
UPS	UV photoelectron spectroscopy
WF	work function
WVTR	water vapor transmission rate
XPS	X-ray photoelectron spectroscopy
XRD	X-ray diffraction

SUMMARY

Organic electronic devices are attractive for their potential to produce lightweight, scalable, and flexible electronics as opposed to traditional inorganic electronics. In spite of these advantageous properties, the implementation of organic electronics in many applications is still challenging because of the potential for rapid degradation upon environmental exposure to oxygen, humidity, and mechanical stress. To enhance the stability of the devices, a reliable barrier layer to prevent the ingress of moisture and oxygen is required as well as more stable functional layers inside the device. Both of these goals can be partially achieved using defect-free conformal atomic layer deposition (ALD) films integrated into the devices. However, the practical electrical performance as well as the chemical stability of ultrathin ALD films has not received much attention from researchers. In some cases, characterization methods for the ultrathin ALD films have not been established. Therefore, this dissertation work proposes to investigate the functional properties of ultrathin (<10 nm) ALD films to create an encapsulation barrier film as well as to create environmentally robust coatings for electron selective contacts in organic electronics to improve their reliability.

First, the chemical stability of ALD in aqueous environments was evaluated. Based on the results, select ALD films were applied as either electron selective functional layers to modify ITO contacts in an organic solar cell or as a robust encapsulation barrier layers for organic solar cells. In addition, the gas barrier performance of ultrathin ALD films was investigated using an improved calcium corrosion test, which can discriminate between the intrinsic film permeation and the defect-assisted permeation. Also, the

mechanical failure of the barrier films in the presence of particle defects observed in the fabrication process of ultrathin thin films are discussed, and a method to circumvent such issues is suggested. Finally, this research developed two methods to improve the characterization of ultrathin barrier films, first in improving the measurement of the effective water vapor transmission rate and then a method to measure the intrinsic and defect assisted permeation rate through barrier films. These methods together have established chemical, electrical, mechanical, and permeation characterization methods to evaluate the potential of ultrathin ALD film for the enhancement of the stability of organic photovoltaic devices.

CHAPTER 1

INTRODUCTION

1.1 Overview and Motivation

With the development of functional organic materials,[1, 2] organic electronics such as organic photovoltaics (OPVs), organic light emitting diodes (OLEDs), and organic thin film transistors (OTFTs) have received much attention from researchers as a new class of electronic devices. Organic electronic devices overcome certain limitations of inorganic materials [3-5] possessing a number of advantages such as being lightweight, having a wide range of tunable properties, flexibility, and being amenability to large-area manufacturing process.[5-7] However, unlike inorganic devices, organic devices are highly susceptible to degradation from environmental exposure to UV, heat, and water vapor or oxygen because of their intrinsic chemical reactivity.[7-11] Therefore, resolving the issue of the chemical reliability of organic electronic devices is one of the top priorities for the long-term performance and the adoption of these devices with the advantages.

A major effort to extend the lifetime of organic electronic devices is to prevent any oxidation of layers in the devices. Methods to prevent the oxidation of layers in organic electronics can be accomplished either by introducing chemically stable materials or by encapsulating the device with a gas barrier film. In conventional OPVs, low work function materials, such as calcium (Ca) and lithium fluoride (LiF) have been successfully used as electrode modification layers for low work function electrodes, but their susceptibility to oxidation limits the lifetime of device operation.[12-14] To prevent the oxidation of the low work function electrodes, an inverted OPV was introduced by

researchers by reducing the surface work function of more stable high work function electrode materials through chemical modification or the use of coatings such as phosphonic acids,[15, 16] polyethylenimine exothylated (PEIE),[17-19] or zinc oxide (ZnO) (**Figure 1.1**).[19-22] By creating low work function electrodes such as indium tin oxide (ITO) modified with the aforementioned coatings, it is possible to use high work function electrodes such as molybdenum oxide/silver (MoO_x/Ag) as an anode electrode, thus providing electrical contacts with improved chemical stability.[19, 23, 24] To date, ZnO modified ITO has been the primary modified electrode used in inverted organic photovoltaics,[20, 25-27] but ZnO is also susceptible to degradation upon exposure to moisture,[28-30] thus providing a reliability issue in OPVs.[31, 32] **Figure 1.2** shows stability study of inverted OPVs with ZnO layers, and it indicates that the device performance degrades and the degradation rate is affected by the types of ZnO layer. Other modifiers such as phosphonic acids[15, 33] and PEIE[17, 18] have not undergone chemical stability testing in the presence of moisture in OPVs, so their susceptibility is still unknown. Therefore, it is still required to investigate low work function modification layers with good chemical stability and required electrical properties.

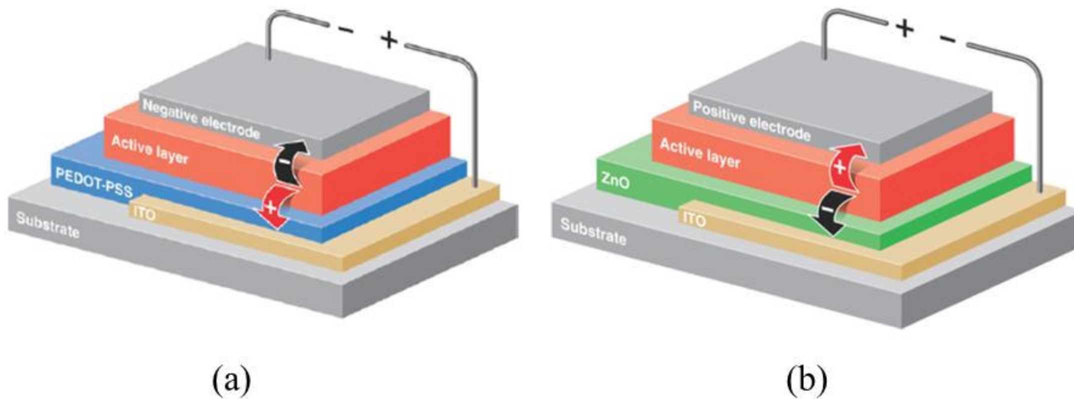

Figure 1.1 Architectures of (a) conventional organic photovoltaics which use a highly reactive low workfunction material for electron collection and (b) inverted organic photovoltaics which use a less reactive material for electron collection to improve stability. Adapted from reference [34].

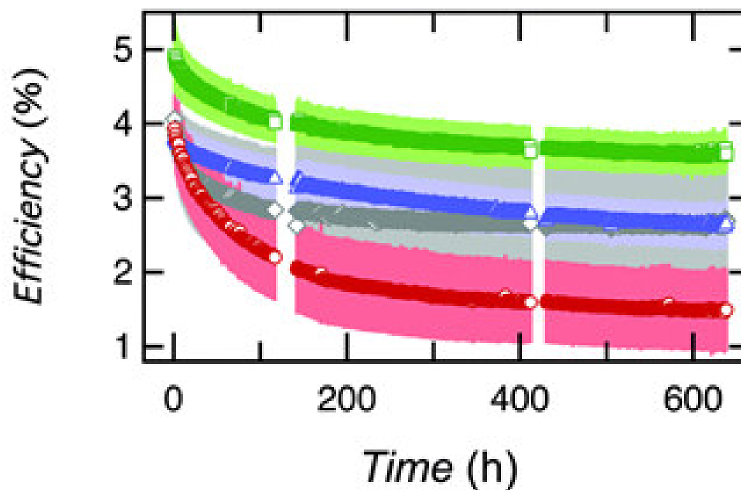

Figure 1.2 Inverted OPV performance over time with sol-gel processed ZnO as an low work function modification layer using different zinc precursors: Zinc acetate (red), diethylzinc (blue), phosphonic acid-modified Zinc acetate (green), and phosphonic acid-modified diethylzinc (gray) electrodes. Adapted from reference [31].

As a promising candidate for the use of low work function modification layer, titanium oxide (TiO_x) has been watched with interest. TiO_x is a semiconductor that has similar band energy structure with ZnO, and thus provides electron/hole selectivity that is required for the electrode of organic solar cells. TiO_x has been widely used in dye-

sensitized solar cell (DSSC) as an electron acceptor [35, 36]. In addition, the use of photocatalyst in water treatment applications has proven the water resistance of bulk TiO_x material. **Table 1.1** compares electric and chemical properties of bulk TiO_x and ZnO materials. Compared to ZnO, TiO_x has advantages in terms of fast charge injection rate, and fewer sub-band gap states that reduce the potential for charge recombination. Therefore, it is expected to serve as a good electrode contact layer with environmental stability. However, the challenge is that the electron mobility of TiO_x is much lower (0.1-4 cm^2/V s) than that of ZnO (200-300 cm^2/V s) so that it is difficult to replace ZnO in the same structure. Therefore, in order to use TiO_x as a low work function modification layer, the high resistance of TiO_x should be compensated for by methods such doping or fabricating an extremely thin layer to minimize resistance of the layer. Using conventional film deposition methods such as evaporation, sputtering, chemical vapor deposition methods, however, thin films in the range of 10 nm are difficult to produce without sacrificing the film coverage and allowing defects such as pinholes which lowers the shunt resistance of a photovoltaic. Therefore, atomic layer deposition (ALD), which can be used to control the film thickness on the order of 0.1 nm,[37, 38] is an interesting method to fabricate ultrathin TiO_x layers for the use of low work function modification layers that may serve as a replacement for unstable ZnO layers.

Table 1.1 Property comparison of TiO_x and ZnO. Adapted from reference [39, 40].

Properties	TiOs	ZnO
Electron mobility	0.1-4 cm^2/V s	200-300 cm^2/V s
Charge injection rate	fast	Moderate
Stability	good	Poor
Sub band gap states	few	Many
Band gap	3.2-3.6 eV (anatase)	3.2-3.4 eV

In addition, while such electrodes are in improvement over the conventional OPV structure, it is still desired to have a hermetic packaging to block the ingress of moisture and oxygen into the OPV to both prevent the potential of electrode degradation as well as protect the active layers of the OPV. For this purpose, commercial organic electronic devices still rely on conventional packaging methods such as metal lids or glass encapsulation to protect the device from environmental exposure. However, the advantages of organic electronics have not been fully utilized with these rigid type packaging. To prevent gas permeation into organic devices using thin film barrier, the film should possess no defects as well as have good coverage on a device or a substrate. Therefore, defect-free conformal ALD films have the potential to meet the thin-film barrier requirements for OPVs and other organic electronics.[26, 37, 41, 42] Moreover, ALD has potential to fabricate conformal thin films for the above applications to improve the environmental reliability of organic electronic devices. However, the chemical stability of ultrathin ALD films, that is precedence property, have not been studied actively. Also, characterization methods to evaluate the environmental stability of the ultrathin (<=10 nm) ALD films have not been established yet.

Even if ALD has the potential to produce defect-free and chemically stable films, actual films may possess defects by external factors such as dust particles.[43, 44] The defects can provide stress concentrations as well, and may result in structural failure such as cracks in the film. In addition, those extrinsic defects contribute to the gas permeation rate, and reduce the barrier performance of films. Therefore, a proper investigation method that can identify the permeation mechanism of barrier films as well as that is sensitive enough to measure the low permeation rate is required to evaluate barrier film performance. For the measurement of gas permeation, calcium corrosion method has been used in recent studies.[45-47] However, those studies still have not provided the information of defect-assisted permeation in a barrier film.

Therefore, the goal of this dissertation is to investigate the properties of ultrathin ALD films regarding its chemical stability, electric properties of ALD TiO_x for a stable low work function modification layer, and gas barrier property for an external device packaging application. For the chemical stability study, an optical sensor method using photoluminescence spectroscopy will be introduced to investigate the stability of ultrathin ALD films in water. For an electrode modification layer, the electrical and chemical properties of ultrathin TiO_x films will be investigated and demonstrated in OPV devices. For barrier film applications, the defect-related structural issues will be discussed first, and then the measurement of gas permeation will be addressed with improved gas permeation characterization procedures using calcium corrosion test.

1.2 Objectives and scope of dissertation

As has been discussed above, this research will seek to improve the reliability and lifetime of organic electronic devices using ALD films. The research will focus on two strategies to achieve the goal of the reliability improvement: an internal approach to improve the intrinsic device reliability by employing an environmentally stable work function modification layer to create electron selective contacts, and an external approach to improve the lifetime of device by creating ALD based barrier films. In both approaches, the salient film properties will be characterized based on the purpose of applications. If necessary, new or improved characterization methods will be also introduced. **Figure 1.3** shows the overview of research objectives of the dissertation.

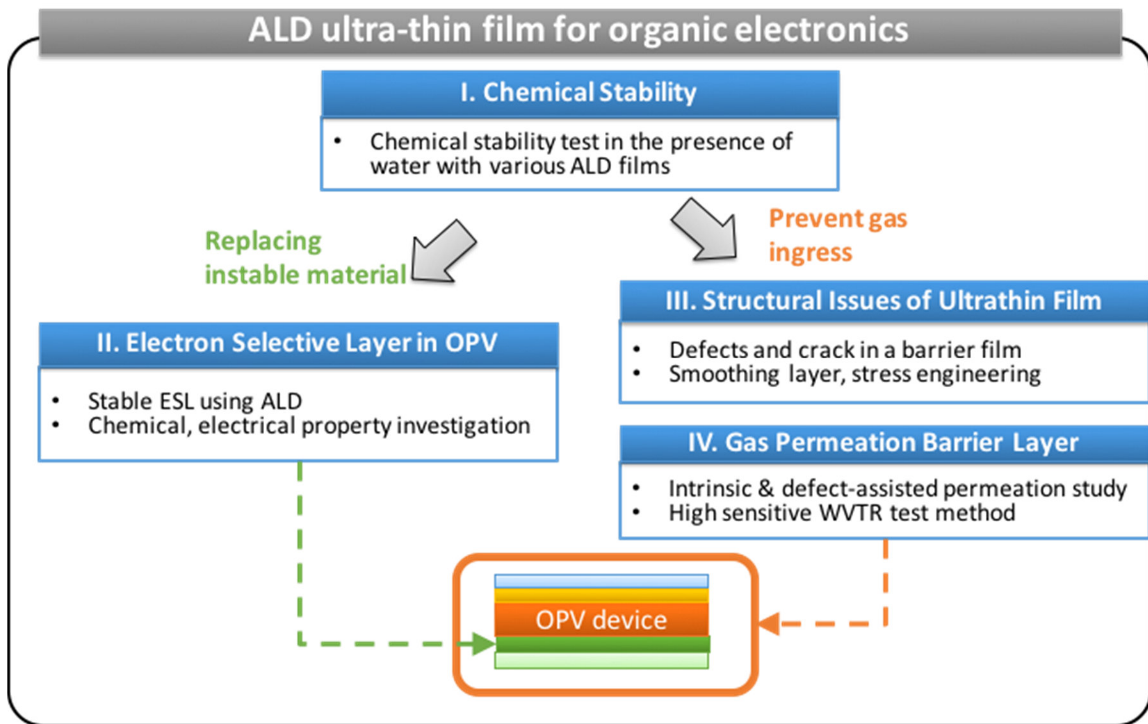

Figure 1.3 Overview of the dissertation objectives.

According to the objectives described above, this dissertation is organized as follows. First, Chapter 2 will give background information regarding organic photovoltaic devices and their current status regarding their reliability. Chapter 3-6 will present the details of ALD film study for improving device lifetime. The details of Chapter 3-6 are as follows:

- Chapter 3 will investigate the fundamental chemical stability of ultrathin ALD films. For the investigation, the passivation performance of various ALD films exposed to water will be tested by introducing a zinc oxide (ZnO) photoluminescence (PL) sensor technique. Additional film characterization will be also performed to understand the chemical stability of the ALD films.
- Chapter 4 will utilize an ultrathin ALD TiO_x layer to create an electron selective contact for OPV devices. In this effort, ALD titanium oxide (TiO_x) film will be investigated, and its chemical, structural, and electrical properties will be examined. Chapter 4 will also demonstrate OPV devices with the ultrathin ALD films.
- Chapter 5 will discuss the structural issues of thin ALD films for barrier film application. This chapter will address mechanical issues such as cracks and defect that can arise during the film deposition process, and will introduce possible solutions to avoid those structural issues using a smoothing layer and residual stress arrangement.
- Chapter 6 will investigate the gas barrier performance of ALD films for the application of external device packaging. Chapter 6 will show improved barrier

performance test procedures using calcium corrosion. Also, improved analysis procedures to allowing the separation of intrinsic permeation and defect assisted permeation to the barrier performance will be shown for the first time.

Finally, Chapter 7 will summarize the achievement and the contribution of this dissertation. Chapter 7 will also address future work that can strengthen the research and extend the research for further applications.

CHAPTER 2

BACKGROUND

2.1 Introduction

Chapter 2 will explain the fundamentals of organic photovoltaic (OPV) devices, and will describe the degradation issues of the devices related to environmental exposure. Afterwards, current studies to improve the environmental reliability will be discussed. Finally, atomic layer deposition (ALD) will be explained as a thin film fabrication method and its potential to fulfill the requirements of films used in the fabrication of OPVs such as environment stability, converge, thickness control.

2.2 Device principle of organic photovoltaic

2.2.1 Organic Semiconductors

Organic thin film electronics such as OPVs are comprised of organic semiconductors. The organic semiconductors can be broadly classified into small-molecules and polymers depending on their molecular weight and basic units.[48] The electro-chemical properties of the organic semiconductors such as energy levels and charge transport rate can be tailored by modifying the chemical structure of organic molecules, which provides more versatility than inorganic semiconductors. The common optical and electronic characteristics of organic semiconductors arise from electronic conjugation, the alternation of single and double bonds between carbon atom.[49] The delocalized π molecular orbitals formed by overlapping π atomic orbitals along the

backbone define the frontier electronic levels, highest occupied molecular orbital (HOMO, bonding orbital) and lowest unoccupied molecular orbital (LUMO, anti-bonding orbital), depending on the configuration of signs of the p_z orbital. The HOMO and LUMO are separated by an energy band-gap (E_G) that makes such an organic compound a semiconductor. The HOMO and LUMO bear analogy to the valence band and the conduction band, respectively, in an inorganic semiconductor. **Figure 2.1** illustrates the energy band diagram of organic (inorganic) semiconductor, which shows location of E_{vac}, LUMO, HOMO, and presents the E_G, ionization energy (IE), electron affinity (EA), and work function (*WF*). However, being different from inorganic semiconductors, the organic semiconductors can be processed at low-temperature and large-scaled by casting or roll-to-roll process that can reduce the manufacturing costs. This section will introduce the fundamental knowledge of OPV device, representative organic electronic devices.

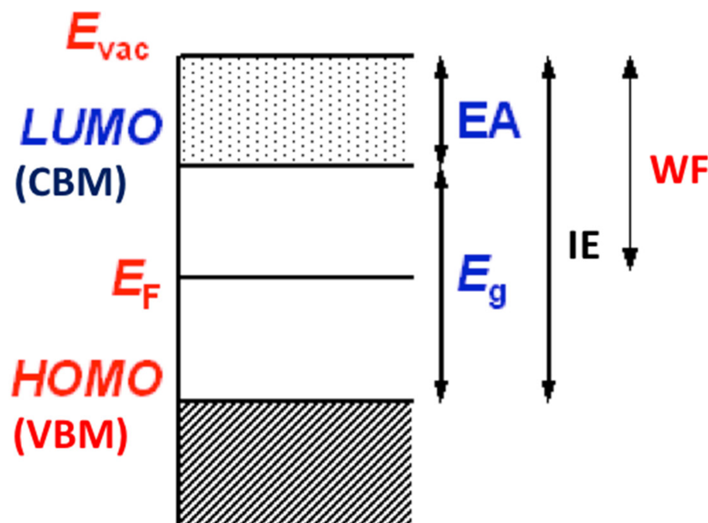

Figure 2.1 Energy band diagram of an organic semiconductor. The ionization energy (*IE*) is the energy difference between vacuum energy level (E_{vac}) and the highest occupied molecular orbital (HOMO) energy level. Electron affinity is the energy difference between the vacuum energy level (E_{vac}) and lowest unoccupied molecular orbital (LUMO) energy level.

2.2.2 Organic Photovoltaics

Organic photovoltaics (OPVs) are devices that convert sunlight into electricity by employing thin films of organic semiconductors. After the first invention of organic photovoltaics by Tang in 1986,[1] the operating principles of OPVs have been researched intensively. One of the most essential parts in organic photovoltaics is the light-absorbing semiconducting layer, also referred to as the photoactive layer. As described previously, if a photon with energy larger than the E_G is absorbed in the light-absorbing donor layer, an electron is excited and forms an exciton, *i.e.*, a bound electron-hole pair. Excitons diffuse to an electron acceptor layer where they dissociate and transfer an electron into the acceptor layer while the hole is transported in the donor layer. The energy difference of lowest unoccupied molecular orbital (LUMO) of donor material and the highest

occupied molecular orbital (HOMO) of the accepter layer help to generate an open circuit voltage in the OPV. In general, electron donor layer has low ionization energy (IE), and the electron acceptor layer has a high electron affinity (EA).[49] Depending on the configuration of the donor and accepter layers, the OPV can be categorized by a single, bilayer, disordered bulk heterojunction, and ordered heterojunction OPV as seen in **Figure 2.2**.

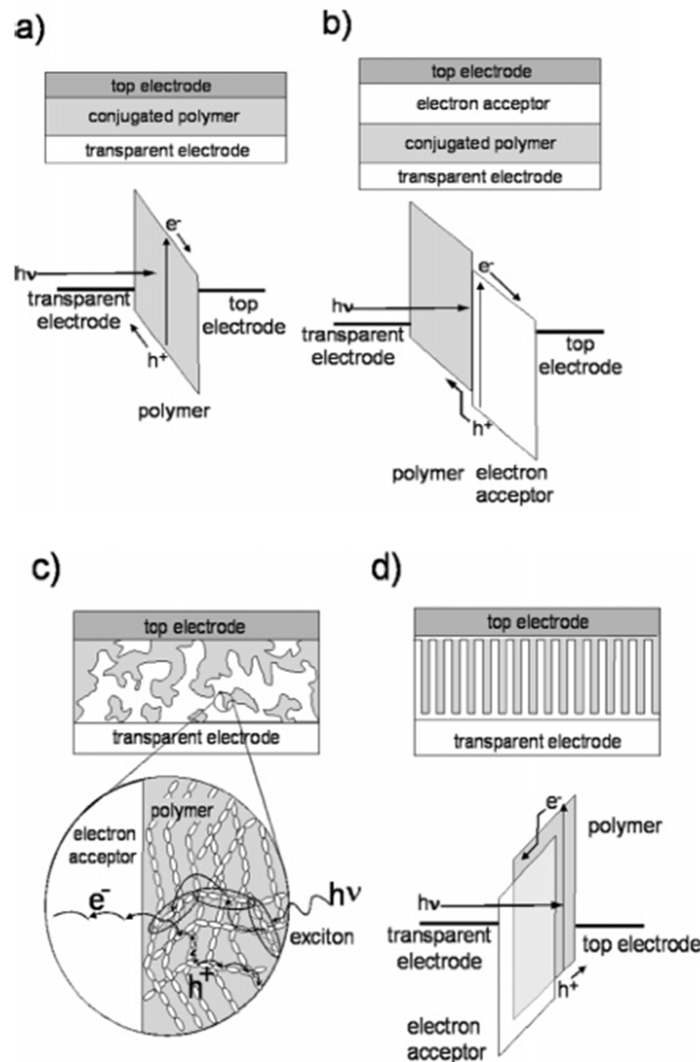

Figure 2.2 Four device architectures of conjugated polymer-based photovoltaic cells: (a) single-layer PV cell; (b) bilayer PV cell; (c) disordered bulk heterojunction; (d) ordered bulk heterojunction. Adapted from reference [50].

Figure 2.3 depicts the operating principle of a heterojunction OPV device in further detail through an energy band diagram. First as show in **Figure 2.3** (a), photons with an average energy larger than the optical band-gap of the photoactive layer are absorbed in the photoactive donor layer, and excite an electron in the ground state to a higher energy state. The excited electron relaxes down to the lowest excited state and forms an exciton that is generally known as Coulomb-bound electron-hole pairs.[51] Since the binding energy of the exciton is on the order of 500 meV at room temperature and is larger than their thermal energy (25 meV),[52] a donor-acceptor interface is required to dissociate an exciton into free charge carriers, which is called a hole selective layer or an electron selective layer, respectively, as in **Figure 2.3** (b). Once excitons reach the donor-acceptor interface, they can dissociate to free charges and transport to their respective electrodes as in **Figure 2.3** (c). Still, many factors such as the energy level mismatch between the work function (WF) of charge-collecting electrodes and the EA or IE of the organic semiconductor, the interfacial charge distribution, *etc*., can affect the charge collection efficiency at the interface.[51, 53] In addition, since the diffusion length of the exciton is short, 4- 20 nm, a bulk heterojunction structure with dimensions of nanoscale heterogeneity on the order of the diffusion length is preferred in order to minimize the charge recombination that can occur if charges were not dissociated and transferred to the electrode interface within.[50, 51]

Figure 2.3 also presents common material comprising a conventional OPV device. Poly 3-hexylthiophene (P3HT) and phenyl-C_{61}-butyric acid methyl ester (PCBM) are common donor and accepter materials used in organic photovoltaics. For the hole collecting electrode, indium tin oxide (ITO) is used as a transparent electrode, and

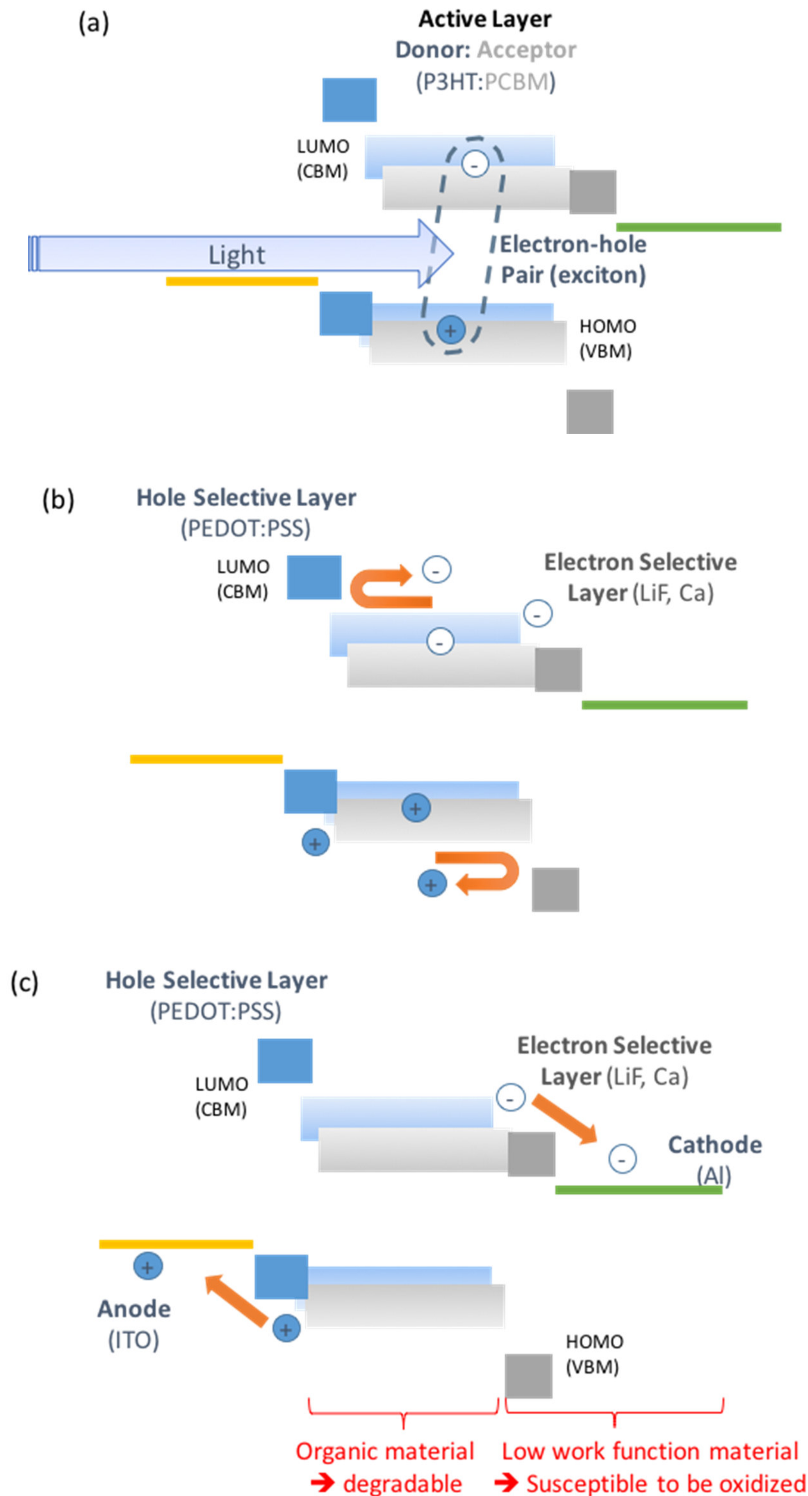

Figure 2.3 Photovoltaic processes of a conventional bulk-heterojunction OPV device structure illustrated using an energy band diagram: (a) The light absorption and exciton formation process, (b) the charge selection process at the modification electrode interfaces, and (c) charge collection process.

poly(3,4-ethylenedioxythiophene) polystyrene sulfonate (PEDOT:PSS) is used for the high work function hole selective layer (HSL) with high WF. In an electron collecting electrode (cathode), aluminum is used for an electrode, and low WF materials such as lithium fluoride (LiF) or calcium (Ca) is widely used for an electron selective layer (ESL).

Currently, the majority of research is focused on improving the power conversion efficiency (PCE) of the photovoltaics by finding high efficiency photoactive materials and improved charge selective layers. The bottleneck of the OPV cells or hybrid cells still lies in the reliability of the devices. Particularly, the low work function materials used for an electron collection layer such as LiF and Ca are highly susceptible to oxidation and limit the lifetime of the device in practical application.[54] Therefore, avoiding the degradation of those layers is primary concern for the application of OPV devices. In the following section, the degradation issues will be discussed, and efforts to suppress the degradation will be addressed by an inverted configuration, new materials, and barrier encapsulation.

2.3 Device degradation

The previous section 2.2 introduced a representative organic photovoltaic device, OPVs, and explained the principle of operation the device. Even though there has been significant improvement in OPV devices in terms of device performance, the critical challenge of OPV devices still exists in the issue of environmental stability. One approach to address the stability is to improve the chemical stability of the active layers. For example, P3HT was found to be orders of magnitude more stable than poly-

phenylenevinylene (PPV) derivatives, which had been widely used as a p-type semiconducting polymer in early stage OPVs.[14, 55, 56] In addition to active layers, the stability issues also occur at the cathode layer and electron selective layer (ESL), whose work functions are low and they are susceptible to being oxidized. However, even as more air-stable materials are being developed, the development of such materials has not reached a stage which is sufficient to address the lifetime of organic electronics.[9, 57-60] Thus, the subsequent approach is to encapsulate organic electronic devices with a gas barrier layer on each side, which prevents oxygen and water vapor permeation. While most barrier research is focused on developing high performance barrier films to be placed around the exterior of the device, a few studies have begun to investigate methods to integrate the barrier into the electrode structure of the organic electronic devices.[11, 61-63] Such integrated approaches simplify the structure of organic electronics and are attractive from a manufacturability point of view. In general, both the electrode modification and barrier films can be deposited by atomic layer deposition that allows for excellent control over the thickness and composition of the modification and/or barrier layers. Thus, the work proposed here will investigate the use of this technology to create both ESL and barrier films to address the stability in organic electronics.

Figure 2.4 demonstrates the degradation of organic devices with and without encapsulation.[64, 65] The performance of organic devices degrades rapidly without encapsulation, whereas the devices with encapsulation work for an extended time. In 2012, International Summit on Organic Photovoltaic Stability carried out a life time test for various OPV devices from 6 research laboratories: Institute of Physics, Ilmenau University, German (IAPP), National Renewable Energy Laboratory, USA (NREL),

Interuniversity Microelectronics Centre, Belgium (IMEC), Holst Centre, Netherlands (HOLST), Fraunhofer Institute for Solar Energy Systems, German (ISE), and Risø National Laboratory for Sustainable Energy, Denmark (Risø).[66] **Figure 2.5** plots the results of the study in terms of power conversion efficiency (PCE) versus time. OPVs from IAPP and ISE have glass encapsulation, and the devices last up to 1,800 hours. OPV devices from Risø have thin film barriers, and lasted for 1,800 hours but with low PCE. The OPV device from IMEC is an inverted OPV, which will be discussed in the next section, also lasted for 1,800 hours. However, the performances of the other conventional OPVs without encapsulation decrease rapidly within 200 hours. These results suggest that OPV devices are very sensitive to environmental exposure, and how important the barrier encapsulation is to improve the environmental reliability of OPV devices.

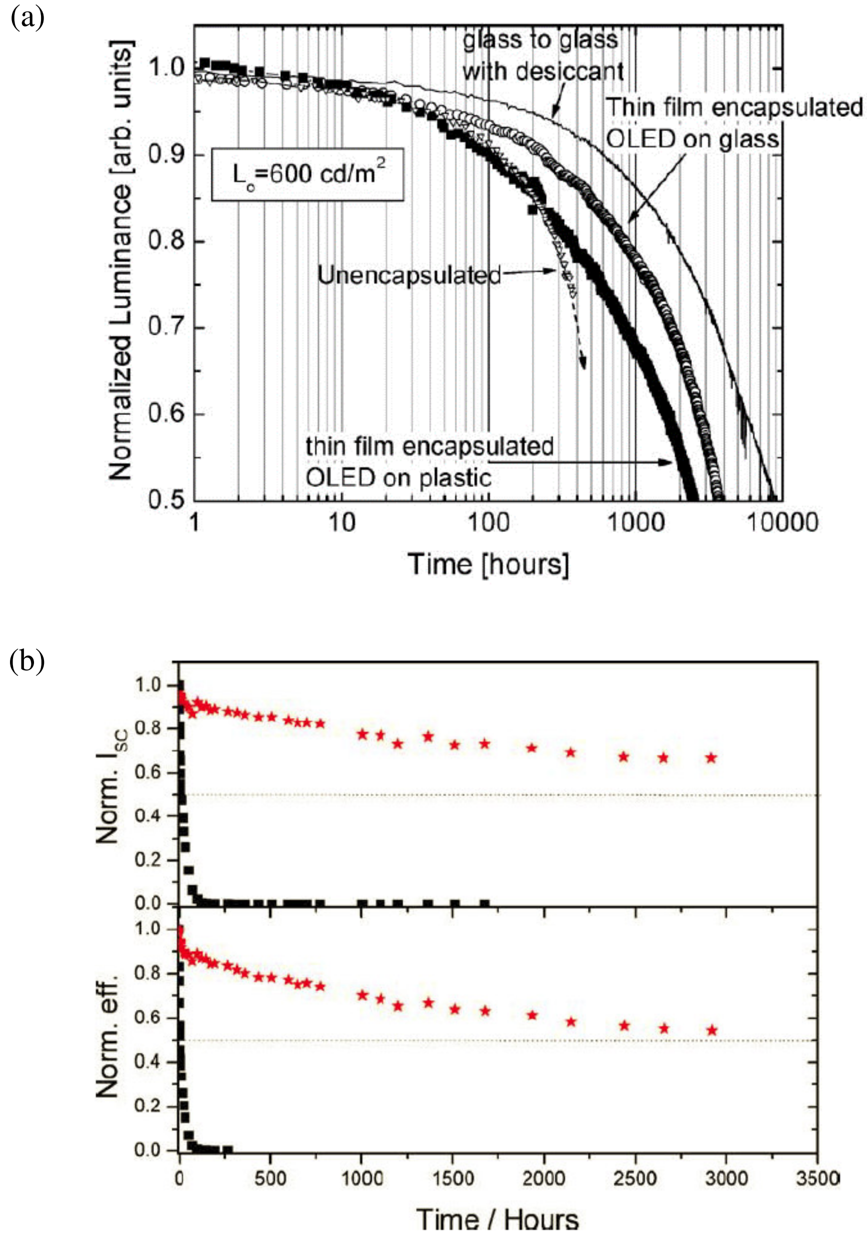

Figure 2.4 Degradation of organic electronic devices with and without encapsulation. (a) OLED devices with various encapusation showing that unencapsulated OLED degraded within 500 h, whereas thin film or glass encapsulated OLED last more than 2000 h,[64] (b) Short-circuit current (Isc) and effeciency of OPV devices (red) with and (black) without a barrier film.[65]

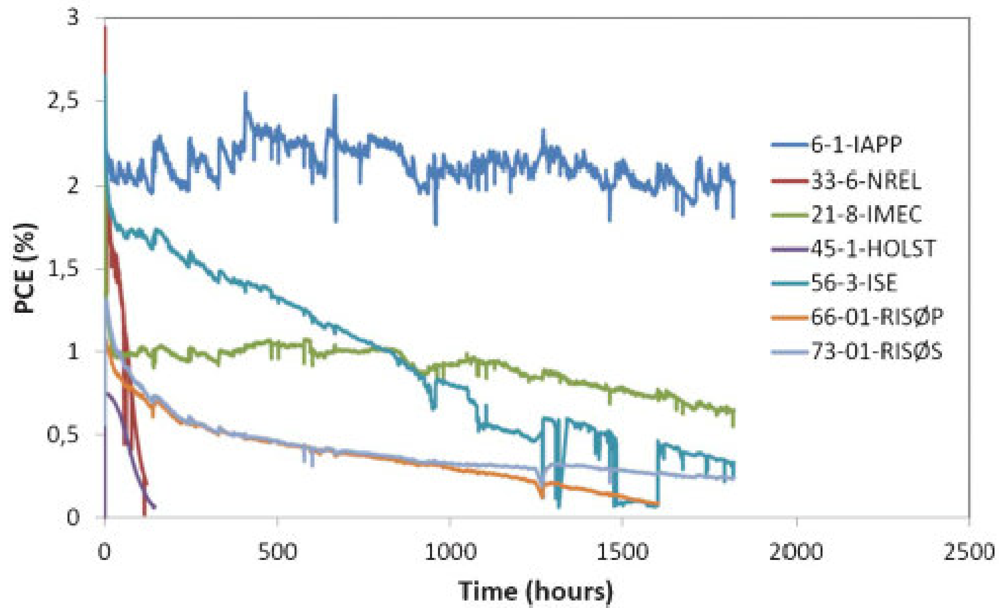

Figure 2.5 Lifetime test of various types of OPV devices from 7 research groups: Institute of Physics, Ilmenau University, German (IAPP), National Renewable Energy Laboratory, USA (NREL), Interuniversity Microelectronics Centre, Belgium (IMEC), Holst Centre, Netherlands (HOLST), Fraunhofer Institute for Solar Energy Systems, German (ISE), Risø National Laboratory for Sustainable Energy, Denmark (Risø). IAPP and ISE devices have glass encapsulation, the devices last more than 1,500 h. NREL, HOLST devices have no encapsulation showing that the power conversion efficiency (PCE) drops rapidly within 100 h. IMEC device is an inverted OPV, Risø devices have thin film encapsulation, and operate up to 1,500 h. Adapted from reference [66].

The major cause of the device degradation over time is reported as a chemical instability of functional layers in organic devices.[7, 9, 55, 67, 68] In particularly, the oxidation of layers due to the ingress of moisture and oxygen results in the chemical-electrical property changes and raises the degradation of the device performance. **Figure 2.6** (a) shows the schematic of oxidation in an OPV device. Permeated oxygen and moisture react with functional layers at various locations of the device. In particular, the oxidation process is more dominant in low work function materials, In addition, hygroscopic organic materials such as PEDOT:PSS and P3HT can accelerate the permeation of

moisture, and cause more rapid oxidation process in a device.[67, 69] For example, **Figure 2.6** (b) shows the oxidation of calcium. In an extreme case, the oxidation process can cause the delamination between the layers because of the formation of gaseous products, which results in adhesion failure in a device as well.[70, 71]

Therefore, major goals of research to improve the environmental reliability are focused on replacing the sensitive materials with more stable materials and preventing oxygen and moisture permeation by packaging.

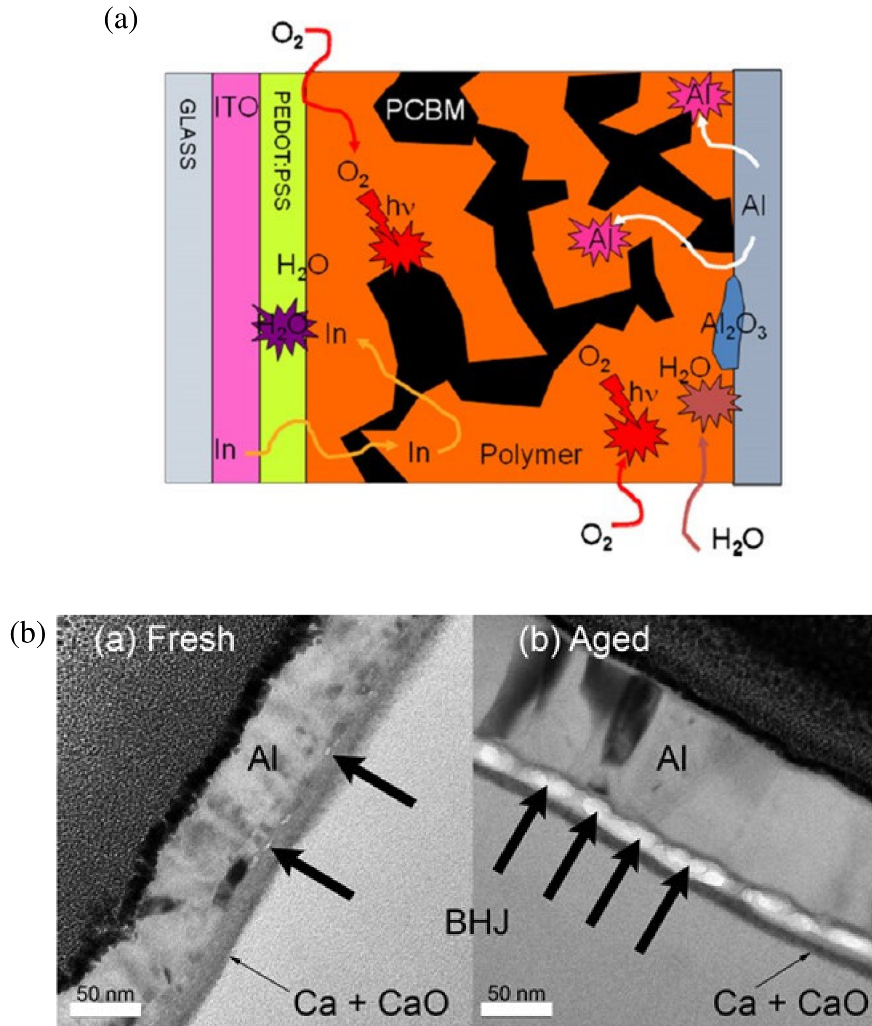

Figure 2.6 Chemical degradation of OPV devices. (a) Many process that conspire to degrade OPV devices related to ingress of oxygen and water including photo-oxidation effects as well as the diffusion of Al from contacts into the cell,[9] (b) TEM images for (left) freshly prepared and (right) aged ITO/BHJ/Ca/Al OPV devices. The calcium layer oxidized and formed thick calcium oxide (CaO) after operation..[54] Adapted from references.

2.4 State of efforts to improve device lifetime

Section 2.3 explained the degradation issue of organic photovoltaic devices, and the major cause of their degradation, which is chemical instability of materials. This section will introduce the status of research to improve the device reliability as well as more details of practical devices. While the issues described here are focused on OPVs, some of the issues are similar to those found in other organic electronic systems such as organic light emitting devices (OLEDs) and organic thin film transistors (OTFTs) and some solutions discussed herein can be applied to them (e.g., barrier film technology).

2.4.1 Improving the intrinsic material stability

One of the goals to improve the device reliability is to improve the intrinsic chemical stability of materials that used in devices. In OPV devices, the ESL layer or the cathode metal was one of the critical locations of oxidation. Still, thin interlayer materials are essential to act as hole blocking layers at the ESL or electron-harvesting contact, to enhance charge collection efficiency and reduce recombination, leading to enhanced device fill factor (*FF*) and increased device shunt resistance (R_P), without undo increases in series resistance (R_S).[72] In standard OPV devices, Ca or Al/LiF can be used as electron harvesting contacts.[19, 73, 74] However, it is well known that low work function metals with low ionization energies are highly reactive and not environmentally stable, thus limiting the lifetime of OPV devices when employed.[54]

One elegant way to overcome such an issue is the so-called "inverted" BHJ PSC as shown **Figure 1.1**, a device geometry in which the charge collection is inverted in comparison with the standard geometry device. In the inverted structure, the electrons

are collected by the bottom electrode and the holes by the top electrode (in contact with air in **Figure 1.1**). The inverted configuration removes the use of highly reactive low work function materials to improve device lifetime.[75, 76] The transparent conductive oxide contact (e.g., ITO) is modified to become an electron harvesting contact by lowering its work function through the introduction of interlayer materials such as phosphonic acids, polymer layers, and metal oxides.[9, 15, 19-21, 26, 33, 76-80] This inverted geometry allows one to use a high work function top metal electrode, like silver or gold (thus avoiding its fast oxidation and degradation), and eliminates the need of a polymeric hole transport layer such as PEDOT:PSS, typically of an acidic and hygroscopic material, on top of the transparent metal oxide bottom electrode. In this configuration, an additional benefit is that the permeation of oxygen or moisture takes longer time to reach the electron harvesting contact, and thus the device can work for longer time with less degradation. This is the reason that the IMEC inverted photovoltaic works for long lifetimes compared to other convention OPVs.[66]

For inverted photovoltaics, Zinc oxide (ZnO) is typically used as an ESL interlayer since its conduction bands are located close to the LUMO level of electron acceptor materials such as $PC_{61}BM$, and they possess a wide band gap that blocks hole transport to the electron-collecting contact, thus minimizing surface recombination.[13, 20, 21, 39, 53, 78-85] **Figure 2.7** plots the energy band diagram of an inverted OPV with ZnO interlayer. ZnO is a promising candidate as a hole-blocking layer because it is low-cost, earth abundant, and provides high electron mobility for transporting charge carriers.[20, 76] Even if ZnO is reported to be more stable than LiF and Ca,[85-87] ZnO can be still hydrolytically unstable,[31, 88] and thus may present concerns in terms of long term device

stability for OPVs. In addition, the rich defect chemistry of ZnO films has also been well documented and these defects, which are believed to be less prominent in other oxides, may act as recombination centers in OPV platforms as shown in **Figure 2.8**. [89-93] Therefore, the current effort would be to find a stable electron harvesting contact layers that is not only chemically stable but also can provide required electrical properties to work as an electron harvesting layer instead of ZnO.

As an other candidates for ESL, titanium dioxide (TiO_x), caesium carbonate (Cs_2CO_3), and niobium pentoxide (Nb_2O_5) have been researched,[36, 94, 95] but they still suffer from the issue of uniform film deposition or lack of requirements of electrical properties for ESL such as energy band alignment with a photoactive layer.[13] Among those candidates, TiO_x has been already used as an electron accepting material in DSSC devices. Also, recently, server studies have been reported the use of TiO_x films in BHJ OPV devices.[81] However, due to the low mobility of TiO_x material, there still need further improvement to compete with ZnO. One strategy to reduce the resistance of TiO_x layer would be to fabricate ultrathin films (< 10 nm) using a noble deposition method such as atomic layer deposition.

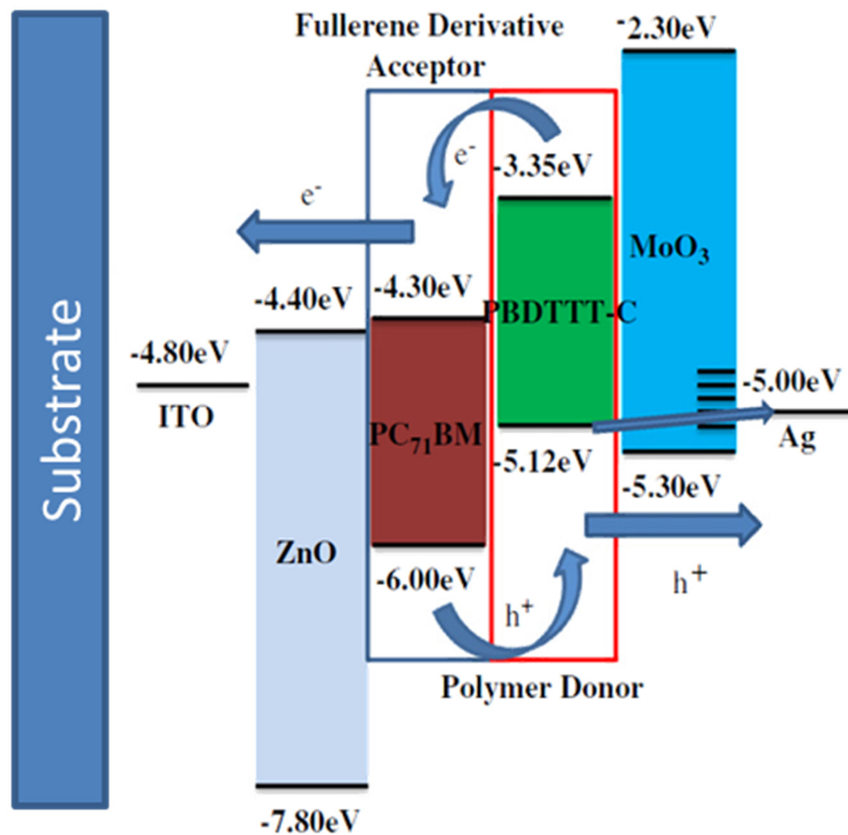

Figure 2.7 General band structure of inverted an OPV using ZnO as an electron selective layer. Adapted from reference [87].

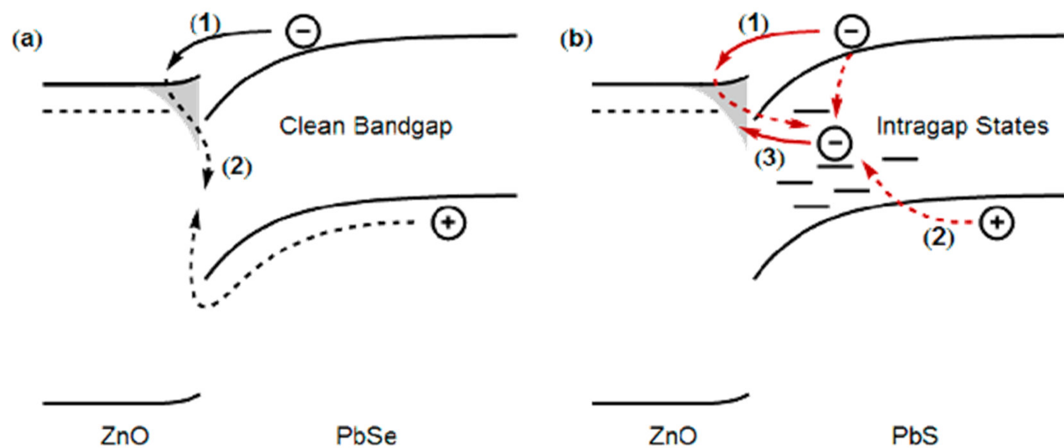

Figure 2.8 Charge recombination (a) in clean bandgap material (b) in the material with sub bandgap states (defect states) at the interface of ZnO and PbS in a QDSC device. The sub bands gap states increase the chance of recombination, resulting in decrease of OPV performance. Adapted from reference [96]

2.4.2 Development of Barrier Film Technology

As mentioned previously, an alternative method to improve the device lifetime is to protect devices from the ingress of oxygen and moisture by packaging.[60, 64, 97] **Figure 2.9** (a) shows a traditional device packaging method using a metal lid or glass substrate can be used for the rigid device application. However, if thin film device encapsulation can provide considerable barrier performance, the organic thin film electronic devices can take their advantages such as lightweight and flexibility over inorganic electronic devices. In this case, the packaging can be done in two ways depending on the barrier film preparation. In one case, a barrier film can be deposited on a separate substrate and then bonded to the device (**Figure 2.9** (b)) or secondly, the barrier film can be directly deposited on the device (**Figure 2.9** (c)). The first method is called indirect encapsulation. In the indirect encapsulation method, since the barrier film growth process does not affect the device, there is a wider range of materials and processing conditions that can be used to create the barrier film technology, limited primarily by the compatibility with the substrate material chosen. However, the lamination or bonding process of the barrier film on a device can be challenging using an adhesive and sealant. The second method is called direct encapsulation. In the direct encapsulation method, a barrier film is deposited on the device directly without the lamination issues, but the deposition process is limited by the process compatibility with the device based on factors such as temperature, reactants, plasma, and pressure.

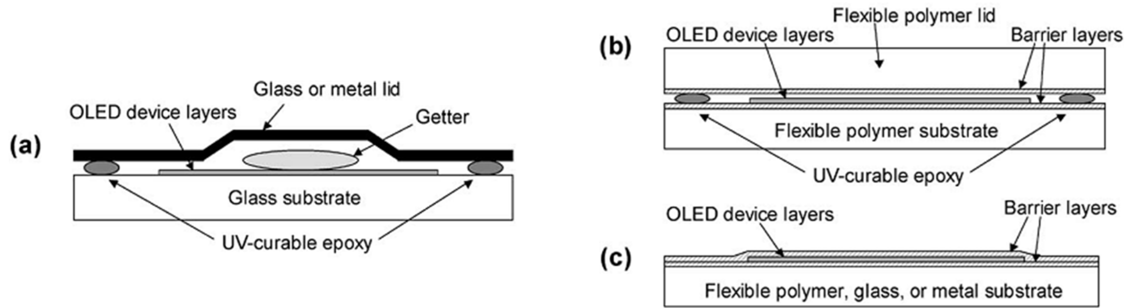

Figure 2.9 Schematic diagrams for OLED device encapsulation structures. (a) The first structure shows a traditional package with a metal lid. The second structure (b) laminated shows a barrier-coated lid (indirect encapsulation) sealed onto the device. The third structure (c) shows a monolithic thin film barrier grown onto the device (direct encapsulation). Adapted from reference [64].

<u>2.4.2.1 Gas permeation in a barrier film</u>

The major goal of a barrier film is to reduce oxygen and moisture permeation. The permeation of gas occurs due to the presence of pores or defects in a barrier film as seen in **Figure 2.10**. Depending on the size ratio of permeates and pores (Knudsen number), the diffusion can be progressed in different diffusion mechanisms: Knudsen diffusion and molecular (continuum) diffusion.[98] If the mean free path of a permeate is larger than or same order as the pore dimension, Knudsen diffusion mechanism governs. Otherwise, molecular diffusion process occurs through large pores or defects in a barrier film. In both cases, the effective diffusion coefficient can be defined that combines all permeation mechanisms, and the diffusion coefficient can be obtained experimentally as well.

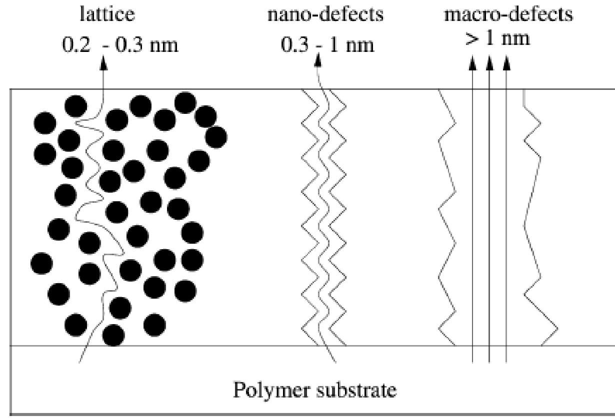

Figure 2.10 Different permeation mechanism depending on defects sizes. Lattice permeation is responsible for intrinsic permeation of the material, and nano/macro defects leads to intense gas permeation depending on their size by molecular diffusion. Adapted from reference [99].

Once the effective diffusion coefficient is known, then the Fick's second law can be used to predict the flux of a permeate through a barrier film in one-dimension,[98]

$$\frac{\partial C}{\partial t} = D\frac{\partial^2 C}{\partial x^2} \tag{2.1}$$

where C is the concentration of a permeate, t is time, D is diffusion coefficient, x is the position in a barrier film. Using Eq. (2.1) with constant concentration conditions at the boundary, $C(0,t)=0$ and $C(l,t)=C_1$, the total cumulative flux of permeate can be derived as,[100]

$$Q(t) = \frac{DtC_1}{l} - \frac{lC_1}{6} - \frac{2lC_1}{\pi^2}\sum_{n=1}^{\infty}\frac{(-1)^2}{n^2}e^{-Dn^2\pi^2 t/l^2} \tag{2.2}$$

where Q is the cumulative flux, l is the barrier film thickness. As time passes, the flux increases but saturated finally, and the steady state flux becomes,

$$Q(t\rightarrow\infty) = \frac{DC_1}{l}\left(t - \frac{l^2}{6D}\right) \tag{2.3}$$

Figure 2.11 plots the cumulative permeation flux over time in a transient permeation using Eq. (2.2). The slope, which is the flux, approaches to DC_1/l in the steady state region as time passes. In addition, using the slope lag-time (L) can be defined as Eq. (2.4), which is the intercept of the slope line and the x-axis in the plot.

$$L = l^2 / 6D \tag{2.4}$$

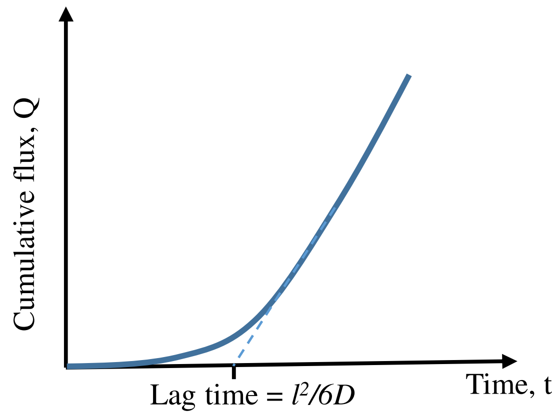

Figure 2.11 Conceptual plot of cumulative permeation flux, defining lag-time and steady state regime for a single barrier layer.

In the steady state regime, the flux can be rewritten from Eq. 2.2. depending on the gas of interest: water vapor transmission rate (WVTR), and oxygen transmission rate (OTR), which are measures of passage of water or oxygen through a barrier film, respectively. The derived WVTR is written in Eq (2.5). **Figure 2.12** plots the requirements of WVTR and OTR for a number of applications along with reported barrier film performances. As seen **Figure 2.12**, widely accepted WVTR requirement for OLED device is less than 10^{-6} g/m^2/day. Burrows *et al.* suggests this WVTR requirement by estimating the amount of water that reacts with a 50 nm thick Mg electron injection layer completely.[97] This estimation, again, emphasizes the importance of the stable low

work function material on the cathode side as has been mentioned previously. Thus, it may be possible to change the barrier film requirements for organic electronics by introducing more stable materials into the device architecture.

$$WVTR(t) = \frac{DC_s}{l}\left[1 + 2\sum_{n=1}^{\infty}(-1)^n \exp\left(-\frac{Dn^2\pi^2 t}{l^2}\right)\right] \quad (2.5)$$

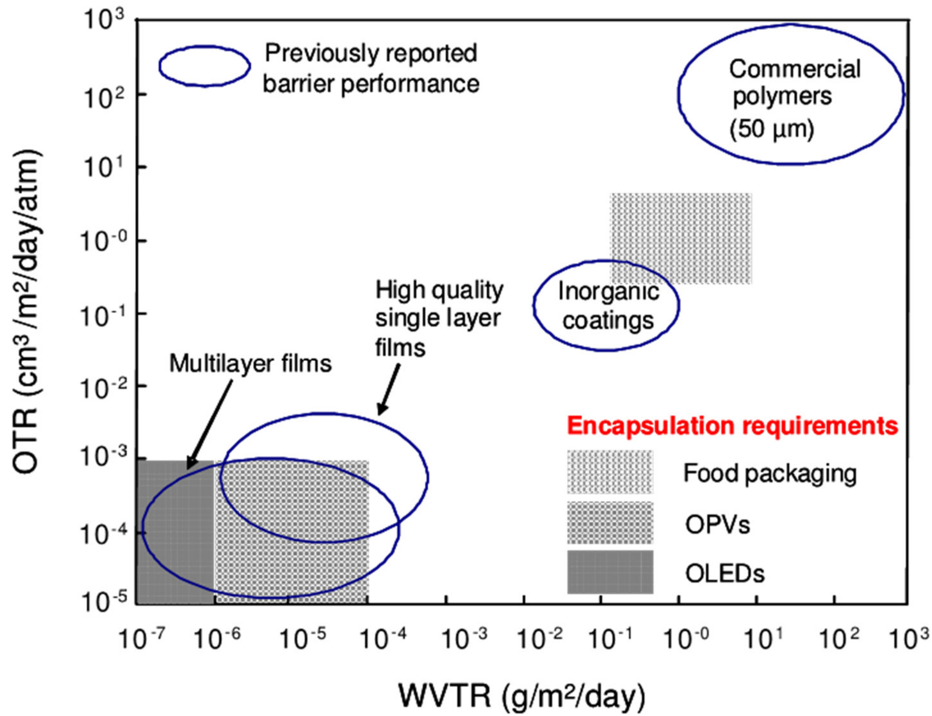

Figure 2.12 Estimates of barrier film performance requirements for various applications, including organic electronics, along with the reported barrier performance. Adapted from references [58, 101-103].

Considering permeation theory, possible methods to reduce gas permeation through a barrier film are decreasing the diffusion coefficient or increase the barrier film thickness. However, the diffusion coefficient is the intrinsic property of the barrier film material. Even if inorganic films are, theoretically, almost impermeable due their small lattice dimensions compared to the diameter of moisture, the imperfection of the film

deposition process results in defects or pinholes in the deposited inorganic films. Then, the embedded defects can contributes to increasing diffusivity of inorganic film. Therefore, it demands to fabricate a uniform defect-free film with less porosity, and it claims a high-quality film deposition process such as ALD, rather than sputtering, evaporation, and CVD.

As an alternative approach, Eq. (2.3) suggests that the lag-time can be increased by increasing the film thickness, delaying the start of the steady state permeation so that it postpones the maximum permeation rate condition. However, since the film thickness of thin film electronics is limited within the range of micrometers, it is problematic to increase the film thickness enough to achieve required length scale. Instead of this, state-of-the-art barrier films employ a multilayer structure as shown in **Figure 2.14**. In a multilayer structure, impermeable inorganic layers are alternatively stacked with smoothing layers. The laminate structure reduces the growth of defects, and separates the defects in each layer by reinitiating the nucleation process of material deposition. Therefore, the permeant should go through a long tortuous pathway to pass through the multilayer barrier film as shown in **Figure 2.13**. **Figure 2.14** (a) shows a cross section SEM image of an organic/inorganic multilayer barrier film. In this structure, the organic layer performs as a smoothing layer, which reduces the impact of surface topology and presence of large particles. **Figure 2.14** (b) shows a cross section TEM image of inorganic/inorganic multilayer barrier film. In this alternating configuration suppresses the formation of crystal structures, and reduces the boundary defects related to the crystal structures.[104] In addition, similar to multilayer structures, mixed nanoparticle barrier films are also introduced, which simplify the film fabrication process.[105]

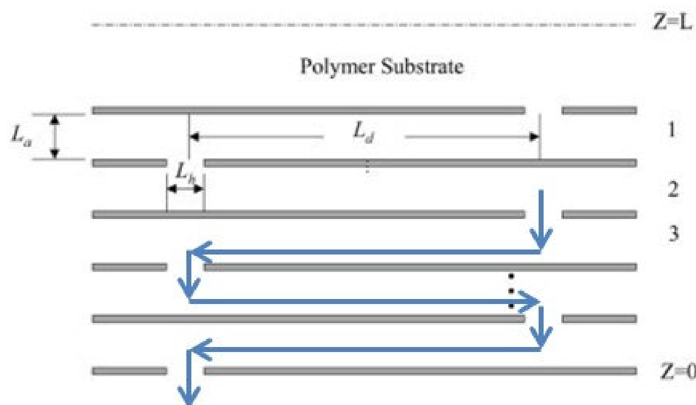

Figure 2.13 Tortuous pathway by multilayer structures. Adapted from reference [106].

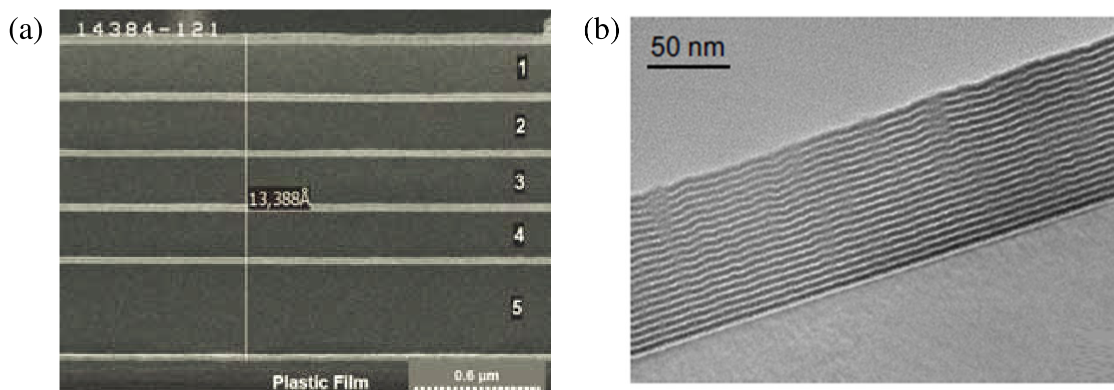

Figure 2.14 Cross-sectional image of multilayer barrier structures. (a) inorganic/organic multilayer, (b) inorganic/inorganic ALD multilayer. Adapated from reference (Barix^{TM}, Vitex systems) and [104].

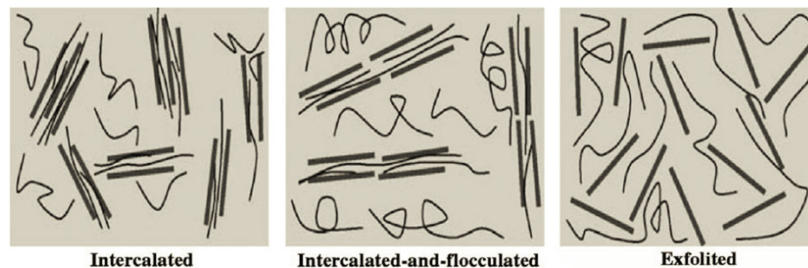

Figure 2.15 Nanoparticles in a barrier film. Adapted from reference [105].

2.4.2.2 Issue of particles and cracks

Even if an intrinsic barrier film property of a certain type of barrier film is expected to satisfy the WVTR requirement, there is another issue when the barrier is fabricated practically. For example, common polymeric substrate embeds small particles called anti blocking particles as shown in **Figure 2.16**. The purpose of the anti blocking particles is to prevent substrate adhesion between two substrates due to the van der Waals force. In addition, dust particles in a fabrication facility can lie down on substrates and affect the film deposition process. **Figure 2.17** shows SEM images of defects of films due to presence of anti-block particles and dust particles. Moreover, the nature of conventional deposition process can bring about more numbers of defects in a deposited film. **Table 2.1** tabulates defect density and defect sizes of films deposited using different deposition methods.

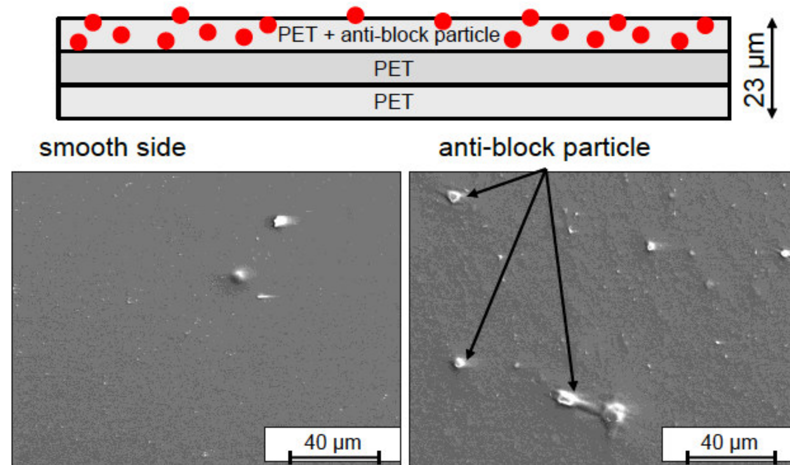

Figure 2.16 SEM images of Hostaphan RD 23 PET-film containing anti-block particles. Adapated from reference [43].

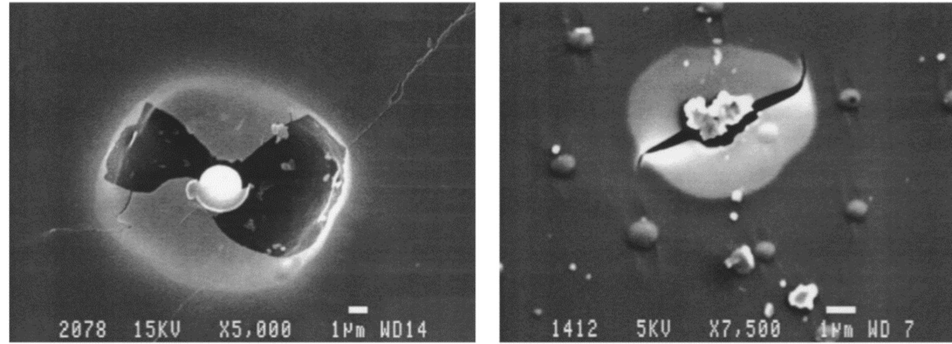

Figure 2.17 SEM images of film defects caused by an antiblock particle and dust particles. Adapted from reference[107]

Table 2.1 Measured defect sizes and defect densities for single-layer inorganic barrier films deposited on polymeric substrates. Adapted from reference [100].

Defect radius (μm)	Defect density (mm^{-2})	Coating material	Deposition method	Substrate
0.6	11-1100	SiO_2	PECVD	PET
0.6	5-1000	Si_3N_4	PECVD	PET
1.0	25-400	Al	Evaporated	PET
1.0	100-300	Al	Evaporated	PET
2-3	200	Al	Sputtering	PET
0.5-1.4	600	AlO_xN_y	Sputtering	PET
0.4	100-1000	Al	Evaporated	BOPP
0.5	700	AlO_xN_y	Sputtering	PET

In addition to particle-related defects, cracks can occur in a fabricated film. The reason of the crack formation is the mechanical stress during or after the film deposition process. For examples, the mismatch of the thermal expansion coefficient and elastic constants between the film and substrate materials result in bi-axial stress in the film after high-temperature deposition processes. Post deformation cracks can be generated if a barrier film undergoes mechanical stress such as bending and elongation. **Figure 2.18**

shows optical microscopic images of barrier films, where cracks were generated after bending tests.

As a result, both pinhole defects and cracks lead to local failure of barrier film, and play an important role in gas permeation process. Therefore, the barrier film test should consider the contribution of intrinsic permeation and defect-related permeation, separately in order to understand the real permeation characteristic of barrier films. However, current research is focused on only one-type of permeation or total permeation without discrimination.

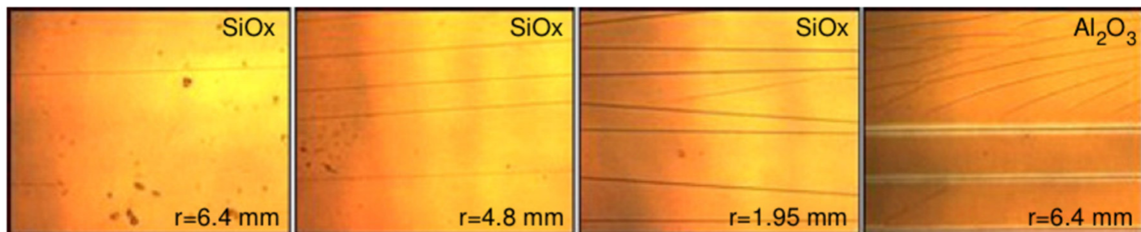

Figure 2.18 Crack formation of SiO_x and Al_2O_3 barrier films after a bending test. Adapted from reference [103]

2.4.2.3 WVTR of recent barrier films

As previously mentioned, considerable effort has been made to fabricate high performance barrier films for organic electronics. **Table 2.2** tabulates the WVTR values of number of barrier films deposited using a PECVD process. In addition, **Table 2.3** tabulates WVTR values of single and multilayer barrier films deposited using an ALD process. As seen in the table, however, direct comparison of reported WVTR values among the barrier films is difficult because the tests were carried out at different temperature and humidity conditions. Overall, many of the films are reported to attain

ultrabarrier performance, but determining which film is best cannot be done due to the differing test conditions for WVTR measurement.

Table 2.2 Summary of performance of PECVD barrier films. Adapted from reference [108].

Coating Material	Structure	Substrate	Deposition Temp.	WVTR ($g/m^2/day$)	Reference
SiO_xN_y /SiO_xC_y	Graded layer	Polycarbonate	<100°C	5×10^{-6} (23°C/50%RH)	Schaepkens *et al.* (2004)[109]
SiC_x	Multilayer	PET	120°C	2.5×10^{-7} (23°C/40% RH)	Chen et al. (2007)[110]
SiC_x	Single layer	PET	25°C-50°C	10^{-4}	Zambov et al. (2006)[111]
SiO2 /pp-HMDSO	Single layer	OLED on glass	<80°C	-	Mandlik et al. (2008)[112]
Nitride	Multilayer	OLED on glass	80°C	-	Van Assche et al. (2004)[113]
SiN_x/SiO_x	Nitride/oxide multilayer	OLED on glass; PET	<130°C	3.5×10^{-6}	Rosink et al. (2005)[114]

Table 2.3 Summary of process and performance of ALD barrier films. Adapted from reference [57, 108].

Material	Method	Structure	Substrate	Deposition Temp.	WVTR ($g/m^2/day$)	Reference
Al_2O_3 25 nm	ALD	Single layer	PEN	120°C	1.5×10^{-5} (38°C/85%RH)	Carcia et al. (2006)[115]
Al_2O_3 1-26 nm	ALD	Single layer	PEN, Kapton	100-175°C	1×10^{-3} (RT)	Groner et al. (2006)[116]
Al_2O_3 40 nm	PEALD	Single layer	PEN	100°C	5×10^{-3} (21°C/60%RH)	Langereis et al. (2006)[117]
Al_2O_3/ZrO_2 100 nm	ALD	Nano-laminate	Si/SiO_2	80°C	3.2×10^{-4} (85°C/85%RH)	Meyer et al. (2010)[118]
Al_2O_3/SiO_2 26 nm/60 nm	ALD	Multilayer	PEN, Kapton	175°C	5×10^{-5} (RT/100%RH)	Dameron et al. (2008)[119]
(SiO_x/SiN_x) /Al_2O_3 100 nm/50 nm	ALD/ PECVD	Multilayer	Glass	110°C	2×10^{-5} (20°C/50%RH)	Kim et al. (2005)

Moreover, since there is no standard measurement procedure to evaluate the ultra-low permeation rates of high performance barrier films, there is a great challenge in the evaluation of gas permeation rate through the films. As mentioned previously, the target water vapor transmission rate (WVTR) for barrier films used in most organic electronic devices is 1×10^{-6} g/m^2/day,[97] but the resolutions of many standard WVTR measurement techniques may be a few orders of magnitude higher or have safety issues.[46]

Figure 2.19 demonstrates a number of WVTR measurement methods that are commonly used in the research:[46] the gravimetric cup test,[120] isostatic method,[121], isostatic methods with infrared sensor (Permatran, MOCON)[122] or with coulometric sensor (Aquatran, MOCON),[122] mass spectrometry,[123] radioactive tracing,[124, 125] residual gas analyzer,[126] or the calcium corrosion test with optical measurement[127] or electrical measurement.[45, 128] Of these, only mass spectrometry, radioactive tracing, and calcium corrosion test can meet the WVTR resolution requirement of 1×10^{-6} g/m^2/day.[46] Furthermore, mass spectrometry requires expensive equipment, and radioactive tracing method requires special facilities with radioactive materials. Thus, methods such as the calcium corrosion test with electrical or optical measurements are the most feasible to implement, but must be done in a specific manner to improve its sensitivity.

In addition to the sensitivity of measurement, it is beneficial if the measurement technique provide spatial information of the permeation rate in a test barrier film because a barrier film can contain pinholes or cracks, which may contribute to the permeation rate regardless of the intrinsic barrier film property. If the information about the local permeation can be acquired, the reason of gas permeation can be determined, which helps to determine pathways to improve the barrier film fabrication. However, most of the

WVTR measurement methods can measure only a total or effective WVTR, and lack spatial data except an optical calcium corrosion test.

Therefore, for a barrier film application on OPV devices, it is required not only to fabricate the high quality barrier film, but also to provide a precision measurement that can investigate high performance barrier films.

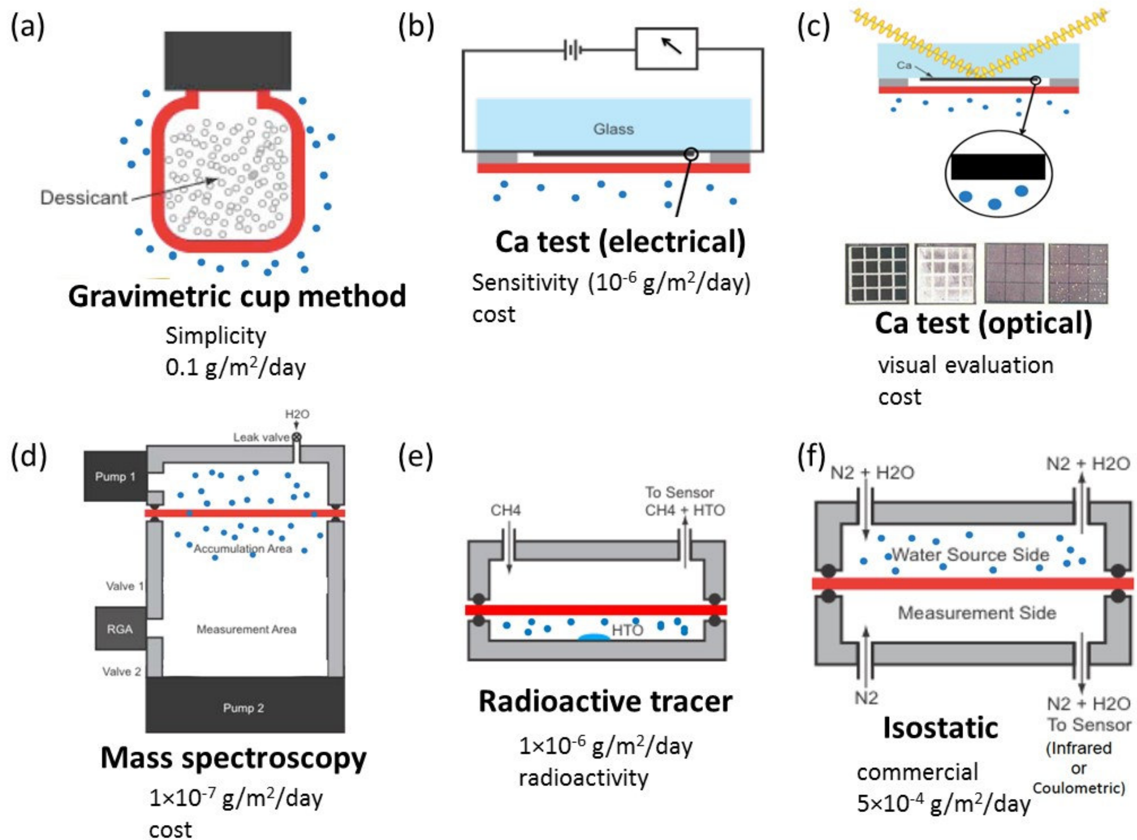

Figure 2.19 Various methods for WVTR measurement: (a) gravimetric cup method, (b) electrical calcium corrosion test, (c) optical calcium corrosion test, (d) mass spectroscopy, (e) radioactive tracing method, and (f) coulometic sensor method. Adapted from reference [46].

2.5 Atomic layer deposition

As previously mentioned, the first requirement for the ESL using TiO_x is to reduce the film thickness to lower the layer resistance. The ultrathin film structure also benefits the mechanical reliability as well because the crack onset strain is inversely proportional to the thickness of film. **Table 2.4** lists theoretical expression of crack onset strain with respect to film thickness, showing that the crack onset strain is inversely proportional to the film thickness. **Figure 2.20** also presents experimental results of the crack onset strain of thin films depending on its film thickness. As seen in **Figure 2.20**, the crack onset strain increases rapidly when the film thickness is below 20 nm. To fabricate the films in this thickness range, ALD is a one of the most promising fabrication methods to control the film thickness less than 1 nm.

Table 2.4 Theoretical expression for crack onset strain vs. coating thickness. Adapted from reference [129].

Author	Crack onset strain ϵ_{onset}	Scaling
Laws and Dvorak, 1989	$\sqrt{\frac{2G_c \xi h_s E_s}{h_c(h_s+h_c)E_c E}}$	$h_c^{-1/2}$
Nairn and Kim, 1992	$\sqrt{\frac{G_c}{E_c^2 C_3 h_c \lim_{D\to 0} Y(D)}} - \varepsilon_{rc}{}^{a}$	$h_c^{-1/2}$
Takeda and co-workers, 1998	$\sqrt{\frac{2G_c}{3E_c^{3/2}\sqrt{(1+\nu_c)h_c h_s/E_s}}} - \varepsilon_{rc}{}^{a}$	$h_c^{-1/4}$
Hu and Evans, 1989	$G_c = \left(\frac{\sigma_{onset}^2 h_c}{E_c}\right)\left(\frac{\sigma_{onset}}{3\tau} + \pi F(\Sigma)\right)$	$h_c^{-1/3}$
Leterrier and Andersons, 2000	$\frac{1-\nu_c^2}{1-\nu\nu_c} 3\sqrt{\frac{3G_c\tau}{E_c^2 h_c\left(1-\nu_c^2+\frac{E_c h_c}{E_s h_s}\left(1-\nu_s^2\right)\right)}} - \varepsilon_{rc}\frac{1+\nu_c}{1-\nu\nu_c}(1)$	$h_c^{-1/3}$

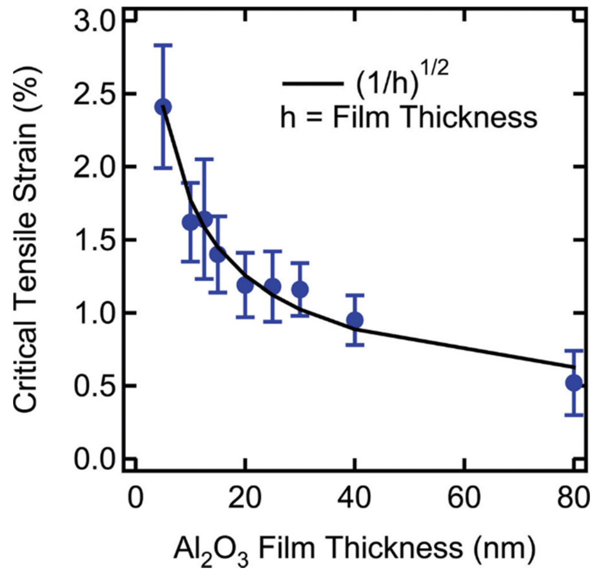

Figure 2.20 crack onset strain of Al_2O_3 films depending on the film thickness. Adapted from reference [130].

In addition, for barrier film application, the films should be defect-free. With conventional deposition methods such as evaporation, sputtering, CVD, defects are unavoidable due to the nature of the film growth mechanism. **Figure 2.21** shows the cross section TEM images of CVD and ALD films. As seen in the figure, the CVD film has grain features while the ALD film is smooth without any grainy feature. The grain features can play as defects for a films, and can leads to either local electrical leakages in an electrical application or local gas permeation pinholes in a barrier application. Due to the nature of ALD process, the nucleation and formation of film process is highly uniform, and thus it produces defect-free film that is necessary for the barrier film application.

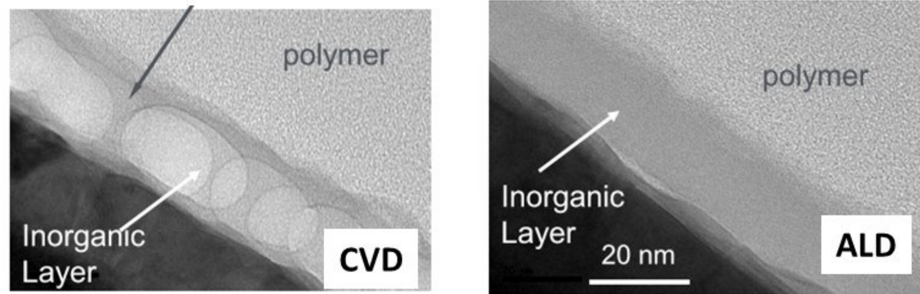

Figure 2.21 Cross section TEM images of CVD and ALD films. CVD film shows the grainy feature while the ALD film is uniform. Adapted from reference (Lin Wang, Dupont 2010)

2.5.1 Principle of atomic layer deposition

Atomic layer deposition (ALD) is a film fabrication method that utilizes the precursor properties of self-assembled monolayer formation as shown in **Figure 2.22**. Because of the nature of ALD deposition process, the film thickness is controllable down to sub-nanoscale (*ca.* 0.1 nm), and the film is extremely conformal without pinhole defects.[37] Due to this fact, among various thin film fabrication techniques such as chemical vapor deposition (CVD), thermal or e-beam evaporation, sputtering, and etc., ALD is considered to be a good candidate for fabricating a defect-free uniform film.[47, 60, 131-133] Previously, ALD was not regarded to be compatible with organic electronic devices because it requires high temperature process condition. The low growth rate of the ALD process, which is in the order of 0.1 nm/cycle, was also an issue for ALD films to be applied to mass-production. However, recently, the development of new ALD systems such as plasma-enhanced ALD, spatial ALD, and atmospheric ALD have widened the application space for ALD films to many other applications including organic electronic devices with processing rates as high as 1 nm/s.[134] Also, with the

development of new precursors, various materials can be deposited through ALD including metal oxides, metal nitrides, metals, and even organic materials through molecular layer deposition (MLD).[135] Furthermore, by alternating ALD precursors during each cycle, ALD can produce a composite material or a nanolaminate film, which tunes the material properties. Therefore, ALD films possess great potential to implement into organic electronic devices with various applications, particularly for barrier film applications because the ALD film has the potential to be conformal without defects.

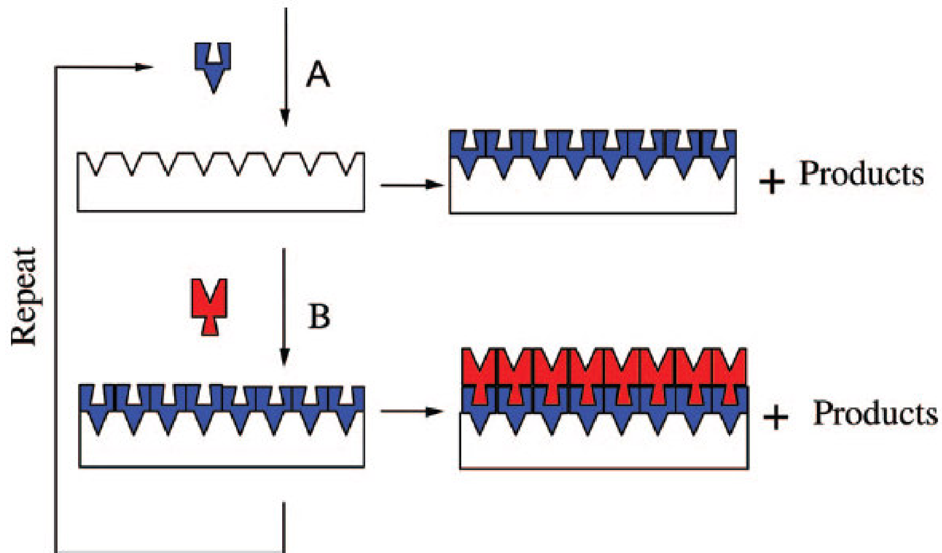

Figure 2.22 Schematic representation of ALD using self-limiting surface chemistry and an A-B binary reaction sequence. Adapted from reference [136].

In general, the ALD process is a two-step process as explained previously. For example, the most common ALD process is aluminum oxide (Al_2O_3) deposition using trimethylaluminum (TMA, $Al(CH_3)_3$) and water vapor (H_2O) precursors. The surface chemistry of Al_2O_3 ALD process can be described as, [37, 136]

$$AlOH^* + Al(CH_3)_3 \rightarrow AlOAl(CH_3)_2^* + CH_4 \quad (2.6)$$

$$AlCH_3^* + H_2O \rightarrow AlOH^* + CH_4 \quad (2.7)$$

In the first precursor pulsing step, TMA precursors react only with hydroxyl group on a substrate and form solid $AlOAl(CH_3)_2$ and methane(CH_4) by-product (Eq. (2.6)). Then, the chamber is purged with noble gas such as argon, which removes excessive TMA and methane. In the second precursor pulsing step, H_2O precursors react with $AlCH_3$ and form solid AlOH and methane by-product (Eq. (2.7)). The followed purging step removes the excessive water vapor and methane, and the ALD step repeated from the first TMA pulsing.

In order to achieve the ALD process, however, several conditions must be met. Not only the self-limiting property of a precursor, but also the condensation and desorption processes are important. The condensation and desorption processes should allow the precursor to form a monolayer. Since the condensation and desorption rate is affected by the temperature, there is an available temperature range called the ALD window. **Figure 2.23** plots the behavior of the ALD growth with respect to temperature. The ALD window is generally a chemical property of a precursor, thus much research is invested into looking for a better ALD precursor with the desired ALD temperature window.

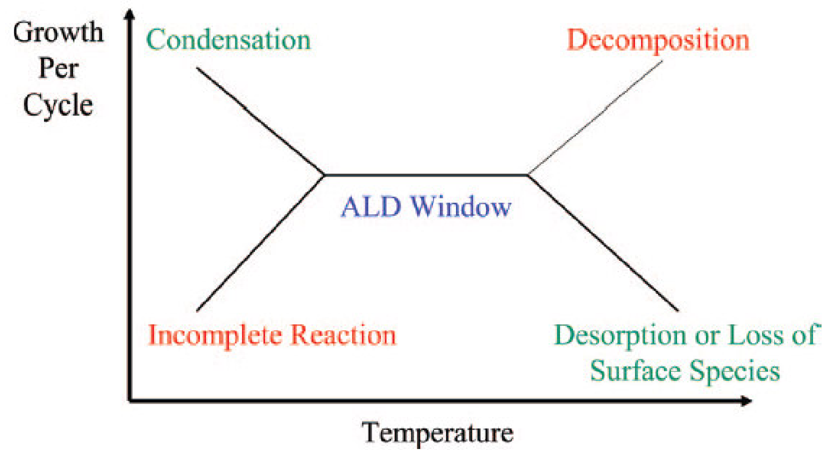

Figure 2.23 Schematic of possible behavior for the ALD growth per cycle versus temperature showing the ALD window. Adapted from reference [38].

2.5.1.1 Thermal and plasma enhanced ALD

In order to complete the ALD reaction, the temperature must be within the ALD temperature window that is determined by a given precursor. Therefore, certain precursors may not be compatible with polymeric substrates or organic semiconductors due to the need of high process temperatures or thermal energy. In order to overcome the temperature limitation, plasma-enhance ALD (PEALD) has been suggested. Different from the conventional thermal ALD, PEALD utilizes a plasma to create the second precursor, which provides sufficient reaction energy even at low temperature.[137] Moreover, by eliminating water as the oxidizer at low temperatures, it is easier to remove excess oxygen from the vacuum chamber than water vapor which typically sticks to the walls of the vacuum system. Thus, ALD reactions and growth even at room temperature are possible with PEALD. **Figure 2.24** illustrates the schematic representation of thermal ALD and PEALD. The first cycle is the same in both process, but in the second cycle, the reactant is plasma in PEALD process. Depending on the chamber configuration of the

plasma system, various PEALD systems were introduced as shown in **Figure 2.25**.[137] Among them, remote plasma systems (**Figure 2.25** (a) and (c)) are commonly used for commercial PEALD system that reduces the direct effect of plasma on substrates.

In addition to reduced process temperature, PEALD films show improved material properties with increased growth rate. Also, PEALD can control film stoichiometry and composition, and increases choice of precursors and materials [137, 138] **Figure 2.26** compares the purging time of thermal ALD and PEALD process, which indicates that the process time of PEALD is faster than that of thermal ALD at low temperature condition. Therefore, it is more appropriate to use PEALD films than thermal ALD if the film needs to be deposited at low temperature but with high quality.

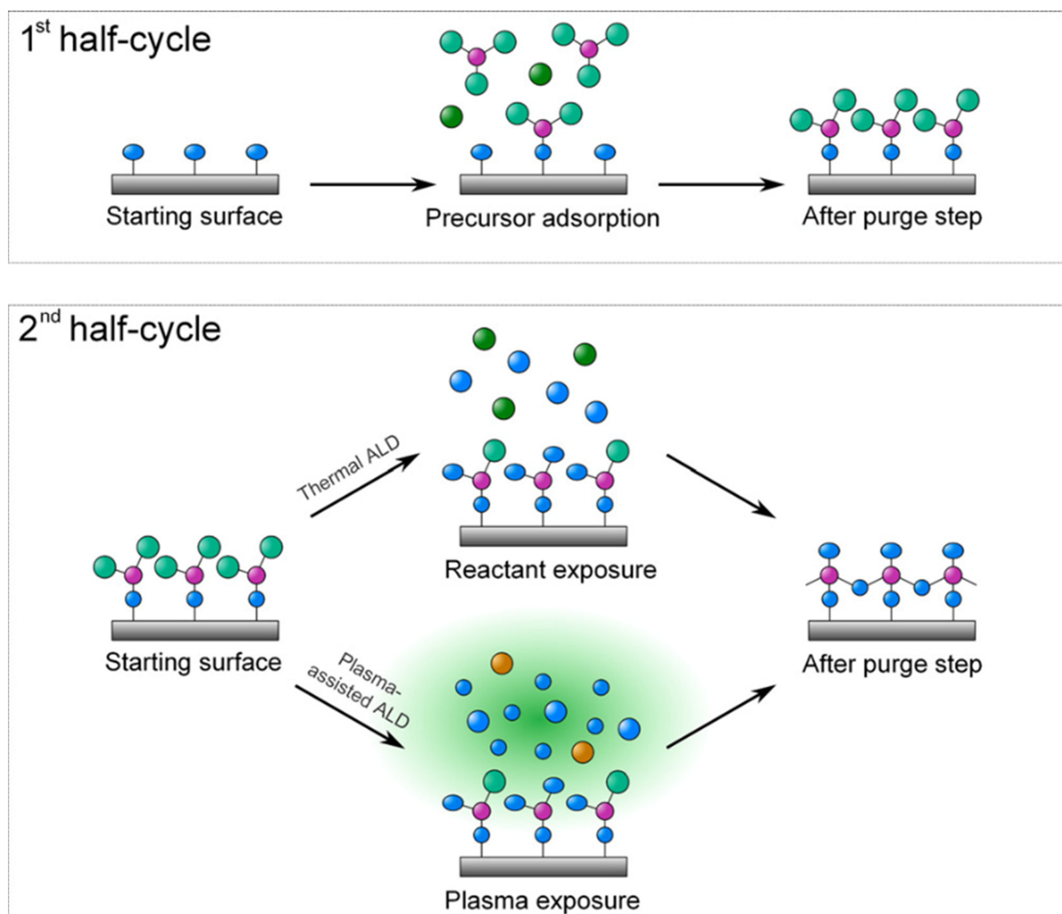

Figure 2.24 Schematic representation of thermal ALD and PEALD. Adapted from reference [137].

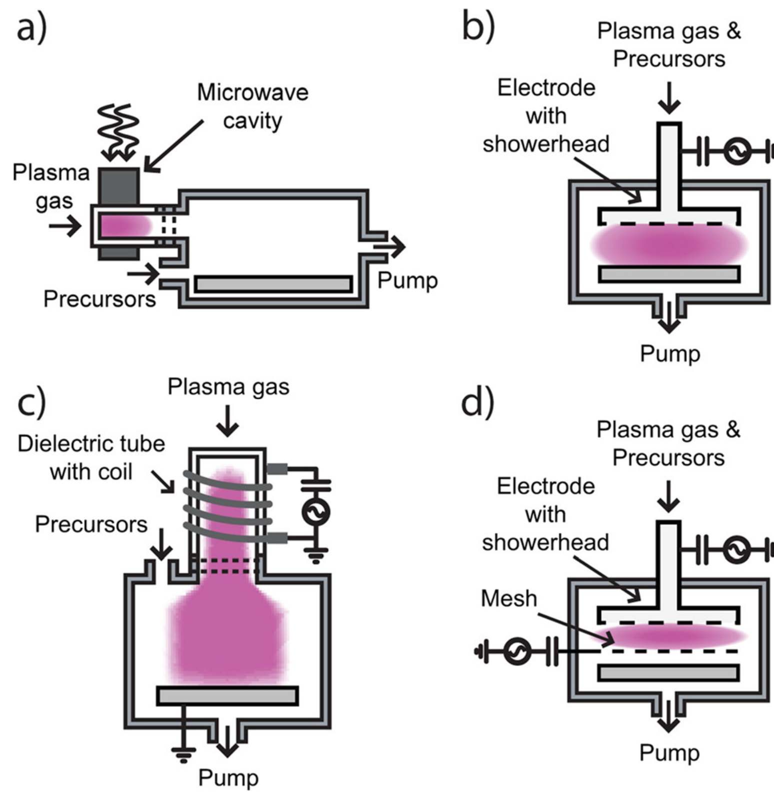

Figure 2.25 Schematic of various PEALD systems. Adapted from reference [137].

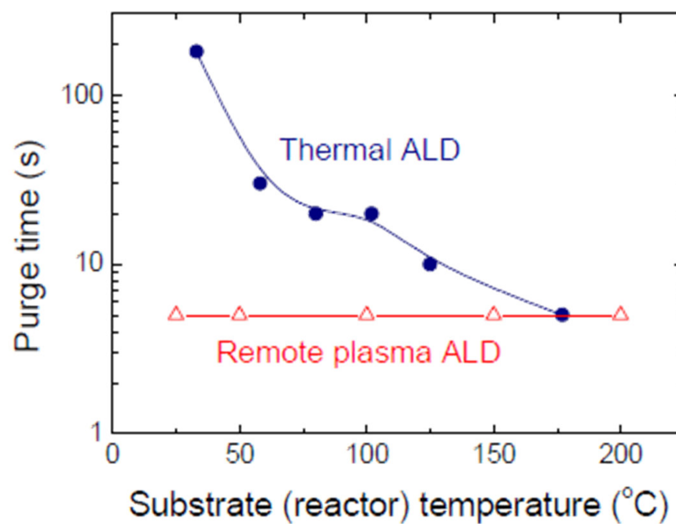

Figure 2.26 Purging time comparison of thermal ALD and PEALD at various processing temperatures.

2.6 Summary

This chapter introduced the operating principle of OPV devices. The chapter also addressed their reliability issues and efforts to resolve the reliability issues. Finally, ALD films were introduced for the application of organic electronic devices to improve the device reliability.

Even if the ALD film is a strong candidate to be used with the organic thin film electronics, the research of ultrathin ALD films for device reliability is still sparse. Moreover, important questions are still remain concerning the utilization of ALD films for the application of organic electronics regarding: (1) whether ultrathin ALD films are chemically stable in the range of the film thicknesses intended for OPV use (< 10 nm), (2) whether ALD films have proper electrical and chemical properties to perform as an ESL for a OPV to replace the instable ZnO layer, and (3) whether ALD films provide sufficient gas barrier properties for the use of external encapsulation barrier film of a device.

In addition, there is no standard characterization to test the environmental stability of ultrathin films. Also, further improvement is required to measure the barrier performance down to the required level. (WVTR < 10^{-6} g/m^2/day). Therefore, this dissertation research will address these questions as well as introduce appropriate characterization techniques accordingly in the following chapters 3, 4, 5, and 6.

CHAPTER 3

CHEMICAL STABILITY OF ALD METAL OXIDES

3.1 Introduction

A key goal of this chapter is to determine the environmental stability of ALD films for use as electrode modifiers for electron selective contacts and as barrier films in the packaging of organic and sensitive electronics.

The environmental stability of a material is tested by observing any physical/chemical change or change in critical properties after exposing the material to various environmental conditions. There are standard methods to evaluate the environmental stability of materials such as salt spray test (DIN 50021 SS), Kesternich test (DIN 50018 KFW 0,2S), climate test (DIN 58390-12-120), dilution resistance (alcohols and ketones) and tarnishing test. **Figure 3.1** presents one example of accelerated thioacetamide (C_2H_5NS) tarnishing test (ISO 4538) showing the color changes of uncoated and coated silver coins in the exposure to thioacetamide.[139] Abdulagatov *et al.* presented a study on the water resistance of ALD films by observing ALD coated copper surface with a microscope.[133] However, these tests are difficult to acquired quantitative information of material stability. On the other hand, chemical composition analysis techniques, such as X-ray photoelectron spectroscopy (XPS) and time of flight secondary ion mass spectroscopy (TOF-SIMS), can investigate the chemical composition changes due the reaction with environmental exposures such as

oxygen, water, but they are destructive analysis methods. Thus, continuous measurement with an identical sample is difficult with XPS or TOF-SIMS.

Figure 3.1 Accelerated thioacetamide tarnishing test of ALD coatings on silver coins (ISO 4538). The color of the coin without an ALD coating changes over time due to the thioacetamide exposure. Adapted from reference [139].

Therefore, this chapter suggests a new analysis procedure to evaluate the environmental stability of ALD layers. Similar to the calcium corrosion method, as a trace layer is prepared and coated with ALD films of interest. An optical measurement technique is used to detect the trace layer noninvasively and nondestructively after exposing the ALD coated trace samples to environmental conditions such as deionized (DI) water. For the trace sensor material, ZnO is chosen because it is known to be unstable in water. ZnO films have been found to contain numerous hydroxyl groups (OH-) and hydrogen interstitial defects,[140, 141] and which hydroxyl groups can initiate chemical reaction with water.

In order to observe ZnO optically, photoluminescence emission of ZnO can be used. Photoluminescence (PL) spectroscopy is a characterization technique to determine

the bandgap of a semiconducting material. While illuminating a semiconductor with a light source whose photons have an energy that exceeds the bandgap, photoemission can be observed in some semiconductor materials with energy equal to the bandgap energy as well as energy of defect states within the bandgap. Thus, ZnO, a direct bandgap semiconductor with a band gap of 3.4 eV, emits PL light when it is excited with photons that have an energy greater than the bandgap such as 325 nm UV light source as used in this work.

This chapter investigates the environmental stability of ultrathin ALD films exposed to a water environment using the ZnO PL emission technique as a sensor to determine degradation in the ALD films coated on top of the ZnO. The water environment is chosen for studying corrosion since the stability of the ALD films as barrier layers and as electrode modifiers in the presence of water that can be experienced by an OPV is of prime importance. Since the major cause of the OPV degradation is moisture permeation, and the permeate moisture can condense on the inner porous surfaces of the ALD films during water permeation. While it is understood that water soaking is not the exact same as what ALD films will see in practice, the use of water soaking in terms of studying corrosion and stability will provide a harsh environment test for the ALD films. It is expected that if the films can survive the water soaking test, they will also show stability in humid environments. The ZnO PL test is still an indirect method to investigate the stability of capping layers by means of ZnO trace layer. Therefore, additional film characterization methods are used to explain the results of ALD film stability

3.2 Experimental

3.2.1 Sample fabrication using PEALD

To create samples for stability testing, ALD films were fabricated on silicon (Si) substrates using a commercial PEALD system (Fiji, Cambridge Nanotech) as shown in **Figure 3.2**. First, a 11 nm thick ZnO sensor layer was deposited on solvent cleaned Si substrates at 250°C. A polished Si wafer was cut into 2.5 cm by 2.5 cm square pieces, and cleaned in acetone with sonication for 10 min, followed by cleaning in IPA with sonication for 10 min. Then, the Si pieces were rinsed in flowing DI water and were dried with a gentle N_2 flow from a nitrogen gun. The Si pieces were then transferred into the PEALD processing chamber. Before the deposition process, the substrates were kept in the processing chamber under vacuum for 15 min to achieve temperature equilibrium between the substrate and the chamber at 250°C. Afterward, 3 cycles of Al_2O_3 PEALD films were deposited as a nucleation layer, which improves the nucleation of the ZnO layer when compared to the growth on a native SiO_2 surface. Trimethylaluminum (TMA) was used as the Al precursor using 40 sccm Ar as the carrier gas with pulses lasting 0.06 s followed by 5 s of purging with Ar followed by a remote oxygen plasma generated by flowing 20 sccm of oxygen in a 200 sccm Ar flow and applying an RF electric field of 300 W upon its entrance for 20 s. Next, ZnO sensor layer was deposited in the same manner using diethylzinc (DEZ) as a Zn precursor. After a 0.06 s pulse of DEZ, the chamber was purged for 5 s, and a remote oxygen plasma was applied with 20 sccm of oxygen in a 200 sccm Ar flow for 30 s, followed by 5 s of purging. The process was repeated for 100 cycles, which produced an 11 nm thick ZnO layer. The thickness of the film was measured using a spectroscopic ellipsometer (M-2000, J.A. Woollam Co.)

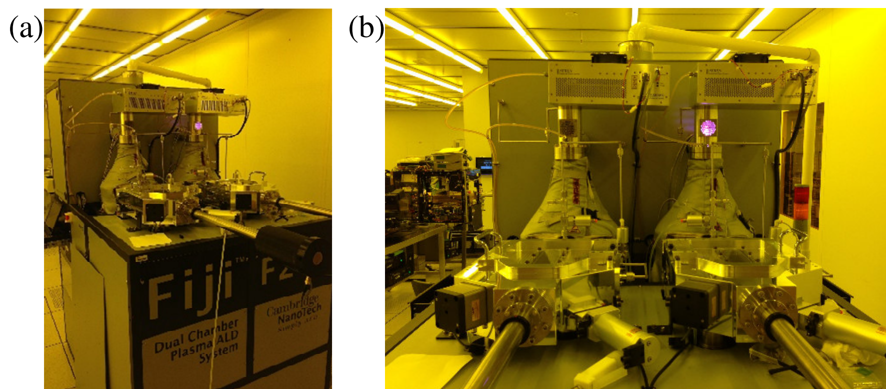

Figure 3.2 The dual chamber Fiji PEALD system. The right chamber is used for running the PEALD ZnO deposition, and a purple glow is observed due to Ar/O_2 plasma in the window port of the system during the oxidation step.

After ZnO deposition, metal oxide ALD films of interest were deposited on the ZnO sensor layers at two temperature conditions, 100°C and 250°C. Al_2O_3, TiO_x, ZrO_x, and HfO_x were selected due to their potential for high quality barrier films. Also, TiO_x is of interest for the application of ESL to replace ZnO ESL in inverted OPV devices. The deposited ZnO sensors samples were taken out to atmosphere with Ar purging, and then loaded again to deposit interest ALD capping layers in a similar manner using different precursors of the metal organic. TMA, tetrakis(dimethylamido) titanium (TDMAT), tetrakis(dimethylamido) hafnium (TDMAH), tetrakis(dimethylamido) zirconium (TDMAZ) were used for Al_2O_3, TiO_x, HfO_x and ZrO_x deposition, respectively, as shown in **Figure 3.3**. The ALD run was repeated by 100 cycles to produce *ca.* 10 nm thick capping layers for Al_2O_3 HfO_x, ZrO_x, and For TiO_x, 100 cycle and 200 cycles of ALD process was done to produce ca. 5 nm, and 10 nm thick film. All precursors were purchased from Sigma-Aldrich as packaged jacket for use of deposition systems. **Figure 3.4** depicts the structure of ZnO PL sensor samples with protecting ALD films, and **Table 3.1** tabulates the detail parameters of ALD process and parameters for each material

deposition. Also, at the 100°C processing temperature, the purging time increased for the adsorption and desorption processes of each precursors to be completed (**Table 3.2**).

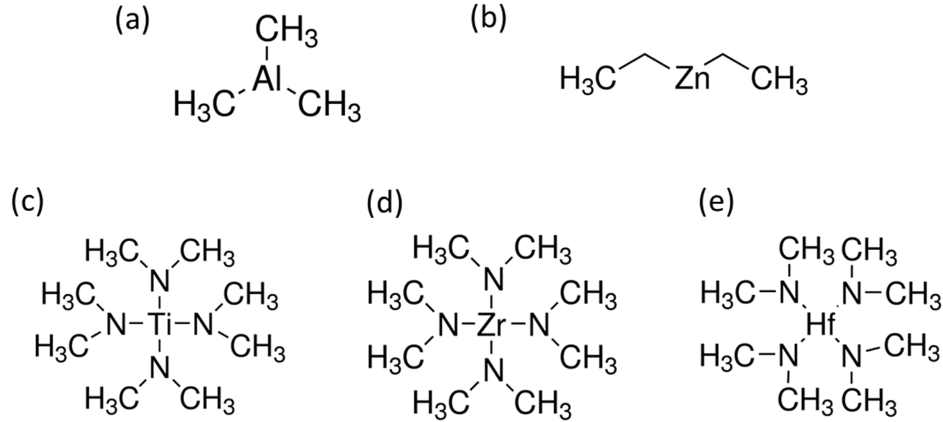

Figure 3.3 Chemical structure of metal precursors used for ALD process. (a) TMA, (b) DEZ, (c) TDMAT, (d) TDMAZ, and (e) TDMAH.

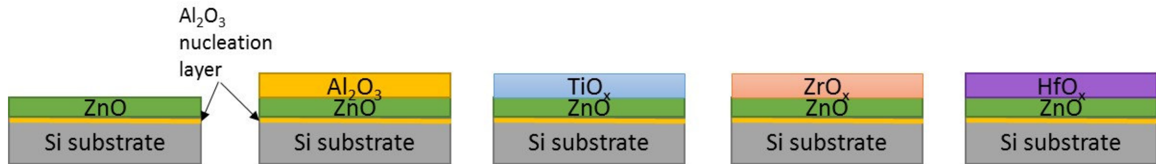

Figure 3.4 Schematic diagrams of tested ALD films in this PL study. From the left, an uncapped ZnO sensor sample, an Al_2O_3-coated ZnO sample, a TiO_x coated sample, a ZrO_x-coated sample, and a HfO_x coated sample.

Table 3.1 Parameters for metal oxide deposition at 250°C using PEALD.

	ZnO	Al_2O_3	TiO_x	HfO_x	ZrO_x
Metal precursor	DEZ	TMA	TDMAT	TDMAH	TDMAZ
Ar flow rate for precursor delivery (sccm)	40	40	40	40	40
Ar flow rate for plasma source (sccm)	200	200	200	200	200
Pulsing time (s)	0.06	0.06	0.2	0.06	0.06
1st Purging time (s)	5	5	5	5	5
Oxygen flow rate (sccm)	20	20	30	20	20
Plasma time (s)	30	20	20	20	20
2nd Purging time (s)	5	5	5	5	5

Table 3.2 Parameters for metal oxide deposition at 100°C using PEALD.

	ZnO	Al_2O_3	TiO_x
Metal precursor	DEZ	TMA	TDMAT
Ar flow rate for precursor delivery (sccm)	40	40	40
Ar flow rate for plasma source (sccm)	200	200	200
Pulsing time (s)	0.06	0.06	0.2
1st Purging time (s)	60	45	90
Oxygen flow rate (sccm)	20	20	30
Plasma time (s)	30	20	20
2nd Purging time (s)	10	10	10

3.2.2 Photoluminescence

Photoluminescence (PL) spectroscopy is one of the photoemission spectroscopic (PES) techniques which can investigate the electronic structure by observing light emission from semiconductor materials. When intense high energy light such with photon energy greater than the bandgap is illuminated on the surface of a semiconductor, a ground state electron is excited to the conduction band and relaxes back to the ground

state by a radiative transition processes (**Figure 3.5**). From the energy of the radiation light, the bandgap of a direct semiconductor, such as ZnO, can be investigated.

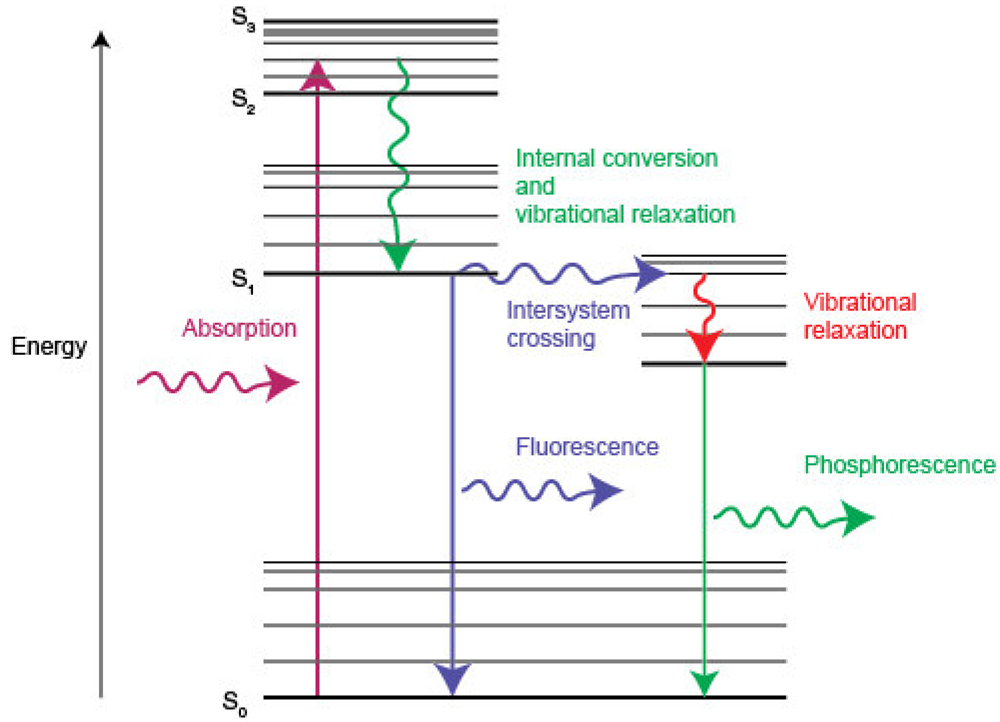

Figure 3.5 Energy diagram showing absorption of light and the processes involved in the emission of light as fluorescence and phosphorescence. Adapted from reference [142].

In this dissertation, PL emission spectra of the ZnO layer were obtained using a Horiba Jobin Yvon LabRAM HR800 Raman Spectrometer equipped with a backside-illuminated liquid nitrogen cooled charged-coupled device (CCD) detector (Symphony, Horiba) (**Figure 3.6**). A 325 nm (3.81 eV) Helium-Cadmium (He-Cd) laser was used as the excitation source with an incident laser power of 3.2 mW on a spot size of approximately 3 μm. A 40x UV achromatic objective (LMU-40x, Optics for Research) was used to acquire ZnO near band edge (NBE) PL emission that lies in UV region (340 nm-400 nm).

The intensity of the PL emission measured in this experiment is dependent on the power of excitation source, radiative recombination rate of a material, sensitivity of the photodetector, and the efficiency of the collection optics. To quantify the PL emission spectra of samples, the UV laser source was turned on 1 hour before the measurement. The spectrometer position was calibrated using a 4H silicon carbide (SiC) sample from Cree with its Raman shift peak at 776 cm^{-1}. The measured PL intensity was affected by the fluctuation of the laser source intensity and alignment changes of optical mirrors in the spectrometer, thus a control sample was prepared to track and compensate for the fluctuations after alignment and calibrations were performed. For the control sample, a TiO_x coated ZnO sample was prepared and stored in a nitrogen-filled glove box (MB10, MBraun) at the conditions of both water and oxygen levels below 0.5 ppm.

In addition, the PL intensity is highly dependent on how well the sample is in focus, particularly of a thin ZnO film (< 10 nm). Therefore, the Z-stage mapping was carried out to find the stage position for the maximum intensity. After all, PL spectra were scanned over the range of 340 nm to 450 nm with a D0.3 attenuator filter and 3 s acquisition time. Each scan was repeated 3 times to acquire single average spectrum, and 3 spots were measured for each sample.

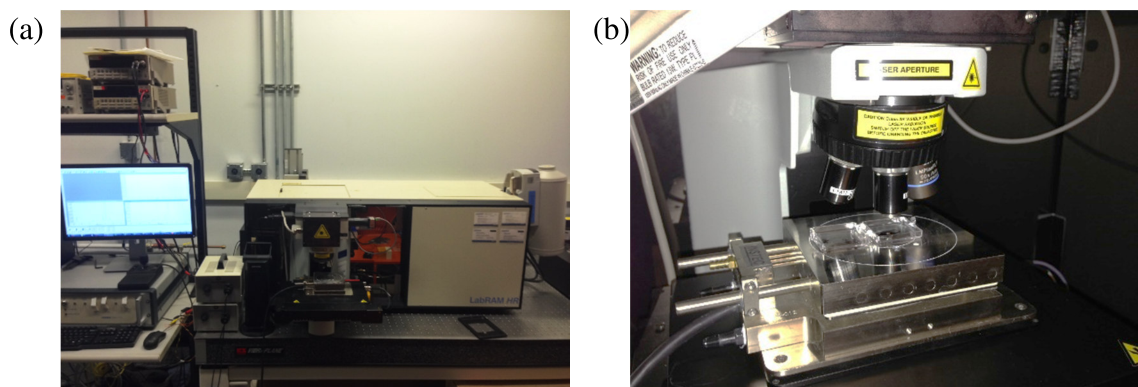

Figure 3.6 The LabRAM HR800 Raman system for PL measurment. (a) whole system, (b) a sample under a microscope objective during testing.

3.2.3 Water soaking test

After the initial PL emission measurement, the samples were soaked in 15 ml deionized (DI) water in beaker at room temperature to determine the stability of the various ALD layers to aqueous media as shown in **Figure 3.7**. The DI water acidity was pH 7 (measured with Model 2100 pH meter, VWR). After water soaking, the samples were taken out from the water and dried out with a mild N_2 air gun. PL spectra of the samples were repeated and the samples were placed back into the water. The PL measurements were carried out at 0, 1, 3, 5, 7, and 10 days. For each day, the PL emission of the control sample, a TiO_x coated ZnO sample, was also acquired.

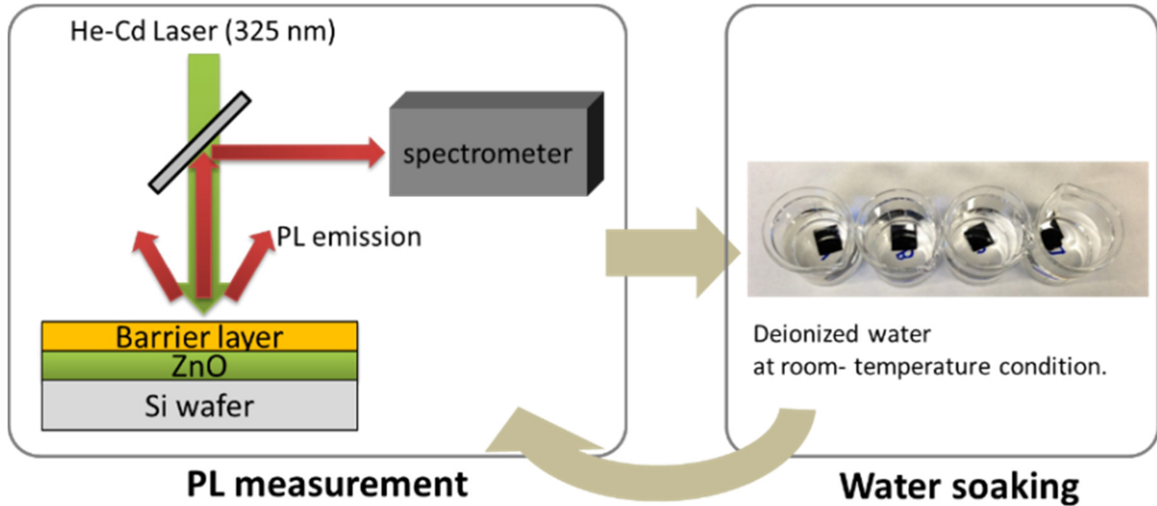

Figure 3.7 Experimental procedures of water stability testing using photoluminescence spectroscopy. PL emission spectra of samples acquired periodically after water soaking at room temperature condition

3.2.4 Spectroscopic ellipsometry

For additional characterization, spectroscopic ellipsometry (SE) was used. SE is a primary characterization tool to investigate the thicknesses and the optical refractive indices of ALD films. **Figure 3.8** illustrates the schematic of light pathways in an ellipsometer. The focus of ellipsometry is to measure how parallel (p-) and perpendicular (s-) polarization components change upon reflection or transmission in relation to each other based on interactions with the sample. In this manner, a known polarization is reflected or transmitted from the sample and the output polarization is measured. The change in polarization is the ellipsometry measurement, commonly written as,

$$\text{polarization change} = \tan(\Psi)e^{i\Delta} \qquad (3.1)$$

The incident light is linear with both p- and s- components. The reflected light has undergone amplitude and phase changes for both p- and s- polarized light, and ellipsometry measures their changes.

(a)

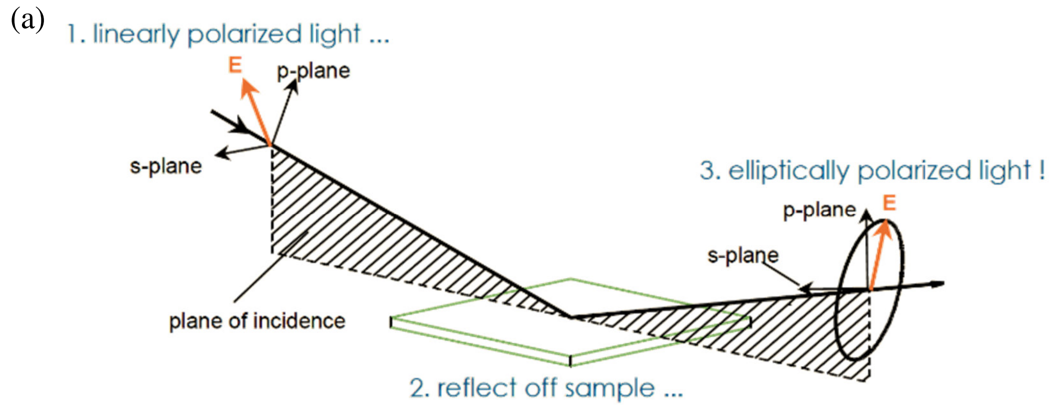

(b)

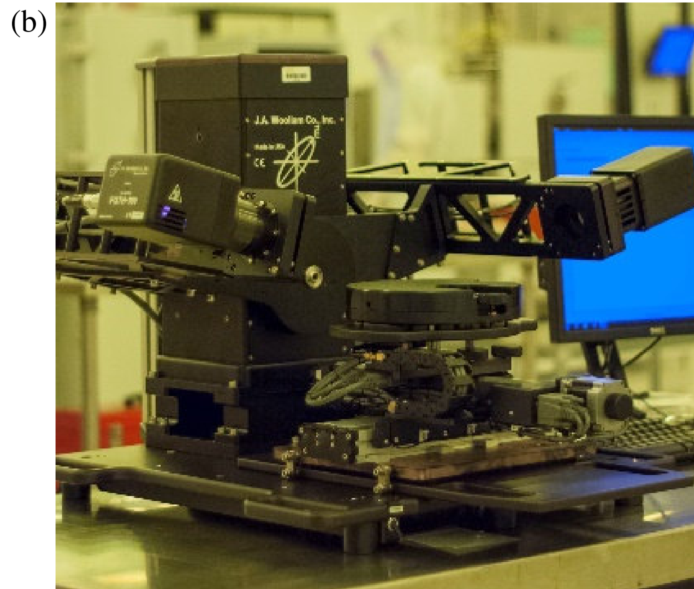

Figure 3.8 (a) Typical ellipsometry configuration, where linearly polarized light is reflected from the sample surface and the polarization change is measured to determine the sample response. (www.jawoollam.com) (b) Photograph of M-2000 variable angle SE system.

In order to evaluate the optical properties, the measured data must be fitted with an optical model such as Cauchy's equation,[143] which is the one of the most common

empirical models for a transparent material. The general form of the refractive index with respect to wavelength is,

$$n(\lambda) = C_0 + \frac{C_1}{\lambda^2} + \frac{C_2}{\lambda^4} \quad (3.2)$$

where n is the refractive index, and C_0, C_1, and C_2 are coefficients that need to be fitted from the experimental data. From this model, the refractive index and film thickness can be estimated.

In this dissertation, the film thickness and refractive index were evaluated using variable angle spectroscopic ellipsometry (M-2000, J.A. Woollam Co.) at four incidence angles: 60°, 65°, 70°, and 75°. The fitting variables, C_0, C_1, C_2, and the film thickness, of a Cauchy model layer were fitted with the measured SE date to estimate the refractive index and film thickness using the CompleteEASE software.

3.2.5 X-ray photoelectron spectroscopy

In order to explore chemical compositions of the ALD films, X-ray photoelectron spectroscopy (XPS) was used. The sample was placed in a high vacuum environment and irradiated with a focused beam of X-rays allowing photoelectrons to be emitted from the surface, as shown in **Figure 3.9** (a). The emitted electrons are collected by the electron analyzer and the kinetic energy of the emitted photoelectrons was determined by a spectrometer, which finally presents intensity vs. binding energy data. The binding energy (E_b) of individual electrons that exist on the surface is determined using Eq. (3.3) with known information such as the energy of X- ray photons (hv), the kinetic energy of the emitted electron, and the work function (WF) of the spectrometer.

$$E_b = h\nu - E_k - WF \quad (3.3)$$

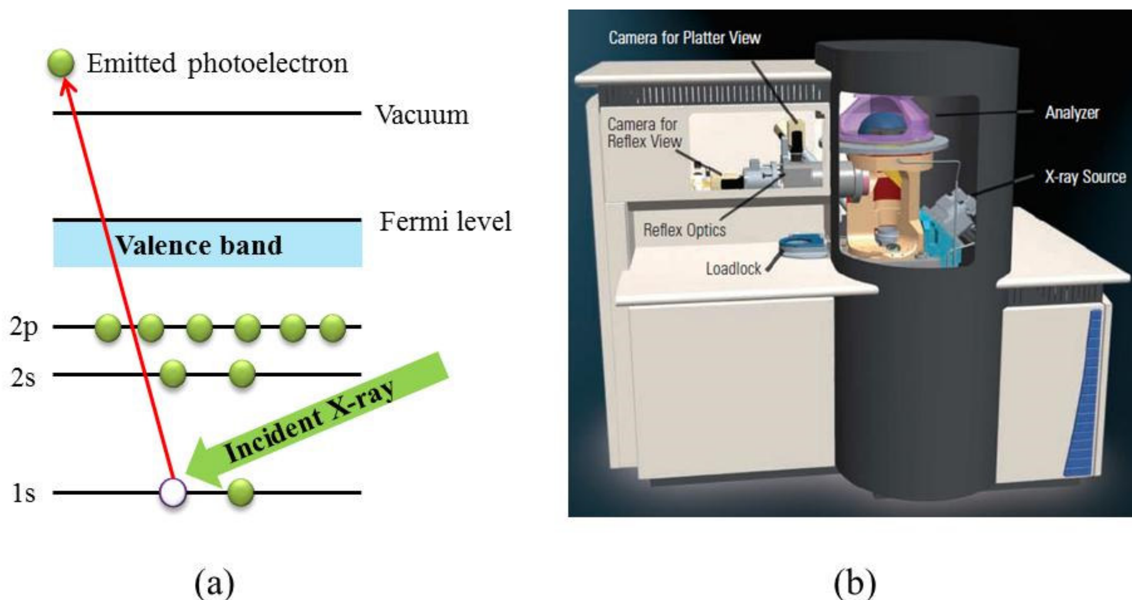

Figure 3.9 (a) Schematic showing the processes that occur during XPS where xray energy ejects a core electron which is picked up by a detector and (b) a Thermo K-Alpha X-ray photoelectron spectroscope similar to the one used in this study (www.thermoScientific.com).

In this dissertation, a Thermo K-alpha XPS system (Thermo Scientific) was used for the elemental analysis of ALD films in a depth-profiling mode. Al K-alpha X-ray (1486.3 eV) was used as an excitation source, and the diameter of X-ray gun was set at 400 μm to define the sampling area. Also, a flood gun was used to compensate the binding energy shift due to charge condensation. For the depth profiling, a sputter gun was used at 2000 eV ion energy and mid-range current (*ca.* 3.8 μA). The sputtering process was carried out for 30 s for each step between the XPS analysis steps. At this sputtering conditions, the etch rate of Al_2O_3 layer is expected to be 0.081 nm/s, which leads to 2.4 nm per etch step.

The acquired data were analyzed using a commercial analysis software (Avantage Data System, Thermo Scientific). The primary core level elemental peaks were fitted to Lorrentz-Gaussian peaks. Since the spectra can be shifted due to argon bombardment during the sputtering, the spectra were calibrated so that the peaks are consistent to the spectra of the first scanning step.

3.2.6 Scanning electron microscopy

Scanning electron microscopy (SEM) images were taken using Ultra60 FE-SEM (Zeiss) to investigate the surface morphology and the conformality of the films. Both a secondary electron image and backscattered electron image were used for imaging. In general, topography differences are more clearly visualized by the secondary electrons while backscattered electrons provide better material contrast.

In order to acquire a high resolution image, 10 keV acceleration voltage at short working distance (*ca.* 4 mm) was used. Also, both the secondary electron image and back scattered image were combined for better contrast accordingly. For a cross sectional image, the sample was broken and mounted on a sample holder with the broken edge facing to the detector.

3.3 Stability of ultrathin ALD films

3.3.1 PL Emission of ZnO

Figure 3.10 shows the photoluminescence spectra performed on the baseline ZnO sensor before and after soaking in DI water for 24 hours at room temperature conditions.

The as-deposited ZnO peak shows near band edge (NBE) UV emission at around 340 nm and defect related deep level emission (DLE) between 450 eV to 650 eV attributed to Zn and O vacancies produced in the diethyl zinc precursor based PEALD ZnO films.[144] Following soaking in DI water for 24 hours, the ZnO layer was observed to have completely disintegrated in the DI water with no observable PL signal detected despite scanning at multiple locations. This result is compatible with that observed by Yamabi *et al.* [145] where they observed that solid state ZnO is unstable in water with pH *ca.* 7. The result also suggests that ALD ZnO can be used as a tracer sensor in this water soaking test to investigate the stability of other ALD films to water environment.

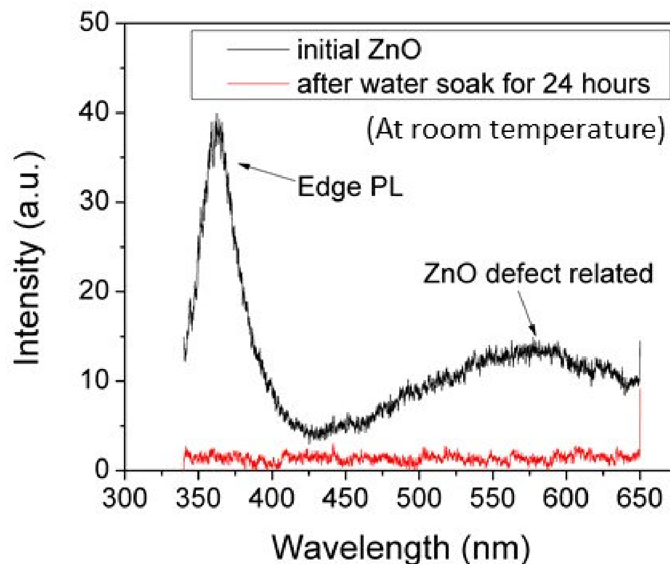

Figure 3.10 The PL emission from ALD. PL emission of ALD ZnO layer on a Si substrate showed a primary peak near 350 nm and defect band between 450 and 650 nm. The signal was not detectable after water soaking for 24 h.

3.3.2 ZnO PL emission with ALD capping layers

The PL emission spectra of all samples were measured at 0, 1, 3, 5, 7, and 10 days. **Figure 3.11** shows the integrated area of the PL emission spectra of the prepared control sample over this period of time. As seen in the figure, the intensity fluctuates over this period and thus, the variation must be accounted for when measuring the actual devices exposed to water soaking. To do this, the intensity of the samples was divided by the intensity of the control sample on a given day to normalize the response and to compensate for the fluctuation of the measurement system.

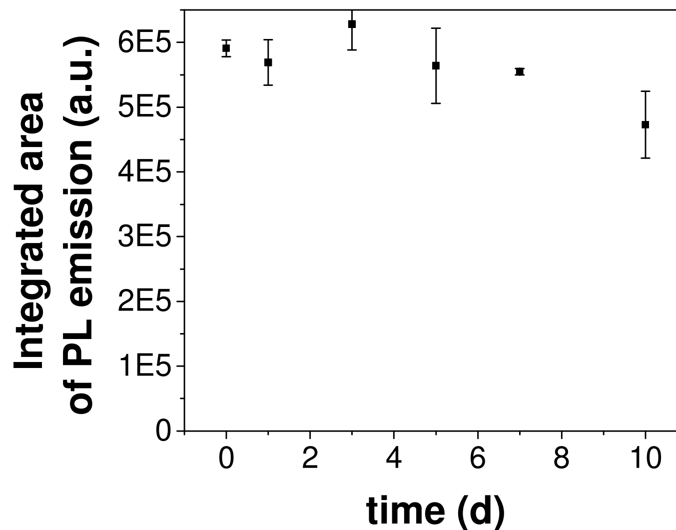

Figure 3.11 Integrated area of PL emission spectra of the control sample, N2-stored TiO_x coated ZnO.

Figure 3.12 plots the PL spectra of ALD coated ZnO films that are deposited at 250°C, and **Figure 3.13** plotted in the PL spectra of ALD coated ZnO films that are deposited at 100°C.The peak intensity was compensated by dividing the intensity of the

control samples. In the preliminary test, the PL emission of 10 nm ZnO without protection was not observed after 18 hours in water soaking. However, with the 10 nm thick capping ALD layer, the PL spectrum was observed for 10 days during water soaking experiments except for two cases. As seen in **Figure 3.12** (c) and **Figure 3.13** (a), the PL spectra of Al_2O_3 coated ZnO samples decreased after 5 days and was not observed for the full 10 days, whereas the PL spectra of TiO_x, ZrO_x, and HfO_x coated ZnO samples survived up to 10 days. The results suggest that 10 nm thick Al_2O_3 is hydrolytically unstable for long exposure to water which has been observed previously in barrier film experiments.[119]

Figure 3.14 plots the normalized peak area of a ZnO NBE emission peak over time. There is some fluctuation in the peak area over time, but the graph suggests that TiO_x, ZrO_x, and HfO_x coated ZnO samples are stable for 10 days. However, Al_2O_3 coated ZnO and unprotected ZnO is unstable in DI water for both deposition temperatures: 100°C and 250°C.

The PL tests can be used to determine whether or not an ALD films is susceptible to corrosion in water, but it is not quantitative in nature. Overall, the reason or the kinetics of the ZnO removal process is unclear. For example, it is unclear whether ZnO is dissolved in water or is converted into some other compound. Also, it is also unclear whether the protecting Al_2O_3 film is also removed completely or not. Therefore, further investigation is necessary to understand the degradation behavior of ZnO and Al_2O_3 films.

(a)

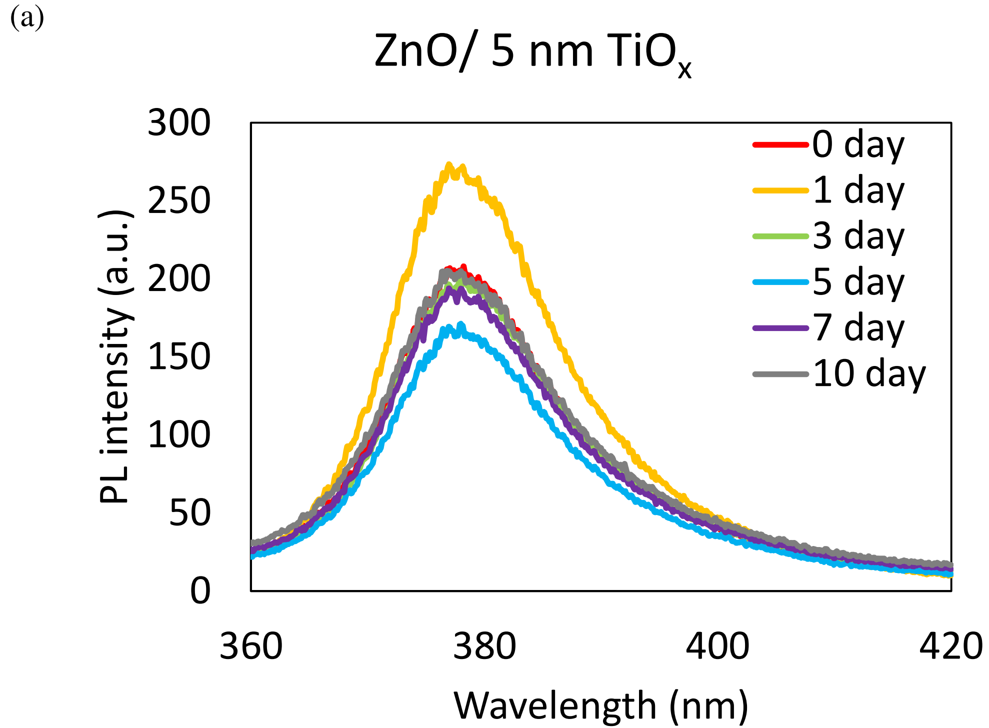

(b)

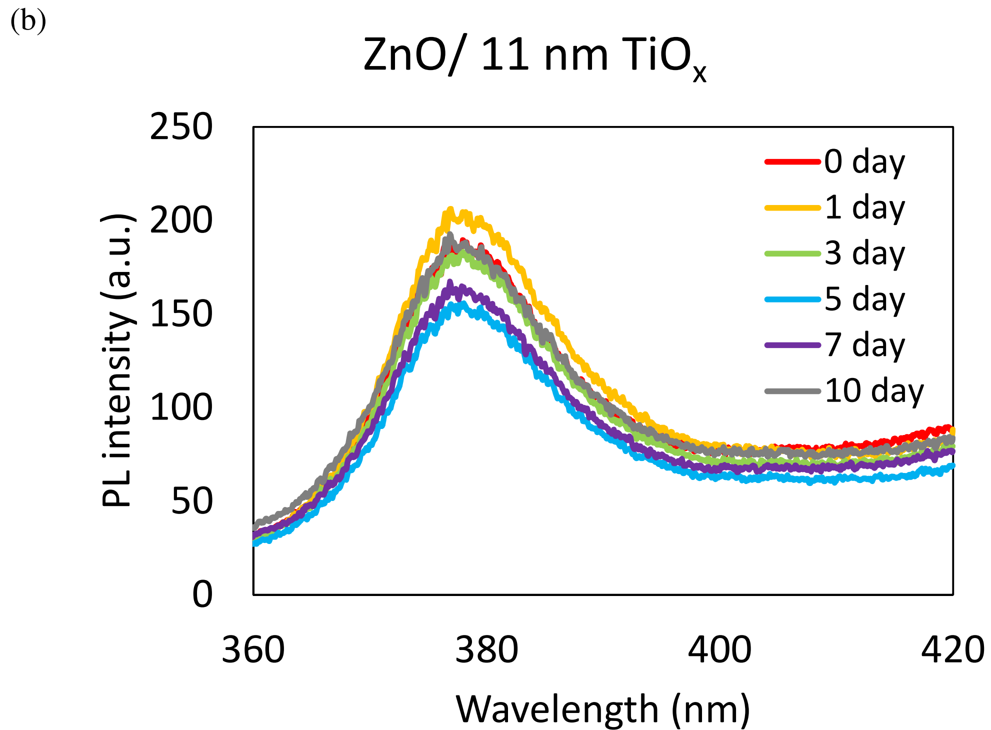

Figure 3.12 PL emission spectra of ALD film protected ZnO sensor samples. (a) 5 nm TiO_x, (b) 11 nm TiO_x, (c) 10 nm Al_2O_3, (d) 10 nm HfO_x, and (e) 10 nm ZrO_x capping layer. The ALD capping layers were deposited at 250°C.

(c)

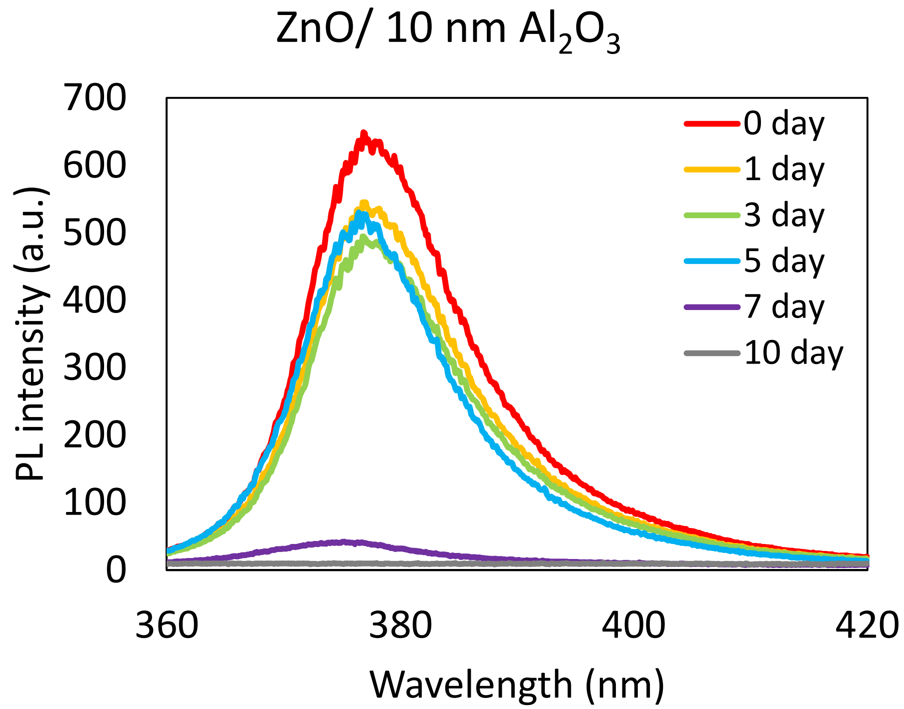

(d)

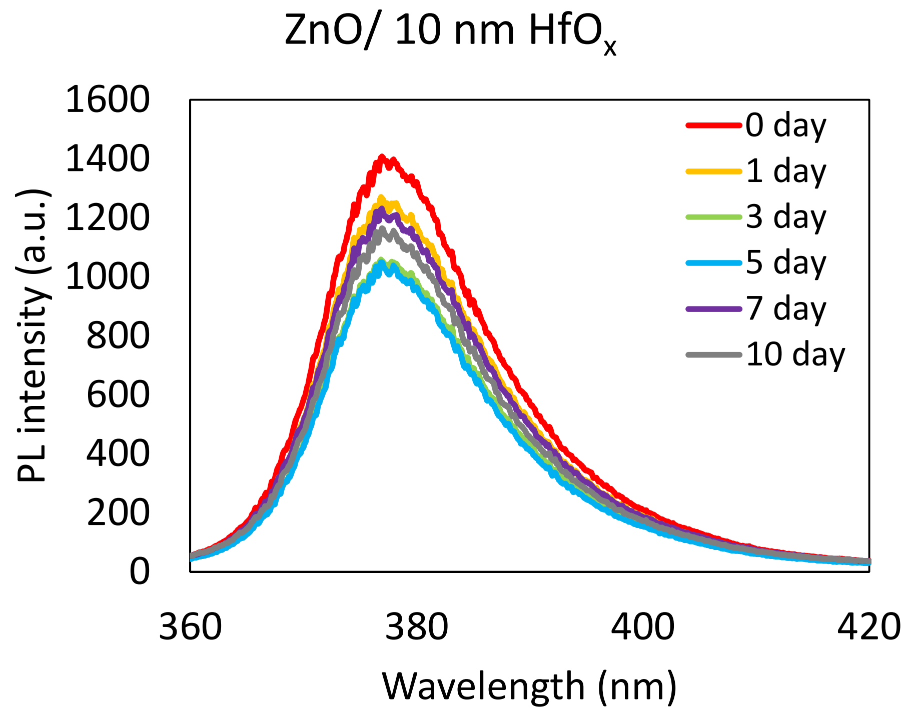

Figure 3.12 (continued) PL emission spectra of ALD film protected ZnO sensor samples. (a) 5 nm TiO_x, (b) 11 nm TiO_x, (c) 10 nm Al_2O_3, (d) 10 nm HfO_x, and (e) 10 nm ZrO_x capping layer. The ALD capping layers were deposited at 250°C.

(e)

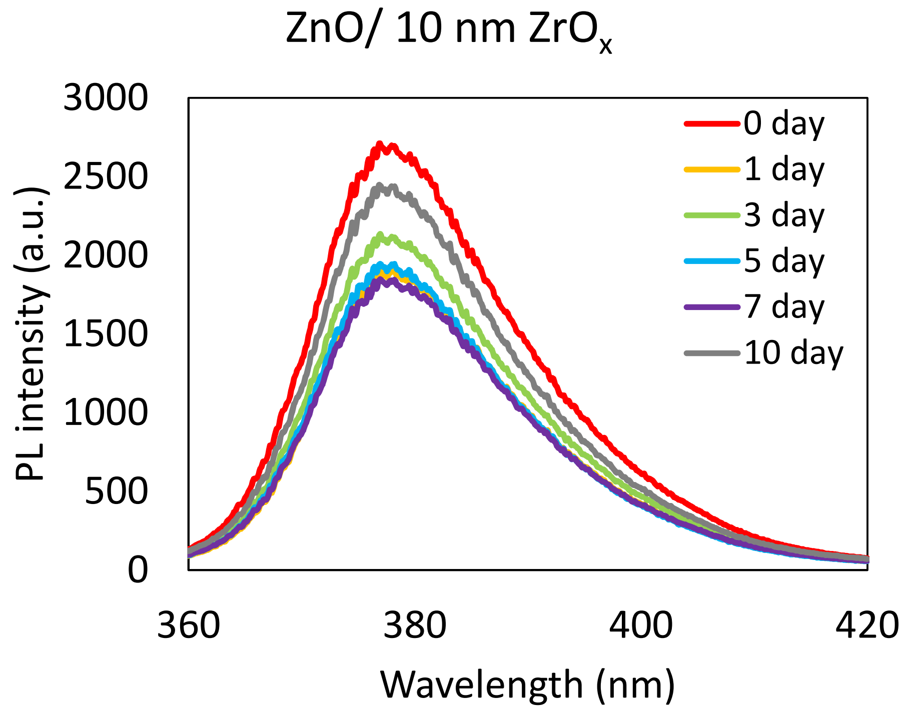

Figure 3.12 (continued) PL emission spectra of ALD film protected ZnO sensor samples. (a) 5 nm TiO_x, (b) 11 nm TiO_x, (c) 10 nm Al_2O_3, (d) 10 nm HfO_x, and (e) 10 nm ZrO_x capping layer. The ALD capping layers were deposited at 250°C.

(a)

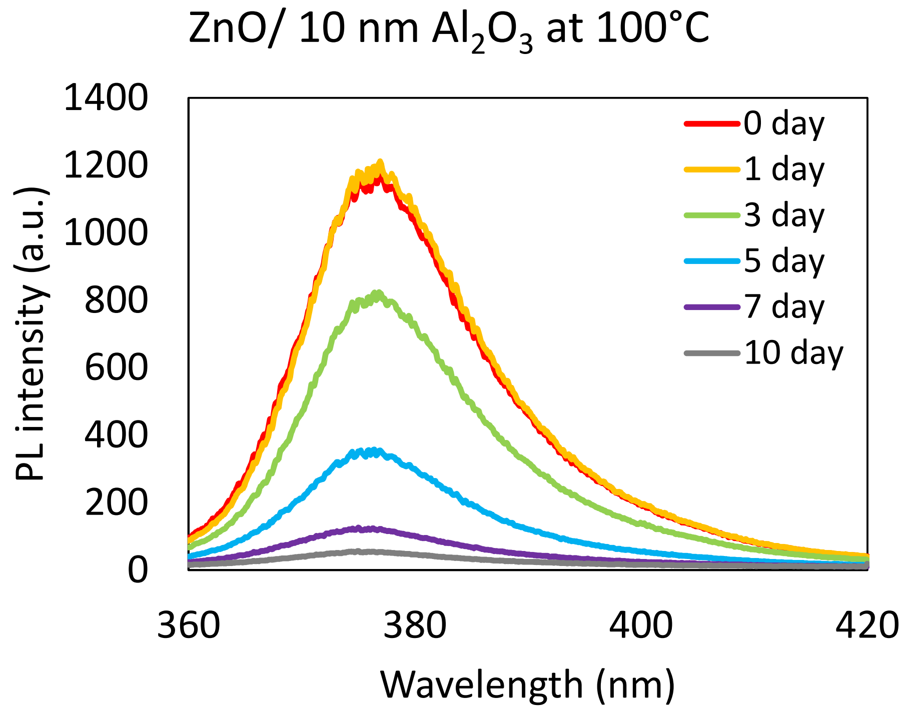

(b)

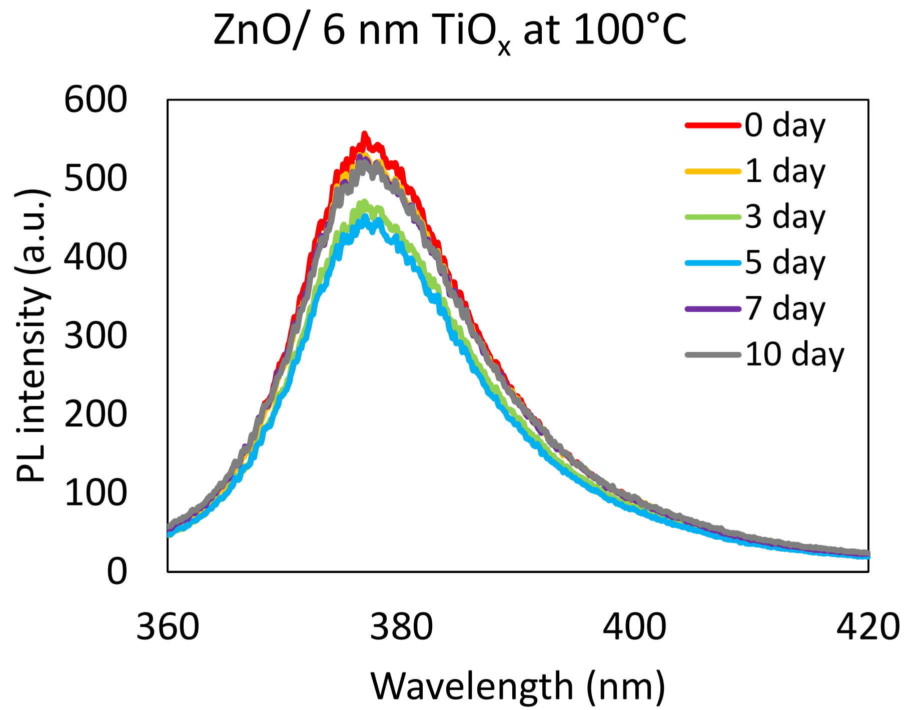

Figure 3.13 PL emission spectra of ALD film protected ZnO sensor samples. (a) 10 nm Al_2O_3 and (b) 6 nm TiO_x. These capping layers were deposited at 100°C

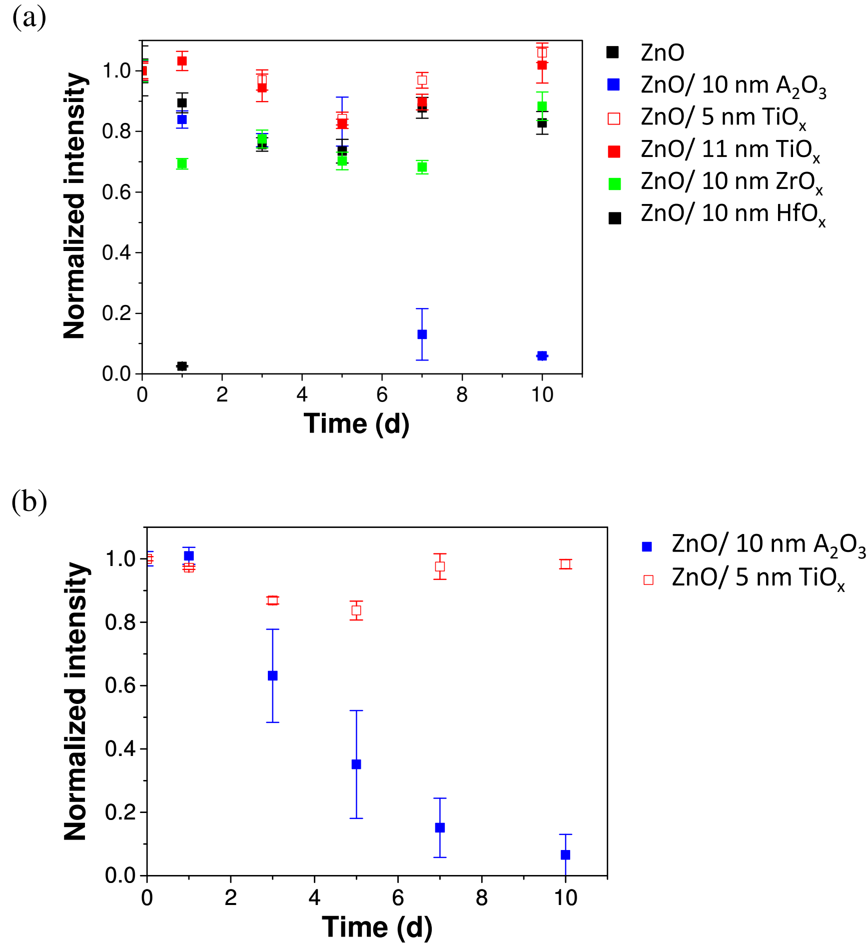

Figure 3.14 Normalized peak intensity of ZnO PL emission after water soaking. (a) ALD films that are deposited at 250°C and (b) ALD films that are deposited at 100°C.

3.3.3 Spectroscopic ellipsometry

In order to support PL test results, SE data were measured for each sample before and after water soaking. **Figure 3.15** plots the SE data of representative ALD films: (a) ZnO, (b) Al_2O_3-coated ZnO, and (c) TiO_x-coated ZnO. The refractive index (n) and the film thickness of 100 cycle ZnO layer is estimated to be 1.95 and 11 nm, respectively. After one day of water soaking, the SE data becomes almost identical to a bare silicon substrate (**Figure 3.15** (a)), and no film is expected on the samples. In other words, the

ZnO sensor layer dissolved in water. On the other hand, for the Al_2O_3-coated ZnO samples, the refractive index and the thickness of Al_2O_3 was estimated to 1.76 and 10 nm, respectively, initially. After 10 days water soaking, the SE data suggest that an unknown film still remained on the Si substrate. The SE data cannot be fitted with the Cauchy model for Al_2O_3 or ZnO showing a dramatic change in the film has occurred. The estimated total film thickness is slightly thicker than the initial total film thickness, but the refractive index is lower than Al_2O_3, which may indicates removal of underlying ZnO trace layer and/or partial degradation of Al_2O_3 capping layer. Finally, in the TiO_x coated ZnO sample, the change of the SE data after water soaking was negligible, and indicates that the film is stable in water for 10 days. The results of ZrO_x-coated ZnO and HfO_x-coated ZnO are also identical as expected from the results of the PL test.

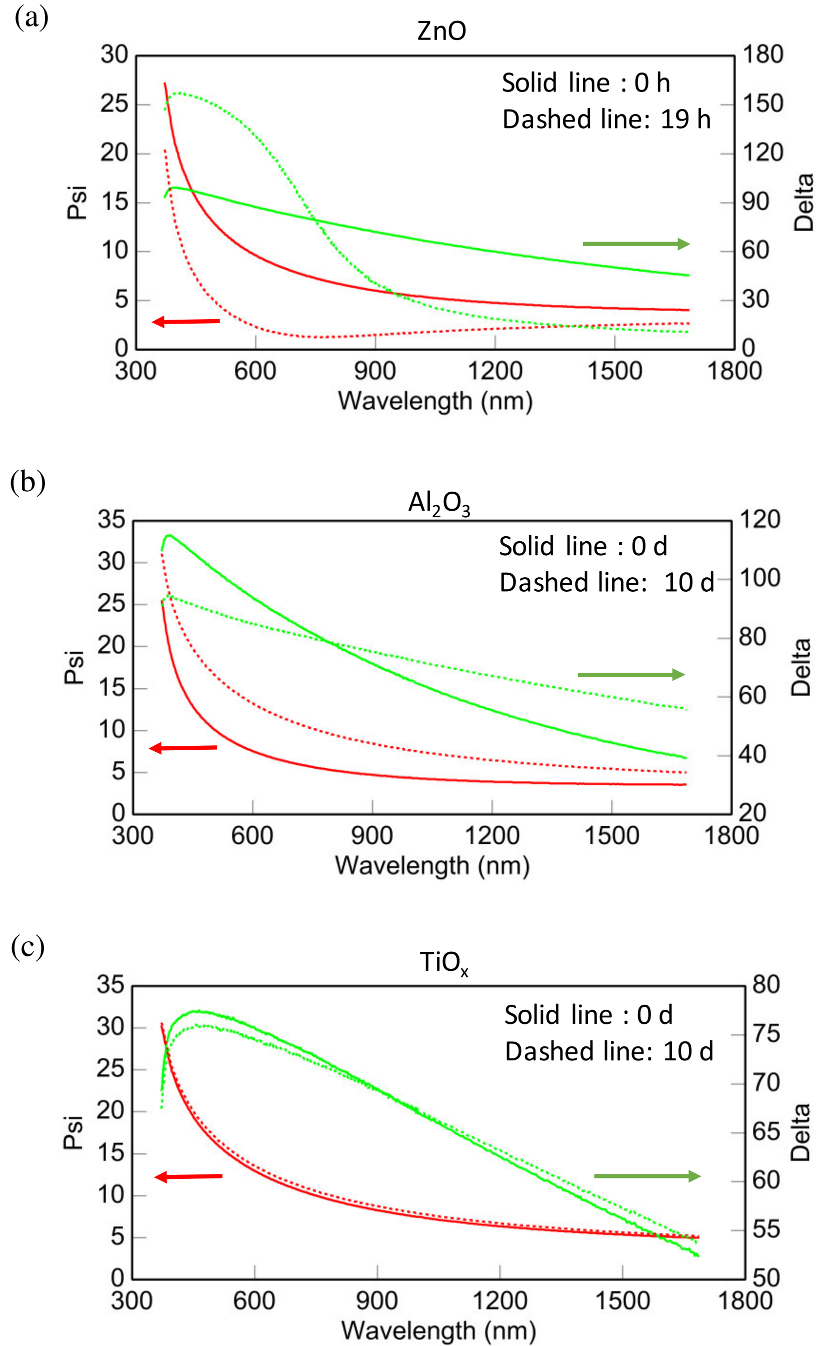

Figure 3.15 Ellipsometry data of ZnO and ALD protection layer before (solid lines) and after water soaking (dashed line). The light incident angle is 75°. (a) 10 nm thick ZnO layer was not measurable after 19 h water soaking. (b) Optical density and/or thickness changed in Al_2O_3 coated ZnO sample. (c) TiO_x coated ZnO shows almost no change in the ellipsometry data.

3.4 Investigation of degradation behavior

The optical characterization methods in the previous section provided only indirect evidence to determine the existence and degradation of the ALD films. Therefore, the results are not clear how the degradation progressed in an Al_2O_3-coated ZnO samples. Therefore, this section performs direct characterization techniques such as XPS and SEM.

3.4.1 XPS depth profiling

Al_2O_3 samples showed instability in water, elemental composition and binding energy of the elements in Al_2O_3 were analyzed using XPS before and after water soaking. **Figure 3.16** plots the electron binding energy distributions of (a) Al 2p level and (b) O 1s level. **Figure 3.16** (a) indicates that no binding energy change was observed in the Al element, suggesting the remained Al_2O_3 stays without chemical change. In O 1s spectra (**Figure 3.16** (b)), the portion of hydroxyl group peak at 532.8 eV increases after water soaking due to surface contaminations. However, the O 1s peaks of fresh and water soaked samples are almost identical after removing the top surface by sputtering.

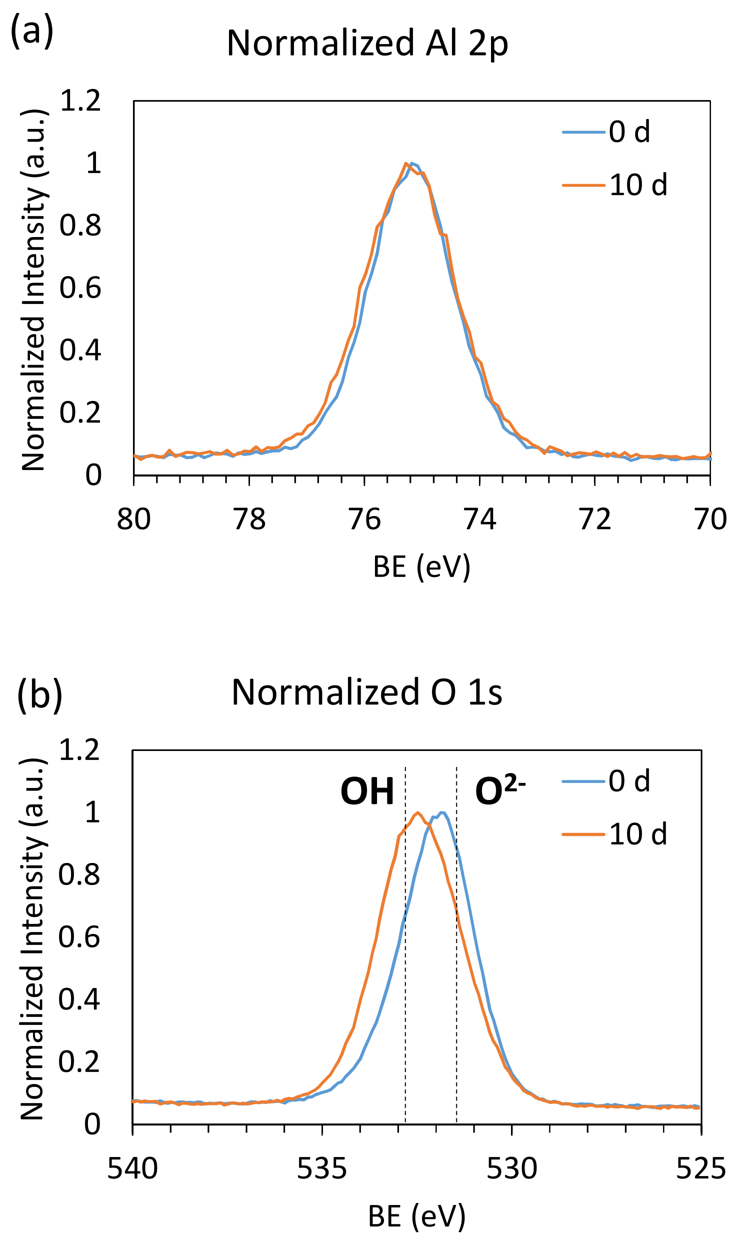

Figure 3.16 XPS results of Al_2O_3 samples before and after 10 day water soaking. (a) Al 2p spectrum showed no binding energy change, suggesting no chemical state change in Al_2O_3. (b) O 1s peak has more hydroxyl (OH^-) groups after 10 day water soaking due to surface.

For the elemental compositions of entire film thickness, XPS depth profiling was carried out on selected samples; Al_2O_3, Al_2O_3 coated ZnO, and TiO_x-coated ZnO. **Figure**

3.17 plots the atomic ratio of Al_2O_3 films and Al_2O_3-coated ZnO films on silicon. **Figure 3.17** (a) is the initial Al_2O_3 films. Considering the alumina film thickness is 10 nm and the XPS surface sensitivity is also around 10 nm, the results indicates alumina forms a uniform film and has a clear boundary between the alumina film and silicon substrate. However, after 5 days in water (**Figure 3.17** (b)), the film became slightly thinner, and the boundary become vague. In addition, Si was observed from the first scan (etch time). Since single crystal Si is stable at room temperature, these results suggest that alumina may be partially removed during water soaking which is in agreement with other studies that have shown that ALD alumina films can be unstable in the presence of water.

In case of the Al_2O_3 coated ZnO sample, two distinct films, Al_2O_3 and ZnO, are clearly observed initially (**Figure 3.17** (c)). However, after 10 days, Zn was not detected at all, only aluminum and oxygen are detected through the entire film on silicon. Furthermore, the boundary becomes undefined again. These results indicate that alumina still exists on the silicon substrate, but could not provide enough protection to prevent the dissolution of ZnO in water. Also, the reason for failure may be due to the local or partially degradation of the Al_2O_3 film. The results also coincide to the result of the PL test and the SE data.

On the other hands, TiO_x coated ZnO sample showed no elemental composition changes after 10 day water soaking. **Figure 3.18** plots the atomic percentage of TiO_x coated ZnO samples (a) before and (b) after water soaking. As proved in PL emission test, ZnO sensor layers were preserved by TiO_x coating, and the depth profiling results also suggest that the thickness of TiO_x does not change.

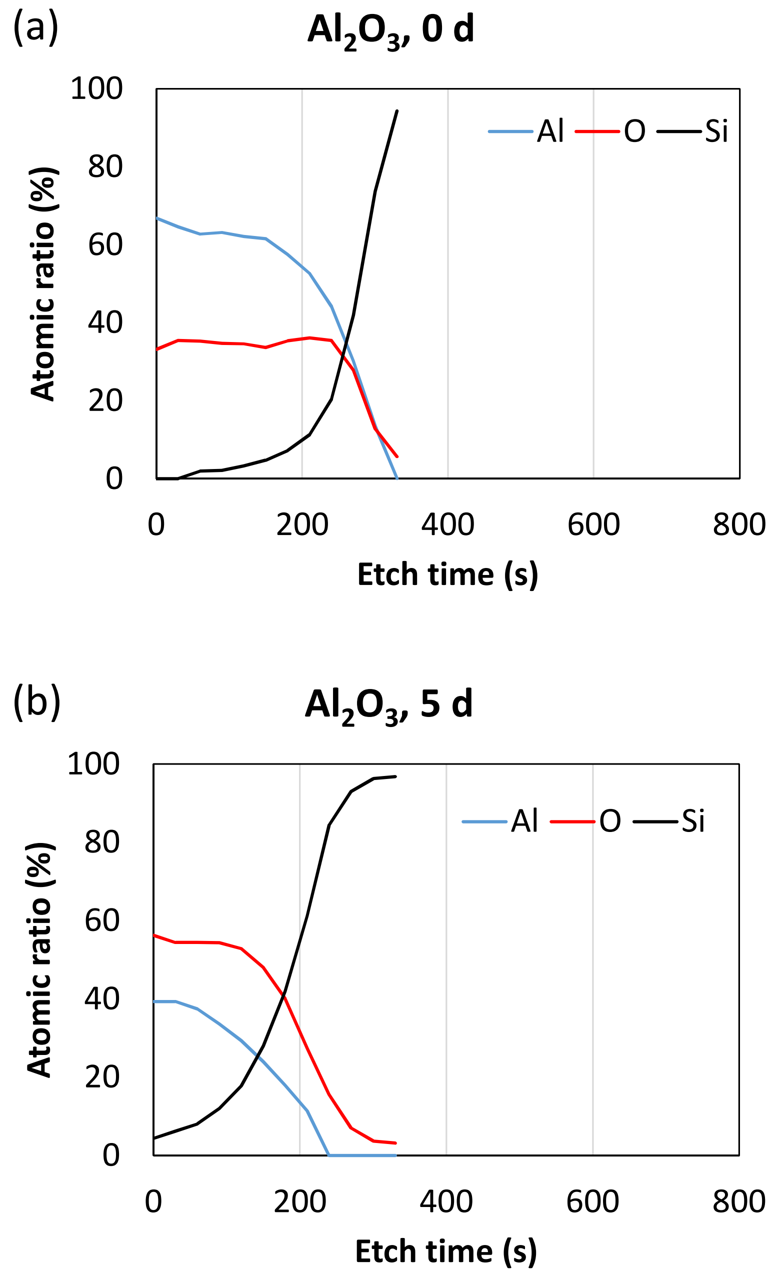

Figure 3.17 XPS depth profiling of ALD films, atomic percentage vs. etching time. X=0 corresponds to the surface of samples, and as the etch time increase the percentage represents the composition of the sample in the lower location from the surface. (a) Fresh 10 nm Al_2O_3, (b) Al_2O_3 after water soaking, (c) fresh Al_2O_3 coated ZnO, and (d) Al_2O_3 coated ZnO after 10 day water soaking.

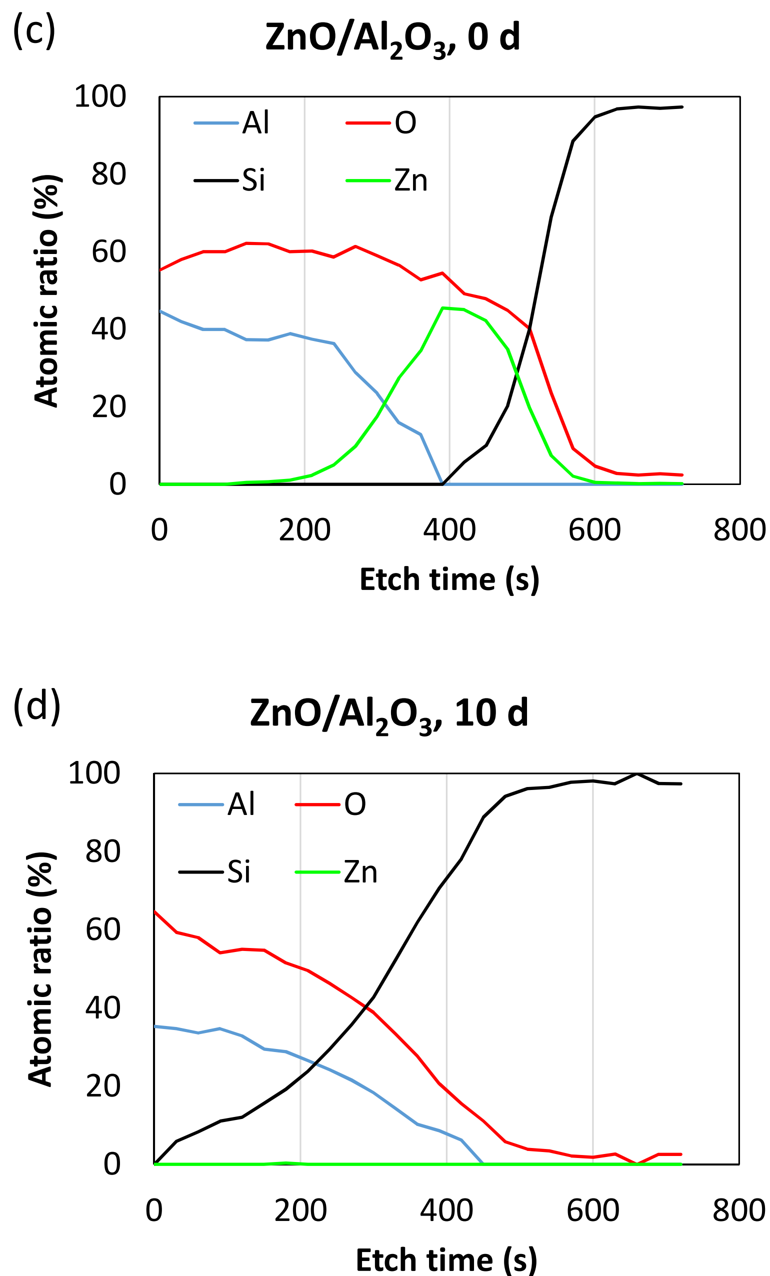

Figure 3.17 (continued) XPS depth profiling of ALD films, atomic percentage vs. etching time. X=0 corresponds to the surface of samples, and as the etch time increase the percentage represents the composition of the sample in the lower location from the surface. (a) Fresh 10 nm Al_2O_3, (b) Al_2O_3 after water soaking, (c) fresh Al_2O_3 coated ZnO, and (d) Al_2O_3 coated ZnO after 10 day water soaking.

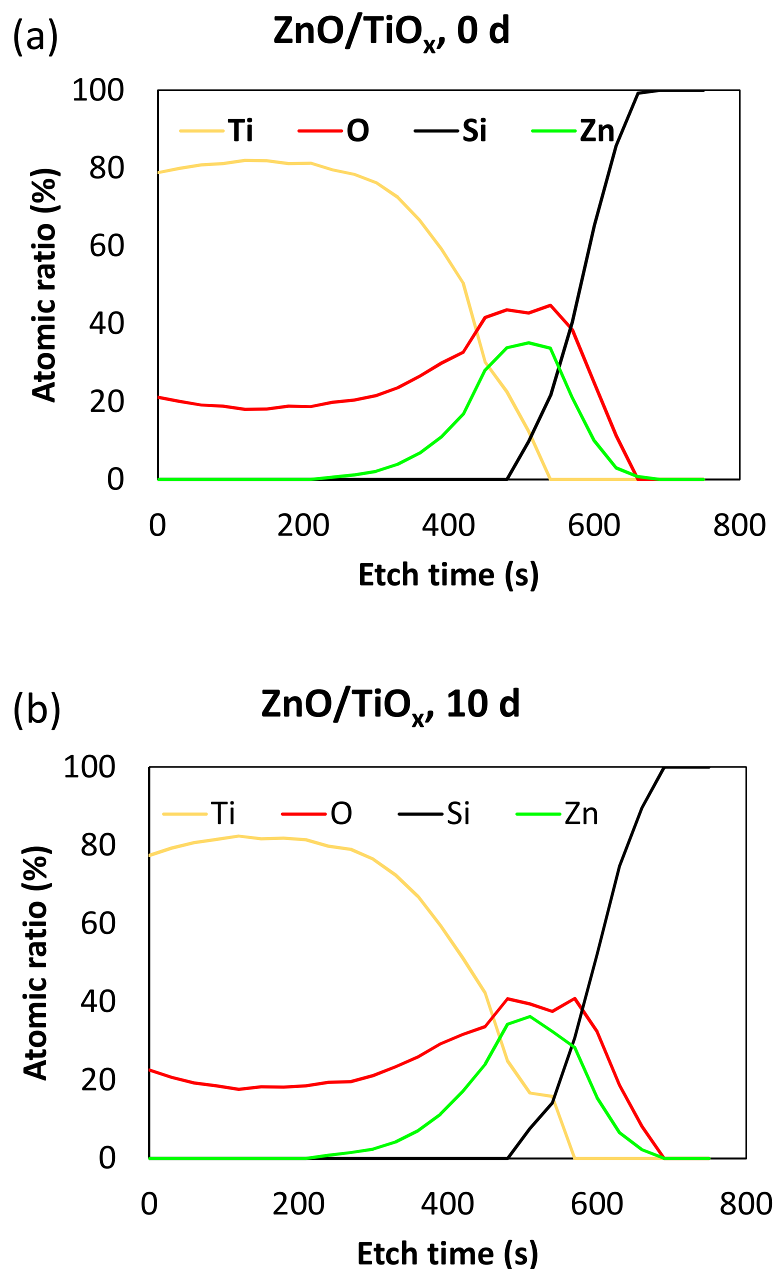

Figure 3.18 XPS depth profiling of ALD films, atomic percentage vs. etching time. X=0 corresponds to the surface of samples, and as the etch time increase the percentage represents the composition of the sample in the lower location from the surface. (a) Fresh TiO_x coated ZnO, and (b) TiO_x coated ZnO after 10 day water soaking.

3.4.2 SEM

Finally, SEM images were taken to support the previous results and explanation. The samples were broken into pieces along with Si crystal direction to make clear cross sectional faces. High resolution FE-SEM (Ultra 60, Zeiss) with back scattered electron and secondary electron detectors was used to capture images at 10 kV acceleration voltage.

Figure 3.19 (a1), (a2), and (a3) shows the top view, the inclined view, and the side view SEM images of fresh Al_2O_3-coated ZnO films on Si substrate, respectively. The top surface is extremely uniform, and the contrast of the film cross-section is fairly uniform except several highlights due to morphology of the breakage. After 10 days in water, however, the top surface has numerous black spots (**Figure 3.19** (b1)), and the contrast of the film's cross-section is stronger (dark black areas was observed.). The tilted image view (**Figure 3.19** (b2)) clearly shows the roughened surface of the water soaked sample. In conclusion, ZnO can easily dissolve in water. Al_2O_3 is also unstable, but partially degrades in water.

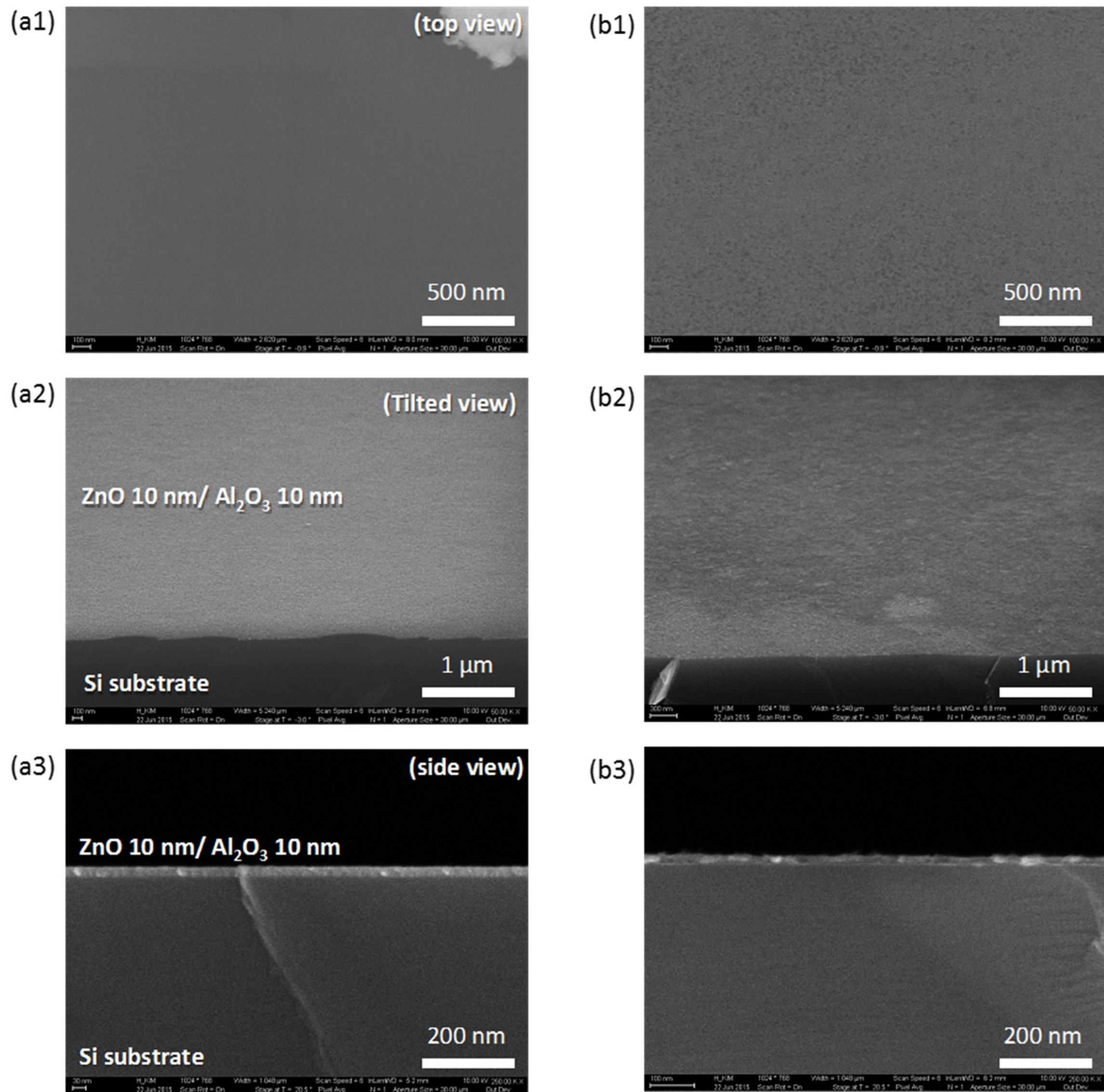

Figure 3.19 SEM images of ZnO/Al_2O_3 samples before water soaking (a1, a2, a3) and after water soaking for 10 days (b1, b2, b3). (a1, b1) are the top views, (a2, b2) are the tilted views, and (a3, b3) are the cross sectional side views. The Al_2O_3 surface was smooth and uniform before water soaking, but the surface has numerous black spots after water soaking.

3.5 Conclusion

This chapter investigated hydrolytic stability of thin ALD films, and introduced ZnO sensing technique to evaluate the protection performance of the ALD films. The first achievement is that a non-invasive atmosphere characterization technique was newly introduced to test the stability of thin ALD films when exposed to water. Using the ZnO PL tracing test, more ALD films at various harsh conditions also can be tested in the future.

Second achievement in this chapter is that hydrolytic stability of ultrathin (10 nm) ALD films was identified. ZnO is widely used semiconducting material, particularly in inverted OSC devices. However, the thin ALD ZnO layers have been shown to be unstable both in the PL studies as well as in actual solar cell testing. Al_2O_3 is one of the most popular materials for a dielectric layer in an electronic device as well as a barrier film application. However, the results indicate that a thin ALD film is not stable enough to sustain its properties in water for a long time as also seen in high temperature accelerated barrier testing by research groups. Thus, while the PL test method is not quantitative, its quick screening method does show the ability to detect two oxides that have been known to show hydrolytic instability. On the hand, the method does suggest that other oxides such as TiO_x, ZrO_x, and HfO_x are stable enough to protect ZnO sensor at least 10 days in water conditions which suggests that they may serve as replacements for ZnO an Al_2O_3 in solar cell applications, provided other properties are sufficient for its targeted use. Therefore, TiO_x, ZrO_x, and HfO_x are recommended candidates if one wants chemically stable ALD films for devices.

Since the method is not quantitative or provides the ability to determine the kinetics of the corrosion of the films, it must be combined with other analysis methods in order to determine the mechanism or rate of degradation. In this study, it was shown through ellipsometry and XPS that ZnO films dissolve in the presence of water while Al_2O_3 films partially remain, possibly even changing chemical composition in some areas. Correspondingly, measurements of the other oxides used in this study show little or no chemical or physical changes in correlation with the PL measurements.

Based on the results of this chapter, the stable ALD films from this work will form the basis to be applied to replace ZnO as the electron selective layer and to replace Al_2O_3 as an ALD barrier film in OPV devices in the following chapters.

CHAPTER 4

ALD TiO_X AS A STABLE ELECTRON SELECTIVE LAYER

4.1 Introduction

As a major cause of the OPV device degradation, Chapter 2 addressed the oxidation of electron-harvesting contacts or electron selective layers (ESL). Even with an inverted OPV device that is more stable than a conventional OPV, ZnO ESLs (**Figure 4.1**) in an inverted OPV are still susceptible to degradation from exposure to moisture.[31] Chapter 3 also showed the chemical instability of ALD ZnO by a DI water soaking test. Therefore, to replace unstable the ZnO ESL in inverted OPVs, TiO_x has received interest for its similar energy band structure and environmental stability.

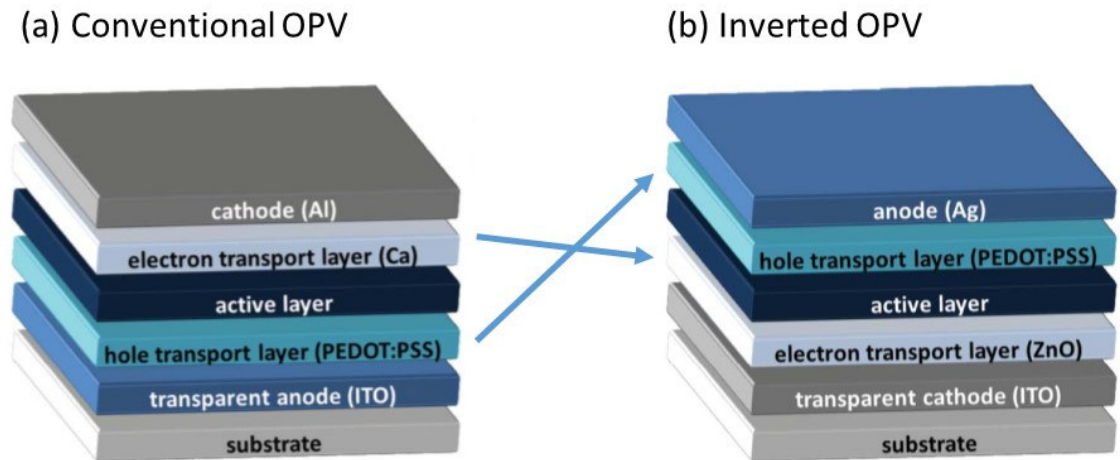

Figure 4.1 Schematics of common layer structures of OPV devices in (a) conventional and (b) inverted geometries with typical materials noted. Adapted from reference [146].

As found in the Chapter 3, TiO_x is highly stable, and TiO_x interlayers that are highly stable have been used to create electron-harvesting contacts in OPV devices with similar band energy structure.[82-84, 147-149] **Figure 4.2** shows the band structure of semiconductors, ZnO, TiO_x ZrO_x, and HfO_x, that were investigated in Chapter 3, showing

that TiO_x has the closest band gap as well as Fermi energy (E_F) position to that of ZnO. For film fabrication, TiO_x films have been processed using sol-gel methods,[82] solution processed at room temperature,[148] atomic layer deposition (ALD),[79, 147, 150] chemical vapor deposition (CVD),[81] and a layer-by-layer method using titania nanosheets[149] and have shown power conversion efficiencies as high as 3.5% with poly(3-hexylthiopene) (P3HT):$PC_{61}BM$ OPV cells. While titania layers have shown their utility in creating electron harvesting contacts in OPV, their lower electron mobility and overall lower conductivity, compared to ZnO films, presents a challenge, as these layers can add to the seriese resistance (R_S) in the OPV to an extent which impacts the device efficiency.[72, 151, 152] Thus, doping of the titania layers to improve electrical conductivity or the use of extremely thin, but non-porous layers of titania, is of interest in order to improve the performance of OPV utilizing electron selective contacts.

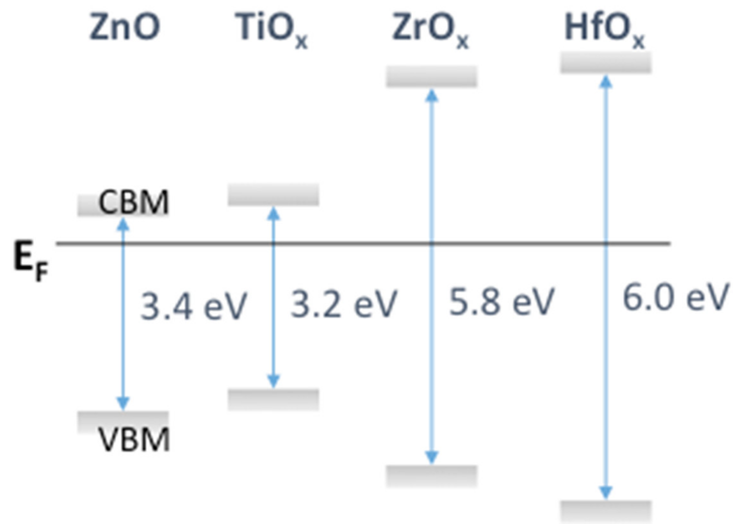

Figure 4.2 Band energy structure for selected metal oxides showing that TiO_x is the most similar to ZnO in terms of the water stable oxides measured in Chapter 3. Adapted from reference [153, 154]

The use of ultrathin layers of titania (<3 nm) have been demonstrated through solution processing, CVD,[81] and through the use of nanosheets deposited in a layer-by-

layer approach.[149] While such processes are scalable, care must be taken in eliminating pinholes that lower the shunt resistance, R_P, in the solar cell. Thus, excellent conformal coverage of the electrode is a foremost requirement of the deposition of the TiO_x layer, regardless of the technique. In this regard, methods such as ALD are quite attractive for modifying the electrode with metal oxide layers, providing excellent control over thickness and the potential for pinhole free films. ALD TiO_x films as hole blocking layers have been demonstrated with thicknesses as low as 6 nm, deposited by atmospheric spatial ALD methods, or as thin as 0.5 nm when used in conjunction with a thick ZnO layer.[79, 83, 147, 155] Thus, it is not clear how well monolithic ALD TiO_x layers behave as rectifying contacts as the thickness is taken below 6 nm, nor do we understand how these electrical properties vary with TiO_x thickness. It is therefore of interest to understand the constraints on ALD TiO_x thickness and morphology, which lead to optimized rectification and OPV response, and it is of interest to have characterization methods which can rapidly assess oxide film quality, especially with respect to film porosity.

Titanium oxide can exist in various crystal structures such as anatase, rutile, brookite, Magnéli phase *etc.*, or as an amorphous film, and the electrical properties such as bandgap, electrical conductivity, and carrier concentration are closely related to the structure of the oxide.[156-159] If the crystal structure of TiO_x changes via post-processing such as annealing, the electrical properties also change.[158-160] Also, the nucleation process of film deposition may affect the structure of thin films.[161, 162] Several studies have shown that ALD TiO_x films start to grow as an amorphous phase and transform to the crystalline anatase form as the film grows, even at constant processing

temperature.[163-166] The critical thickness where the ALD films undergo a phase transformation has been reported to be around 7-8 nm in these studies. However, the effect of the phase transformation on the performance of TiO_x as an ESL is unknown. Therefore, we targeted films with thickness up to 10 nm to determine where an optimal thickness regime occurred for ALD TiO_x films. It should also be noted that thin ALD TiO_x films have been extensively used in recent attempts to both chemically stabilize semiconductors such as Si, GaAs, GaP, etc. in photoelectrochemical water splitting platforms. As in OPV, these films also provide hole-blocking and attenuation of surface recombination of these energy conversion platforms, and we note that extremely thin, conformal and amorphous TiO_x films are often the most desired outcome.[61, 167, 168]

4.2 Experimental

4.2.1 Sample fabrication

For the sample for spectroscopic ellipsometry, XPS, TEM, and Si heterojunction diode test, PE-ALD TiO_x was deposited on highly-doped p-type (<0.02 Ω cm) or n-type (<0.005 Ω cm) silicon wafer. The Si wafers were cut into samples 20 mm by 20 mm size, and then dipped into buffered oxide etchant (6:1) for 1 min to remove the native silicon oxide on the substrates before ALD film deposition. The Si substrates were then rinsed with deionized (DI) water, and dried by blowing with dry nitrogen (N_2) gas. The samples were then immediately placed into the processing chamber of PEALD (Fiji, Cambridge Nanotech). The substrates remained inside of the chamber for 10 min under vacuum (0.2 Torr) so that the temperature of the substrate could equilibrate with the chamber temperature which was 250 °C prior to starting the ALD deposition. For TiO_x

deposition, TDMAT was pulsed into the chamber via argon gas flow (60 sccm), then the chamber was purged for 5 s to remove excessive precursor gas. Then, as an oxidizer, oxygen remote plasma is generated at the top of the processing chamber by applying 300 W RF field on oxygen flow (30 sccm), and is delivered into the chamber in the 200 sccm of argon gas flow. The chamber was purged for 5 s again to remove excessive oxygen and reaction byproducts. This cycle was repeated until the desired film thickness was reached. For the experiment of angle-resolved XPS, CV measurement, conductive AFM, and OPV device fabrication, TiO_x films were deposited on low surface roughness ITO substrates (ρ=20 Ω sq^{-1}, Thin Film Devices Inc.). The ITO substrates were cut into 25 mm by 2.5 mm size, and rinsed with acetone, isopropyl alcohol, and DI water, sequentially, for each 10 minute with sonication. After blowing dry with N_2, the substrates were transferred into the PE-ALD chamber and followed the same procedures in the Si/ TiO_x sample case for TiO_x deposition.

4.2.2 Film characterization

After ALD film deposition, the films were analyzed using various-angle spectroscopic ellipsometry (M-2000, J. A. Woollam Co., Inc.), XPS (Thermo K-alpha, Thermo Scientific), angle-resolved XPS (Kratos Axis Ultra), UPS (Kratos Axis Ultra), grazing incidence XRD (Rigaku Dmax 2000), and C-AFM (Veeco Dimension 3100).

4.2.2.1 Angle resolved XPS

In order to profile the chemical composition along the film thickness, angle-resolved XPS (ARXPS) was used. The information depth for XPS is a few nanometers,

depending upon the kinetic energy of the electrons and the material being analyzed. ARXPS, however, is a technique that varies the emission angle at which the electrons are collected, thereby enabling electron detection from different depths. ARXPS provides information about the thickness and composition of ultrathin films. Such measurements are non-destructive, unlike sputter profiling.

In this chapter, the Kratos Axis Ultra system was used in collaboration with the research group of Professor Neal R. Armstrong at the University of Arizona for ultrathin TiO_x ALD study. Two collection angles, normal (0°) angle and 60°, were used by tilting the sample stage accordingly.

4.2.2.2 UV photoelectron spectroscopy

In order to investigate the work function (WF) and ionization energy (IE) of semiconductor, UV-photoelectron spectroscopy (UPS, Kratos Axis Ultra) is used in collaboration with the research group of Professor Neal R. Armstrong at the University of Arizona. UPS is similar to XPS except the excitation source is UV light (He I, 21.22 eV) that is much lower energy than X-ray. Therefore, only the valence band electron can be excited and reaches the detector. From the distribution of kinetic energies of the electrons that reach the detector, WF and IE can be evaluated. The analysis was done in the ultrahigh vacuum (5×10-6 Torr) chamber, and the spectrometer was calibrated frequently with a clean gold foil, to ensure that a work function of *ca*. 5.1 eV was obtained. **Figure 4.3** shows the electron transition process in UPS. Further details of WF and IE analysis will be discussed later with measurement data.

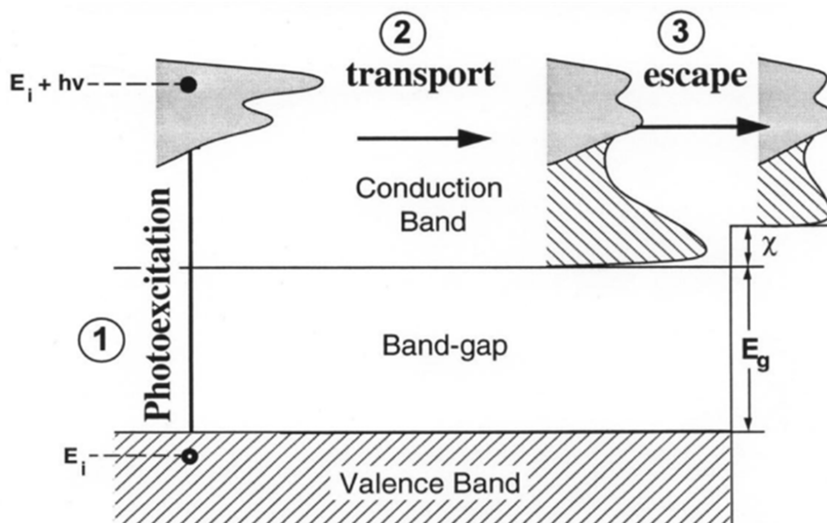

Figure 4.3 Schematic illustration of election transitions in UPS.[169] The distribution of kinetic energy of excited electrons, WF and IE can be evaluated with respect to vacuum energy level.

4.2.2.3 X-ray diffraction

X-ray diffraction (XRD) is a primary method for determining the arrangement of atoms in minerals and metals. In this research, XRD was used to detect the crystalline phases present in the film. In order to acquire a detectable signal from ultrathin ALD films, grazing incidence XRD (GIXRD, Rigaku Dmax 2000) was carried out in collaboration with the research group of Dr. Joseph Berry at the National Renewable Energy Laboratory. The X-ray beam angle was 0.18°, and the X-ray source is Cu Kα line, whose wavelength is 1.5406 Å.

4.2.2.4 Transmission electron microscopy

The atomic structure of the TiO_x film was investigated using scanning transmission electron microscope (STEM, JEOL 2200FS) at the Oak Ridge National Lab. Cross-sectional specimens were prepared using an ion-beam milling, and mounted on a copper ring for STEM.

For the TEM specimen, a 10 nm think ALD TiO_x film was deposited onto a Si substrate. Two same samples were adhered to each other using epoxy and cured for 2 hours at 100°C on a hot plate. This sandwiched structure was then diced into smaller pieces of 1mm x 1mm x 2.2mm using a dicing saw. These small pieces were then dipped into a small drop of epoxy and then baked for 2 hours at 100°C. They were then attached to stub using wax and polished from one side using SiC papers of grit size 800, 1200, 2400 and 4000, in the same order so as to make one side of the sample smooth and free of cracks. After this, the sample was flipped and trimmed into a circular disc of 3mm diameter. After this, it was again polished using the same procedure until the sample thickness reached approximately 100 μm. After this, the whole sample, along with stubs was taken for dimpling using copper wheel and diamond paste. The diamond paste particles used were of 3 μm size. The thickness of sample after dimpling was reduced to about 10 μm at the center. The thickness of the samples was measured using an optical microscope. The samples were then detached from the stubs by placing them in acetone to dissolve the wax. Samples were then fixed onto a Cu ring using epoxy. Afterwards, the samples were ion-milled using precision ion polishing system (PIPS) for final thinning.

The prepared specimen was shipped to the Oak Ridge National Lab for TEM imaging. High-resolution STEM images were acquired with a probe current of 30 pA and probe size of roughly 0.8 Angstroms.

4.2.2.5 Atomic force microscopy

The surface morphology and surface roughness of the metal oxide thin films were studied by AFM (Dimension 3100, Veeco) in collaboration with the research group of Professor Thierry Mélin at the Institute of Electronics, Microelectronics and

Nanotechnology in France. The surface morphology was measured is in the intermittent-contact mode (or a tapping mode) AFM. In the intermittent-contact mode AFM, the film surface was probed with a sharp tip that was attached to a cantilever. The system vibrates the cantilever near its resonance frequency that depends on the distance between the tip and the sample surface. Changes in the frequency were then used for imaging the surface topography. The tip vibrates very close to the surface just barely hitting the surface so that no lateral forces are applied to the surface.

In addition to surface topology, the conductive AFM (CAFM) was also carried out in the same tool by adding an external module for CAFM. A platinum-iridium coated silicon probe tip (SCM-PIC, Bruker) AFM tip was used to acquire current data during CAFM scanning. For CAFM, contact mode scanning was carried out to acquire current mapping images. The underlying ITO layer was grounded using silver epoxy and a probe tip was biased from 0 V to -2 V. Current mapping images and I-V curves of specific locations were measured at room temperature conditions.

4.2.3 Cyclic voltammetry

The cyclic voltammetry (CV) is an electrochemical characterization method to investigate charge transport behavior of metal and semiconductor. Nicholson and Shain performed quantitative simulations of CV in 1964 and explained that all reversible voltammograms look the same and the typical shape, called Nernstian system as in **Figure 4.4** (b).[170] Also, the peak current (i_p) can be expressed as,

$$i_p = (2.69 \times 10^5) n^{3/2} A D^{1/2} v^{1/2} C \quad (4.1)$$

where n is the number of electrons transferred, A is the electrode area, D is the diffusion

coefficient, C is the bulk concentration of species, and v is scan rate. Observing the peak current, the amount of oxidation and reduction of analyte at the electrode. If the electrode is coated with a semiconductor, charge transport property of the semiconductor can be investigated.

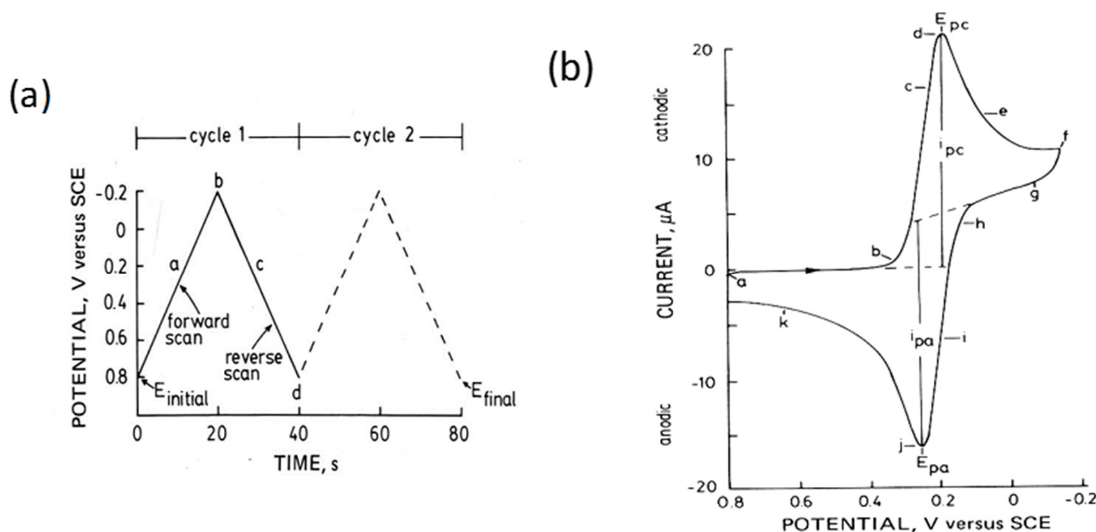

Figure 4.4 (a) Typical excitation signal for cyclic voltammetry, and (b) acquired cyclic voltammogram. Adapted from reference [171].

In this dissertation, hole blocking properties of ALD TiO_x films were studied in collaboration with the research group of Professor Neal R. Armstrong the University of Arizona. CV experiment was carried out using a CHI 660c potentiostate with a three-port electrochemical cell consisting of platinum counter electrode, Ag/Ag^+(BASi, 10 mM $AgNO_3$ in 0.1M $TBAPF_6$ electrolyte) reference electrode, and ALD TiO_x/ITO working electrodes (area = 0.671 cm^2) (See **Figure 4.5**). Probe molecules Decamethylferrocene (97%, Aldrich), 1,1-Dimethylforrocene (97%, Aldrich), and TPD (N,N′-Bis(3-methylphenyl)-N,N′-diphenylbenzidine) (99%, Aldrich) were prepared as 0.5 mM with $TBAPF_6$ (0.1 M) in acetonitrile (HPLC grade, EMD). Voltage is scanned at 0.05 V/s.

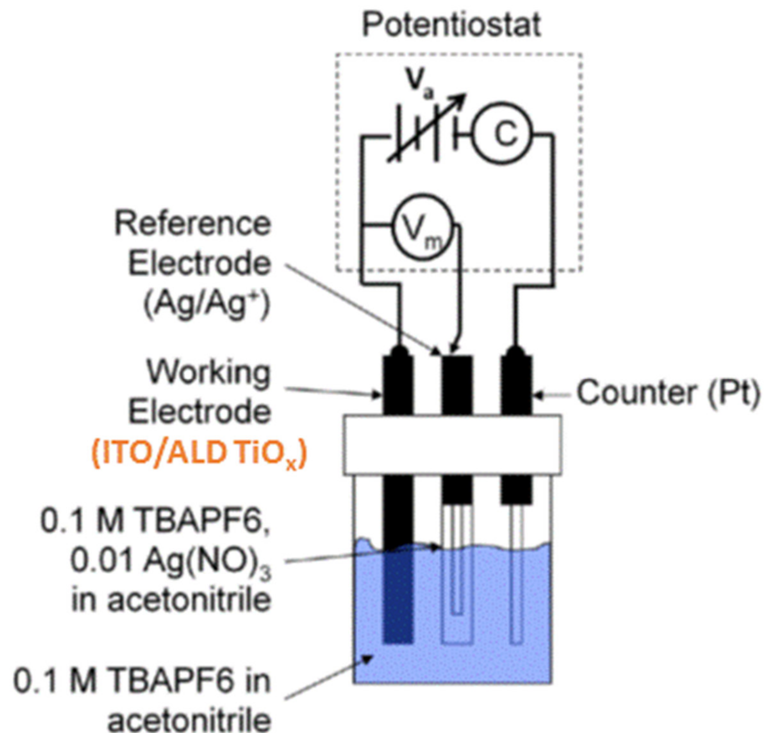

Figure 4.5 Schematic diagram of the CV measurement. ITO/ALD TiO_x samples were used as a working electrode in the measurement.

4.2.4 Si heterojunction diode device fabrication and characterization

In order evaluate the hole blocking property of CVD TiO_x layer, Avasthi *et al.* proposed a Si/TiO_x heterojunction diode (**Figure 4.6**).[172] In the same manner, Si/TiO_x heterojunction test diodes were made by depositing Al and Ag metal contacts on the Si/TiO_x samples using an e-beam evaporator (Denton E-beam evaporator). After the ALD deposition on Si substrates, samples were transferred into the e-beam evaporator chamber within 30 min. First, 100 nm silver layers were deposited on the bottom side of the Si substrate at the pressure of 3×10^{-6} Torr, and 50 nm thick aluminum layers were deposited on the top side of the ALD layers with a shadow mask. Using the patterned shadow mask,

an array of circular shaped Al electrodes were fabricated with an area of 0.114 cm^2. The metal thickness was monitored by an *in-situ* quartz crystal during deposition.

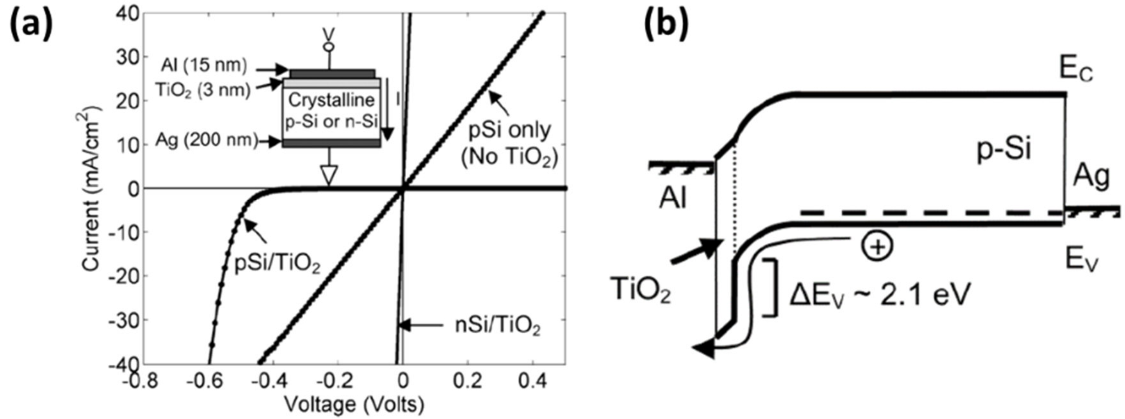

Figure 4.6 Si/TiO_x heterojunction diode test for charge selectivity test. (a) I-V curves of Al/TiO_x/p-type Si/Ag heterojuntion diode test device, showng retification contact was made with TiO_x and p-type Si. (b) energy band diagram of the TiO_x/Si heterjuntion diode, showng the energy barrier 2.1 eV is built at the interface of TiO_x and Si in their the valence band. Adapted from reference [172].

The *J-V* characteristic of the fabricated heterojunction devices was tested with a custom-made 4-point probe stage and a source meter (Keithley 2400). The stage used gold-coated spring pins for top and bottom plane contacts using the 4-point configuration reduced the effects of parasitic resistance from wires and contacts. The voltage was swept from -1 V to 1 V with 0.02 V step on the Al contact, and the current flow was measured. **Table 4.1** summarizes the samples made in this chapter. **Figure 4.7** (a) and (b) shows a device structure and the configuration of the measurement, respectively. **Figure 4.8** shows (a) a fabricated Si/TiO_x heterojunction test diode, and (b) a custom 4 point spring-pin probe stage used in this experiment.

Table 4.1 List of TiO_x/Si heterojunction test diode devices with various configurations.

Cathode	Substrate	Hole-blocking layer	Anode
Al 50 nm	n-type Si (500 µm)	-	Ag 100 nm
		TiO_x 3.0 nm	
	p-type Si (500 µm)	-	
		TiO_x 0.5 nm	
		TiO_x 1 nm	
		TiO_x 3 nm	
		ZnO 3 nm	

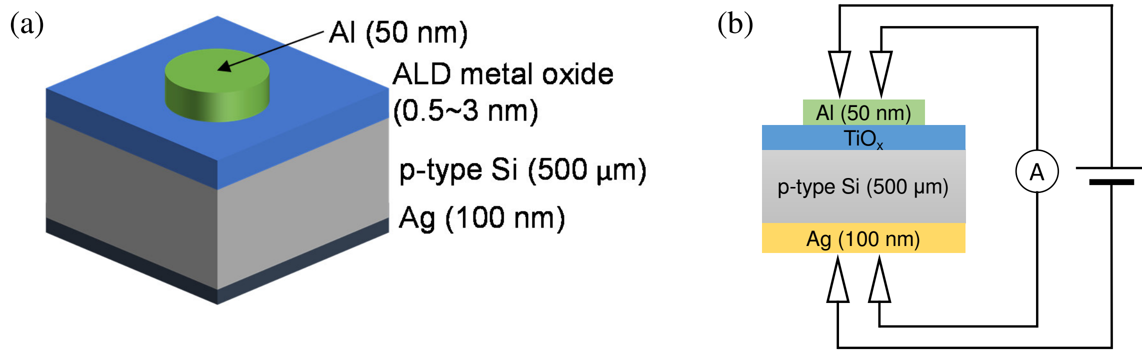

Figure 4.7 Test structure of metal oxide/Si diode for testing the hole blocking capability of ALD TiO_x films. (a) Schematic illustration of the diode with a patterned top Al electrode, and (b) current-voltage measurement configuration by a 4 point probing method.

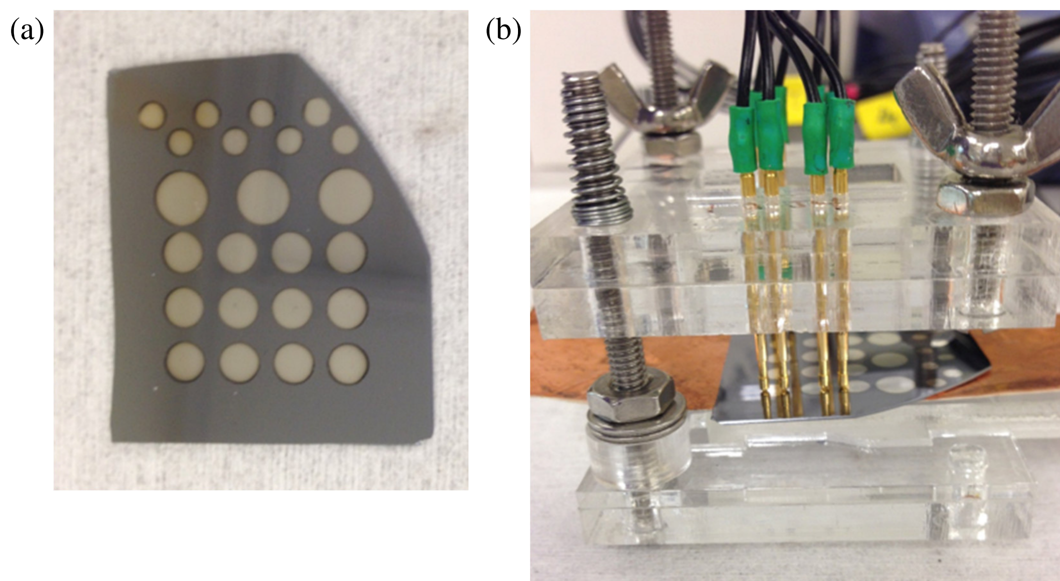

Figure 4.8 Heterojunction Si/TiO_x diode devices. (a) Fabricated test sample and (b) custom probing stage, probing the top Al pads using 2 spring pins, and the bottom Ag layer is connected on the bottom copper surface.

4.2.5 OPV device fabrication and characterization

General procedures for the OPV device fabrication and characterization are described in previous studies.[81, 173] ALD films with thicknesses including 0.5 nm, 1 nm, 3 nm, and 10 nm were prepared using PEALD (Fiji, Cambridge Nanotech), and shipped to the research group of Professor Neal R. Armstrong the University of Arizona to complete TiO_x OPV device fabrication and characterization and a travel grant allowed me to go and work in his laboratory. **Table 4.2** lists the samples fabricated for this set of tests. A solution for the BHJ layer were prepared by dissolving P_3HT(20 mg, Rieke Metals) and $PC_{61}BM$ (16 mg, Nano-C) into 1,2-dichlorobenzene solvent (1 mL), and the solution was stirred at 60 °C for at least 3 hours. At room temperature, a 150 μL solution was obtained to spin on ITO/TiO_x substrates at 700 rpm for 1 minute. The substrate was then stored in covered Petri dish right after spin-coating. On the following day, the

substrates were annealed at 100 °C for 10 minutes on a hot plate. Then poly(3,4-ethylenedioxythiophene) polystyrene sulfonate (PEDOT:PSS, Hereaus) solution with Triton X-100 (1 wt%, Fisher Scientific) was spin-coated at 4000 rpm for 1 min. The PEDOT:PSS layer was rinsed off with ethanol and isopropanol and spin coated repeatedly until a full uniform PEDOT:PSS layer is obtained. Thereafter each substrate was transferred to a hotplate and annealed at 110 °C for 10 min in a N_2 filled glovebox. Finally 100 nm Ag (99.99%, Kurt J. Lesker) was deposited by thermal evaporation at 10^{-6} Torr with a shadow mask defining the cell area as 0.125 cm^2. All device creation steps were undertaken a in N_2 filled glovebox (Mbraun Labmaster) except for the PEDOT:PSS spin-coating steps.

Table 4.2 List of organic photovoltaic cells.

Substrate/ Bottom electrode	Hole-blocking layer	Active layer	Electron-blocking layer	Top electrode
Glass/ITO	TiO_x 0.5 nm	P_3HT:PCBM	PEDOT:PSS	Ag
	TiO_x 1 nm			
	TiO_x 3 nm			
	TiO_x 10 nm			

The performance of photovoltaics was evaluated by current density-voltage (*J*-*V*) characteristic. The main device performance parameters such as power conversion efficiency (PCE), open-circuit voltage (V_{OC}), short-circuit current density (J_{SC}), and fill–factor (FF) was measured using a source meter (Keithley 2400) while illuminating the device with a simulated solar light in a glove box. These parameters were extracted from the measured current density-voltage curves as shown in the **Figure 4.9**.

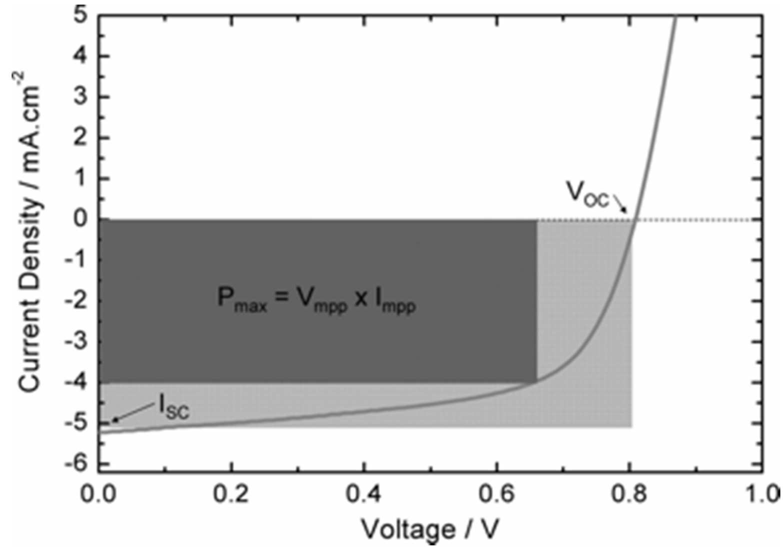

Figure 4.9 A typical *J-V* curve of a solar device.

The J_{SC} (current density at V=0), V_{OC} (voltage at I=0), and voltage (V_{max}) and current density (J_{max}) at the maximum power point (P_{max}) are also shown in the figure. *FF* is defined as the ratio of the actual maximum generated power ($V_{max} \times J_{max}$) to the theoretical maximum power ($V_{OC} \times I_{SC}$) and is given by,

$$FF = \frac{J_{\max} \times V_{\max}}{J_{SC} \times V_{OC}} \qquad (4.2)$$

The power conversion efficiency of a photovoltaic is expressed as follows

$$PCE = \frac{J_{\max} \times V_{\max}}{P_{in}} = \frac{FF \times J_{sc} \times V_{OC}}{P_{in}} \qquad (4.3)$$

where P_{in} is the incident light power density. In addition, the device series resistance (R_s) and shunt resistance (R_P) can be estimated with the inverse slope of a *J-V* curve.

In this chapter, the *J-V* characteristics were measured using a source meter (Keithley, model 2400) and custom software (National Instruments LabView) in a N_2 filled glovebox under a 300 W Xe arc lamp (Newport). The light passed through a neutral

density filter (Thorlabs), an AM 1.5 filter (Melles Griot), and a 40 degree output angle optical diffuser (Newport). The light intensity on the devices was calibrated by a response thermopile (Newport) and a silicon photodiode (Newport–Model 818-SL with OD3 Attenuator) to be 100 mW cm^{-2}.

4.3 Film properties of ALD TiO_x films

4.3.1 Chemical composition

The chemical composition of ALD TiO_x films were analyzed from high resolution Ti 2p and O 1s XPS spectra for the TiO_x film. The shape and peak positions of the Ti $2p_{3/2,1/2}$ peaks were consistent with the formation of TiO_x with no observable lower oxidation state mid-gap defects as shown in Fig. S2 in the Supplementary Information section.[174] **Table 4.3** summarizes the analyzed composition ratio of the OH^- and O^{2-} components from the O 1s XPS spectra at 2 collection angles, 0° and 60° (**Figure 4.10**). As the film becomes thicker, the relative intensity of the O 1s peak for OH^- decreases for both collection angles. As the TiO_x film thickness increases from 0.5 nm to 3 nm, the ratio of OH^- peak decreases from 18.3% to 11.1% at 0° collection angle, and 21.1% to 13.7% at 60° collection angle. This suggests that the stoichiometric titanium dioxide component becomes dominant as the film thickness increases to 3 nm. Also, the hydroxyl components were found more at the 60° collection angle than at 0° collection angle, which suggests that the hydroxyl component resides on the top surface of the layer rather than inside of the layer, and some of this hydroxide may have formed when the PE-ALD films were briefly exposed to atmosphere, before containment in the argon-filled vessel for transport to the surface analysis system. In any case it is clear that the

thinner (< 3 nm) TiO_x film are slightly more susceptible to hydroxylation, as would be expected for a thin film which still contains a few pin-holes, allowing exposure of the remaining ITO substrate.[161, 175]

Table 4.3 Ratio of oxide O 1s and hydroxyl O 1s in various thickness of TiO_x layer on ITO.

XPS collection angle (°)	TiO_x thickness (nm)	Percent composition of oxide O 1s[a] (%)	Percent composition of hydroxyl O 1s[b] (%)	O 1s components ratio Oxide/hydroxyl
0	0.5	81.7 ± 0.3	18.3 ± 0.1	3.47 ± 0.01
	1	84.5 ± 0.3	15.5 ± 0.1	5.44 ± 0.02
	3	88.9 ± 0.3	11.1 ± 0.1	8.03 ± 0.03
60	0.5	78.9 ± 0.3	21.1 ± 0.1	3.74 ± 0.01
	1	81.4 ± 0.3	18.6 ± 0.1	4.39 ± 0.02
	3	86.3 ± 0.3	13.7 ± 0.1	6.29 ± 0.02

[a]Binding energy at 530.6 eV; [b]Binding energy at 532.0 eV.

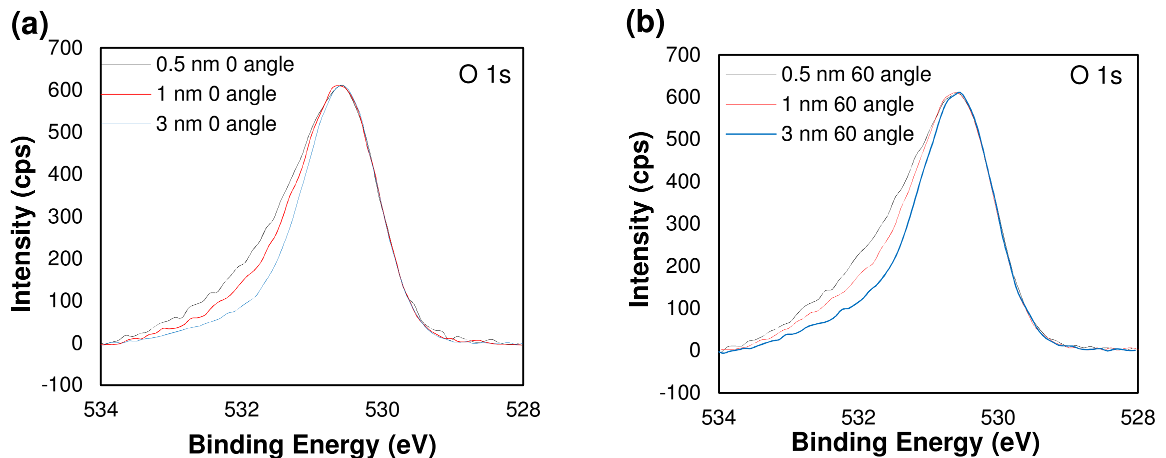

Figure 4.10 Angled resolved XPS spectrum of normalized O 1s peaks of TiO_x, (a) spectrum of normal detection angle, 0°, and (b) spectrum of shallow detection angle, 60°. As the film thicker, the ratio of hydroxyl O1s peak (532.0 eV) to oxide O 1s peak (530.6 eV) decreases in both cases.

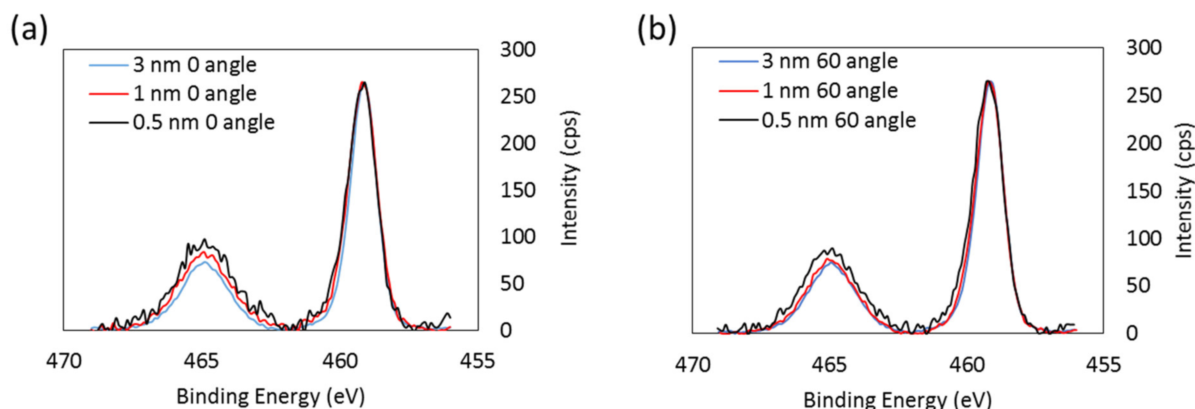

Figure 4.11 Angled resolved XPS spectrum of normalized Ti 2p peaks of TiO_x (a) at normal detection angle 0°, and (b) a shallow detection angle, 60°. No difference was observed in Ti 2p spectrum.

4.3.2 Electron band energy structure

UPS was used to characterize both the work function and E_{VB} for the 3 nm PEALD TiO_x film deposited on a p-type Si substrate (**Figure 4.12** (a)), and 1 nm, 3 nm PEALD TiO_x film on ITO substrates. As in several previous studies,[81, 176, 177] the effective work function of the TiO_x film was evaluated by estimating the energy difference (w) between the low kinetic energy edge (LKE) of the photoemission spectrum, and the spectrometer/sample Fermi energy (see **Figure 4.12**), and subtracting this difference from the source energy, 21.2 eV: $\Phi = 21.2\ \text{eV} - w$. In the same manner E_{VB} was estimated by computing the difference (w') between LKE and the high kinetic energy edge for photoemission from the oxide film (HKE) and subtracting that from the source energy: $E_{VB} = 21.2\ \text{eV} - w'$. Thus, the work function and the VBE with respect to the vacuum level for 3 nm TiO_x film on Si was 3.7 eV and -7.1 eV, respectively. Also, the work functions of 1 nm and 3 nm TiO_x films on ITO substrates were 3.6 eV and 3.7

eV, respectively. These values are close to those expected for stoichiometric TiO_x thin films or bulk semiconductors, even though the absolute thickness is just above the sampling depth for the UPS experiment, which is about less than 3 nm.[178, 179] Clearly the PE-ALD process leads to the stoichiometric oxide, at thicknesses predicted to lead to good electrical properties (see below), avoiding some of the resistance effects seen for thicker TiO_x films.

Based on these UPS results, **Figure 4.12** (b) shows a proposed general band energy diagram of Ag/p-type Si/TiO_x/Al test device structures, which were used in the Si diode experiment later. The energy band in the diagram is aligned at the Fermi level when the device is at short-circuit condition, and pre-contact energy levels of Ag, p-type Si, and Al were taken from other studies.[81, 172] According to the diagram, holes in the valence band of the silicon must overcome an energy barrier to travel to the Al metal contact due to the large band gap and low valence band energy of the TiO_x layer. This low valence band energy introduces a valence band offset (or a barrier height for hole transport) $\Delta E_V \approx 2.0$ eV which would be more than sufficient for hole-blocking in these devices, when the TiO_x film is of sufficient thickness.

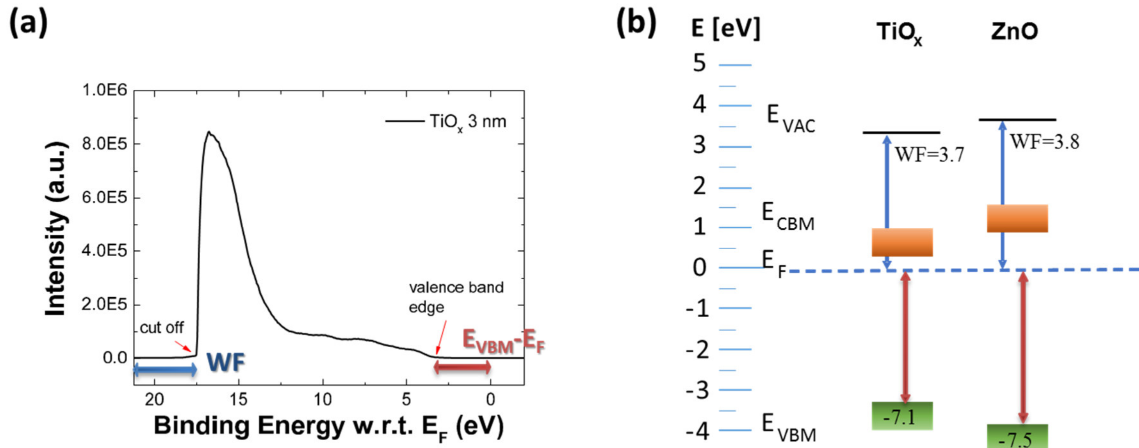

Figure 4.12 Electron band energy structures of ALD TiO_x and ZnO films. (a) UPS spectra of a 3 nm TiO_x film on Si substrate, and (b) band energy diagram from UPS spectra.

4.3.3 Structural properties (XRD, TEM)

The crystal structure of TiO_x films on Si substrates were investigated using GIXRD with an incident angle of 0.18°, and **Figure 4.13** shows the GIXRD patterns of 3 nm, 5 nm, and 10 nm TiO_x films. The 10 nm TiO_x film shows peak patterns that completely overlap with those for anatase TiO_x except a peak at 50.5°, which was caused by diffraction from the Si substrate.[163] However, 5 nm TiO_x films show no diffraction peaks suggesting that these are amorphous films, while 10 nm TiO_x films are predominantly in the anatase form. Thus, there is a clear phase transition as film thickness increases. This result also agrees with previous studies that show there is a critical thickness that ALD TiO_x structures develop from amorphous to anatase during film deposition.[35, 163-166]

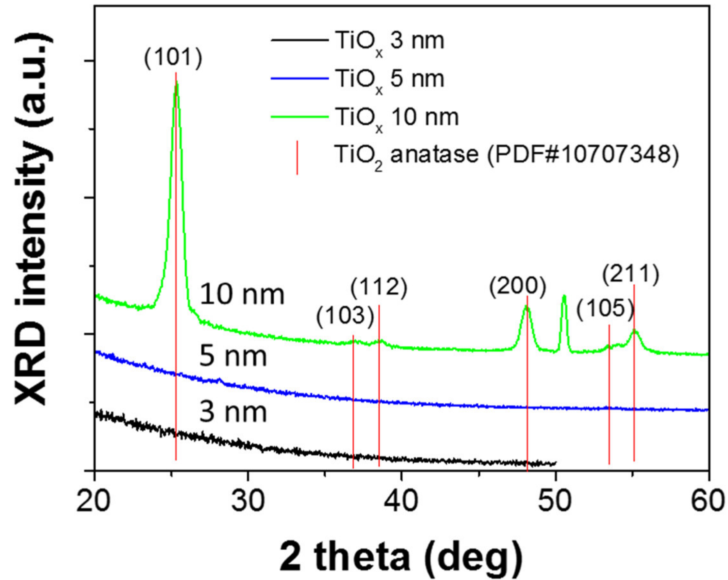

Figure 4.13 XRD peak analysis of 3 nm, 5 nm and 10 nm TiO_x films on Si substrates. 3 nm and 5 nm film have no peak, suggesting amorphous TiO_x. On the other hand, 10 nm TiO_x film shows XRD peaks corresponding to anatase structure.

Cross-sectional TEM images in **Figure 4.14** support the formation crystal phase in 10 nm thick TiO_x film on Si substrate. However, the crystal phase exists partially in the film, and that may results in localized variance in electrical properties as some regions remain amorphous while some are crystalline.

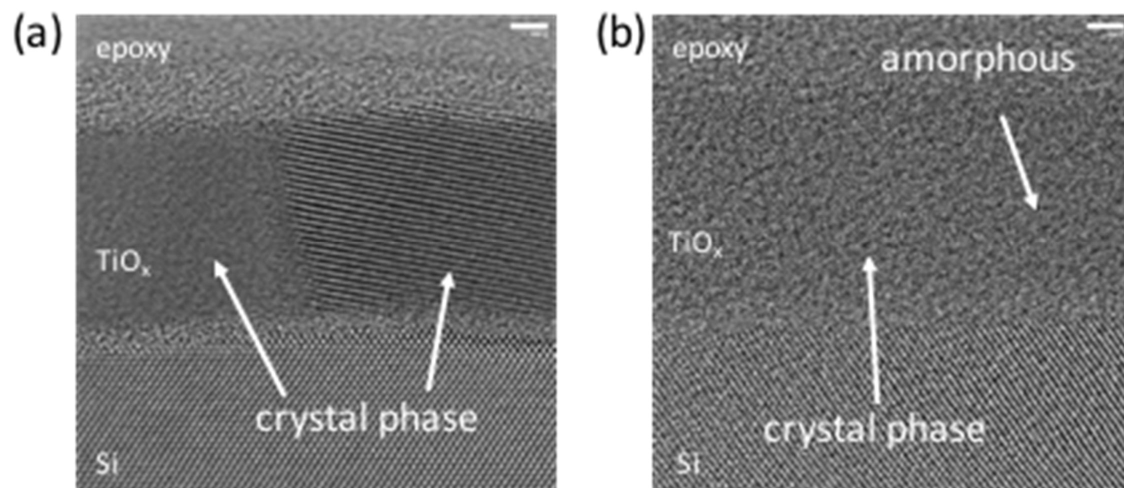

Figure 4.14 Cross-sectional TEM images of 10 nm TiO_x film on Si substrate at two locations. (The top right scale bar is 2 nm) At location (a), two crystal phases was observed in 10 nm TiOx film, and at location (b), both amorphous and crystal phase were observed.

4.3.4 Out-of-plane conductivity

We also used C-AFM to investigate details of microscopic electrical properties of these ALD TiO_x films, acquiring both current mapping images and current-voltage profiles. **Figure 4.15** shows surface morphology and corresponding current mapping images with 1, 3, and 10 nm TiO_x layers on glass/ITO substrates. Successive scans showed that there is no noticeable difference in the morphology among 3 different thicknesses of TiO_x on ITO surfaces, and root mean square roughness values are 0.4 nm for all cases, which is consistent to that of bare ITO. However, the current mapping images by C-AFM showed that the average currents are different depending on TiO_x film thickness. As seen in **Figure 4.15** (d), the average current for 1 nm TiO_x is -164 pA at -1.3 V bias, and the current distribution is quite uniform. With 3 nm TiO_x films, the average current, -160 pA was measured when the sample is biased down to -1.5 V as seen

in **Figure 4.15** (e). The high current in 1 nm TiO_x film seems to be affected by the contribution of the tunneling current while the tunneling current was suppressed with thick 3 nm films. Finally, **Figure 4.15** (f) shows C-AFM images of a 10 nm TiO_x film, and the average current was -155 pA at -1.5 V bias. However, as the film thickness increases, local dark spots appear that indicate localized large current flows. For detailed electrical behavior of TiO_x films, current-voltage (I-V) curves were acquired sweeping bias from 0 V to -2 V.

Figure 4.17 (a) plotted I-V curves of bright areas and dark areas in the 10 nm TiO_x C-AFM image. In the dark area, higher current flowed even at lower bias than in the bright area. These results suggest that highly conductive areas form locally as the TiO_x film become thicker, which may be related to the formation of anatase crystalline structures in thick TiO_x film as we observed in GIXRD and TEM results. It has been proposed that the crystallinity of the anatase phase results in high conductivity as charge can transport along the grain boundaries of the TiO_x.[159, 180] **Figure 4.17** (b) shows the average I-V curves of bright area in 1, 3, and 10 nm TiO_x film, and thresholds voltages were evaluated by finding x-intercept of the tangent line of data points where current flows more than -30 pA. As discussed, because of the tunneling current, lower threshold voltage, *ca.* -1.3 V, and higher current were observed with 1 nm TiO_x film than 3 nm or 10 nm TiO_x film. In 10 nm TiO_x films, the current is higher than that of 3 nm TiO_x film at above the threshold voltage, even if the threshold voltages were similar, *ca.* -1.5 V. This also indicates that thick TiO_x film is more conductive because of the different crystal phase of TiO_x that we observed in the GIXRD results as well as TEM analysis.

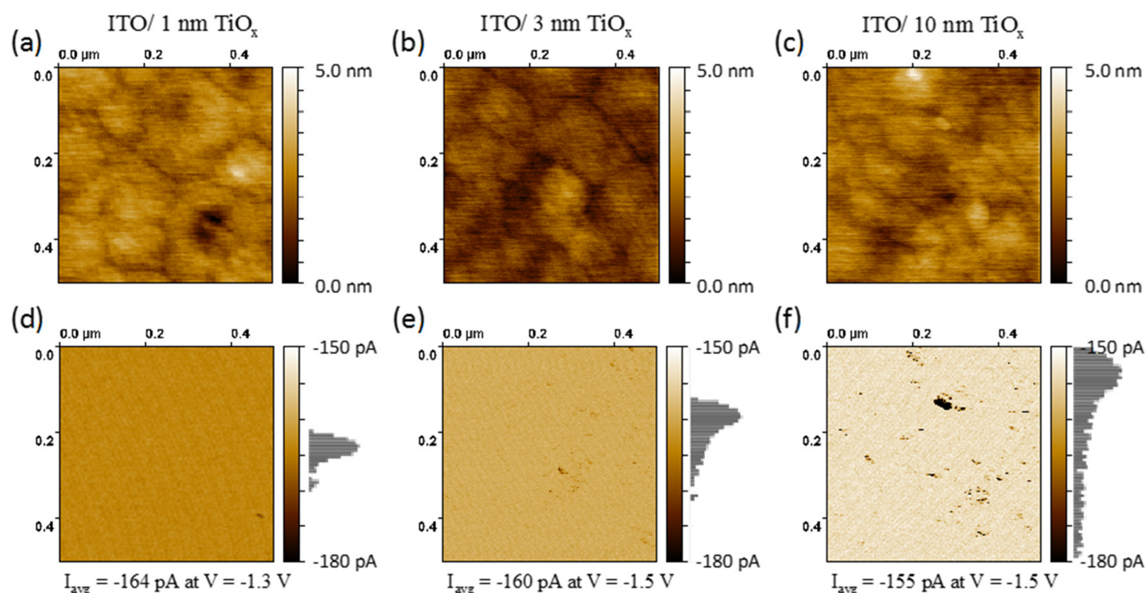

Figure 4.15 Conductive AFM of the ALD TiO_x films on glass/ITO substrates. Surface morphology images of (a) 1 nm TiO_x, (b) 3 nm, and (c) 10 nm thick TiO_x films on ITO; Current mapping images of (d) 1 nm TiO_x, (e) 3 nm, and (f) 10 nm thick TiO_x films on ITO. The dark spots in the current mapping images show regions of high current. These regions increase with increasing film thickness which act to reduce the shunt resistance of the film in spite of increased film thickness. This is believed to be due to the growth of anatase crystals in the films.

Figure 4.16 compared the histogram of current distribution of the 1, 3, and 10 nm thick ALD TiO_x films. As seen in the figure, the distribution is narrow with the 1 nm film while the distribution widens as the film thickness increase. As previously mentioned, the formation of the high leakage current region is related to the crystal phase of TiO_x, and may lead to the increased leakage currents in OPV devices, which is unfavorable.

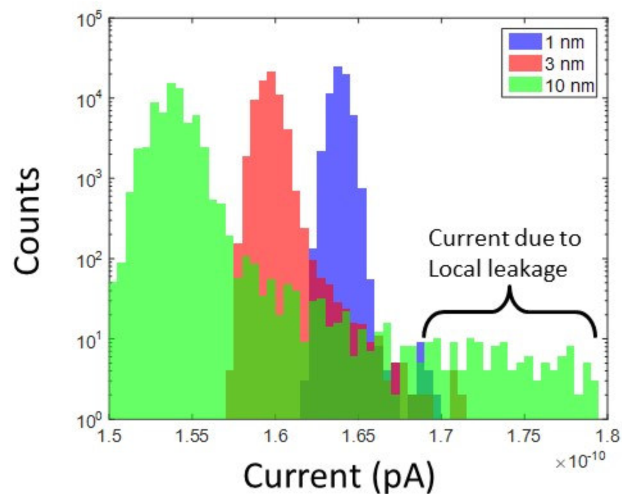

Figure 4.16 Histogram of conductive AFM current distribution for 1 nm, 3 nm, and 10 nm TiO_x films showing that the distribution of current widens as the film thickness increases. Overall, the shunt resistance deteriorates with increasing film thickness.

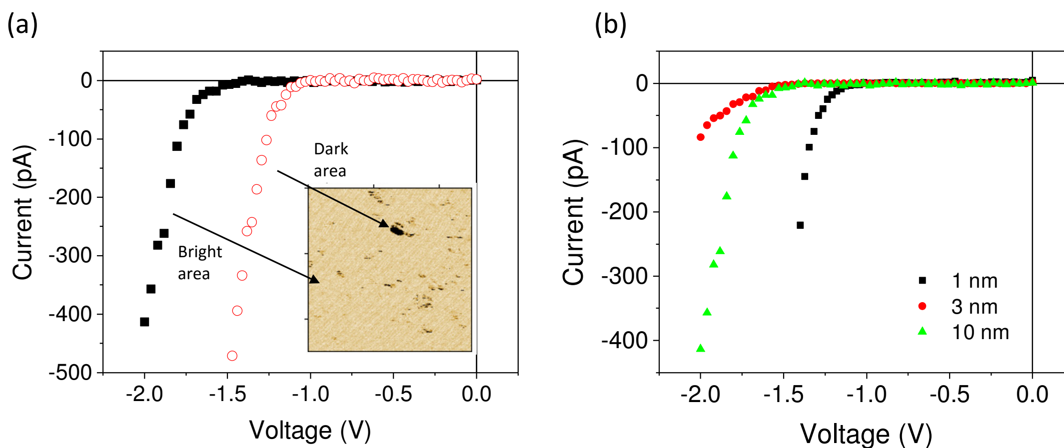

Figure 4.17 Current-voltage (*I*-*V*) curves with C-AFM. (a) *I*-*V* curves of two distinguishable areas of 10 nm TiO_x C-AFM images (inset image). The dark curve comes from the bright areas where current flow is lower and the red curve comes from dark features where current flow through the film is highest. (b) Average *I*-*V* curves of bright areas with 1, 3, and 10 nm TiO_x films on glass/ITO substrates.

4.4 Investigation of charge selectivity

4.4.1 Electrochemical characterization of charge selectivity

As a first approach to evaluate the charge selectivity of TiO_x layers on ITO prior to full BHJ OPV device characterization, we pursued electrochemical studies of redox processes for solutions of probe molecules in contact with the ITO/TiO_x electrodes. This is an approach that has been used successfully in the past to evaluate the pinhole density (porosity) of thin oxide and polymer layers covering indicator electrodes of a variety of types, including ITO, and to verify that charge injection pathways are blocked in wide bandgap semiconductors, such as oxide films.[81, 151, 181, 182] As Ou *et al.* have shown recently for characterization of CVD TiO_x films on ITO,[81] we chose the following redox couples: N,N-Bis(3-methylphenyl)-N,N'-diphenylbenzidine (TPD), 1,1-Dimethylforrocene (Me_2Fc), and Decamethylferrocene ($Me_{10}Fc$), whose redox potentials on an absolute energy scale are *ca*. -5.6, -5.0, and -4.6 eV respectively vs. vacuum, *i.e.* they lie within the TiO_x band gap energy range: -3.4 (CB) to -7.4 (VB) vs. vacuum level. If the oxide film is stoichiometric, without significant mid-gap states through which charges can be injected, no charge transfer reactions are anticipated in the dark, provided that the oxide film is also thick enough to suppress charge injection through tunneling.[183] As discussed recently by Bard and coworkers,[181] pinholes and defects within the oxide films permit diffusion of these probe molecules to the underlying ITO contact where charge transfer can occur, and in general we have found that these voltammetric probes are an excellent indicator of the conformal nature of both CVD and ALD oxide films.

Figure 4.18 shows the voltammograms (from left to right: TPD, Me_2Fc, and $Me_{10}Fc$) of bare ITO, ITO/TiO_x 0.5 nm, ITO/TiO_x 1 nm, ITO/ TiO_x 3 nm, and ITO/ TiO_x

10 nm samples. In the case of bare ITO (**Figure 4.18** (a)), typical voltammograms were seen for all three probe redox couples, with good symmetry in the oxidation/reduction waves, narrow separation in anodic/cathodic peak potentials, consistent with reasonably fast and reversible charge transfer events on the bare ITO surface.[81] Strikingly, even for TiO_x ALD films with thicknesses of only 0.5 nm and 1 nm (**Figure 4.18** (b) and (c)), the voltammetric responses become significantly distorted, with much larger separation in the anodic/catholic peak potentials. As shown in previous voltammetric studies on passivated electrodes these results are consistent with even the 0.5 nm TiO_x films exposing less than *ca*. 1% of the geometric area of the underlying ITO, suggesting nearly conformal coverage for *ca.* 10 ALD cycles.[184, 185] Charge transfer is completely blocked for ITO films coated with 3 nm and 10 nm TiO_x ALD films (**Figure 4.18** (d) and (e)), where we only observe capacitive charging currents (non-Faradaic) that become smaller as TiO_x thickness increases. It should be noted that previous experiments of this type using CVD TiO_x layers on the same ITO contacts showed that 10-20 nm thicknesses were required to achieve the same degree of blocking of these redox probes.[81] In work to be reported elsewhere, we have observed that even thicker sol-gel derived ZnO films are required to achieve the same degree of electrochemical blocking of these redox probes, and that in all cases this voltammetric characterization of these redox probes is a rapid and useful means of predicting which types of interlayer films will be useful in OPV device platforms for electron harvesting.[186]

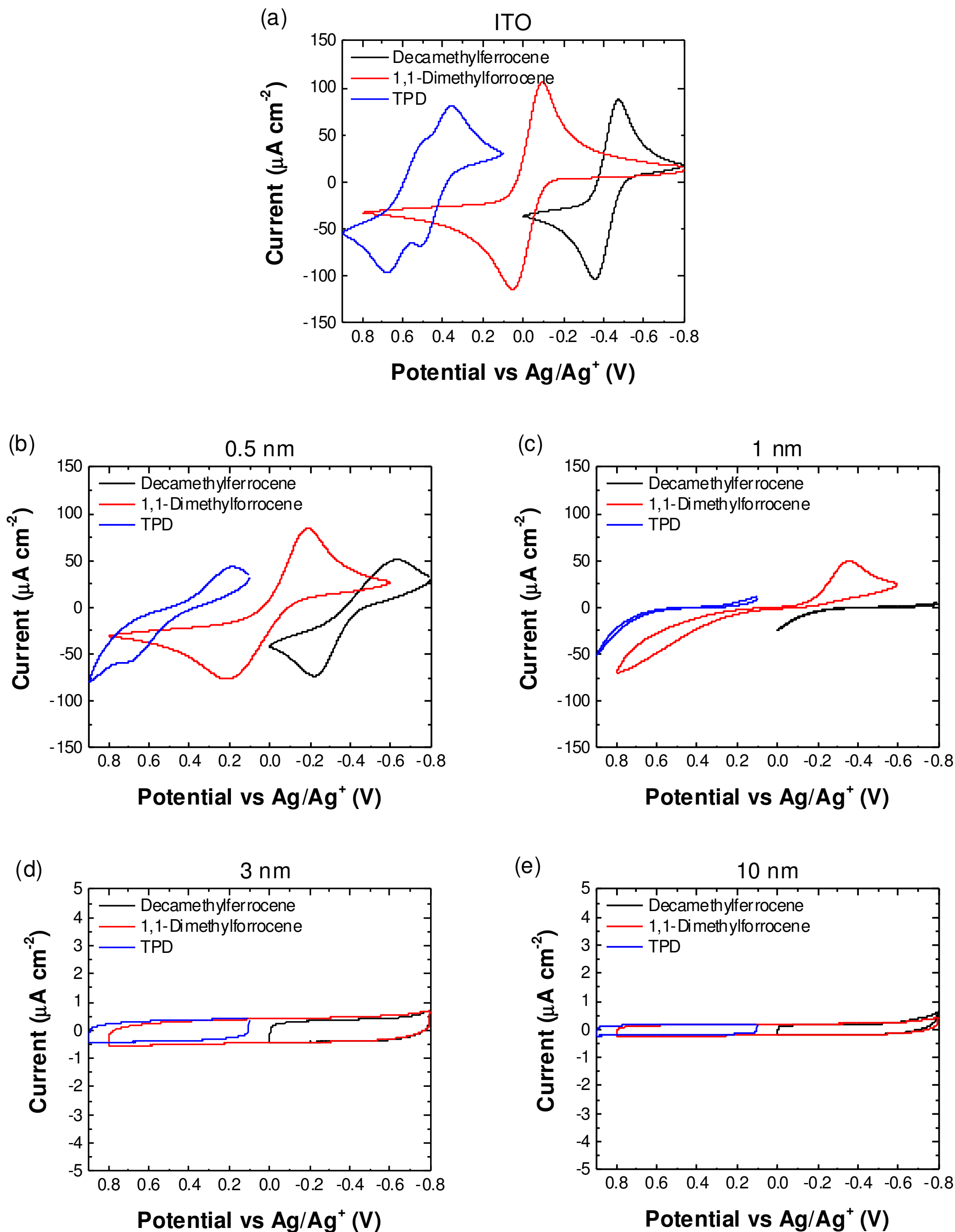

Figure 4.18 Cyclic voltammograms of probe molecules Decamethylferrocene, 1,1-Dimethylforrocene, and TPD(N,N′-Bis(3-methylphenyl)-N,N′-diphenylbenzidine) with (a) bare ITO, (b) ITO/ TiO_x 0.5 nm, (c) ITO/ TiO_x 3 nm, and (d) ITO/ TiO_x 10 nm. Potential showed in graph is referenced to Ag/$AgNO_3$. The data show that current blockage begins with 0.5nm thick films and is sufficiently blocked by 3nm thick films.

4.4.2 Si/TiO_x heterojunction diode characterization

Figure 4.19 shows the *J-V* characteristics of Al/p-type or n-type Si/Ag devices with and without the TiO_x layer between the Al contact and the Si active layer. For both p- and n-type Si devices, without the PE-ALD TiO_x layer, there is no evidence of rectification consistent with ohmic Al-Si and Si-Ag contacts, with negligible interface resistance. With the n-type Si diode using a 3 nm PE-ALD TiO_x layer between the Al contact and Si, ohmic behavior is still seen, with a higher device series resistance of *ca.* 0.071 Ω cm^2. This again is consistent with electron injection/extraction at both contacts, with minimal energy barriers, as expected given the low work function of both Ag and Al contacts, and the fact that the conduction band edge for TiO_x and its effective work function provide for minimal energy barriers for electron flow in either direction.[172] For the Al/TiO_x (3 nm)/p-type Si/Ag device the *J-V* response clearly demonstrates rectifying behavior. While the current density increased exponentially under negative bias on the Al electrode and was 1.46 A cm^{-2} at -0.4 V bias, the current flows was less than 30.2 mA cm^{-2} in positive bias up to +0.4 V showing a rectification ratio of 48. The rectification ratio was higher for even thicker TiO_x films, however this response was accompanied by a higher series resistance in the device, which would be problematic in an energy conversion platform.

Figure 4.20 shows *J-V* characteristics of Si/ TiO_x heterojunction diode devices with 0.5 nm, 1 nm, and 3 nm thick TiO_x films on (a) a linear scale and (b) a semi-log scale. In all three cases, the current density was more than 6000 mA cm^{-2} at -0.5 V bias, and current densities below 40 mA cm^{-2} were observed for positive bias up to 0.5 V, which indicates the rectification ratio is higher than 150 at ±0.5 V. The turn-on voltages,

estimated by linear fitting of the current flow curves, were -0.39 V, -0.37 V, and -0.36 V for 0.5 nm, 1 nm, and 3 nm TiO_x layer, respectively. The decrease of the turn-on voltage may be caused by either the decrease of the band energy barrier, or the decrease of different interfacial resistance. As seen in **Figure 4.20** (b), the rectification ratio was more than 500 in 0.5 and 1 nm TiO_x samples. Similar to the cyclic voltammetry results, this suggests that PE-ALD TiO_x films are highly uniform and have low pinhole or defect densities over the 0.114 cm^2 area. Also, a sub-nanometer scale film demonstrates that it is possible to flow a large amount of current via this ultrathin TiO_x while maintaining the hole-blocking property. Compared with previous studies of modified-CVD TiO_x/Si diodes with layer thicknesses between 1-3 nm,[172] the overall current densities of these devices are 100 times higher. Considering the Si wafer resistivity in the previous work is lower (<0.005 Ω cm) than that of ours (< 0.02 Ω cm), there is a clear improvement in the current density by the use of ALD TiO_x, and not from the doping level of the substrate. In addition, the data in **Figure 4.20** shows an increase in current density with increasing film thickness. For now, it is not clear as to why this occurs, but two reasons may be possible for this behavior. First, the work functions of TiO_x layer can vary with thickness in these ultrathin layer regimes, and are different from the work function of bulk TiO_x film. The UPS results reveal that the work function of 1 nm and 3 nm TiO_x film on ITO are 3.6 eV and 3.7 eV, respectively. Considering that the work function of 24 nm CVD TiO_x film was 3.74 eV in a previous study,[81] the work function variation is uncertain to affect the current density. The second is the leakage current that is related to the crystal structure of TiO_x films. As discussed previously with XRD results, TiO_x film develops from amorphous to anatase crystal structure as the TiO_x thickness increases during ALD

processing at 250 °C. Studies by Shin *et al.*, and Dang *et al.* reported that the grain boundaries of anatase structure can contribute to increased conductivity or leakage current of TiO_x films.[159, 180] Even if anatase TiO_x was not detected in our films by GIXRD until they reached 10 nm in thickness, the possibility of nano crystal domain formation can lead to an increased number of current pathways via grain boundaries.

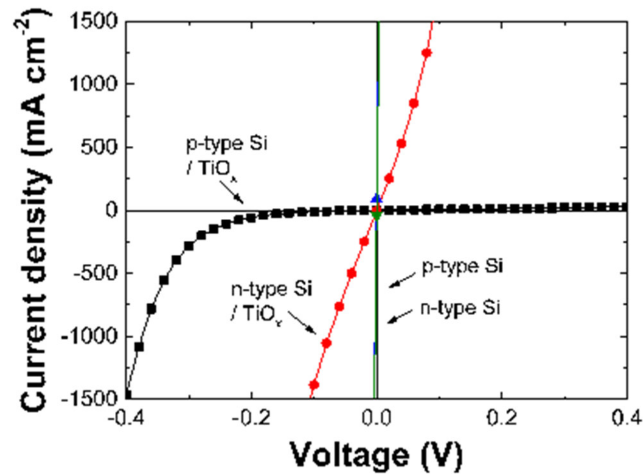

Figure 4.19 Current density - voltage characteristics of 3 nm TiO_x layers on p-type and n-type silicon wafer (Ag/Si/TiO_x/Al) The p-type Si/TiO_x junction shows rectification behavior, whereas n-type Si/TiO_x junction is an Ohmic contact. Without TiO_x, the Si wafer showed a good Ohmic contact for both p-type, and n-type wafer.

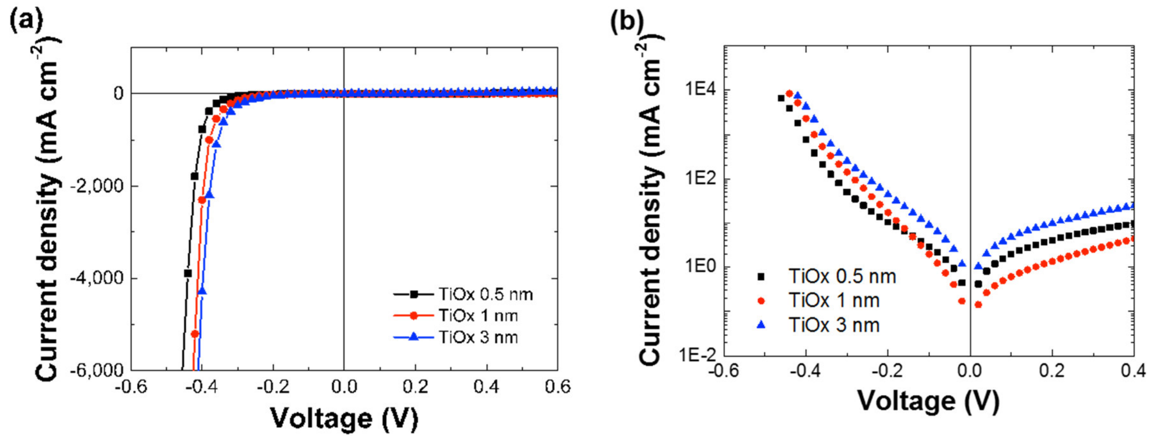

Figure 4.20 TiO_x heterojunction diode results in (a) linear scale and (b) log scale. The heterojunction diodes with all 0.5 nm, 1 nm, and 3 nm thick TiO_x films showed noticeable rectification performance. The turn on voltage of the diode decreased with increasing film thickness in this study as well.

4.5 OPV performance

Figure 4.21 shows *J-V* characteristics of inverted configuration OPV devices, which consists of ITO/ TiO_x / $P_3HT:PC_{61}BM$/ PEDOT:PSS/ Ag, under light and dark conditions, and **Table 4.4** tabulates the summary of the *J-V* characteristics including short-circuit current density (J_{SC}), open-circuit voltage (V_{OC}), fill factor (FF), power conversion efficiency (PCE), shunt resistance (R_P), and series resistance (R_s). With OPV devices with 0.5 nm, 1 nm, 3nm, and 10 nm TiO_x hole-blocking layer, J_{SC} ranged from -9.24 to -9.66 mA cm^{-2}, and V_{OC} ranged from 0.61 to 0.64 V. Even if the variation of J_{SC} and V_{OC} with various thicknesses of TiO_x layers was insignificant, the FF of the each devices showed noticeable changes depending on the thickness of the TiO_x layer as shown in **Table 4.4**. Among these various TiO_x devices, the maximum FF, 0.51, and the

maximum PCE, 2.98%, was achieved with devices using 3 nm PE-ALD TiO_x layers, which is a favorable performance when compared to other similar TiO_x OPV devices whose PCEs range from 1-2.6%.[83, 147, 149] In these results, we also observed an interesting variation in device resistance (R_S and R_P) versus the TiO_x thickness. First, the shunt resistance increases from 0.4 kΩ cm^2 to 3 kΩ cm^2 when the thickness increases from 0.5 nm to 3 nm, but it decreases slightly back to 2 kΩ cm^2 when the thickness is increased to 10 nm. The increment of R_P may be due to the better hole-blocking performance with more stoichiometric TiO_x with increases film thickness as we observed in the CV measurement results, but the reason for the decrease of R_P with 10 nm TiO_x is posited to be related to the crystal structure change from amorphous to anatase when the film thickness reaches 10 nm as we observed in the GIXRD results. We observed that ALD TiO_x film starts to grow as an amorphous film initially, and starts to form anatase crystalline structure later between 5-10 nm thick regions. Also, C-AFM results showed that increased and localized conductivity with 10 nm TiO_x film compared to 3 nm. Thus, the crystallinity of the anatase phase is believed to result in the lower shunt and series resistances seen in the thicker TiO_x films as charge can transport along the grain boundaries of the TiO_x.[159, 180] The higher conductivity of anatase TiO_x is also reported in the annealing study of amorphous TiO_x films.[187] Thus, anatase TiO_x films may actually lead to decreased hole blocking properties versus a thinner amorphous TiO_x film, as has also been seen for ALD TiO_x stabilization of semiconductors (such as Si, GaAs) used in photoelectrochemical water splitting processes.[61, 167] However, the R_P values in this work are still larger than other similar studies; 0.65 kΩ cm^2 with atmospheric-ALD TiO_x,[147] 1.1 kΩ cm^2 with layer-by-layer-deposited TiO_x,[149] 0.8 kΩ cm^2 with sol-gel

prepared TiO_x,[82] and 0.4 kΩ cm^2 with chemical-vapor-deposited TiO_x.[81] Even if the thickness of the PEALD TiO_x is thinner than any of these other studies, R_P is higher than that of the other studies, which implies that PEALD TiO_x provide improved hole blocking properties with superior uniformity.

Second, the series resistance of the devices decreases from 19 Ω cm^2 to 9 Ω cm^2 as the TiO_x thickness increases from 0.5 nm to 10 nm. This relationship shows that the resistance is inversely proportional to the film thickness over this range unlike bulk materials, whose resistance is linearly proportional to the film thickness according to Ohm's law. As we observed in the XPS results that the ratio of hydroxyl O 1s and oxide O 1s changes depending on the film thickness, the film resistivity may not be constant either, and this also affects the current density increases in the previous Si heterojunction device as well as the series resistance of the OPV devices. As mentioned previously, this may be due to different crystallization status of TiO_x, such as amorphous or anatase. On the other hand, the changes of R_P and R_S can be resulted from the different phase structure in P3HT:PC_{61}BM heterojunction layer which is spin-coated on top of the TiO_x layer. Ye *et al.* reported that anatase TiO_x is more hydrophilic than amorphous TiO_x, and thus enhance the vertical phase separation of the heterojunction layer with more of the fullerene phase, which is more hydrophilic than P3HT.[13, 188, 189] Eventually, the reduction in the series resistance and increase in the shunt resistance with increasing film thickness shows that 3 nm thick films are the most optimal for the range ultrathin TiO_x layers tested in this study.

In summary, the inverted OPV device with less than 10 nm thick TiO_x film as a hole-blocking layer provides excellent photovoltaic performance, comparable to that

observed with solution-processed ZnO or TiO_x films of much greater thickness, and CVD deposited TiO_x films that were *ca*. 10 times thicker than these PE-ALD films. Even with 0.5 nm thick PE-ALD TiO_x films, the PCE of these OPV devices was 2.7%, much thinner than previous OPV studies using TiO_x films ranging from 6 nm to 100 nm.[81-84, 147, 149] Considering the potential disadvantage of long deposition times for some ALD processes, 0.5 nm thick, (only 10 ALD cycles) TiO_x films, with good uniformity on a variety of electrical contacts, would appear to be extremely advantageous, and might also provide enhanced environmental stability for films such as ZnO, or other hydrolytically unstable semiconductor systems.[61, 167]

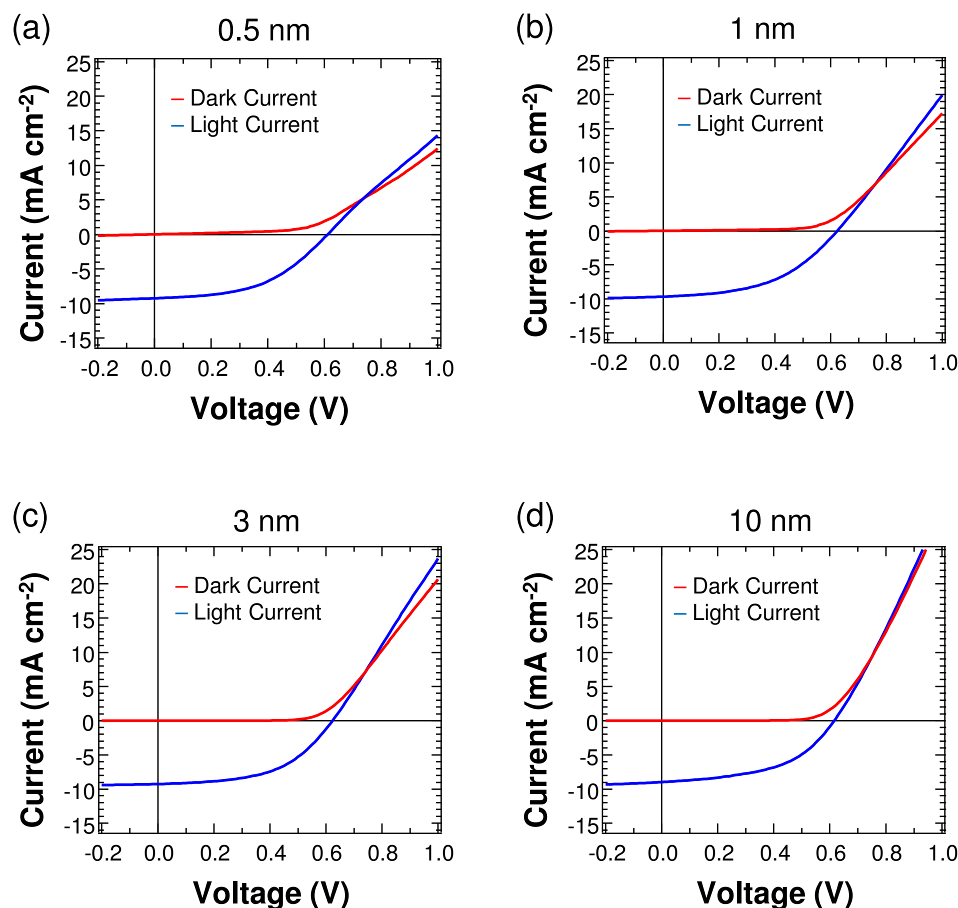

Figure 4.21 *J*-*V* characteristics of fabricated organic photovoltaic cells with various TiO_x hole-blocking layer thicknesses: (a) 0.5 nm TiO_x, (b) 1 nm TiO_x, (c) 3 nm TiO_x, and (d) 10 nm TiO_x.

Table 4.4 Summary of *J*-*V* characteristics for $P_3HT:PC_{61}BM$ photovoltaics with various TiO_x hole-blocking layer thicknesses.

TiO_x thickness (nm)	J_{sc} (mA/cm^2)	V_{oc} (V)	FF	PCE (%)	R_P[a] (kΩ·cm^2)	R_S[b] (Ω· cm^2)	n[c]
0.5	-9.24 ± 0.04	0.612 ± 0.01	0.48 ± 0.01	2.70 ± 0.09	0.4 ± 0.1	19 ± 2	10 ± 2
1	-9.66 ± 0.29	0.623 ± 0.003	0.47 ± 0.01	2.86 ± 0.10	1 ± 1	16 ± 1	8 ± 2
3	-9.26 ± 0.21	0.623 ± 0.003	0.51 ± 0.02	2.98 ± 0.04	3 ± 2	15 ± 2	1.9 ± 0.7
10	-8.97 ± 0.09	0.615 ± 0.002	0.50 ± 0.01	2.73± 0.06	2 ± 0.7	9 ± 1	3.1 ± 1.0

[a]Shunt resistance (R_P) is estimated from the inverted slope of *J*–*V* curves at -1 V; [b]Series resistance (R_S) is estimated from the inverted slope of light *J*–*V* curves at +1; [c]Ideality factor(n) is estimated from the dark *J*-*V* curves at 0.4 V.

4.6 Conclusion

This work has demonstrated the hole blocking properties of ultrathin TiO_x films deposited using PE-ALD process. Even with 0.5 nm thick TiO_x films, these layers have shown the ability to form conformal, pin-hole-free films (as revealed electrochemically) and charge selective and rectifying contacts that produce high current density in TiO_x/p-type Si heterojunction diode device, and noticeable photovoltaic efficiency, 2.98%, in an inverted OPV device with P3HT:PCBM active layer. While TiO_x is known to more resistive than ZnO, it is possible to reduce the thickness in order to address the series resistance of the contact while maintaining hole blocking capability. Also, in this thickness region (<10 nm), the chemical composition, crystal structure, and electrical properties are dependent on the film thickness, and which affect the overall OPV device performance. Moreover, previous studies have shown that TiO_x is more environmentally stable than ZnO. Thus, TiO_x electrodes with such ultrathin layers may be used as more stable contacts in devices such as OPV, perovskites, and other thin film photovoltaics where the environmental stability of the contact may impact overall device reliability.

In addition to these results, for further understand of charge transfer behavior in the ultrathin ALD TiO_x layers of OPV devices, it is recommend to investigate the charge lifetimes in the TiO_x layer by means such as transient photovoltaic analysis.

CHAPTER 5

STRUCTURAL ISSUES OF ALD BARRIER FILMS

5.1 Introduction

As mentioned in Chapter 2, barrier film packaging is mandatory to protect the organic electronics from the ingress of oxygen and moisture that leads to the degradation of device layers.[190-195] For high performance barrier films, ALD processed films are promising for their film properties such as low porosity, defects, and conformality.[43, 117-119, 196] Metal oxide films such as Al_2O_3, TiO_x, and ZrO_x fabricated by ALD have gained interest as very effective water vapor barriers due to the dense and conformal coatings they form.[37, 132, 197, 198] These ALD barrier films, usually a few nanometers thick, have been grown in various combinations either as a monolithic barrier layer or in combination with other inorganic films such as plasma-enhanced chemical vapor deposition (PECVD) grown silicon nitride (SiN_x) or as nanolaminates with other ALD metal oxides or polymer layers to create tortuous pathways to extend the lag time of the water vapor permeation.[190, 199-201]

Films made by ALD have been shown to possess desired ultra-barrier properties (WVTR< $1x10^{-4}$ g/m^2/day), but face challenges when directly grown onto device surfaces with varying composition and topography. On the other hand, even if the barrier film is fabricated on a separate polymer substrate for indirect packaging, ultrathin barrier films by ALD still encounter morphological surface defects on the polymer film such as anti-blocking particles that are embed in polymer substrate and dust particles that are found during fabrication processes. The challenges in depositing barrier films on polymer

substrates or polymer films arise in the form of stress concentrations in the presence of particles as well as the coefficient of thermal expansion (CTE) mismatch and elastic constant mismatch between the barrier film and substrate that may impact the performance and reliability of the ALD barrier. The stress concentrations can cause localized cracking in the vicinity of defects that can allow for moisture and oxygen permeation and lead to failure of the device.[202, 203] Keuning *et al.* [200], studied the effect of particle contamination on the barrier performance of Al_2O_3 ALD films and SiN_x/Al_2O_3 hybrid films using electroluminescence measurements of OLEDs and determined that ALD films are more effective at conformally coating smaller defects but larger particles or defects remained either uncoated or localized stresses possibly resulted in cracking of the ALD film leading to moisture permeation. The presence of particle contamination was addressed through the use of polymer coating layers that are used to smooth over the particle defects prior to the deposition of the barrier film.[200, 201, 203, 204] Other groups have used multiple layers of PECVD SiN_x and ALD Al_2O_3 layers in order to try to passivate defects, which has shown promise.[200] Finally, other groups have utilized multiple layers of PECVD SiN_x and SiO_x in order to create better barriers and it was found that films with lower intrinsic stresses worked better than films with higher intrinsic stresses.[205] Of these methods, the use of polymer layers can provide planarization of the sample and may be more desirable in protecting devices from subsequent deposition steps, especially those involving plasma processes during direct encapsulation processes.

The use of polymer planarization layers also brings additional challenges in the form of mechanical reliability of the barrier films deposited on top of the polymers. Cordero *et al.,*[206] studied through numerical modeling the cracking modes in

inorganic/polymer/inorganic multilayer barrier films to determine the optimal structure to maximize the strain to failure. They found that the critical fracture strain increased as a function of the fracture energy of the polymer with all other parameters being equal. They found that there is an optimal thickness of the polymer interlayers to limit the driving forces for channel cracking in the inorganic layer. When the polymer interlayer is too thick, the inorganic layer is decoupled from the inorganic layer underneath the polymer and the critical strain to failure decreases. Thus, thinner polymer interlayers will allow for increased constraint on the crack driving forces for channel cracking in inorganic layers. However, thin polymer layers may not be as effective in planarization and passivating any particle defects that can occur in device deposition. Thus, these issues provide challenges in developing robust barrier films for direct deposition on planarized devices. **Figure 5.1** (a) shows their results of critical strains of three crack opening cases which include a combination of channel cracks and tunnel cracks in inorganic layers sandwiched between organic layers as found in multilayer organic/ inorganic barrier films. For the case of an ALD barrier film grown on a polymer substrate, Figure 5.1 shows us from case (a) that the normalized critical strain to failure decreases as the ratio of the polymer to inorganic film thickness increases. Since ALD films are thin (~10 nm), even thin polymer films on the order of 100 nm are expected to lower the critical strain in ALD barrier films. However, this is a numerical study, but the effect has not been observed experimentally and methods to improve the critical strain in ALD barriers have not been explored based on this fracture mechanics approach.

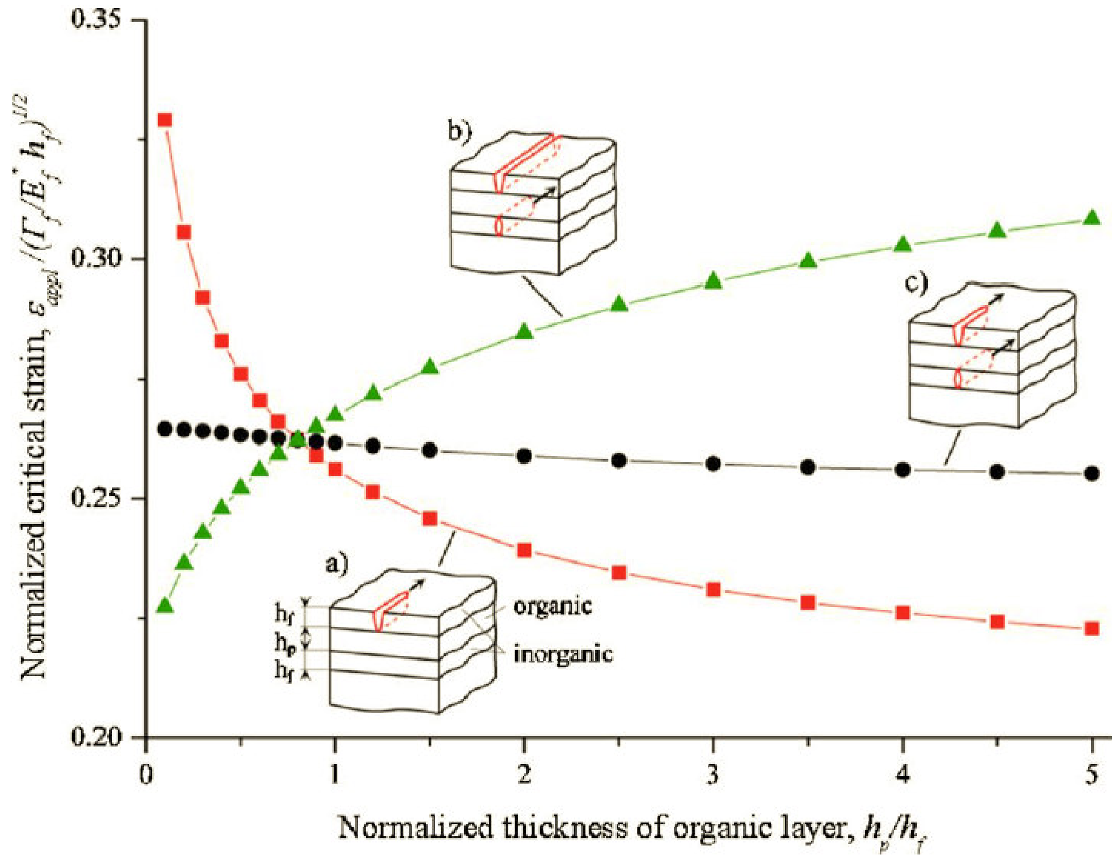

Figure 5.1 Normalized critical strain as a function of the normalized thickness of the organic layer for cracks in inorganic layers. (a) A channel crack in the top inorganic layer, (b) a channel crack in the top inorganic layer and a propagating tunnel crack in the bottom inorganic layer, and (c) a propagating channel crack in the top inorganic layer and a propagating tunnel crack in the bottom inorganic layer sandwiched between organic layers. Adapted from reference [206].

In this chapter, the barrier performance of ALD Al_2O_3/HfO_x nanolaminate films deposited on polymer coated glass substrates was studied using an optical calcium corrosion test. Since the hydrolytic instability of a monolithic Al_2O_3 film was shown in the Chapter 3, Al_2O_3/HfO_x nanolaminates are chosen as a barrier film to utilize the multilayer architecture for tortuous diffusion pathway as well as the water stability of HfO_x.[104, 106, 207] The barriers are built on top of a CYTOP (CTL-809M, Asahi Glass Company) layer, which is a hydrophobic amorphous fluorinated polymer. The effect of

the thickness of CYTOP polymer planarization on barrier performance was investigated in terms of passivating particle-assisted defects in the ALD barrier films. All barriers were tested at 50°C/85% relative humidity (RH) and their qualitative performance analyzed based upon the degradation in calcium sensor area.

5.2 Experimental

First, calcium sensor samples were prepared to investigate the ALD nanolaminate barrier films. In order to investigate the effect of the polymer planarization layer, a fluorinated polymer (CYTOP) was coated on top of calcium sensors with various thickness: 40 nm, 200 nm, 780 nm, 1000 nm, and 4300 nm. Afterwards, ALD nanolaminate barrier films were deposited on top of the CYTOP layer. **Figure 5.2** shows the schematic of calcium corrosion test samples with the two barrier structures. In addition to optical imaging, scanning electron microscope (SEM) images were obtained using a Hitachi SU8230 FESEM with an energy-dispersive X-ray spectroscope (EDS) system, which was used to provide additional detail of defects found in the barrier films. Among the fabrication procedures, calcium layer deposition, CYTOP coating, ALD deposition were done in collaboration with the research group of Professor Bernard Kippelen at the Georgia Institute of Technology.

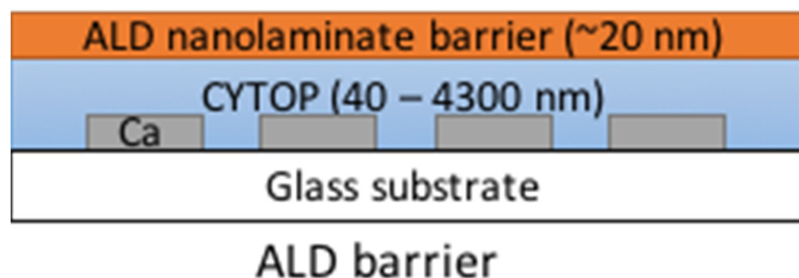

Figure 5.2 Structures of calcium corrosion test samples ALD barrier film deposited directly on a CYTOP layer.

5.2.1 Sample fabrication

5.2.1.1 Thermal evaporation of the calcium sensor layer

For calcium deposition, thermal evaporation (EvoVac, Angstrom Engineering) was used in this work. In the thermal evaporation system, the substrates and source materials were loaded in a vacuum chamber below 10^{-7} Torr. Then, the source material contained in a crucible was heated up, and evaporated or sublimed. The evaporated Ca was deposited onto the substrate and the deposition rate was monitored using a quartz crystal microbalances and controlled by the heating power on the source crucible. The calcium was deposited with a deposition rate of 1.0 Å/s. The system was connected to a glove box (MBraun) in order to process the sample and begin the application of the barrier films without exposing the calcium to air.

For the calcium corrosion test samples, 16 calcium squares were deposited through a shadow mask on top of detergent solvent cleaned 38 mm x 38 mm glass substrates as shown in **Figure 5.4**. Each calcium square sensor size was 5 mm x 5 mm and 100 nm-thick.

Figure 5.3 Thermal evaporation system (EvoVac, Angstrom Engineering) used for calcium deposition, which is installed in a glove box (MBraun).

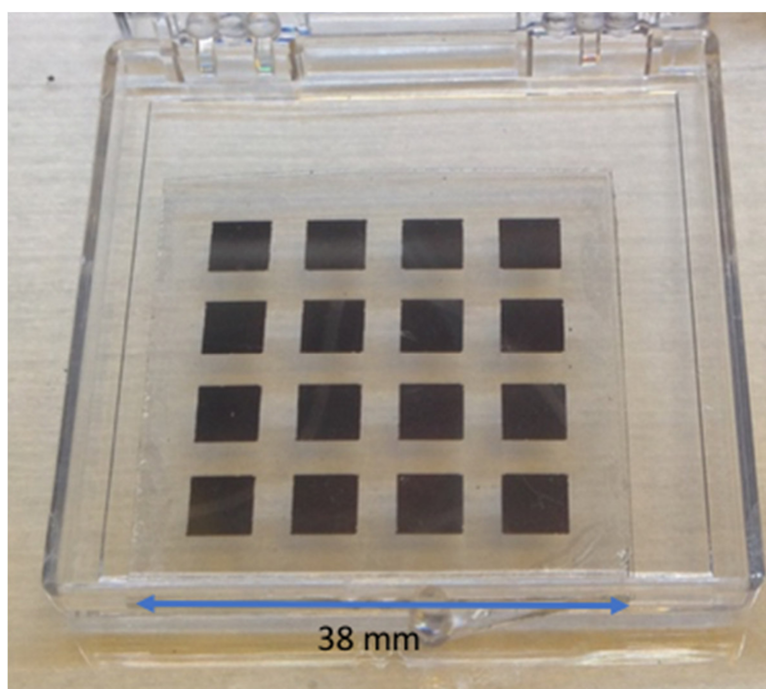

Figure 5.4 Calcium sensor layer fabricated using the thermal evaporation.

5.2.1.2 Spin-coating of a smoothing layer

Following Ca deposition, the samples were transported to a spin coater located within the glove box and coated with CYTOP as a smoothing layer; an amorphous fluoropolymer (CTL-809M, Asahi Glass Company). The CYTOP was mixed with the solvent (CT-SOLV180) and stirred for one hour at room temperature. The spin-coated

polymer films were cured at 100°C for 30 min. CYTOP films with six different thicknesses ranging from 40 nm to 4300 nm were produced by varying the mixing ratio of the CYTOP and the solvent. The thickness of the CYTOP films was determined by spin-coating the films on glass substrates and measured using spectroscopic ellipsometry (M-2000, J.A. Woollam) and a stylus profilometer (Dektak 6M, Veeco).

5.2.1.3 ALD of barrier films

Following the spin-coating of CYTOP, the substrates were transferred into a N_2 filled stainless steel canister that was sealed and quickly transported to the ALD chamber for barrier film deposition. The CYTOP films were found to protect the Ca squares from oxidizing in air for roughly 6 min, thus providing time for the transfer. The time taken for transporting the substrates in the N_2 filled canister from the glove box to the start of pump down of the ALD chamber usually lasted less than 60 s.

ALD films were deposited in a Savannah 100 thermal ALD system from Cambridge Nanotech Inc (**Figure 5.5**). Trimethylaluminum (TMA) was used as the Al_2O_3 precursor and tetrakis(dimethylamido) hafnium (TDMAH) as the HfO_x precursor with water vapor (H_2O) as the oxidizer for both cases and nitrogen (N_2) as the purge gas. The growth rates for Al_2O_3 and HfO_x were 1.1 Å/cycle and 1.27 Å/cycle on Si witness samples, respectively. All depositions were performed at 100°C, and the ALD chamber had a constant N_2 flow at 20 sccm. For Al_2O_3 growth, the oxidation step was first performed by pulsing H_2O for 0.015 s, followed by a 45 s wait time. TMA was pulsed next for 0.02 s followed by a 45 s wait time for a total of 90 s per cycle. For HfO_x, the H_2O oxidation step was performed with a 0.015 s pulse and 60 s wait time followed by a pulse of TDMAH for 0.4 s and a 60 s wait time for a total of 120 s. The nanolaminate

was produced by depositing 5 cycles of Al_2O_3 followed by a 45 s wait before depositing 5 cycles of HfO_x, repeated for a total of 20 dyads. Previous studies [208] showed that the ALD Al_2O_3 films on CYTOP suffer from a delay in the initiation of film growth due to the fluorinated polymer, with very little film growth after 100 cycles. The nucleation delay was found to be overcome (measured using XPS) with the deposition of a buffer layer of 200 ALD cycles of Al_2O_3 on top of the CYTOP prior to Al_2O_3/HfO_x nanolaminate barriers.

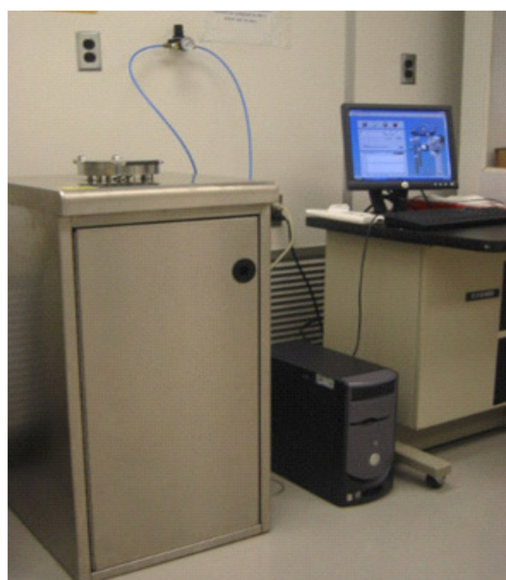

Figure 5.5 Savannah ALD system (Cambridge Nanotech).

5.2.2 Optical calcium corrosion test

In order to evaluate the barrier performance of barrier films, a calcium corrosion test was used, which is briefly introduced in Chapter 2. The calcium corrosion test utilizes the rapid reactivity of calcium metal with oxygen or water vapor to detect the presence of water vapor in its vicinity. The produced calcium oxide is transparent and

non-conductive, and can be detected either optically or electrically. When calcium meets oxygen or moisture, the following reactions occurs,[45, 128]

$$2Ca + O_2 \rightarrow 2CaO \quad (5.1)$$

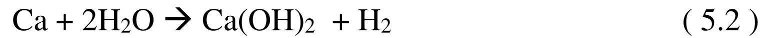

$$Ca + 2H_2O \rightarrow Ca(OH)_2 + H_2 \quad (5.2)$$

Therefore, by determining the remaining mass of metallic calcium in the test calcium layer, one can estimated how much moisture or oxygen has permeated through the barrier and reacted with the calcium.

In this research, the barrier performance of the fabricated films were tested by using an optical calcium test, which evaluates the barrier by optically observing the calcium corrosion rate of samples encapsulated with test barrier films. For an accelerated test, fabricated calcium samples encapsulated with the barrier films were exposed to a controlled environment of 50°C/85% RH in an environmental chamber (Cincinnati Sub Zero MicroClimate System;

Figure 5.6). The samples were taken out of the humidity chamber every 24 hours, and optical images were taken using a high-resolution flatbed photo scanner (Epson V600). The photo scanner was equipped with a white LED light source along with a charge-coupled device (CCD) image sensor and a white back reflector behind the samples. The color images were acquired at 2400 dpi resolution without any color correction algorithm. Then, the images were converted into binary images and analyzed using MATLAB to determine the degraded calcium area. For binary image conversion, an intensity threshold value was determined by Otsu's method using a MATLAB function.[209]

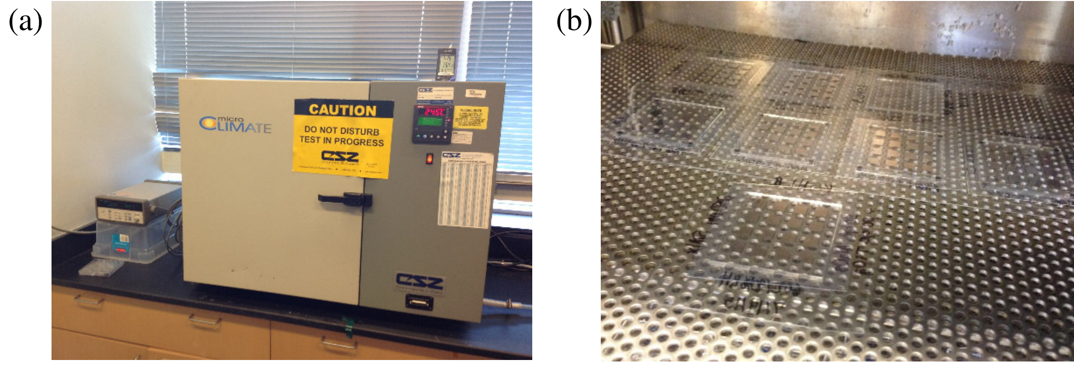

Figure 5.6 (a) A benchtop environmental test chamber (MicroClimate, Cincinatti SubZero, Inc.). (b) Calcium test samples under testing in the environmental chamber.

Figure 5.7 A flatbed photo scanner V800 (Epson). The calcium samples are mounted in a sample frame, and images were scanned while the sample is facing down (toward the image sensor).

5.2.3 Film stress measurement (curvature method)

The residual stress of the barrier films was measured using the wafer curvature method with the Stoney equation.[210, 211] The wafer curvature method assumes that the film is very thin compared to the substrate and that the deformations are very small. The residual stress of the film σ_f is then given by,

$$\sigma_f = \frac{1}{6}\left(\frac{1}{R_{final}} - \frac{1}{R_{initial}}\right)\frac{E_s}{(1-\nu)}\frac{t_s^{\,2}}{t_f} \qquad (5.3)$$

$$\sigma_f = \frac{1}{6}\left(\frac{1}{R_{final}} - \frac{1}{R_{initial}}\right)\frac{E_s}{(1-\nu)}\frac{t_s^2}{t_f}$$

where E_S is Young's modulus of the substrate, R_{final} and $R_{initial}$ are the radii of curvature before and after film deposition, and t_s and t_f are the thicknesses of the substrate and the film, respectively. In this research, R_{post} and R_{pre} of a 4 inch silicon wafer (500 µm thick) before and after film deposition, respectively, were measured using an optical stress measurement system (BowOptic 208) to evaluate the residual stress barrier films.

5.3 Defect-related and mechanical issues of the barrier film fabrication

5.3.1 Issue of particles in practical deposition process

Figure 5.9 shows images of Ca films on glass coated with 200 nm CYTOP layers and the ALD nanolaminate before and after exposure to 50°C/85% RH for 10 days. **Figure 5.9** (b) shows that there is local degradation of the Ca due to defects in the barrier films. **Figure 5.9** (c) shows the image of one of the locally degraded regions where a particle can clearly be observed at the center of the pinhole. While the exact location of the particle within the multilayer stack may be hard to determine, it is very likely that the particle was located below the barrier film since EDS analysis showed the presence of Al and Hf on top of the particle. However, as seen in **Figure 5.9** (d), cracks can be observed around particles which are believed to provide the pathway for oxygen and moisture to enter through the barrier film. The cracks are believed to be caused by stress concentrations around the particles which can cause the brittle ALD films to fracture. Stress measurement of ALD films deposited on 500 µm thick silicon wafers by a curvature method showed that the Al_2O_3 films had a tensile residual stress of 500 MPa on Si while HfO_x had a residual compressive stress of -100 MPa. Thus, the ALD film has a positive tensile stress that can contribute to crack formation and propagation. However,

the cracking does not extend across the barrier film for two reasons. First, the decay of the stress fields around the particle (or crack tip) with radial distance from the particle (**Figure 5.8**) reduces the crack driving force plus the constraint of the glass substrate felt through the thin polymer layer that also reduces the crack driving force.

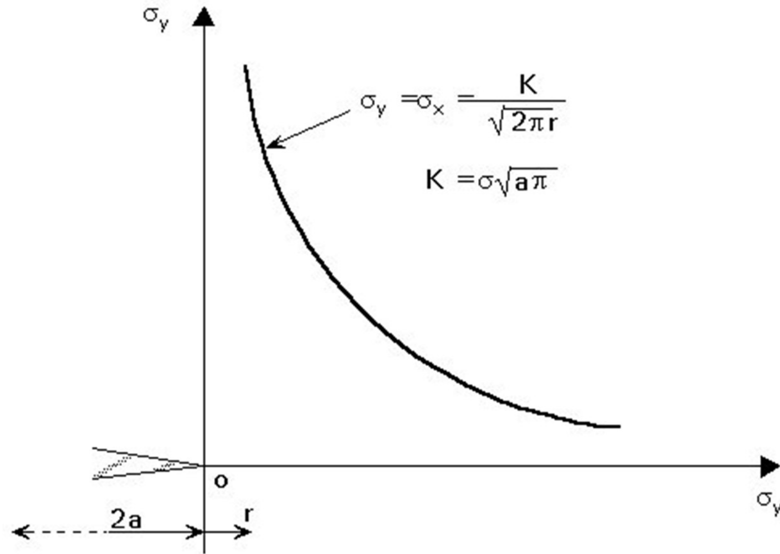

Figure 5.8 Crack tip stress fields in elastic material. For a crack of length 2a in an infinite plate of unit thickness under uniform tension, the direct stress component is given by $K/\sqrt{2\pi r}$, where K is the stress intensity factor.

Based on linear elastic fracture mechanics, the strain energy release rate for channel cracks which form in the ALD layer is given by,

$$G_{ss} = \frac{Z\,\sigma^2\,h}{E_f^*} \qquad (5.4)$$

where G_{ss} is the steady state strain energy release rate, Z is a dimensionless constant, σ is the residual or applied stress in the film, h is the film height, and E_f^* is the plane strain film modulus ($E_f^* = E/(1-\nu^2)$). As shown by Huang et al.[212], Z is a function of the elastic mismatch (α) between the ALD film and polymer layer which is given by,

$$\alpha = \frac{E_f^* - E_s^*}{E_f^* + E_s^*} \quad (5.5)$$

where E_s^* is the plane strain modulus of the substrate . Based on the materials used for ALD barrier structures, α is approximately 0.98 which yields a Z value that approaches 25 as the polymer layer thickness becomes large compared to the ALD layer thickness.[212] Thus, the crack driving force or strain energy release rate increases with polymer layer thickness and with residual stress. Since the stress is elevated around the particles due to stress concentrations, it is expected that cracks will initiate around such defects, if the stress elevation is high. Thus, only local cracking around particles is observed in the ALD barrier films on 200 nm thick CYTOP layers, leading to localized degradation in the Ca sensors around the particles which have cracked. It can also be seen from **Figure 5.9** (b) that in the region away from the particles, the Ca film appears to be well protected by the barrier film even after 10 days of 50°C/85% RH exposure. This undegraded Ca region accounts for the intrinsic protection offered by the ALD barrier films, whereas the radial growth of the locally degraded Ca is related to the permeation through the defects around the particles. Further investigation on these permeations will be discussed later in Chapter 6.

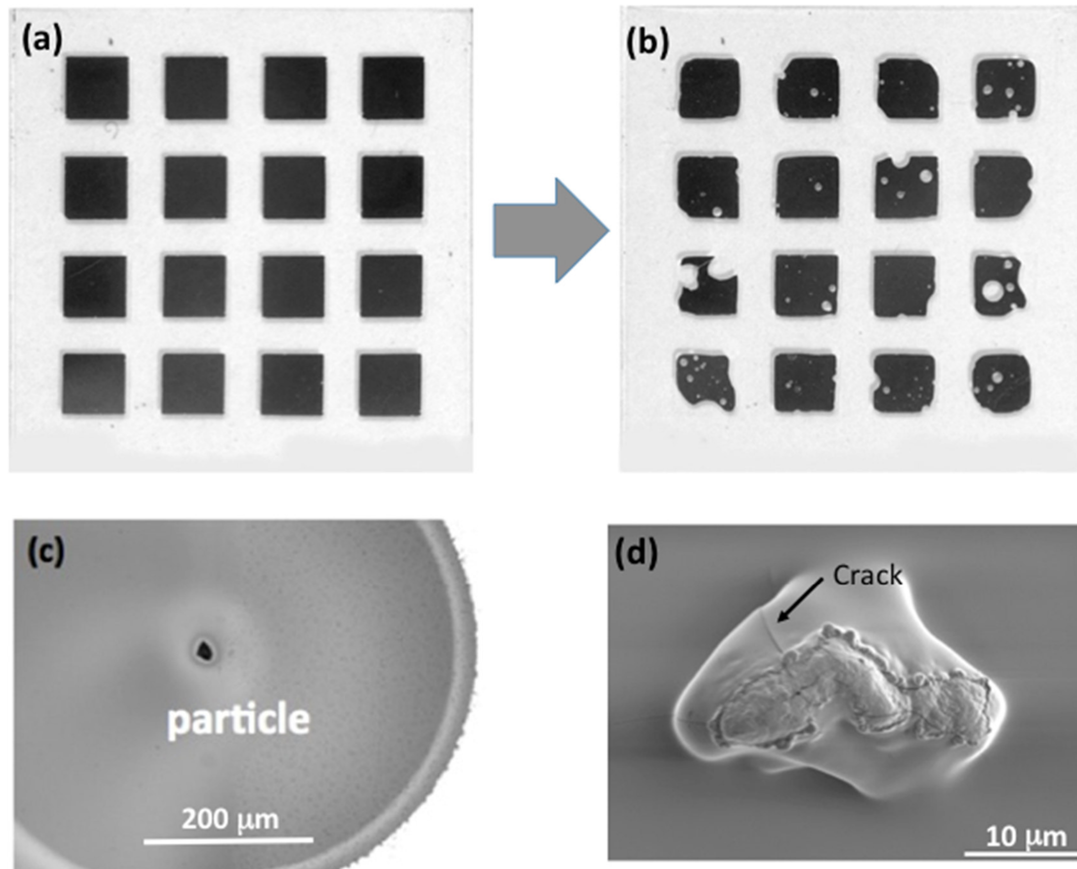

Figure 5.9 (a) Image of Ca films on glass coated with 200 nm of CYTOP polymer and the ALD Al_2O_3/HfO_x nanolaminate. (b) Image of the sample after exposure to 50°C/85% RH for 10 days showing evidence of localized degradation (c) Microscope images showing the presence of a particle and the degradation of the Ca sensor in the vicinity of the particle. (d) SEM image of a particle defect, showing the presence of cracks in the vicinity of the particle.

Optical microscopy and SEM imaging of the various particles showed that the particle sizes ranged from tens of nanometers to a few tens of microns. However, not all of the particles are expected to actively participate in allowing localized permeation around the defects. For the purpose of this study, the number of locally degraded spots in the Ca samples was used to track the impact of the polymer layer on alleviating the effect of particle defects from the deposition process. **Figure 5.10** plots the number density of particles observed in the calcium images as the CYTOP layer increases from 40 nm to

4300 nm. The number density of locally degraded spots in the Ca samples decreased, showing that thicker polymer layers are better at passivating the presence of particles which arise in the deposition process. The number density of active particles decreased from 80/cm^2 to 5/cm^2. As expected, thicker smoothing layer contributes to reduce the particle-assisted defects in a barrier film as shown in **Figure 5.11**. While this is effective, it should be noted that full elimination of particles is desired and the practicality of achieving this will depend on the deposition systems used.

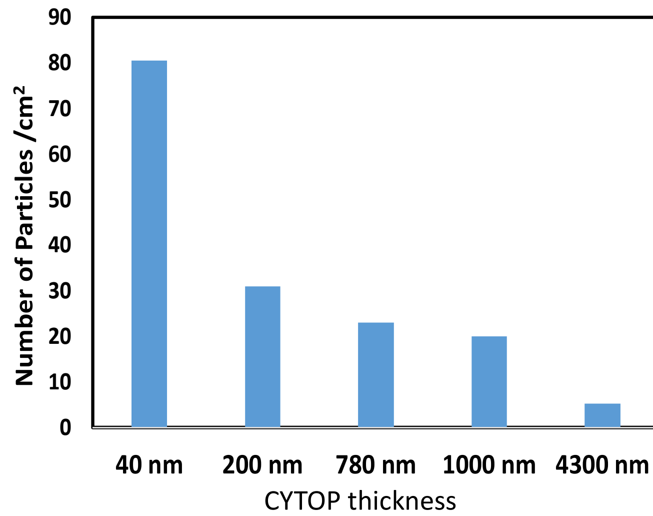

Figure 5.10 Observed degraded calcium spots densities in a ALD films with various CYTOP layer thickness.

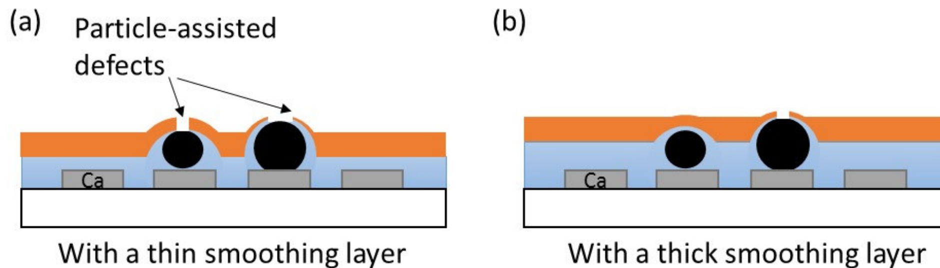

Figure 5.11 Schematic illustration of the effect of a smoothing layer on particle coverage. (a) With a thin smoothing layer more defects can be caused by poor particle coverage, and (b) With a thick smoothing layer, small particles can be covered by the smoothing layer.

5.3.2 Issue of film cracking

While increasing the CYTOP film thickness appeared to reduce the impact of particles on localized degradation, the thicker polymer films led to an additional challenge where cracks appeared in the barriers. **Figure 5.12** shows the images of ALD nanolaminate barriers on 200 nm, 780 nm, 1000 nm and 4300 nm thick CYTOP layers. **Figure 5.12** (a), (b), (c), and (d) show the films immediately after ALD barrier deposition while **Figure 5.12** (e), (f), (g), and (h) show the films after 24 hour exposure to 50°C/85% RH. The barrier layers on the 780 – 4300 nm thick layers of CYTOP all showed the presence of localized degradation of Ca in the form of linear features. These linear features were found to be due to channel cracks that formed in the ALD layer as seen in **Figure 5.13**. It was found that these crack formed around particle defects in the barrier film, promoted by the stress concentration around the particles which provides a large crack driving force (Eq. (5.4)). As proposed by the work of Cordero and Miller, the thicker polymer layers decoupled the barrier from the stiff glass substrate and is thus unable to constrain the channel crack propagation in the vicinity of particles, causing Z in Eq. (5.4) to increase.[206, 213] CYTOP has a modulus of 1.3 GPa [214] which is much lower than that of ALD Al_2O_3 or HfO_x (effective modulus of *ca.* 200 GPa[215-217]). As a result, the compliant CYTOP is unable to constrain the channel cracks that occur in the ALD layer, resulting in a larger driving force with increasing polymer film thickness. The formation of the crack appears more pronounced in the case of the thickest CYTOP film (4300 nm) as seen from **Figure 5.13** (d) where the freshly deposited film started showing crack formation immediately after removal from the deposition chamber. Thus, while thicker polymer layers have benefits in reducing the number of particle defects, they

allow for larger crack driving forces in the ALD barrier film which results in poor performance of the barriers.

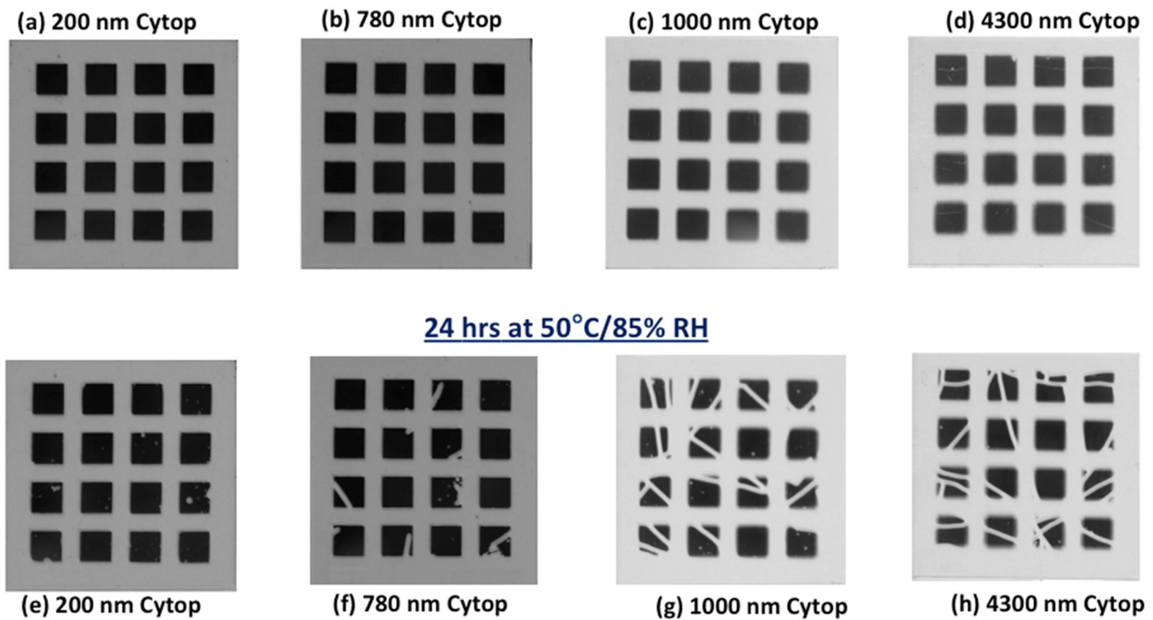

Figure 5.12 ALD barrier films on calcium sensors on glass with various thicknesses of CYTOP polymer layers. Images a-d are as-made samples imaged immediately after barrier film deposition. Images e-h are samples imaged after 24 h at 50°C/85% RH where the Ca degradation along the crack defects are clearly visible for CYTOP layers greater than or equal to 780 nm. (It should be noted that samples with 40 nm of CYTOP did not withstand the first 24 h period and are not shown.)

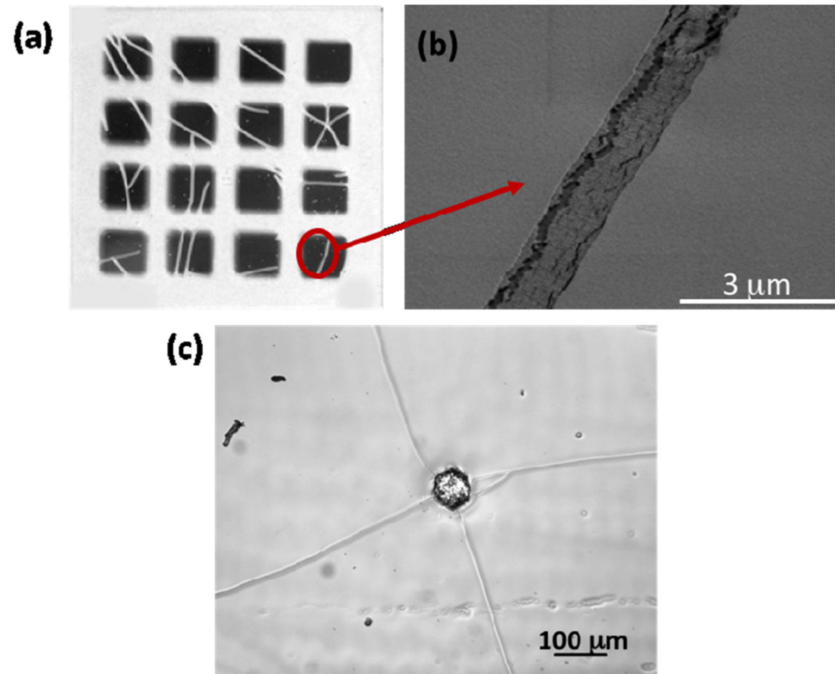

Figure 5.13 (a) ALD barrier films with 1000 nm thick CYTOP coated with an Al_2O_3/HfO_x nanolaminate showing the occurrence of cracks. (b) SEM image of the crack opening due to the residual tensile stress in the film (c) an optical image showing cracks initiating from a particle defect.

5.4 Preventing cracks of ALD barrier films

In order to address the issue of crack formation, we modified the barrier film architecture by introducing a 100 nm thick SiN_x film deposited using PECVD in between the CYTOP and ALD layers as shown in **Figure 5.14** to provide a constraint to fracture and its performance was evaluated.

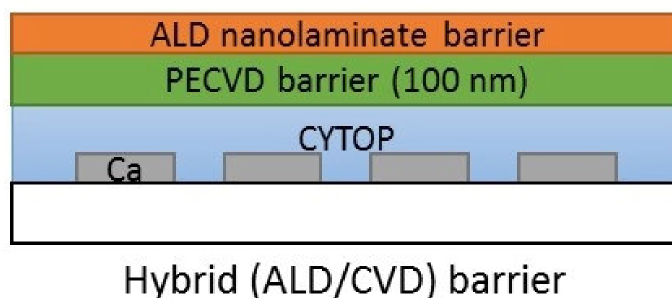

Figure 5.14 Structures of calcium corrosion test samples for a hybrid (ALD/PECVD) barrier film deposited on a CYTOP layer.

5.4.1 Hybrid barrier film fabrication and characterization

For the hybrid barrier film fabrication, PECVD (Oxford PECVD) was used prior to ALD deposition (**Figure 5.2** (b)). PEALD allows industrial-scale deposition of good quality insulating films such as silicon oxide and silicon nitride with good adhesion.[218] One of the main advantages of PECVD is the availability of low temperature deposition compared to other chemical vapor deposition (CVD) methods, such as thermally driven CVD. While temperatures of only 250 °C or lower are sufficient for depositing films by PECVD, deposition temperatures of 700 °C to 900 °C are required to deposit similar films by thermal CVD. This lower temperature capability is very attractive for application of organic electronics (preferably below 100 °C, maximum limit *ca.* 130 °C).[193] **Table 5.1** tabulates the parameters that are used for silicon nitride films at 100°C.

Table 5.1 Summary of PECVD deposition conditions for SiN_x film fabrication.

Parameter	Value
Temperature (°C)	100
Chamber pressure (mTorr)	1000
RF power (W)	20
SiH_4 flow rate (sccm)	12
NH_3 flow rate (sccm)	10
He flow rate (sccm)	50
N_2 flow rate (sccm)	440

Figure 5.15 Oxford PECVD system used to deposit SiN_x films at a low temperature, 100°C.

The characterization procedures of the hybrid films are identical to the previous ALD nanolaminate work. Calcium corrosion was observed, and the residual stresses of SiN_x films were evaluated in the manner by curvature method.

5.4.2 Effects of hybrid configuration on the barrier film integrity

The role of the PECVD films is primarily to provide a stiff layer to constrain the crack opening displacement and reduce the driving force for the propagation of channel cracks in the ALD layers. Moreover, the SiN_x films were measured to have a residual compressive stress of -350 MPa using wafer curvature measurements, thus also helping

to compensate for the tensile residual stress in the ALD nanolaminate film. As shown in **Figure 5.16**, the ALD layer on CYTOP with an elevated tensile residual stress near a particle can cause a crack to form due to the elevated crack driving forces. For the films grown on SiN_x, the modulus of the SiN_x film (*ca.* 200 GPa)[219] and the compressive residual stress acts to create a film with a lower average stress in the vicinity of the ALD film. Thus, energy for fracture and driving forces are expected to be reduced. Measurements of the Ca samples with a 200 nm CYTOP layer and 100 nm SiN_x layer showed that the Ca film was completely degraded after 24 h of exposure to 50°C/85% RH. Thus, the SiN_x is not expected to contribute greatly to the resistance of water vapor permeation, but will contribute to the mechanical robustness of the barrier layers.

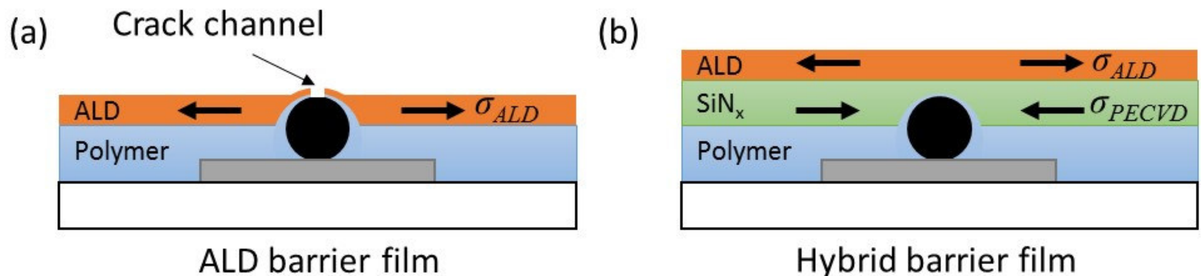

Figure 5.16 (a) Depiction of the tensile stresses acting on a channel crack in an ALD barrier sample where the polymer layer offers little resistance to the crack opening displacement and crack driving force. (b) Depiction of the stiff and compressively stressed SiN_x acting to reduce the overall average stress in the vicinity of the ALD film and reduce the probability of cracking (as well as crack driving force).

The benefit offered by the incorporation of PECVD SiN_x films between the CYTOP layer and the ALD films is confirmed in **Figure 5.17**. In hybrid barrier samples, the CYTOP layer thickness was varied from 200 – 4300 nm, capped with a 100 nm SiN_x layer prior to the ALD deposition. None of the films showed the presence of cracks when

exposed to 50°C/85% RH. The beneficial influence of the SiN_x layer is also very evident in **Figure 5.18** where the normalized Ca area for each sample is plotted as a function of time with and without the PECVD SiN_x layer. From **Figure 5.18** (a), which presents data for samples of ALD barrier films without SiNx, samples with 4300 nm and 1000 nm CYTOP layers show a 30% and 18% degradation in Ca area after just 24 hours of testing, respectively. Samples with 200 nm and 780 nm-thick CYTOP layers show slightly better performance with 7.5% and 2.5% degradation of the Ca films after 24 h, respectively. On the contrary, the samples of hybrid barrier (ALD + SiNx) showed negligible change in the Ca area after 500 h of exposure under the same conditions (**Figure 5.18** (b)). After 240 h of exposure, these samples showed less than 5% degradation in Ca area for films of all CYTOP thicknesses. **Figure 5.18** (b) demonstrates the benefit of using a stiff inorganic layer underneath the ALD barrier films that ensures mechanically robust barrier films that can better withstand processing induced stresses that will otherwise fail almost instantaneously after ALD barrier film deposition. As suggested by Eq. (5.4), the reduction in stress in the films, reducing film thickness, as well as reducing the dimensionless parameter Z appears to be the most important factors in reducing the crack driving forces in the barrier films. To reduce Z requires a reduction in the elastic mismatch between the film and polymer layer which is not practical. Thus, thin layers with low residual stresses may be the best method to creating low crack driving forces in the barriers. Thus, stress engineering and limiting film thickness are options that should be considered in the design of mechanically robust barrier film.

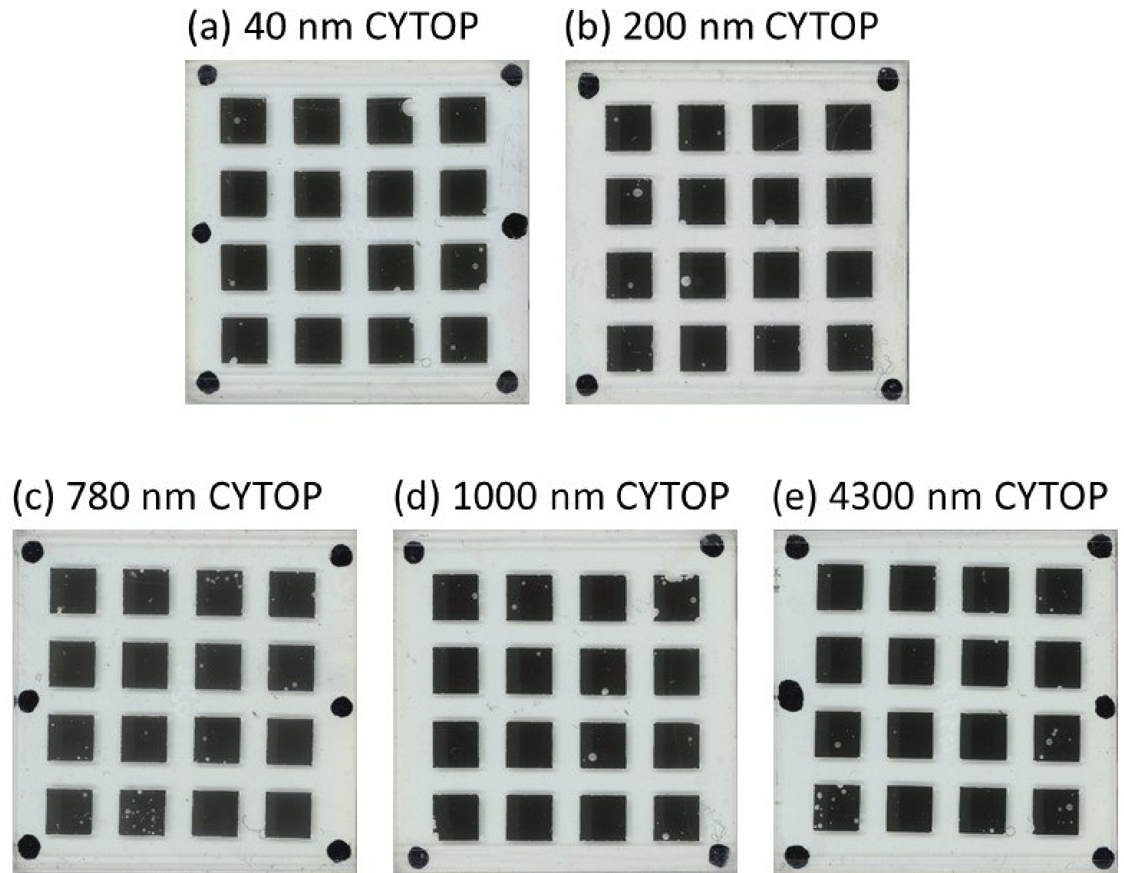

Figure 5.17 Hybrid (ALD/PECVD) barrier films on calcium sensors showing the lack of crack formation after 500 h of exposure to 50°C/85% RH. In contrast to ALD barrier films which do not have the SiN_x layer, these films are more resistant to cracking and show fewer particle defects than ALD barrier films.

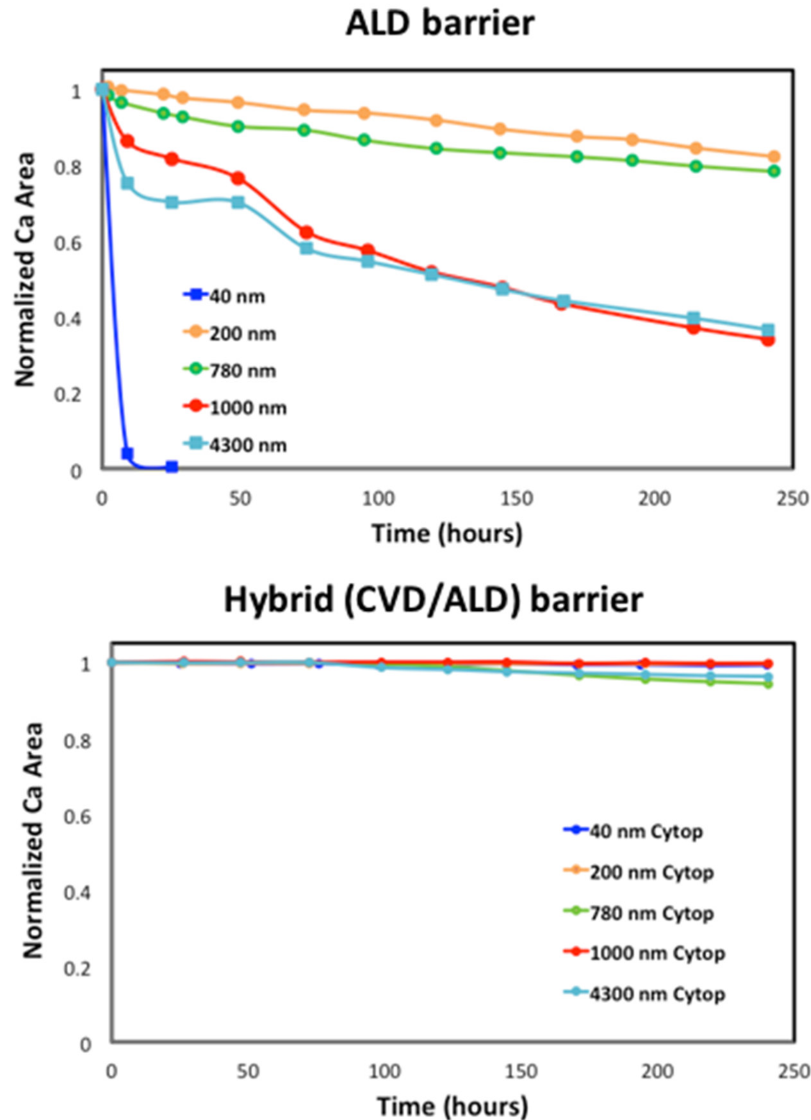

Figure 5.18 Degradation of the calcium sensor layers as a function of time for varying CYTOP film thicknesses for ALD and hybrid (PECVD/ALD) barrier films.

5.5 Conclusion

Particle contamination issues and stress effects are a significant challenge in developing ALD barrier. The use of thick polymer planarization layers to minimize particle-assisted defects is possible, but can lead to cracking in the ALD film due to stress

concentrations around the particles and the increased crack driving forces from the elastic mismatch between the ALD layer and the polymer layer. This becomes problematic in the use of Al_2O_3 ALD layers deposited by both thermal and plasma enhanced ALD at low temperatures (<100°C) since both techniques typically produce films with high tensile stresses. It should be noted that the stress values in the film which lead to cracking can also arise from CTE mismatch and external loading. In all cases, the crack driving force will be enhanced due to the elastic mismatch between the ALD layer and the polymer. Through this work we were able to demonstrate the increase in cracking of ALD films directly deposited onto CYTOP polymer layers for film thicknesses greater than 200 nm. Thus, the management of stress in barrier films containing ALD alumina or reducing the polymer layer thickness in order to reduce the coefficient Z (Eq. 5.4) must be considered if ALD alumina barriers will be deposited directly onto polymer planarization layers where particle defects are present. By inserting a compressively stressed SiN_x layer into the barrier stack, it was possible to reduce the cracking in the ALD layer for the entire range of polymer thickness used in this study. Thus, the use of the SiN_x layer along with alumina containing ALD films is seen as a key component to producing more robust barrier films for direct deposition onto devices.

CHAPTER 6

IMPROVED MEASUREMENTS OF WVTR OF ALD BARRIER FILMS

6.1 Introduction

Chapter 5 discussed the impact of defects in ALD barriers that can arise during the fabrication process due to mechanical and structural conditions such as CTE mismatch, elastic constant mismatch, and residual stresses around particles. In chapter 5, the barrier performance was qualitatively measured by an optical calcium corrosion test. However, the qualitative procedures employed in Chapter 5 accounts for only the defect-related permeation that is observed as a transparent spot or feature in the calcium sensing layer. No quantitative value of the permeation rate was given since the method employed (the global loss of Ca area) does not provide information the local permeation through defects or more importantly, the intrinsic value of permeation, which is the lowest value that can be achieved when the barrier film is fabricated ideally without external defects. Since both permeation mechanisms are present in the barrier (defect driven and intrinsic) the effective WVTR of a barrier film is higher than the intrinsic WVTR due to the presence of pinholes and macroscopic defects that arise during the manufacturing process.[44, 99, 220] Thus, better knowledge of the different contributions from intrinsic permeation and defect permeation will enable better engineering of advanced ultrabarriers, placing the focus more on defect mitigation during manufacturing while improving the intrinsic quality of the barrier.

To measure the WVTR of high performance barrier films, Nisato *et al.* first introduced the calcium corrosion test, and the calcium test has been widely accepted due to its theoretically high sensitivity over other various measurement techniques introduced in Chapter 2.[45, 127] The evaluation procedures to determine the WVTR from calcium layer corrosion vary according to the test apparatus used in different studies. The optical calcium corrosion test measures the transparency increase of a calcium sensor layer[115, 221] or the area increase of a fully oxidized calcium sensor layer,[118] which was used in Chapter 5. On the other hands, the electrical calcium corrosion test measures the conductance decrease of a calcium sensor layer due to the formation of calcium oxide as a result of the oxidation.[45, 222, 223] For both tests, a calcium testing sample should be prepared that is similar to a device structure packaged with a barrier films.

Figure 6.1 illustrates devices packaged with a barrier coating either by direct encapsulation or by indirect encapsulation.[64] Direct encapsulation is a method where the barrier film is coated directly on top of a device, which was used in Chapter 5. Indirect encapsulation is a method where a barrier film is separately prepared on an independent substrate and then subsequently sealed over the device. In the latter case, the barrier film is attached using an edge sealant or an adhesive film.

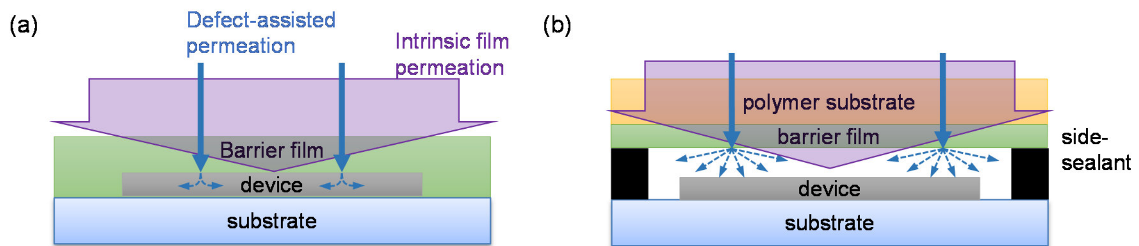

Figure 6.1 Two different approaches of barrier film encapsulation: (a) direct encapsulation where the barrier is grown on the device and (b) indirect encapsulation where the barrier is attached to the device using an adhesive layer. Pathways of the intrinsic film permeation and pinhole-driven permeation are illustrated with arrows.

In order to measure the WVTR of a barrier film, the device in **Figure 6.1** is replaced with a calcium layer which corrodes in the presence of oxygen and water.[127, 223] Using the calcium corrosion test with a direct encapsulation barrier, Carcia *et al.*, and Meyer *et al.* have reported WVTR values as low as 10^{-5} g/m^2/day.[47, 190] However, these WVTR values were estimated with small sized samples (0.25-40 mm^2) which measure very little area of the barrier film which may not be indicative of the distribution of defects or changes in barrier film quality across the size seen in an actual device. In optical tests, the reported WVTR values are estimated either only by evaluating the calcium layer thickness change in the pinhole-free area,[124, 224] or by measuring the area change in a fully degraded region in the calcium layer.[225] Therefore, neither of the methods can differentiate between the dominant permeation mechanisms in the barrier film (e.g., intrinsic permeation through a barrier or by defect-assisted local permeation). In an alternate configuration, the barrier film was tested with a gas space above the calcium sensor as shown in **Figure 6.1** (b). In this case, the measured value is always an effective WVTR since local transport through defects and intrinsic transport are diffused in the gas space above the sensors that smears out regions of high flux. However, the dominant permeation mechanism which contributes to the effective WVTR is not known from such experiments (intrinsic or defect related). Affinito *et al.*, and Roberts *et al.*, have studied theoretically the contribution of pinholes with different sizes for WVTR in an independent barrier film.[99, 226] However, experimental methods to determine the WVTR have not been widely developed and employed.

In addition to the investigation of permeation mechanism of a barrier film, the electrical calcium corrosion test is widely used to measure the effective WVTR for its advantages over the optical calcium test such as ready for automation and compatible for *in situ* measurement in an environmental chamber.[46, 128] Also, depending on the calcium sensor design, the sensitivity can be improved. For example, Reese *et al.* (**Figure 6.2**) introduced an aperture spacer to increase the ratio of a test barrier film area to a calcium sensor size, allowing increased sensitivity by improve the area over which the permeation is measured and then concentrated onto the sensor .[128, 227] However, the increased inner volume in the spacer delays the time for the measurement to reach steady state permeation as well as the absorption and desorption of moisture on the metal spacer can disturb the measurement. In addition, the challenge of the electrical calcium test apparatus still lies in reducing the side permeation that occurs at any bonded interface in the setup in **Figure 6.2** which decreases measurement sensitivity.[227] Therefore, further improvement is recommended to establish a high resolution WVTR measurement technique.

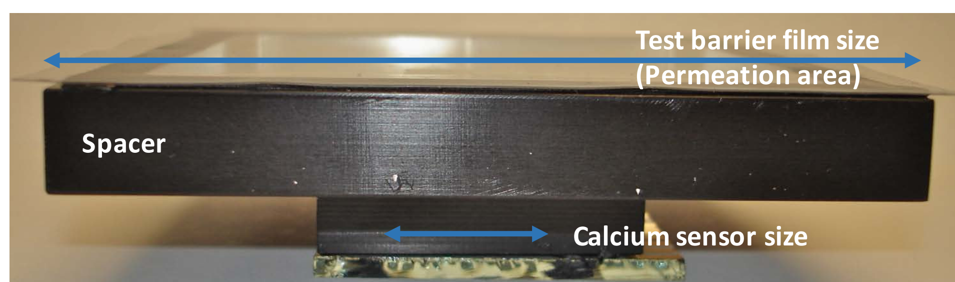

Figure 6.2 Calcium corrosion test cell with a spacer used to improve measurement sensitivity developed by the National Renewable Energy Laboratory. Adapted from reference [128].

Therefore, this chapter introduces WVTR measurement procedures that can evaluate intrinsic permeation and defect-assisted permeation independently using an optical calcium corrosion test. Also, the contribution of intrinsic permeation and defect-assisted permeation will be measured with a hybrid barrier film structure that was found to be the best barrier film among the tested films in Chapter 5. In addition, for the continuous measurement of the effective WVTR values, an improved electrical calcium test apparatus is suggested that can reduces the side permeation error.

6.2 Optical calcium corrosion test for defect-assisted WVTR measurement

As previously described, the optical calcium corrosion test can visualize the defect-driven permeation, which is also observed in Chapter 5. In this section, the optical calcium test images is investigated in detail, and provides further information regarding the intrinsic permeation as well as the defect-driven permeation.

6.2.1 Experimental

Figure 6.3 shows the diagram of the calcium test sample used in this section that is the same structure used in Chapter 5. A 100 nm-thick calcium layer was deposited in the form of 16 square patterns (5 mm × 5 mm) on a 38 mm × 38 mm glass substrate using a thermal evaporator (EvoVac, Angstrom Engineering). The thickness of the calcium layer was controlled using a quartz crystal microbalance *in situ.* After that, a 200 nm polymer layer (CYTOP) was spin-coated on the calcium layer in a glove box. The purpose of the polymer layer was not only to provide a short-term barrier layer that prevents calcium degradation during sample transport from the glove box to the deposition system, but also to reduce pinholes in the barrier film that can be caused by contaminant particles as it shown in Chapter 5. The calcium deposition and CYTOP

coating were done in collaboration with the research group of Professor Bernard Kippelen at the Georgia Institute of Technology.

Afterwards, the sample was transferred to a PECVD system (Oxford) using a vacuum canister, and 100 nm SiN_x was deposited on top of the CYTOP layer at 100°C. After the PECVD deposition, a 20 nm Al_2O_3 layer was deposited by atomic layer deposition (ALD) followed by a 20 nm-thick ALD nanolaminate consisting of Al_2O_3 and HfO_x, alternating every 5 cycles. All ALD film growth was performed in a Savannah ALD system (Cambridge Nanotech) at 100°C.

Directly-encapsulated calcium samples were placed in a humidity chamber (MicroClimate, Cincinnati SubZero) at 50°C and 85% RH. Images of the samples were taken periodically in order to track the degradation of the calcium layer using a high-resolution flatbed photo scanner (Epson V600), which was described in Chapter 5. The color sample images were taken at 2400 dpi resolution in reflection mode as shown in **Figure 6.3** (b) without any color correction algorithm. Then, the images were converted into 256-level gray scale images and then binary images using MATLAB functions for further analysis to investigate the detail features of sample degradation. For binary image conversion, an intensity threshold value was determined by Otsu's method using a MATLAB function.[209]

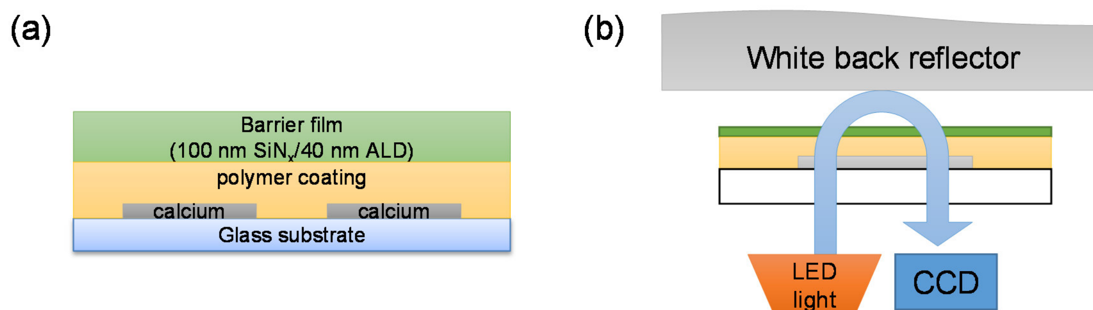

Figure 6.3 Schematic diagram of (a) the calcium degradation test sample and (b) the flatbed photo scanner used to scan the image of the Ca sample to determine changes in light transmission through the Ca and regions of localized defects.

6.2.2 Observation of local degradation spots in optical calcium test

First, the most obvious degradation behavior of the encapsulated calcium layer was the appearance of macro-sized local degradation spots as shown in **Figure 6.4** (a), larger than the pixel size of the 2400 dpi image resolution, being 10.6 μm × 10.6 μm. These macro size local degradation spots were usually accompanied with a particle at the center of the spots. **Figure 6.4** (b) shows a microscopic image of one of the local degradation spots, and the associated particle at its center. Thus, it appears to be clear that the local degradation spots arise from pinholes in the barrier film caused by the presence of macroscopic sized particles; much larger than the tens of nanometer-thick layers used in our test samples. Macroscopic particles can lead to the formation of pinholes in the barrier layer because of either residual stress concentration or poor barrier film coverage on the particle (**Figure 6.4** (c)).[228] According to the classification of pore sizes by the International Union of Pure and Applied Chemistry (IUPAC),[229, 230] the pinhole defects can be classified as macropores (> 50 nm) because the observed particle size is on the order of micrometers under a microscope as in **Figure 6.4** (b). Also, since the radial growth rate of the locally degraded Ca is directly related to the water vapor that is

transported through the pinhole defect, analyzing the growth of the spots will help to understand the water vapor permeation behavior through the defects.

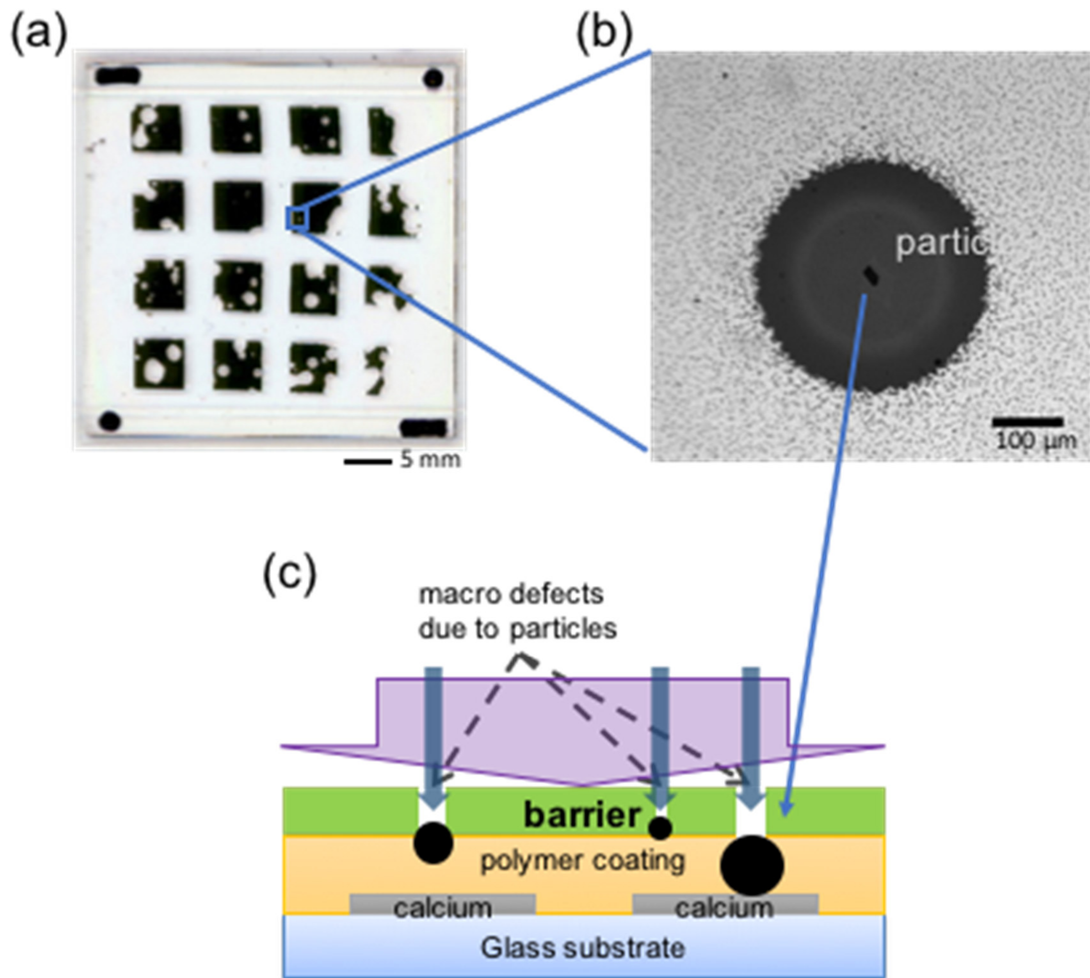

Figure 6.4 An example of pinhole local degradation of a Ca sensor due to the existence of particle defects. (a) A scanned image of the full 16 calcium square sample after degradation, (b) a zoomed in image of a local degradation spot, and (c) a cross-sectional diagram of devices showing localized high permeation in regions with defects.

In addition to the local degradation spots, the images of a calcium sample displayed a change in intensity of the intact, or defect-free, calcium area as in **Figure 6.5** (c). This intensity change is due to the uniform degradation of the calcium layer by water vapor permeation through the barrier film. In this case, the permeation occurs through

uniformly distributed sub-micron defects or porosity in the film. Thus, the reaction of calcium and permeated water vapor flowing through mesoscale porosity is not detectable with the resolution of the image, but manifests itself as a change in the intensity of the image. This change is usually reported in the literature as the intrinsic barrier film performance and the permeation through this region is assumed to be negligible in case of barrier films with macroscale defects as most people assume that local permeation around macroscale defects dominate the film response. Discrimination between the intrinsic permeation rate and the defect-assisted local permeation is critical to better understand the total or effective WVTR of barrier films and which permeation mechanism truly dominates the film behavior.

The effective WVTR of the barrier film arises from both the flux through pinholes or defects and the intrinsic flux through the barrier film. In other words, the effective flux of gas permeation in a barrier film can be expressed as,

$$J_{eff} = -D_{intrinsic} \frac{\partial C}{\partial x} + J_{pinhole} \qquad (6.1)$$

where J_{eff} is the effective flux of a barrier film, $D_{intrinsic}$ is the molecular diffusivity of intrinsic film, C is the concentration of gas molecules, and $J_{pinhole}$ is the flux through a pinhole. The evaluation of the defect assisted local WVTR and the intrinsic WVTR can be conducted using the experimental procedure described in this study.

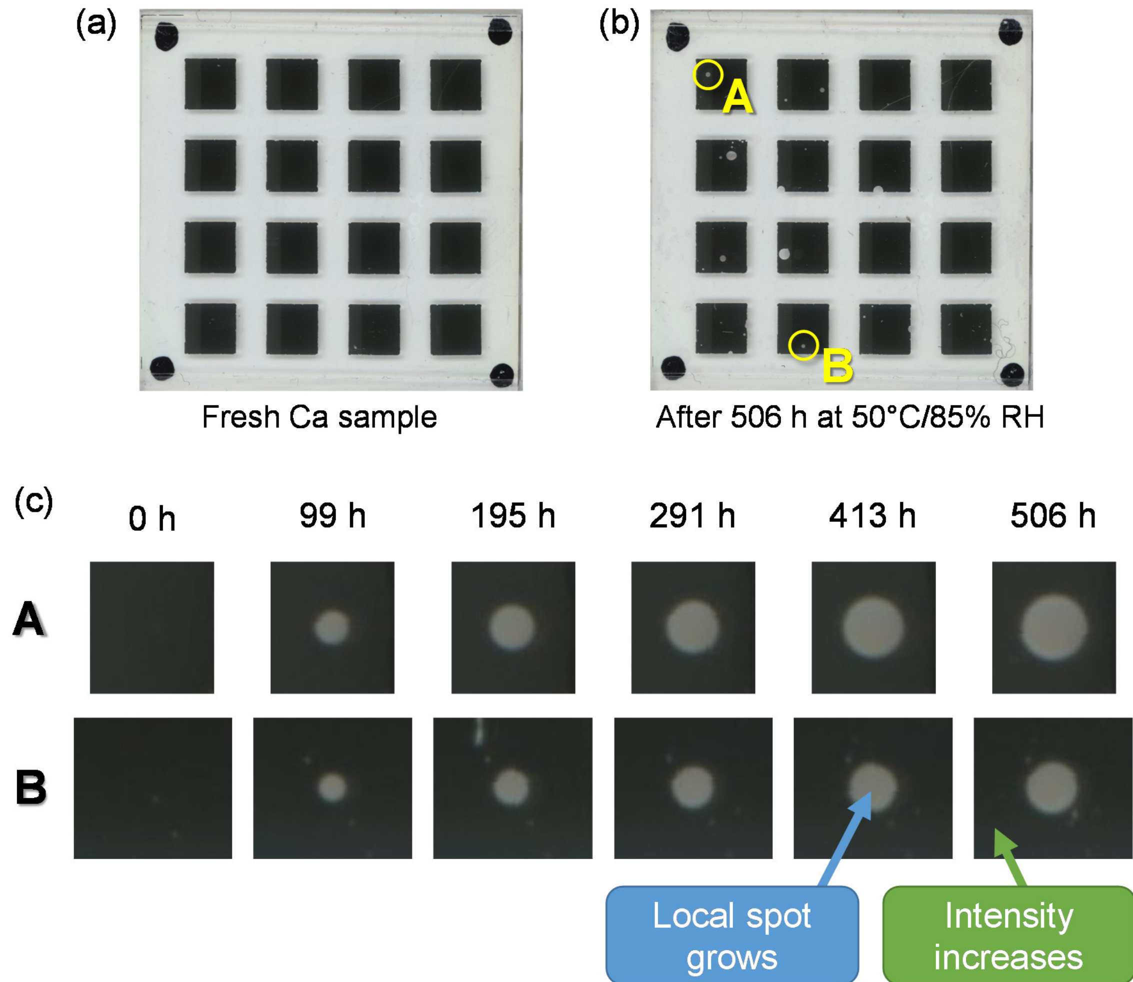

Figure 6.5 Calcium sample image of a tested barrier film (CYTOP/100 nm SiN_x/20 nm ALD/20 nm ALD nanolaminate) after 506 h at 50°C/85%RH condition. (a) Fresh calcium sample, (b) a scanned image of the calcium sample after 506 h of degradation, and (c) images showing the growth of selected local degradation spots over time.

6.2.3 Defect assisted permeation

As described previously, the calcium layer degrades locally due to permeation of water vapor through pinholes or defects in the barrier film, and the degradation appears as a light spot in the sample's image; since calcium hydroxide is transparent optically allowing light to reflect from the white background. As seen in **Figure 6.5** (c), the

calcium hydroxide spot size grows radially over time, suggesting that the permeated water vapor via the pinhole diffuses isotropically inside the layers under the barrier film. **Figure 6.6** (a) shows calcium sample images after 506 h at 50°C/85%RH. From the images, local degradation spots that are independent from each other are selected. Then, the radius and the area of the selected spots are measured from the binary images using a feature extraction function of MATLAB, and plotted in **Figure 6.6** (b) and (c), respectively. Differences in pinhole size lead to a large variance in the growth rate between calcium hydroxide spots. However, the temporal evolution of the spot radii displays a similar functional dependence over time, while the area of each spot increases approximately linearly over time.

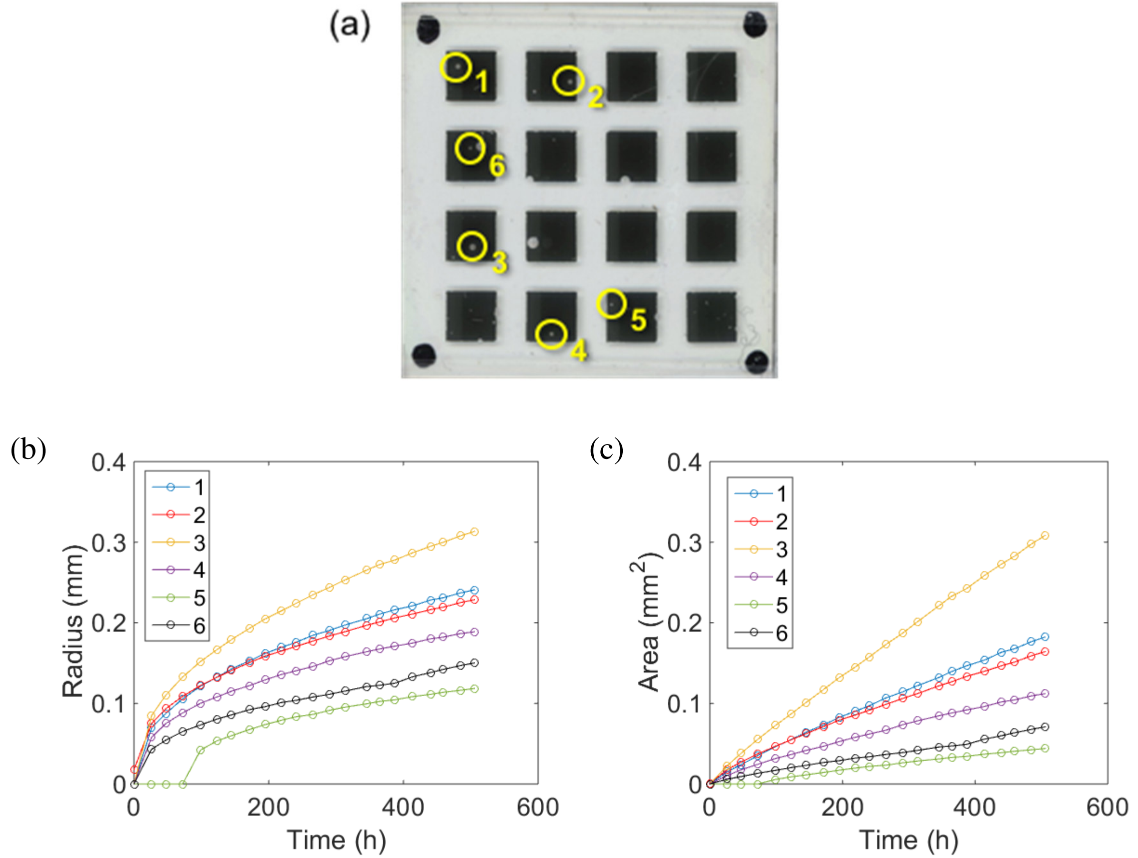

Figure 6.6 Growth of local degradation spots over time: (a) Local degradation spots chosen from the 16 Ca sensors, (b) Change in the radius of the selected local degradation spots versus time, and (c) Change in area of the selected local degradation spots versus time.

From the experimental results, it is reasonable to consider that the growth of calcium hydroxide spot is due to a radial diffusion process of water vapor inside the underlying layer, modeled through a 1-dimensional radial diffusion equation,

$$\frac{\partial C}{\partial t} = D\nabla^2 C = D\frac{1}{r}\frac{\partial}{\partial r}\left(r\frac{\partial C}{\partial r}\right) \qquad (6.2)$$

where t is time and r is the radial position[231] as shown in **Figure 6.7** (a). This model has a semi-infinite boundary condition that $C=0$ as r goes infinity, but the other boundary condition at $r=0$ is not clear. If the boundary condition is a constant concentration, $C=C_0$

at $r=0$, Eq. (6.2) is solvable using the separation of variable method, and the solution of Eq. (6.2) is expressed by Bessel functions,

$$C=\sum_{n=1}^{\infty}\exp(-\lambda_n^2 Dt)\left[C_{1,n}J_0(\lambda_n r)+C_{2,n}Y_0(\lambda_n r)\right] \qquad (6.3)$$

whereas if the boundary condition is a constant total flux condition, $Q=Q_0$ at $r=r_0$, Eq. (6.2) is solvable using a similarity function, and the solution is

$$C=C_0\int_{\eta}^{\infty}\frac{1}{\eta'}\exp\left(-\eta'^2\right)d\eta' \qquad (6.4)$$

where the similarity function, η, is defined as $\eta=r/\sqrt{4Dt}$.

From the solutions for both cases, **Figure 6.7** (b) and (c) plots the contour profiles of the concentration with r versus t for both boundary condition, respectively. Even if the constants such as D, C_0, Q_0, and r_0 were arbitrarily selected, **Figure 6.7** (b) and (c) clearly show the difference of the profiles over time because of the different boundary condition. In case of constant concentration condition at the pinhole, the diffusion rate decreases more rapidly than the case of constant flux condition at the pinhole over time. Between the two conditions, it is apparent that the solution with a constant total flux boundary condition (**Figure 6.7** (c)) coincides with the radial growth profiles from the experimental results (**Figure 6.6** (b)). Knowing that the spot area corresponds to the amount of water vapor in a calcium test and the growth rate of the spot area is constant, these modeling results suggest that the local degradation follows a radial diffusion process with a constant total flux condition. In other words, the permeation rate through a pinhole is constant over time even if the barrier film is directly deposited on the device.

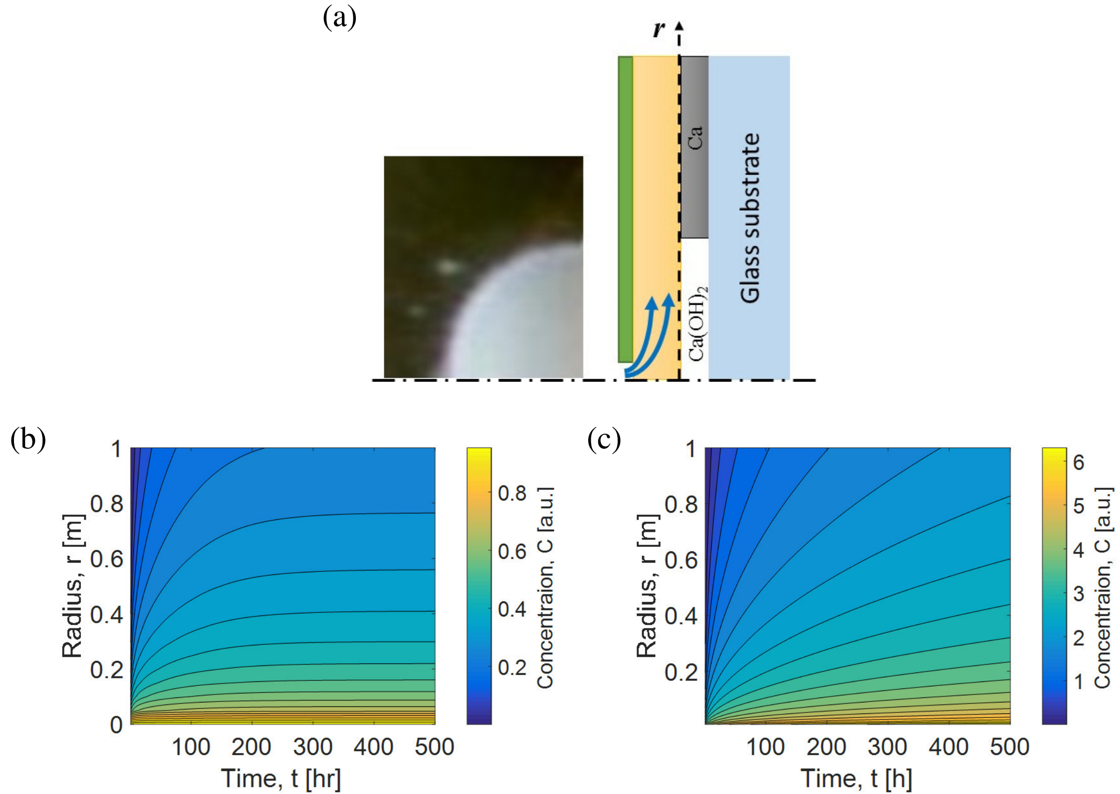

Figure 6.7 A 1D axisymmetric diffusion model of water vapor permeation inside the underlying layers: (a) a diffusion model diagram with a quarter symmetry image of a local degradation spot, (b) The concentration contour plot on radius vs. time plane with a constant concentration boundary condition at the center ($C=C_0$ at $r=0$), and (c) The concentration profile on radius vs. time plane with a constant total flux boundary condition, $Q=Q_0$ at $r=r_0$.

6.2.4 Intrinsic film permeation

In addition to the defect assisted local degradation, the calcium layer appears to degrade uniformly in absence of local pinhole defect, as seen in **Figure 6.5** (c). The uniform calcium degradation appears as a transparency change of the intact calcium layer. If we assume that the calcium oxidation progresses uniformly, forming a calcium hydroxide layer on the top of the calcium layer, the remaining calcium thickness can be determined from the transparency of the calcium layer.

The transparency of the calcium layer in a pinhole-free area is evaluated through the following procedure. From an original image (**Figure 6.8** (a)), the pinhole-free area is selected from an intensity threshold value determined by Otsu's method.[209] In **Figure 6.8** (b) plots the histogram of the original image with the threshold value (red vertical line) and in **Figure 6.8** (c) shows the selected intact calcium area as white color in a binary image. Referring to the binary image, the original intensity of the pixels that are within the selected defect-free area is averaged. Afterwards, the transparency and the thickness of the remaining calcium layer is determined from the average pixel intensity by neglecting interference effects and using Beer-Lambert law,

$$\frac{I_{Ca_area}}{I_{background}} \approx \frac{I_{source}(T_{substrate}T_{Ca}T_{barrier})^2 R_{back}}{I_{source}(T_{substrate}T_{barrier})^2 R_{back}} = T_{Ca}{}^2 = \exp(-\alpha_{Ca}h_{Ca})^2 \qquad (6.5)$$

where I_{Ca_area}, $I_{background}$, and I_{source} are the intensity of selected calcium area, background area, and the light source. T is the transparency of each layer, R_{back} is the reflectance of the white back reflector, and α_{Ca} and h_{Ca} are the attenuation coefficient and the thickness of a calcium layer, respectively. Since α_{Ca} is a function of wavelength, it is difficult to calculate the representative value without knowing the spectrum of the incident light on the calcium layer. Instead, an effective α_{Ca} is estimated using the calcium transparency of the first image ($t=0$) with the assumption that the thickness of calcium layer is 100 nm as deposited. Finally, in **Figure 6.8** (d) plots the average pixel intensity and the estimated calcium thickness versus time. The calcium thickness decreases linearly up to 500 hours in this barrier film test at a 50°C/85% RH.

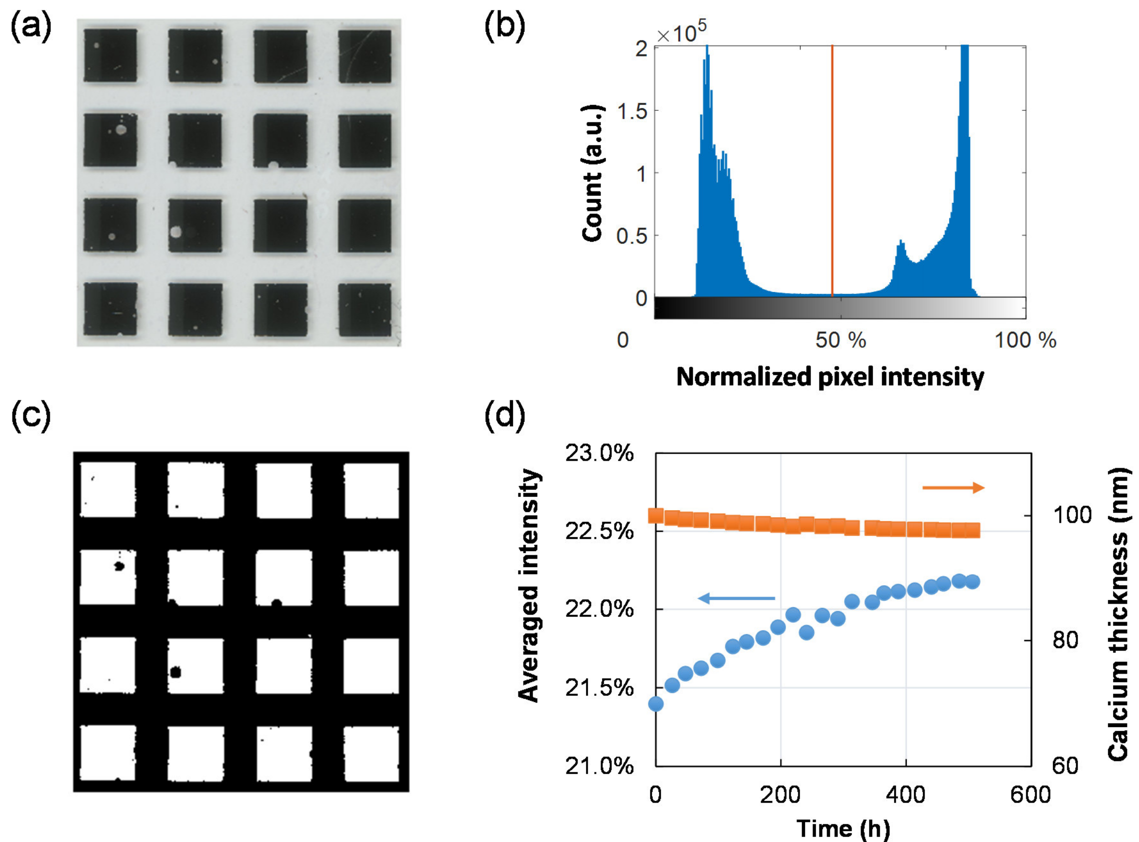

Figure 6.8 Uniform degradation of the calcium layer and the evaluation of the degradation. (a) An original sample image after 506 hours at 50°C/85% RH, (b) histogram of the original image with a threshold value (orange vertical line), (c) intact calcium region, selected using the threshold value, and (d) average intensity change of the intact calcium area over time.

6.2.5 Overall permeation

The WVTR of a barrier film is estimated from the amount of calcium degradation that was analyzed previously for the two permeation pathways; defect assisted local degradation and intrinsic permeation. If we assume that the permeated water vapor has reacted with calcium, the WVTR for each permeation pathway through the barrier film can be estimated from the degree of calcium degradation. For a defect assisted local permeation, the amount of water vapor that permeates is proportional to the mass of

calcium layer that reacts with water, which is measurable from the area of local degradation spot in the scanned image. Therefore, the water vapor transport rate for a single spot is,

$$Q_{defect} = 2\frac{M_{water}}{M_{Ca}}\rho_{Ca}h_{Ca}\frac{\partial A_{spot}}{\partial t} \tag{6.6}$$

where M_{water} and M_{Ca} are the molecular weight of water (18.02 g/mol) and calcium (40.1 g/mol), respectively, ρ_{Ca} and h_{Ca} are the density (1.55 g/cm^3) and the thickness of the calcium layer (100 nm), respectively. Thus, WVTR of all spots per area is the summation of all local degradation spots,

$$WVTR_{defect} = \frac{1}{A_{barrier,0}}\sum_{i}^{N} Q_{defect,i} = 2\frac{1}{A_{barrier,0}}\frac{M_{water}}{M_{Ca}}\rho_{Ca}h_{Ca}\sum_{i}^{N}\frac{\partial A_{spot,i}}{\partial t} \tag{6.7}$$

where $A_{barrier,0}$ is the area of the barrier film (415 mm^2), and N is the number of spots. The total area growth rate of all the spots in the sample is calculated by finding the total spot area changes from whole binary images instead of accounting individual defect spots, and is found to be 0.145 mm^2/day. The average and the standard deviation of the area growth rate of the spots in the 16 calcium squares are shown to be 9.1×10^{-3} mm^2/day and 1.53×10^{-2} mm^2/day, respectively. Since defects are distributed randomly on several calcium squares in the sample, the standard deviation is relatively large. The total area growth rate results in the $WVTR_{defect}$ being 4.84×10^{-5} g/m^2/day using Eq. (6.7).

In addition, intrinsic WVTR of the barrier film is proportional to the rate of thickness decrease of the calcium layer, and is expressed as

$$WVTR_{intrinsic} = 2\frac{M_{water}}{M_{Ca}}\rho_{Ca}A_{Ca}\frac{\partial h_{Ca}}{\partial t}\frac{1}{A_{barrier}} \tag{6.8}$$

where A_{Ca} and $A_{barrier}$ are equal when a barrier film is directly deposited. The rate of thickness decrease of the tested calcium samples was found as -0.102 nm/day using the slope of in **Figure 6.8** (d), and the $WVTR_{intrinsic}$ is calculated as 1.41×10^{-4} g/m^2/day using Eq. (6.8).

Finally, the effective WVTR of a barrier film is the summation of the two WVTR values, Eq. (6.7) and Eq. (6.8).

$$WVTR_{eff} = WVTR_{defect} + WVTR_{intrinsic} \tag{6.9}$$

Using Eq. (6.9) and the previous results of the calcium degradation analysis, the effective WVTR of the tested barrier film was calculated as 1.89×10^{-4} g/m^2/day at 50°C/85%RH. As a result, the intrinsic permeation rate contributes *ca.* 3 times more to the effective WVTR than the defect assisted local permeation rate in the tested barrier film. However, since the defect assisted WVTR is dependent on the defect density in a given barrier film, the ratio is also dependent on the conditions of barrier film fabrication process, such as handling and cleanness of the environment. For example, an inferior barrier film (**Figure 6.4** (a)) that was prepared in uncontrolled environments shows much higher defect density than the tested barrier film (**Figure 6.5** (b)), and the contribution of the defect assisted WVTR is more dominant than the intrinsic film permeation in the inferior barrier film.

6.2.6 Section summary

By studying the contributions to WVTR from the intrinsic and defect driven permeation pathways, a better understanding of the effective WVTR of a barrier film can be obtained. By employing optical calcium corrosion test, it is possible to observe the results of these two permeation mechanisms independently. The defect-assisted WVTR

was estimated from the area growth rate of local calcium degradation spots, and the continuous layer intrinsic barrier film WVTR was evaluated from the transparency change rate of the intact calcium area. Comparing the area growth rate of the local degradation spot with a cylindrical diffusion model, it was found that the WVTR though a pinhole is constant with a negligible lag time. Since the defect-assisted WVTR is dependent on the size of the pinholes and the number density of pinholes in a barrier film, they can contribute a significant amount to the overall permeation, if they are not controlled during the fabrication process. For low defect densities, as shown in this study, the WVTR is dominated by the intrinsic permeation through the barrier film. Thus, efforts to reduce the WVTR should focus on improving the intrinsic properties of the barrier. In addition, local defects should be reduced in order to prevent local degradation of devices in the vicinity of defects. However, other methods such as multilayer films or the use of getters may help address these issues.

6.3 Electrical calcium corrosion test for the effective WVTR measurement

As seen previously in **Figure 6.1**, devices can be packaged by direct barrier deposition or by indirectly using separate barrier films and a method using optical Ca testing was used to help determine intrinsic and pinhole driving permeation in direct encapsulation barriers. In the case of indirect encapsulation, the effective WVTR of the individual barrier film can be measured using an electrical calcium corrosion test.[45, 128] **Figure 6.9** illustrates a simplified calcium corrosion cell to test indirect barrier films and possible permeation pathways with the cells. In an electrical calcium test, there is no method to distinguish between defect assisted and intrinsic permeation since the electrical

measurement is sensitive only to changes in resistance of the Ca layer regardless of the mechanism for its change. The assumption is made that the degradation progresses from the top of the calcium layer, corroding the Ca layer uniformly over time such that the Ca layer thins, but a real shape stays the same (**Figure 6.9**). By measuring the conductivity of the calcium layer, the mass of reacted or degraded calcium can be evaluated from the conductivity change of the calcium layer with the calcium conductivity (ρ_{Ca}) and density (δ_{Ca}) using the Ohm's Law. After that, the WVTR is calculated from the rate of Ca degradation determined by the rate of change in electrical conductance using the reaction ration of calcium and water (n), molecular weight of water (M_{water}) and calcium (M_{Ca}) with the following equation, [45]

$$\begin{aligned} WVTR &= n\delta_{Ca} \frac{M_{water}}{M_{Ca}} \frac{Area_{Ca}}{Area_{window}} \frac{dh}{dt} \\ &= -n\delta_{Ca} \frac{M_{water}}{M_{Ca}} \frac{Area_{Ca}}{Area_{window}} \rho_{Ca} \frac{d(1/R)}{dt} \frac{l_{Ca}}{w_{Ca}}, \end{aligned} \tag{6.10}$$

where $Area_{Ca}$ is the top surface area of calcium layer, $Area_{window}$ is the permeation window area of a barrier film, h is the height of degraded calcium layer, R is measured calcium layer resistance, and l and w are the calcium layer channel length and width, respectively.

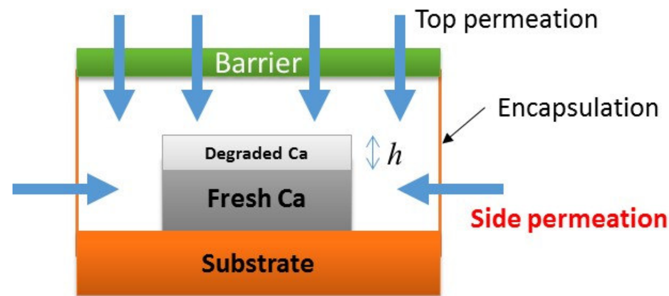

Figure 6.9 Water vapor permeation test of an indirect barrier by calcium degradation.

In order to test the effective WVTR values of individual barrier films, the indirect encapsulation method (**Figure 6.1** (b)) should be used to prepare calcium test samples since water vapor that permeates through the local defects or intrinsically through the layer will be spread out by the gaseous layer over the Ca sample. However, if the side sealing is poor, then the WVTR measurement can be dominated by the permeation through the side sealing (**Figure 6.9**), resulting in higher WVTR values. **Figure 6.10** shows a long-term test of the sealing material to investigate the side permeation through the sealant. As seen in the figure, apparent side permeation was observed through the sealant for a long-term test. As a different approach to identify the side permeation, samples in **Figure 6.11** use 'L'-shape Ca makers at the corners of the sealant, which can indicate whether the side permeation occurs during the test. **Figure 6.11** shows the calcium sensor in case A was more quickly degraded than case B. Observing the L marker is degraded in case A while the maker in case B is fine, side permeation contributed the calcium sensor degradation, and which prohibits the accurate measurement of the WVTR of a test barrier film. Therefore, the side permeation should be suppressed by means of desiccants as well as should be identified whether the side permeation affects the WVTR measurement.

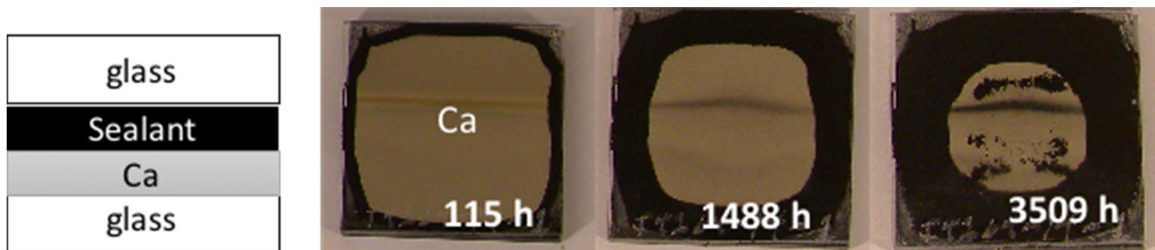

Figure 6.10 Side permeation test of the sealant material (PVS101, ADCO). Calcium was encapsulated with a glass lid using the sealant, and degradation from the sample boundary was observed due to the side permeation. Adapted from reference [232] .

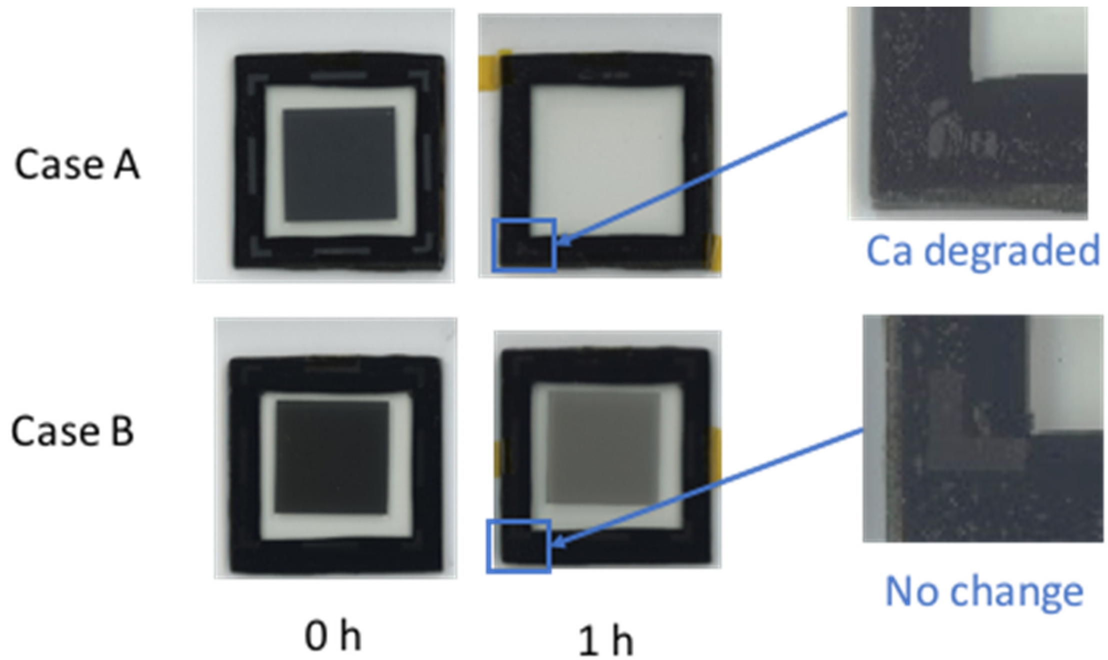

Figure 6.11 Calcium corrosion test with barrier films. 'L'-shape calcium marker was embedded under the side sealant, the marker degraded due to the improper edge sealing procedure.

Also, the electrical measurement can be an issue when it is tested at high humidity condition such that electrode corrosion used to make contact with the Ca layer and the testing equipment can become an issue. Therefore, the issues will arise in resistance measurements needed to sense the Ca degradation as well as from side permeation through the edge sealant in the calcium corrosion test which must be resolved in order to achieve a truly high resolution measurement.

6.3.1 Experimental

In order to achieve a highly sensitive calcium corrosion sensor, the calcium test configuration has been redesigned in order to improve upon previous configurations used in other studies.[58, 233] The goal of the improved design is to improve the accuracy of

calcium conductance measurement and to minimize the side permeation of the calcium test sample. The distinctive features of the new configuration are in the followings.

- 2 calcium sensors for measurement reliability (**Figure 6.12** (a))
- 4 point probing configuration for the accurate measurement of calcium conductance without the effects of contact and wire resistance. (**Figure 6.12** (b))
- Boundary check line to detect the test failure by the side permeation (**Figure 6.12** (c))
- Double side sealants to suppress the side permeation (**Figure 6.12** (d),(f))
- Simple electrode connection using a standard card-edge connector (**Figure 6.12** (b))
- Embedded desiccant that can reduce or eliminate the side permeation (**Figure 6.12** (e))
- Large ratio (7.4) of the permeation window area ($Area_{window}$) and the calcium sensor area ($Area_{Ca}$) to enhance the measurement sensitivity.

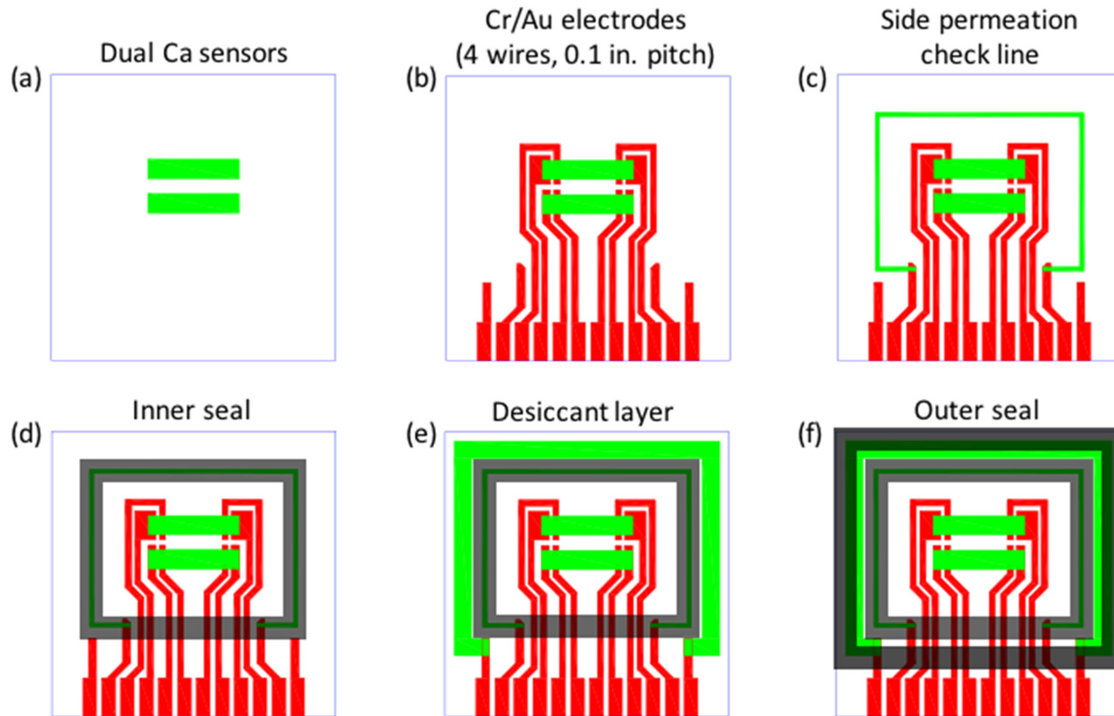

Figure 6.12 Design steps to achieve a high sensitive calcium sensor that is resistance to the side permeation: (a) dual calcium sensor layer, (b) 4 wire Au probing, card edge compatible connection pads, (c) side permeation detecting check line, (d) inner side seal, (e) interim desiccant, and (f) outer side seal.

Figure 6.13 illustrates the final design of calcium test sample for the electrical calcium corrosion test. In this section, the fabrication procedures of the improved calcium sensor are described, and the measurement set up and the fabricated calcium sensor are shown after that.

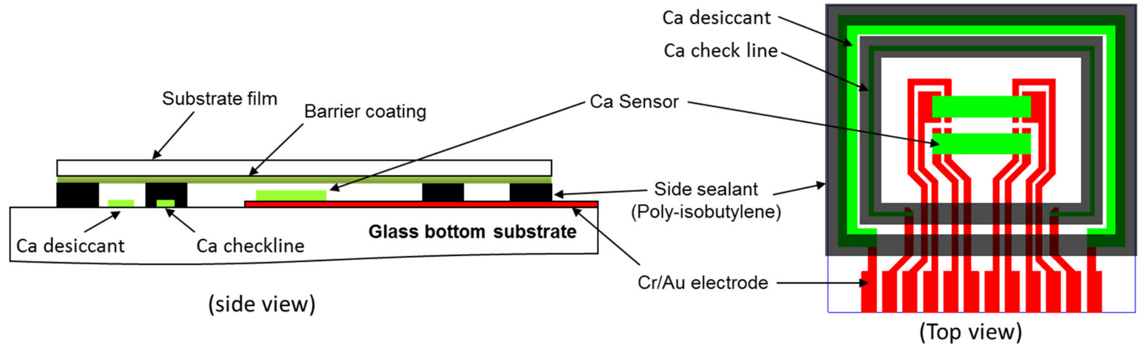

Figure 6.13 Schematic of an improved sample design for electrical calcium corrosion test.

6.3.1.1 E-beam evaporation

For the deposition of electrode layers, E-beam evaporation (Denton Explorer, Denton) was used for chromium (Cr) and gold (Au) deposition (**Figure 6.14** (a)). Similar to the thermal evaporation, target material is evaporated and is deposited on a substrate through a shadow mask. For the fabrication of calcium sensor devices, 38 mm x 38 mm glass substrates were solvent-cleaned using acetone and IPA with sonication for each 10 min, and rinsed with DI water. Then, the substrates were dried on a hot plate for 5 min at 120°C to remove residual moisture that may reduce the adhesion strength of the metallic layers on glass. Afterwards, 20 nm chromium and 100 nm thick gold layers were deposited with the shadow masks. The chamber pressure was pumped down to 10^{-6} Torr before the deposition using a cryogenic pump. The deposition rates for both films were both 1 Å/s, controlled by *in situ* QCM and the controller. A shadow mask (**Figure 6.14** (b)) was made using the patterns illustrated in red color in **Figure 6.13** (right).

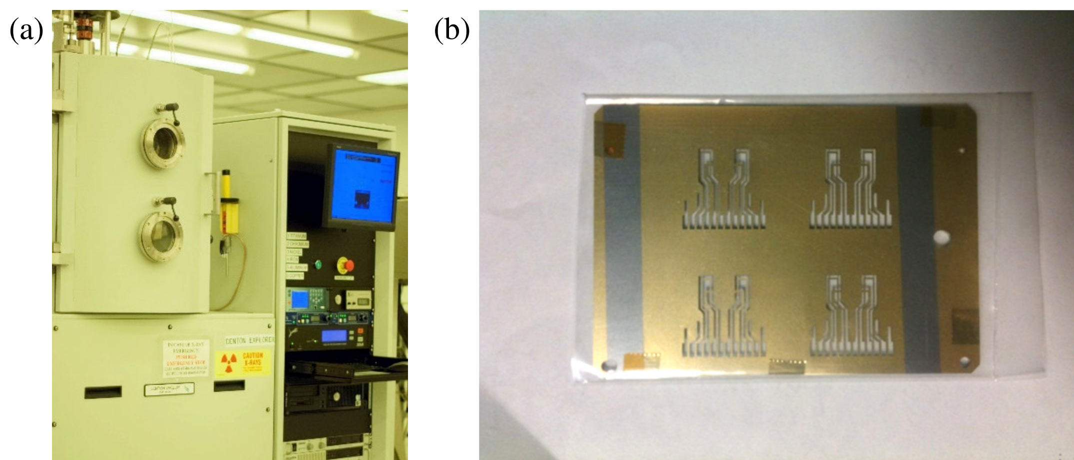

Figure 6.14 (a) Denton E-beam evaporation system for depositing Ca layers. (b) A shadow mask used to fabricate electrode patterns of Cr/Au layers.

6.3.1.2 Calcium sensor layer deposition

The Ca sensor layer was deposited using a thermal evaporation system (Specros, Kurt J. Lesker) in collaboration with the research group of Professor Bernard Kippelen at the Georgia Institute of Technology (**Figure 6.15**). A 100 nm thick calcium layer was deposited on the previous substrates with a shadow mask for patterning (green area in **Figure 6.13** right). The chamber pressure was below 10^{-7} Torr, and the deposition rate was 1 Å/s.

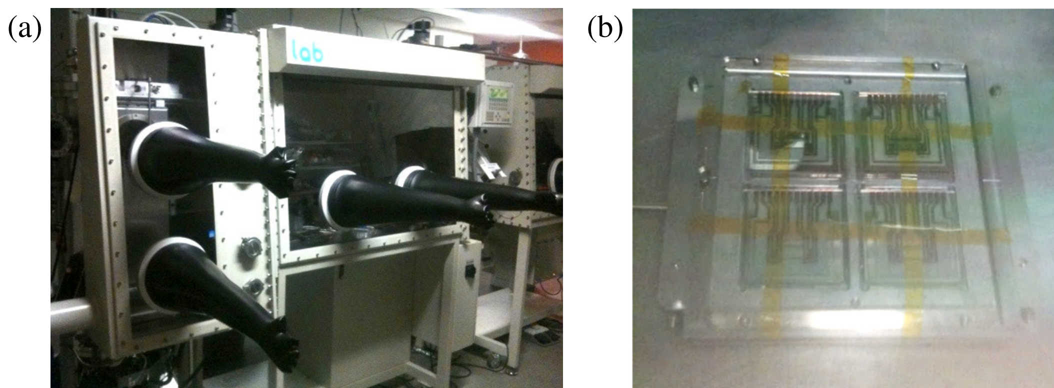

Figure 6.15 (a) Spectros thermal evaporation system (Kurt J. Lesker), which is installed in a glove box. (b) Four 38 mm x 38 mm samples mounted on a deposition holder with a shadow mask for calcium deposition.

6.3.1.3 Barrier encapsulation using a side sealant

After the calcium sensor samples were deposited, barrier films deposited onto PET films were packaged on top of the calcium sensor using a side sealant (HelioSeal PVS 101, ADCO) as seen in **Figure 6.13**. The sealant is a thermoplastic material based on polyisobutylene with integrated desiccant. Since the calcium layer can oxidize even in a N_2 glove box if the water and oxygen levels are too high (>10 ppm), the encapsulation procedure was performed as soon as the calcium deposition was completed..

First, the side sealants were cut into 2 mm wide strips, and a liner film was peeled off from the sealants. Then, the sealant strips were applied on the calcium sensor samples one by one along with the boundary of the sealing as shown in black color in **Figure 6.13**. **Figure 6.16** shows the step-by-step procedures of placing sealant strips on a prepared a calcium sample. When placing the sealant strips, the sealing should not overlap to keep a consistent sealant thickness. **Figure 6.17** (a) shows an improper example, and **Figure 6.17** (b) shows appropriate alignments of the edge sealant. If the width of the sealants is wide enough to cover up the entire calcium samples, **Figure 6.17** (c) is also recommended to avoid inferior junctions at the corners. The samples were then heated up on a hot plate at 110°C for 10 min. Once the sealant was heated and softened, a test barrier film was placed gently with the coating side facing down onto the sealant. Afterward, the whole sample was heated again on the hot plate for 10 min, and pressed evenly. A special heat press can be used for the pressing step, but any small misalignment of the gap can results in the collapse of the samples. In addition, excessive pressure can leads to increased internal pressure in the air gap, which may induce mechanical stress in the barrier films. The pressure needed to make the samples should only be applied until the sealant adheres uniformly on both glass substrate and the barrier film, which is

apparent visually by the color change if their contact is complete. In **Figure 6.18**, the top sealant strip in shows the case when the sealant makes a partial contact between glass and the sealant, whereas the bottom strip completely contacts with glass showing the contact area as dark black.

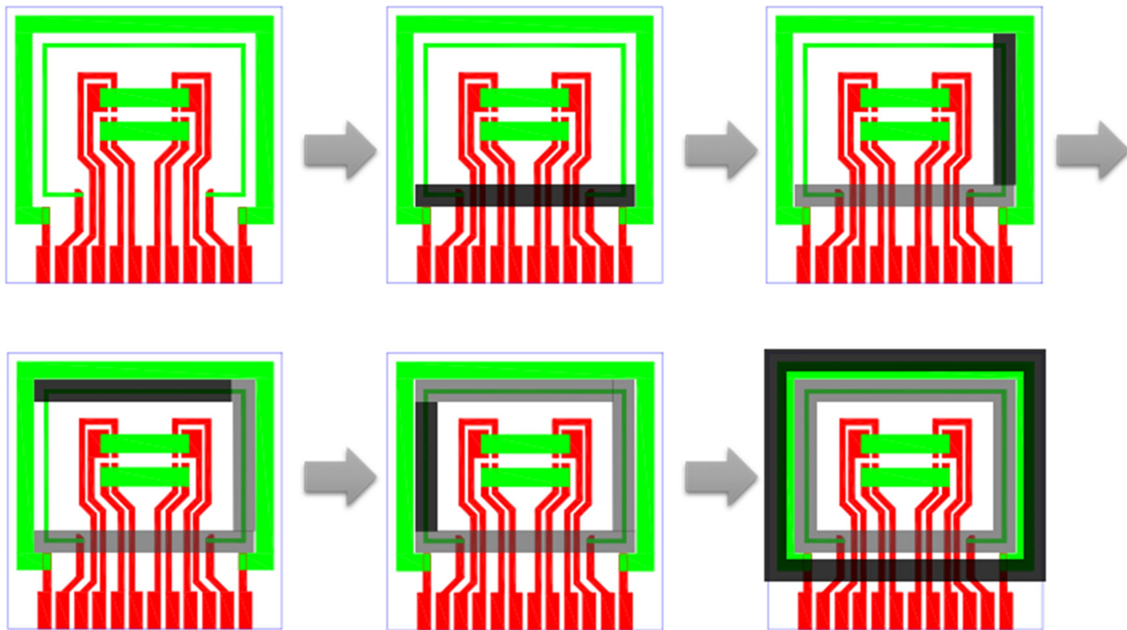

Figure 6.16 Sequence of applying the sealant strips by pieces

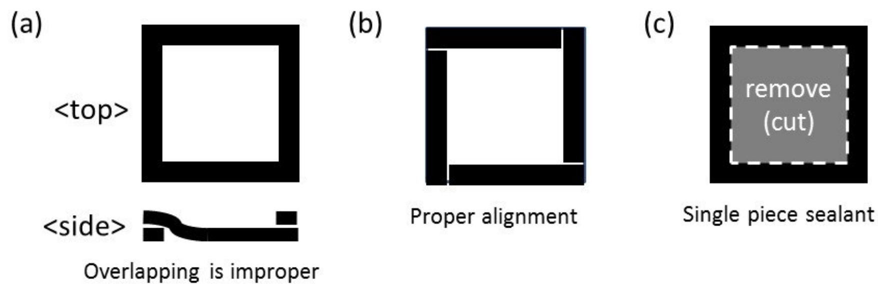

Figure 6.17 Alignment of the ADCO side sealants using 4 strips. (a) Improper alignment due to overlapping, (b) proper alignment, and (c) recommend sealant preparation.

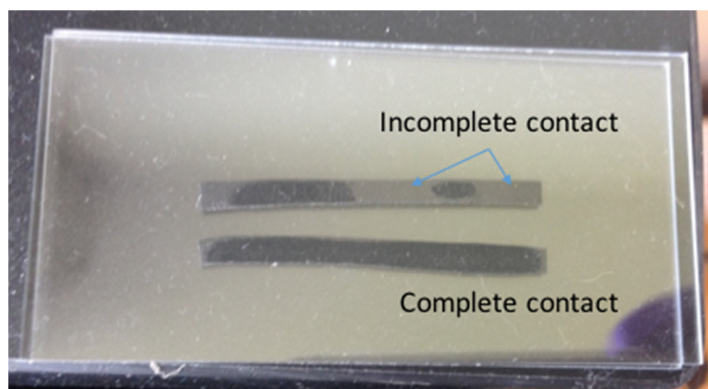

Figure 6.18 Examples of good and bad applications of side sealants. The top sealant strip contacts partially with glass, whereas the bottom sealant strip completely contacts with glass.

6.3.1.4 WVTR measurement

Once the encapsulation was completed, the samples were ready to measure to determine the effective WVTR. The calcium sensor conductance was measured using a data acquisition system (34970A, Agilent) with multiplexer modules (34901A, Agilent) The multiplexer was connected to a card edge (AMC10DRTH, Sullins Connector Solutions) for a single testing module with a multi-conductor (10 wires) cable. The body material of the card edge is thermal stable up to 130°C, and the pins are coated with gold, providing electrical stability in the humidity chamber. **Figure 6.19** shows the data acquisition unit and the multiplexer module used in the measurement. **Figure 6.20** also shows the details of wire connections with a single multiplexer module for 4 calcium samples. Since the data acquisition system can hold up to 3 multiplexer modules, a single system can measure up to 12 calcium samples at a time with 3 multiplexer modules. Finally, **Figure 6.21** shows the electrical calcium corrosion test samples for the WVTR measurement in an environmental chamber. **Figure 6.21** (b) shows a fabricated calcium

sensor sample encapsulated with a test barrier film that is inserted in a card edge for electrical measurement.

(a) (b)

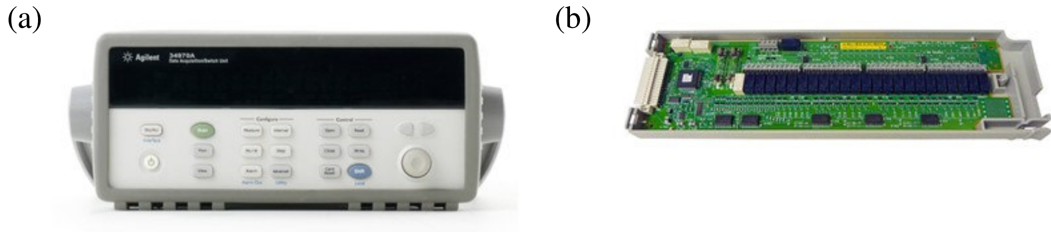

Figure 6.19 (a) Data acquisition system (34970A, Agilent), (b) a multiplexer module (34901A, Agilent).

Ti,NL(AL,Ti) - BenchLink Data Logger 3

Configuration Data Tools Help

Configuration: Status: Ti,NL(AL,Ti) Instruments: 1 Connected Scan Mode: Inactive

Configure Instruments | Configure Channels | Scan and Log Data | Quick Graph

Channels	Enable Channel		Measurement				Scaling (Mx + B)				
Instruments	Scan	Name	Function	Range	Res	More	Scale	Gain (M)	Offset(B)	Label	Test
1. GPIB0::9::INSTR											
34901A											
101	☑	Ch1_A	Four-Wire Ohms	Auto	5.5	...	☐	1	0	OHM	Off
102	☑	Ch1_B	Four-Wire Ohms	Auto	5.5	...	☐	1	0	OHM	Off
103	☑	Ch2_A	Four-Wire Ohms	Auto	5.5	...	☐	1	0	OHM	Off
104	☑	Ch2_B	Four-Wire Ohms	Auto	5.5	...	☐	1	0	OHM	Off
105	☑	Ch3_A	Four-Wire Ohms	Auto	5.5	...	☐	1	0	OHM	Off
106	☑	Ch3_B	Four-Wire Ohms	Auto	5.5	...	☐	1	0	OHM	Off
107	☑	Ch4_A	Four-Wire Ohms	Auto	5.5	...	☐	1	0	OHM	Off
108	☑	Ch4_B	Four-Wire Ohms	Auto	5.5	...	☐	1	0	OHM	Off
109	☑	Ch1_chk	Two-Wire Ohms	Auto	5.5	...	☐	1	0	OHM	Off
110	☑	Ch2_chk	Two-Wire Ohms	Auto	5.5	...	☐	1	0	OHM	Off
111	☐	Ch1_A	Four-Wire Ohms	Auto	5.5	...	☐	1	0	OHM	Off
112	☐	Ch1_B	Four-Wire Ohms	Auto	5.5	...	☐	1	0	OHM	Off
113	☐	Ch2_A	Four-Wire Ohms	Auto	5.5	...	☐	1	0	OHM	Off
114	☐	Ch2_B	Four-Wire Ohms	Auto	5.5	...	☐	1	0	OHM	Off
115	☐	Ch3_A	Four-Wire Ohms	Auto	5.5	...	☐	1	0	OHM	Off
116	☐	Ch3_B	Four-Wire Ohms	Auto	5.5	...	☐	1	0	OHM	Off
117	☐	Ch4_A	Four-Wire Ohms	Auto	5.5	...	☐	1	0	OHM	Off
118	☐	Ch4_B	Four-Wire Ohms	Auto	5.5	...	☐	1	0	OHM	Off
119	☑	Ch3_chk	Two-Wire Ohms	Auto	5.5	...	☐	1	0	OHM	Off
120	☑	Ch4_chk	Two-Wire Ohms	Auto	5.5	...	☐	1	0	OHM	Off
121	☐		DC Current	Auto	5.5	...	☐	1	0	ADC	Off
122	☐		DC Current	Auto	5.5	...	☐	1	0	ADC	Off

Figure 6.20 Configuration of the wiring of a single multiplexer module that can measure four calcium samples at a time. Two 4-wire sensing and one 2-wire sensing for each sample.

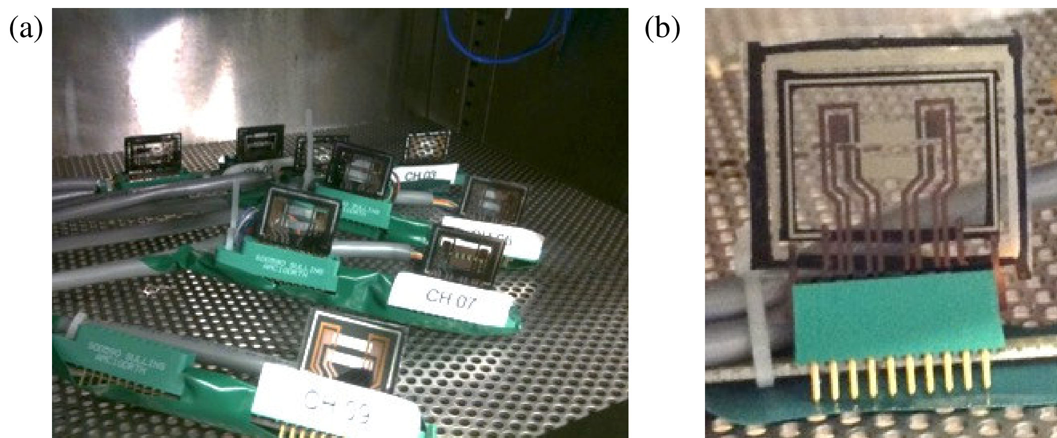

Figure 6.21 Electrical WVTR measurement setup for multiple samples in an environmental chamber. (a) Multiple samples under testing, and (b) a fabricated calcium sample inserted in a card edge for the test.

6.3.2 Results of the effective WVTR

Before testing the barrier films, the sensitivity of the improved calcium test apparatus was investigated using a glass lid. Instead of barrier films, the calcium sensor sample was covered with a glass lid that is impermeable to water as shown in **Figure 6.22** (a). The resistance change of the calcium sensor layers over time is plotted in **Figure 6.22** at two temperature conditions: ambient lab conditions (25°C/35%RH) and at 50°C/ 85%RH in a humidity chamber. As seen in the plot, no resistance increase was observed at room temperature conditions up to 16 days except the daily fluctuations due to the temperature change in the lab. In the meantime, the calcium sensor resistance increased from 2.95 Ω to 2.96 Ω for 8 days in the humidity chamber, which corresponds to a WVTR = 6×10^{-5} g/m^2/day evaluated using Eq. (6.10). This increase was caused by the side permeation through the sealants material whose performance can decrease at high temperature due to its thermoplastic properties and/or deterioration of integrated desiccant of the sealants. Therefore, the improved calcium test configuration can measure

the WVTR values in the region below 1×10^{-5} g/m^2/day at room temperature conditions, and minimum 6×10^{-5} g/m^2/day at 50°C/85%RH conditions.

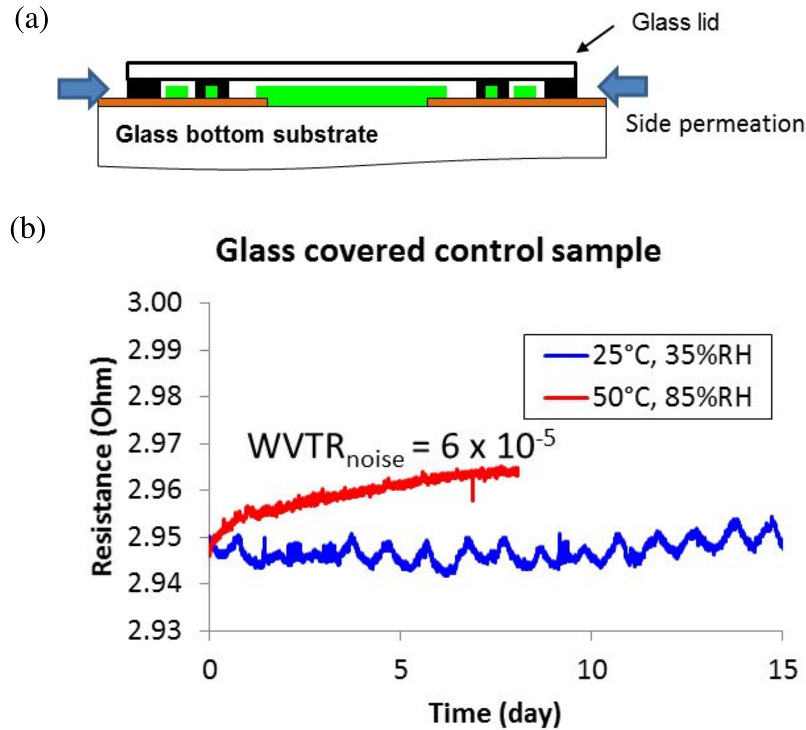

Figure 6.22. Minimum WVTR resolution test using a glass coverted control samples. (a) Schematic of the control samples covered with a glass lid, and (b) measured resistance of calcium sensor over time at two envrionmental conditions: room temperature in a lab, and 50°C/85%RH in a humidity chamber. A WVTR = 6x 10^{-5} g/m^2/day was observed due to the side permeation.

Using the improved calcium test sensor, the WVTR of three types of ALD barrier films were measured. Al_2O_3, ZnO, and nanolaminate of Al_2O_3/ZnO barrier films are fabricated on 125 μm thick polyethylene terephthalate (PET, MELINEX ST-505 DuPont Teijin) substrates using PEALD (Fiji, Cambridge Nanotech) at 100°C. The fabricated barrier films were applied on the calcium sensors, and the WVTR values were evaluated using the calcium test at 50°C/85%RH conditions in the humidity chamber. **Figure 6.23** (a) shows a cross-section SEM image of Al_2O_3/ZnO nanolaminate films on a Si substrate, and **Figure 6.23** (b) plots the conductance changes of calcium sensors for the three

barrier films. In results, the WVTR were estimated as 1.8×10^{-3} $g/m^2/day$, 9.3×10^{-3} $g/m^2/day$, and 9.3×10^{-4} $g/m^2/day$ for Al_2O_3, ZnO, and nanolaminate barrier films, respectively (**Table 6.1**). As reported in other ALD laminate barrier films,[47] the nanolaminate configuration showed the best barrier performance among the three barrier films.

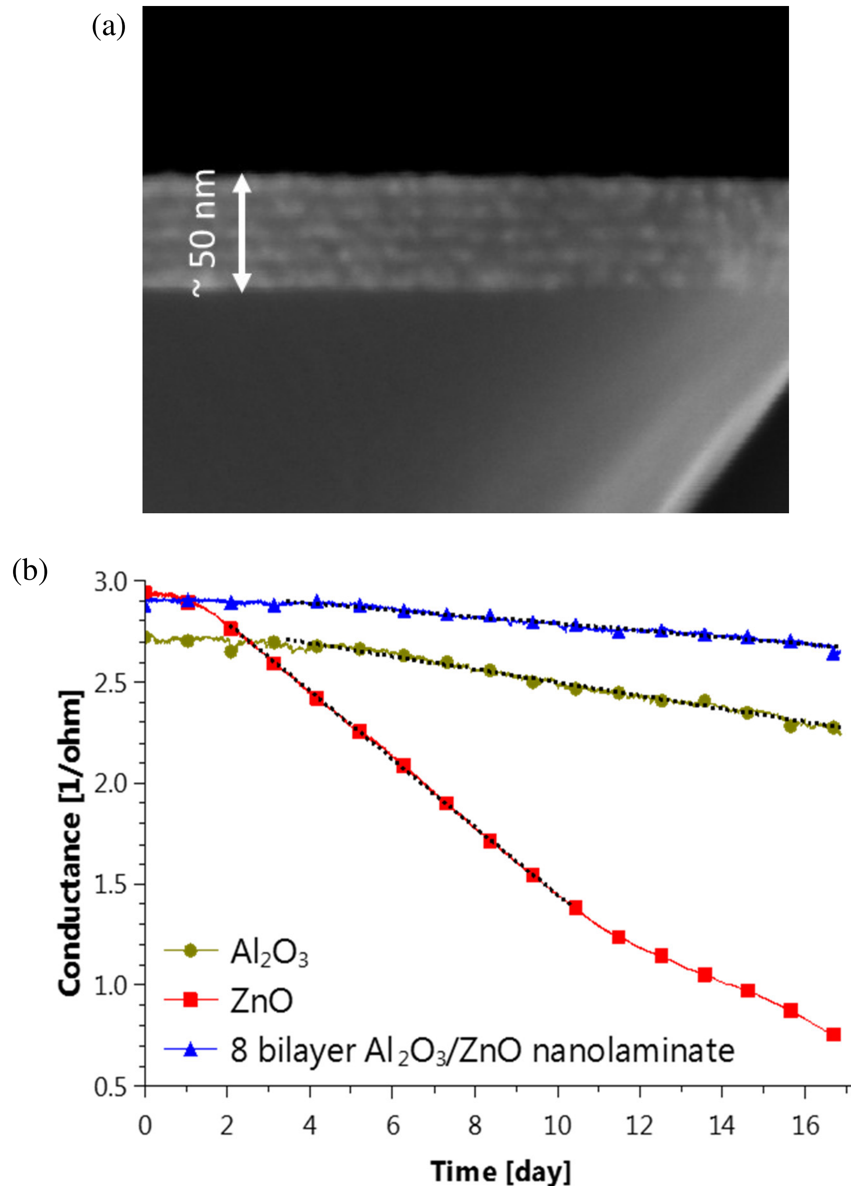

Figure 6.23 A) An SEM image of a nanolaminate Al_2O_3/ZnO barrier film and B) the conductance change of calcium sensors over time for an Al_2O_3, ZnO, and Al_2O_3/ZnO nanolaminate barriers.

Table 6.1 Measured effective WVTR of ALD barrier films prepared on PET substrates.

Sample	WVTR [$g/m^2/day$]
Al_2O_3 400 cycles (*ca.* 50 nm)	1.8×10^{-3}
ZnO 400 cycles (*ca.* 35 nm)	9.3×10^{-3}
8 bilayer Al_2O_3/ZnO nanolaminate (25 cycles for each layer, *ca.* 50 nm)	9.3×10^{-4}

6.3.3 Section summary

In this section, the electrical calcium corrosion test apparatus was redesigned in order to measure the WVTR of high performance barrier films for organic electronics, whose goal is below 1×10^{-6} $g/m^2/day$. The first advantage of the improved electrical calcium test setup is that the sensitivity of measurement was increased by accurate resistance measurement and increased barrier film and calcium sensor area ratio. The resistances of calcium sensors were measured by 4 point probing, which reduces parasite resistances due to wiring and contacts. Also, the ratio of permeation area of a barrier film to calcium sensor area increased from 1.6 to 7.4, increased the measurement sensitivity by 4.6 times. Secondly, side permeation issue was addressed by utilizing double side sealing and desiccant layer between the sealing. In addition, the moisture ingress through the side sealant is detectable with a boundary check line, enabling to determine seal failure.

Throughout the diverse design changes, the redesigned calcium test sensor showed that it can measure the WVTR in the range of 1×10^{-5} $g/m^2/day$ at room temperature. At elevated temperature 50°C/85%RH, the side permeation affected the measurement, and showed a limitation of the WVTR value of 6×10^{-5} $g/m^2/day$. While

this is in the range of ultrabarrier films, it is not as low as 1×10^{-6} g/m^2/day as desired by some testing. This can be done by incorporating some of our advancements with the larger sample area/Ca sensor area ratio shown by the group from the National Renewable Energy Laboratory as seen in **Figure 6.2.**

Since the electrical measurement can be done automatically *in situ* in a humidity chamber as well as accommodates multiple samples, the improved calcium test is anticipated to be a good measurement technique to determine the effective WVTR of high performance barrier films. However, the encapsulation work with side sealants requires careful handling in order to fabricate proper testing samples without damaging the barrier films. Thus, the calcium fabrication procedure needs further improvements to prepare samples with less failure.

6.4 Conclusion

This chapter addressed two types of WVTR measurement techniques. One technique is an optical calcium corrosion test to investigate the intrinsic and defect-assisted permeation separately. The other technique is an electrical calcium corrosion test to measure the extremely low WVTR values sensitively and continuously during an environmental testing.

From the study of the calcium corrosion test, the contribution of defect-driven permeation and the intrinsic permeation on the effective WVTR were evaluated separately. Also, the permeation rate in the defect-driven was found to be consistent over the time in the tested hybrid barrier film. These level of knowledge on the different contributions from intrinsic permeation and defect permeation will enable better

engineering of advanced ultrabarriers, placing the focus more on defect mitigation during manufacturing while improving the intrinsic quality of the barrier.

In addition, the effective WVTR was measurable in the range of OLED barrier film requirement ($<=10^{-5}$ g/m^2/day) using the improved electrical calcium test. The electrical calcium test is beneficial when multiple samples need to be tested continuously and simultaneously at controllable environmental conditions, and thus it can be utilized for the test of high performance barrier films in the future.

CHAPTER 7

CONCLUSION

7.1 Summary and Conclusion

The research in this dissertation has been conducted to investigate various aspects of ultrathin ALD films properties for the application of OPV device reliability. Since OPV devices are highly susceptible to degradation from environmental exposure to UV, heat, and water vapor or oxygen because of their intrinsic chemical reactivity, resolving the issue of the chemical reliability of OPV devices is a primary challenge for long term performance and the adoption of these devices. The issue can be mitigated by the use of intrinsically stable materials and by the use of barrier encapsulation that prevent the ingress water vapor or oxygen, which are deleterious to the performance of these devices. As a research contribution, this dissertation proposed the use of ALD grown thin films, which can produce high quality materials with excellent control over thickness in order to address two key weaknesses of OPV devices. These were namely the replacement of ZnO as an electron selective contact and the use of moisture stable ALD layers as barrier films. However, to utilize ALD films as barrier films to OPV devices, an investigation of chemical stability, electrical properties, and gas barrier properties of thin ALD films was necessary, as well as the development of characterization methods for these properties. Therefore, this dissertation made original contributions by addressing the following major questions regarding the application of ALD films to OPV devices,

- What ALD films are stable in the presence of moisture that can cause rapid degradation of OPV devices? What procedure is available to investigate ALD

stability, without using complex thin film characterization techniques that may require vacuum conditions or may be destructive?

- Using ALD, is it possible to create an electron selective layer (ESL) usable to modify ITO while providing similar performance as ZnO, one of the most popular ESL contact materials used today? If so, what is this material, its properties, and how does it perform in OPV devices?
- In the fabrication of high performance of barrier films using ALD, how can we better perform the measurements of water vapor transmission rate, and how do we resolve issues of localized defects that exist in the barrier films?

To answer the above questions, various aspects of ALD film properties have been investigated thought out the dissertation. Important contributions from this work are:

- Chapter 3 introduced a non-invasive stability testing procedure that can be performed at atmospheric pressure using a ZnO PL emission sensor method to screen ALD films for stability in water environments. Thin ALD Al_2O_3 used to cap ZnO sensors were found to be unstable when exposed to water whereas ALD TiO_x, ZrO_x, and HfO_x capping layers performed well for up to 10 days in water. However, the method was found to be best as a qualitative measurement method and not quantitative. Good correspondence between the degradation of PL signal and other surface science methods indicated the ability of the PL method to tell when a film had completely degraded. Thus, the PL method provides a faster and reliable way of determining large degradation in the ALD materials while finer details of the material

degradation will require other forms of materials characterization such as ellipsometry, XPS, SEM, or TEM.

- Chapter 4 investigated various electrical properties of ultrathin TiO_x films with a target to replace ZnO as an ESL in an inverted OPV. Energy band structure, chemical composition, conductivity, and crystallinity of 0.5, 1, 3, and 10 nm thick ALD TiO_x films grown at 250°C were analyzed. The results show that it is possible to make rectifying contacts even with 0.5 nm thick TiO_x films and that the performances of the films are highly dependent on the film thickness. While it was thought that very thin films were needed to compensate for the high resistance of the TiO_x, it was found that the performance of the films improved with increasing film thickness up to 3 nm and then degraded again once the films became thicker. The dip in performance as the film thickness increased above 3 nm was not due to the series resistance of the films as first hypothesized, but due to the reduced shunt resistance from the phase transformation of the TiO_x from amorphous to anatase. These results were unexpected, but show the use of TiO_x films has an optimal range of *ca.* 3 nm in film thickness when grown at 250°C, but most importantly, results show optimized film thickness relates directly to film structure and the quality of the surface coverage.
- Chapter 5 conducted barrier film fabrication using nanolaminate ALD metal oxides. For the mitigation of particles found on devices during the direct deposition of ALD films, smoothing layers can be used. However, a thick smoothing layer, which is best at covering particles, can lead to cracking in

the ALD film due stress concentrations around the particles and the increase in crack driving forces. Therefore, stress engineering is necessary to eliminate cracking in the directly deposited ALD barriers. Using a fracture mechanics approach, we were able to insert a compressively stressed SiN_x layer to compensate for the large tensile stresses in the ALD layer to reduce the magnitude of the stresses in the vicinity of the particles. In addition, the SiN_x layer acts to reduce crack driving forces. It was observed that ALD nanolaminate films made on 100 nm thick SiN_x layers did not show any cracking on perfluorinated polymer layers that were between 200 – 4300 nm thick. Without this layer, some level of cracking in the vicinity of the particles was observed in all ALD nanolaminates made on the polymers. Since particles are unavoidable in large-scale film fabrication procedures such as roll-to-roll process, the strategies used in this study to resolve the particle and stress issues will contribute to enable particle-tolerant barrier films in the presence of particles that can originate from processing facilities and substrates.

- Chapter 6 investigated the water vapor transmission rate (WVTR) of barrier films by calcium corrosion test. A new optical Ca corrosion test method was developed to determine for the first time the contribution of defect-assisted permeation and intrinsic permeation in barrier films. Such knowledge will allow for better focus in the development of new barriers, focusing on either defect mitigation or improving the intrinsic qualities of the films. In addition, an improved electrical Ca test method for the effective WVTR was developed.

The key to the new technique is the ability to account for and reduce side permeation, which can reduce the sensitivity of the method. In addition, improved electrical calcium corrosion test can continuously measure the effective WVTR *in situ* in an environmental chamber test.

Overall, it was found that ALD films have a great potential to impact these key areas of need for OPV, namely the production of more stable ESL contacts and the production of high quality barrier films. Due to the slow film growth rate of the ALD process, ALD films have not been preferred for manufacturing so far. However, recently introduced novel ALD processes, such as spatial ALD and atmospheric ALD, can reduce the cost and time for ALD film fabrication. In addition, as shown in this study, ALD requires film that are only a few nanometers thick to play their roles on device applications. Therefore, ALD has a great potential for manufacturing, and it can contribute to innovating or to tuning the properties of thin films independently or combined with conventional films for various applications. For this, the characterization of ultrathin ALD films is required, and this dissertation shows several aspects of ultrathin ALD films, including characterization methods and the results of the electrical and chemical properties of ultrathin films. While the results from this dissertation are in both the investigation of ALD films and the development of measurement methods to characterize them, continued efforts to explore them in actual device applications are warranted. To this end, recommendations and suggestions for future research are presented.

7.2 Recommendations for future work

7.2.1 Stability of a TiO_x OPV device and barrier performance of ESL

Chapters 3 and 4 investigated the chemical stability and electrical properties of ultrathin TiO_x films for the use of an ESL layer in inverted OPV. However, the lifetime study of OPVs with ALD TiO_x has not been conducted. To this point, TiO_x layers have shown themselves to be more stable and have shown that layers around 3 nm are optimal for devices. However, a full study showing the lifetime study of OPV devices using ZnO versus TiO_x is warranted.

Since ALD films have low defects and conformally coat surfaces, the use of ALD TiO_x ESL on top ITO cathode electrodes may act to serve as an integrated barrier film and electron selective contact for organic photovoltaics as shown in **Figure 7.1**.[62, 63] At present, ITO coated polymer substrates and barrier film coated polymer substrates are produced independently, but have never been integrated together. Thus, the use of TiO_x ESL may reduce the gas permeation from ITO coated polymer films for flexible devices without an additional barrier layer, and help improve device stability. Therefore, it is recommended to investigate the gas permeation properties of ITO/TiO_x stacks on a polymer substrate.

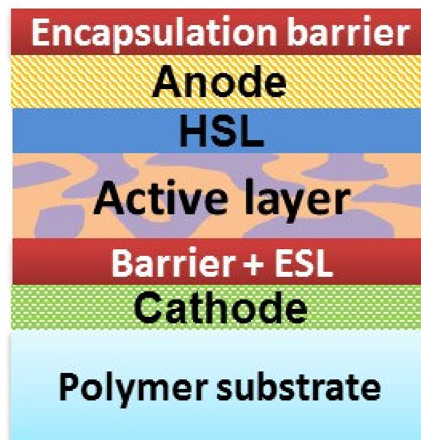

Figure 7.1 Suggested integrated barrier/ESL in an inverted OPV device fabricated on polymer substrate.

7.2.2 Ag NW TiO_x electrode for flexible electrode

One of the advantages of organic electronics is its potential to fabricate flexible devices. However, in the current structure, the bottom ITO electrode is brittle, and cannot provide the flexibility of the devices. As a flexible electrode, silver nanowire (Ag NW) is of interest due to its transparency, large scale processability, and mechanical reliability under strain.[234] However, silver is a high work function material, and thus needs an ESL to collect electrons in an inverted OPV. In the same manner as shown in chapter 4, the investigation of ALD TiO_x coatings on Ag NW for the application of stable and flexible electrical contacts for OPV devices is recommended.

7.2.3 Indirect encapsulation of complete devices using barrier films and adhesive

Chapter 5 and 6 have investigated structural issues of gas barrier film fabrication, and introduced improved calcium corrosion tests to evaluate the barrier films. However,

the effects of barrier films on complete devices have not been shown. Recently, sensitive photovoltaic devices were provided from the research group of Professor Michael McGehee at Stanford University, and the preliminary device lifetime test was carried out with a barrier film encapsulation. The devices are perovskite solar cells, which is an inorganic/organic hybrid solar cell.

Perovskite solar cell is an emerging solar cell device with much higher efficiency (*ca.* 18%) than OPV devices.[235-237] However, it also suffers environmental reliability issues due to the instability of the perovskite active layer, $CH_3NH_3PbI_3$, to moisture.[238] In a dry argon environment, 500 h device stability have been reported,[239] but the devices are unstable in atmospheric conditions, in particularly under light illumination.[237] Therefore, the environmental stability of encapsulated perovskite solar cells should be investigated that are packaged ALD barrier films. Since the process compatibility of perovskite solar cells with vacuum deposition processes were not identified, indirect encapsulation were used in preliminary testing to package the devices.

For indirect encapsulation, barrier films are fabricated on separate polymer substrates. PECVD/ALD hybrid barrier films were used in this research. As a substrate for the barrier film, 125 μm thick polyethylene naphthalate (PEN, Q65HA, Dupont) substrates were used. The PEN substrates came with protection liners on both sides and the top face was treated to create an ultra-smooth surface, which minimized the issue of particle defects. Instead of the Oxford PECVD system, a Unaxis PECVD system was used to fabricate SiN_x layers because the films qualities of Unaxis PECVD films were proven better than Oxford PECVD with less defects (**Figure 7.2** (a)). The PEN substrates with liners were precut using a laser (M-360, Universal Laser Systems) into 14 mm x 50

mm strips, and the precut PEN was mounted on a glass supporting substrate (50 mm x 75 mm) using Kapton tape as seen **Figure 7.2** (b) after peeling off the bottom liner. Following the removal of the top liner, 250 nm thick SiN_x layer was deposited using the Unaxis PECVD system at 110°C. The detail parameters for PECVD process are tabulated in **Table 7.1**.

Afterwards, ALD nanolaminate of Al_2O_3/HfO_x layer was deposited using the PEALD system (Fiji, Cambridge Nanotech) at 100°C. The ALD nanolaminate layer consists of 20 bilayers of 2 Al_2O_3 cycles and 5 HfO_x cycles. The deposition parameters for each material cycle are tabulated in **Table 3.2**. The prepared barrier films were then transferred into a N_2 glove box (MBraun), and stored for at least 3 days for complete drying. All of the procedures were carried out in a glove box to avoid any moisture exposure of barrier films and devices.

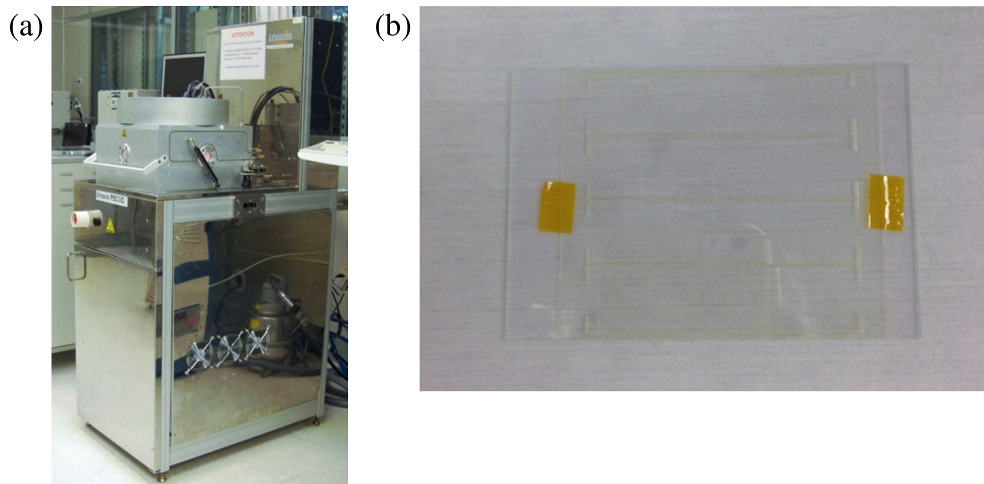

Figure 7.2 (a) Unaxis PECVD system used to deposit SiN_x films at low temperature, 110°C. (b) Hybrid (PECVD/PEALD) barrier films prepared on PEN substrates with 50 mm x 75 mm a glass supporting substrate.

Table 7.1 Summary of PECVD deposition conditions for SiN_x film fabrication.

Parameter	Value
Temperature (°C)	110
Chamber pressure (mTorr)	900
RF power (W)	30
SiH_4 flow rate (sccm)	200
NH_3 flow rate (sccm)	14
He flow rate (sccm)	560
N_2 flow rate (sccm)	720

The fabricated barrier films were then applied on devices using transparent UV-curable barrier tape (Tesa 61500, Tesa Tape, Inc.). The adhesive tape is developed for barrier encapsulation and can be laminated to seal devices with barrier films. As seen in **Figure 7.3**, first, the adhesive tape was laminated on the prepared barrier strips after removing a front transparent liner in a N_2-filled glove box. Then, a metal back liner was peeled off, and UV light was exposed on the adhesive/barrier strips for 45 s using the UV flood system (ELC-4001, Electro-Lite), which initiates slow curing of adhesive tapes.

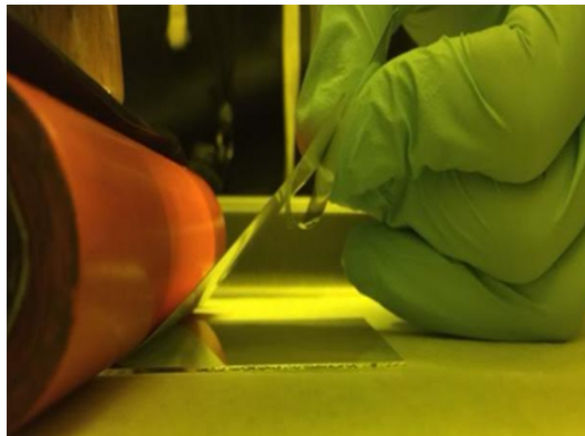

Figure 7.3 Adhesive lamination procedures on barrier films using a soft rubber roller.

To encapsulate devices, the prepared adhesive/barrier strips were cut into individual pieces along the precut lines using a razor blade. Then, each strip was laminated onto devices in the same manner using a soft rubber roller, and excessive parts of the strip were cut using scissors. **Figure 7.5** illustrates the overall processors of the indirect encapsulation.

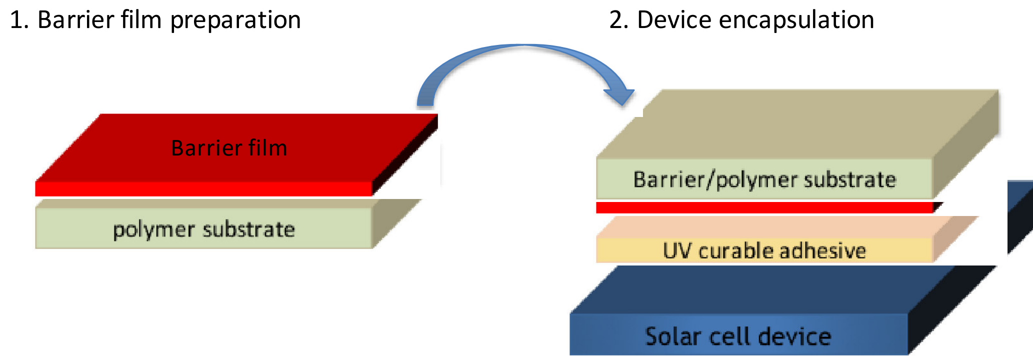

Figure 7.4 Indirect encapsulation of devices using a separate barrier film. A barrier film is prepared on a separate substrate and applied on a solar cell device.

The environmental reliability of devices was tested by periodically measuring photovoltaic performance of the devices after the exposure to the environmental conditions (**Figure 7.5**). Current density–voltage (*J*–*V*) characteristics were measured inside a N_2-filled glove box by using a source meter (2400, Keithley Instruments) controlled by a LabVIEW program. To test the solar cell properties under illumination, a 300 W xenon lamp (6258, Newport) with an air mass (AM) 1.5 filter and an irradiance of 100 mW/cm^2 was used as the light source. The *J*-*V* measurement was carried out in collaboration with the research group of Professor Bernard Kippelen at the Georgia Institute of Technology.

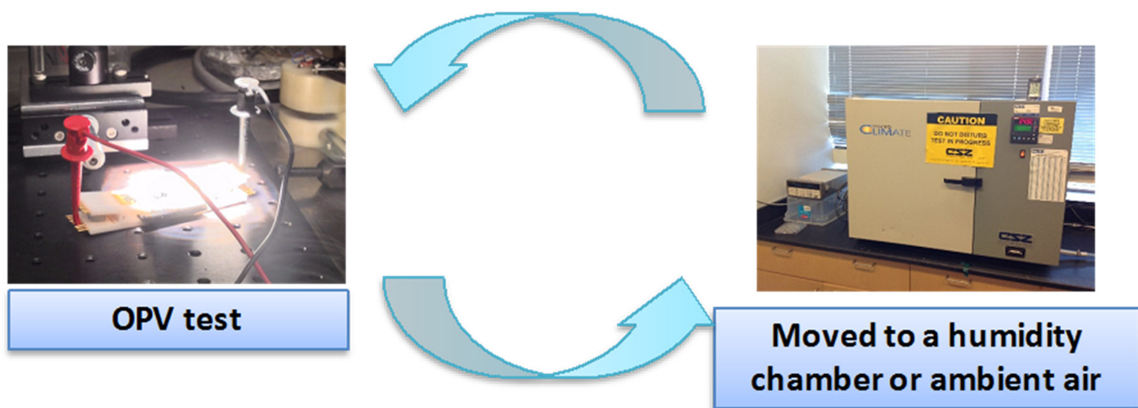

Figure 7.5 Photovoltaic lifetime test at controlled environmental conditions 60°C/90%RH. The measurements are repeated after exposing devices to environmental conditions.

Since the environmental stability of these cells were not studied yet, the test was started in dark and mild conditions, 20°C/30%RH, in the lab. Since the degradation of perovskite cells is related to a photo-oxidation process,[237] the cells were moved to ambient light near the windows of the lab, 25°C/50%RH, after 9 days. The *J*-*V* curves of the devices were measured periodically in the same manner under the 1.5 AM light conditions using a solar simulator. **Figure 7.6** (a) shows the devices exposed to the laboratory environment with ambient light, and **Figure 7.6** (b) shows the photo images of the devices before and after the test. The perovskite layer color was obviously changed from dark purple to light yellow. In contrast, the color of the packaged area in the perovskite cells remained purple for about a month. The color change suggests chemical changes in the perovskite layer, and it may be suppressed by protecting the layer from moisture.

Figure 7.7 plots the measured PCEs of the perovskite cells. The PCEs of perovskite cells with barrier films were more than 10% for up to 36 days, whereas the

PCEs of cells without barrier films decreased to below 5% once they were exposed to ambient light. In conclusion, the photo-stability of perovskite solar cells to air and/or moisture was greatly improved by the indirect encapsulation of PECVD/ALD barrier films. While this work has shown some promise in terms of low temperature testing, additional testing under full continuous illumination by the McGehee group showed that the cells degraded. It is not clear if this was due to a reaction with the adhesive tape since the results are in contrast to what was shown at room temperature and ambient conditions. Thus, additional research is needed to determine the appropriate method to integrate these barrier films with perovskites. In addition, the devices lifetime testing can unveil new challenges in the packaging of such devices.

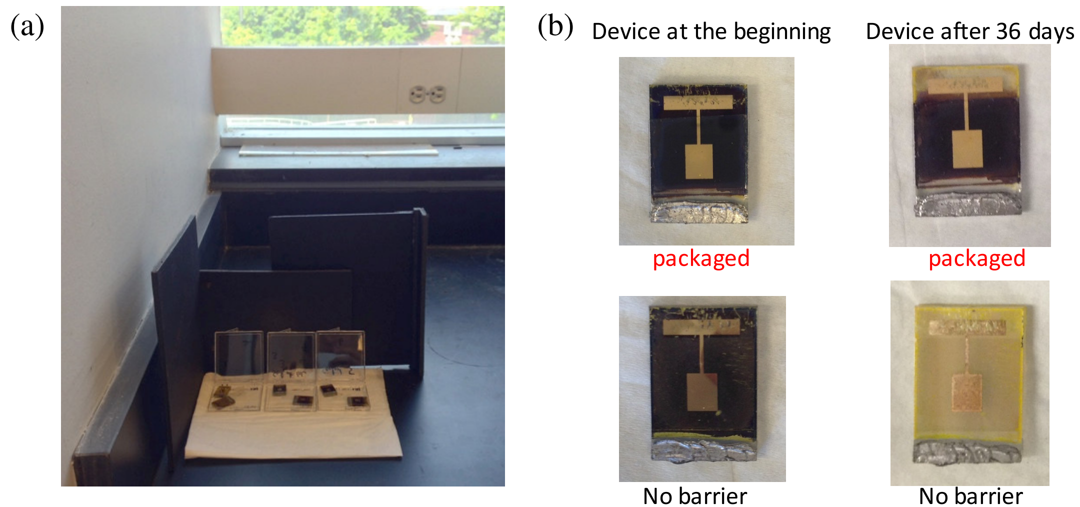

Figure 7.6 Environmental stability test of perovskite solar cells with and with barrier films at room temperature conditions. (a) Devices tested in the laboratory environments and (b) photo images of the devices before and after 36 h.

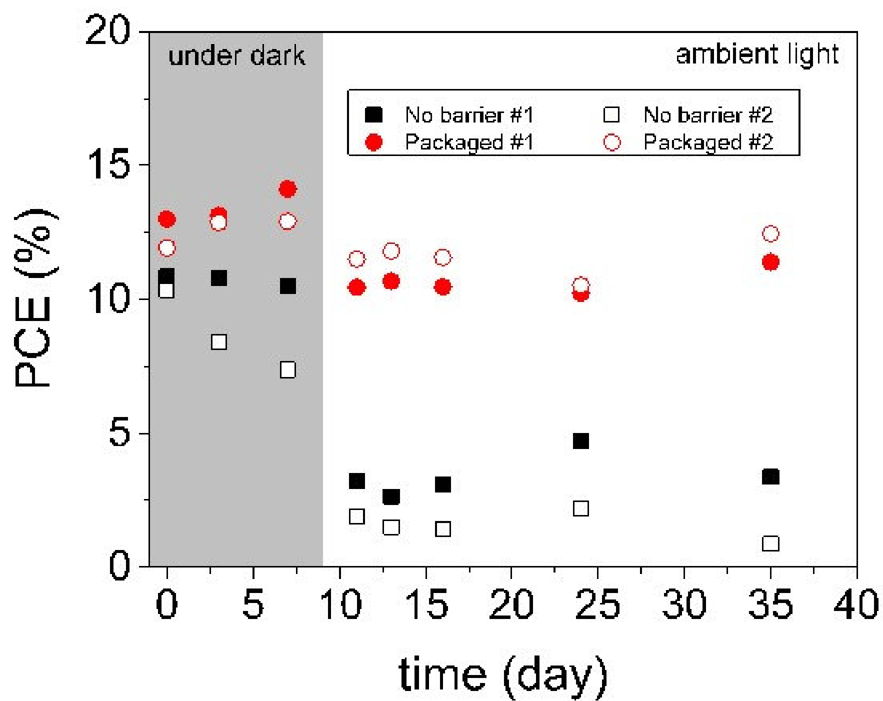

Figure 7.7 PCE vs. time of perovskite solar cells with (red) and without (black) barrier films tested in laboratory condition. The two packaged cells (red) operated with the PCE over 10% up to 35 days, where the two unpackaged cells (dark) degraded rapidly when they exposed to ambient light.

7.3 List of Publications

- D. Choi, **H. Kim**, N. Persson, S. Graham, E. Reichmanis, "Stretchable P3HT seimconductor layer" manuscript in preparation

- D. Moerman, **H. Kim**, S. Graham, D. Ginger, "Transient Photovoltage and Charge Extraction Study on Ultrathin ALD TiO_x Electode Modification Contact," manuscript in preparation

- **H. Kim**, A. Singh, S. Graham, "Investigation of Hydrolytic Stability of ALD Metal Oxides and Their Degradation Mechanism.", manuscript in preparation

- **H. Kim**, A. Singh, C.-Y. Wang, C. Fuentes-Hernandez, B. Kippelen, S. Graham, "Experimental Investigation of Defect-Assisted and Intrinsic Water Vapor Permeation through Ultrabarrier Films," manuscript in preparation

- **H. Kim**, K.L. Ou, X. Wu, P.F. Ndione, J. Berry, N.R. Armstrong, S. Graham, "Investigation of Atomic-Layer-Deposited Ultrathin Titanium Oxides as Hole Blocking Layers at Electrical Contacts for Organic photovoltaics," J. mater. Chem. A, 3, p. 17332, 2015

- L. L. Kelly, D. A. Racke, P. Schulz, H. Li, P. Winget, **H. Kim**, P. Ndione, A. K. Sigdel, J.-L. Brédas, J. J. Berry, S. Graham, and O. L. A. Monti, "Spectroscopy and Control of Near-Surface Defects in Conductive Thin Film ZnO", manuscript submitted for publication.

- A. Bulusu, A. Singh, C.-Y. Wang, A. Dindar, C. F. Hernandez, **H. Kim**, D. Cullen, B. Kippelen, Samuel Graham, "The Role of Architecture in the Direct Encapsulation of Organic Electronics Using Atomic Layer Deposited Barrier Films," manuscript accepted in J. Appl. Phys.

- D.A. Racke, L.L. Kelly, **H. Kim**, P. Schulz, A. Sigdel, J.J. Berry, S. Graham, D. Nordlund, O.L.A. Monti, "Disrupted Attosecond Charge Carrier Delocalization at a Hybrid Organic/Inorganic Semiconductor Interface," J. Phys. Chem. Lett., 6, p. 1935, 2015

- B.A. MacLeod, B.J. Tremolet de Villers, P. Schulz, P.F. Ndione, **H. Kim**, A.J. Giordano, K. Zhu, S.R. Marder, S. Graham, J.J. Berry, A. Kahn, D.C. Olson, "Stability of inverted organic photovoltaics with ZnO contact layers deposited from sol-gel precursors," Energy & Environ. Sci., 8, p. 592, Dec. 2014

- P. Schulz, L.L. Kelly, P.D. Winget, H. Li, **H. Kim**, P.F. Ndione, A.K. Sigdel, J.J. Berry, S. Graham, J.-L. Bredas, A. Kahn and O.L.A. Monti, "Tailoring Electron-Transfer Barriers for Zinc Oxide / C60 Fullerene Interfaces," Adv. Func. Mater., 24 (46), p. 7381, 2014

- P. Winget, L. K. Schirra, D. Cornil, H. Li, V. Coropceanu, P. F. Ndione, A. K. Sigdel, D. S. Ginley, J. J. Berry, J. Shim, **H. Kim**, B. Kippelen, J.-L. Brédas, and O. L. A. Monti, "Defect-driven interfacial electronic structures at an organic/metal-oxide semiconductor heterojunction," Adv. Mater., 26 (27), p. 4711, 2014.

- D. K. Hwang, C. Fuentes-Hernandez, M. Fenoll, M. Yun, J. Park, J. W. Shim, K. a Knauer, A. Dindar, **H. Kim**, Y. Kim, J. Kim, H. Cheun, M. M. Payne, S. Graham, S. Im, J. E. Anthony, and B. Kippelen, "Systematic reliability study of top-gate p- and n-channel organic field-effect transistors," ACS Appl. Mater. Interfaces, 6 (5), p. 3378, 2014.

- Bulusu, **H. Kim**, D. Samet, and S. Graham, "Improving the stability of atomic layer deposited alumina films in aqueous environments with metal oxide capping layers," J. Phys. D. Appl. Phys., 46 (8), p. 084014, 2013.

- Y. Kim, **H. Kim**, S. Graham, A. Dyer, and J. R. Reynolds, "Durable polyisobutylene edge sealants for organic electronics and electrochemical devices," Sol. Energy Mater. Sol. Cells, 100, p. 120, 2012.

- Y. Kim, N. Kim, **H. Kim**, and S. Graham, "The development of thin film barriers for encapsulating organic electronics," in 2011 IEEE 61st Electronic Components and Technology Conference (ECTC), 2011, p. 2101

REFERENCES

[1] C. W. Tang, "Two-layer organic photovoltaic cell," *Applied Physics Letters,* vol. 48, p. 183, 1986.

[2] C. W. Tang and S. A. VanSlyke, "Organic electroluminescent diodes," *Applied Physics Letters,* vol. 51, p. 913, 1987.

[3] J. M. Shaw and P. F. Seidler, "Organic electronics: Introduction," *IBM Journal of Research and Development,* vol. 45, pp. 3-9, 2001.

[4] H. E. Katz and J. Huang, "Thin-Film Organic Electronic Devices," *Annual Review of Materials Research,* vol. 39, pp. 71-92, 2009.

[5] S. Forrest, P. Burrows, and M. Thompson, "The dawn of organic electronics," *IEEE Spectrum,* vol. 37, pp. 29-34, 2000.

[6] M. C. Choi, Y. Kim, and C. S. Ha, "Polymers for flexible displays: From material selection to device applications," *Progress in Polymer Science,* vol. 33, pp. 581-630, 2008.

[7] F. C. Krebs, "Fabrication and processing of polymer solar cells: A review of printing and coating techniques," *Solar Energy Materials and Solar Cells,* vol. 93, pp. 394-412, 2009.

[8] G. J. Jorgensen, K. M. Terwilliger, J. A. DelCueto, S. H. Glick, M. D. Kempe, J. W. Pankow, F. J. Pern, and T. J. McMahon, "Moisture transport, adhesion, and corrosion protection of PV module packaging materials," *Solar Energy Materials and Solar Cells,* vol. 90, pp. 2739-2775, 2006.

[9] M. Jørgensen, K. Norrman, and F. C. Krebs, "Stability/degradation of polymer solar cells," *Solar Energy Materials and Solar Cells,* vol. 92, pp. 686-714, 2008.

[10] M. V. Madsen, K. Norrman, and F. C. Krebs, "Oxygen- and water-induced degradation of an inverted polymer solar cell: the barrier effect," *Journal of Photonics for Energy,* vol. 1, p. 011104, 2011.

[11] A. Seemann, H. J. Egelhaaf, C. J. Brabec, and J. A. Hauch, "Influence of oxygen on semi-transparent organic solar cells with gas permeable electrodes," *Organic Electronics,* vol. 10, pp. 1424-1428, 2009.

[12] H.-L. Yip and A. K. Y. Jen, "Recent advances in solution-processed interfacial materials for efficient and stable polymer solar cells," *Energy & Environmental Science,* vol. 5, pp. 5994-6011, 2012.

[13] S. Lattante, "Electron and Hole Transport Layers: Their Use in Inverted Bulk Heterojunction Polymer Solar Cells," *Electronics,* vol. 3, pp. 132-164, 2014.

[14] S. Gunes, H. Neugebauer, and N. S. Sariciftci, "Conjugated polymer-based organic solar cells," *Chem Rev,* vol. 107, pp. 1324-38, 2007.

[15] P. J. Hotchkiss, S. C. Jones, S. A. Paniagua, A. Sharma, B. Kippelen, N. R. Armstrong, and S. R. Marder, "The Modification of Indium Tin Oxide with Phosphonic Acids: Mechanism of Binding, Tuning of Surface Properties, and Potential for Use in Organic Electronic Applications," *Accounts of Chemical Research,* vol. 45, pp. 337-346, 2011.

[16] Y. Zhou, J. W. Shim, C. Fuentes-Hernandez, A. Sharma, K. A. Knauer, A. J. Giordano, S. R. Marder, and B. Kippelen, "Direct correlation between work function of indium-tin-oxide electrodes and solar cell performance influenced by ultraviolet irradiation and air exposure," *Physical Chemistry Chemical Physics,* vol. 14, pp. 12014-12021, 2012.

[17] A. K. K. Kyaw, D. H. Wang, V. Gupta, J. Zhang, S. Chand, G. C. Bazan, and A. J. Heeger, "Efficient Solution-Processed Small-Molecule Solar Cells with Inverted Structure," *Advanced Materials,* vol. 25, pp. 2397-2402, 2013.

[18] T. H. Lee, H. Choi, B. Walker, T. Kim, H.-B. Kim, and J. Y. Kim, "Replacing the metal oxide layer with a polymer surface modifier for high-performance inverted polymer solar cells," *RSC Advances,* vol. 4, pp. 4791-4795, 2014.

[19] Y. Zhou, C. Fuentes-Hernandez, J. Shim, J. Meyer, A. J. Giordano, H. Li, P. Winget, T. Papadopoulos, H. Cheun, J. Kim, M. Fenoll, A. Dindar, W. Haske, E. Najafabadi, T. M. Khan, H. Sojoudi, S. Barlow, S. Graham, J.-L. Brédas, S. R. Marder, A. Kahn, and B. Kippelen, "A universal method to produce low-work function electrodes for organic electronics," *Science (New York, N.Y.),* vol. 336, pp. 327-32, 2012.

[20] M. S. White, D. C. Olson, S. E. Shaheen, N. Kopidakis, and D. S. Ginley, "Inverted bulk-heterojunction organic photovoltaic device using a solution-derived ZnO underlayer," *Applied Physics Letters,* vol. 89, 2006.

[21] H. Cheun, C. Fuentes-Hernandez, Y. Zhou, W. J. Potscavage, S.-J. Kim, J. Shim, A. Dindar, and B. Kippelen, "Electrical and Optical Properties of ZnO Processed by Atomic Layer Deposition in Inverted Polymer Solar Cells," *The Journal of Physical Chemistry C,* vol. 114, pp. 20713-20718, 2010.

[22] S. R. Cowan, P. Schulz, A. J. Giordano, A. Garcia, B. A. MacLeod, S. R. Marder, A. Kahn, D. S. Ginley, E. L. Ratcliff, and D. C. Olson, "Chemically Controlled Reversible and Irreversible Extraction Barriers Via Stable Interface Modification of Zinc Oxide Electron Collection Layer in Polycarbazole-based Organic Solar Cells," *Advanced Functional Materials,* vol. 24, pp. 4671-4680, 2014.

[23] Z. He, C. Zhong, S. Su, M. Xu, H. Wu, and Y. Cao, "Enhanced power-conversion efficiency in polymer solar cells using an inverted device structure," *Nat Photon,* vol. 6, pp. 591-595, 2012.

[24] N. Zhou, X. Guo, R. P. Ortiz, S. Li, S. Zhang, R. P. Chang, A. Facchetti, and T. J. Marks, "Bithiophene imide and benzodithiophene copolymers for efficient inverted polymer solar cells," *Advanced Materials,* vol. 24, pp. 2242-2248, 2012.

[25] H.-J. Park, K.-H. Lee, B. Kumar, K.-S. Shin, S.-W. Jeong, and S.-W. Kim, "Inverted Organic Solar Cells with ZnO Thin Films Prepared by Sol–Gel Method," *Journal of Nanoelectronics and Optoelectronics,* vol. 5, pp. 135-138, 2010.

[26] H. Cheun, C. Fuentes-Hernandez, J. Shim, Y. Fang, Y. Cai, H. Li, A. K. Sigdel, J. Meyer, J. Maibach, A. Dindar, Y. Zhou, J. J. Berry, J.-L. Bredas, A. Kahn, K. H. Sandhage, and B. Kippelen, "Oriented Growth of Al_2O_3:ZnO Nanolaminates for Use as Electron-Selective Electrodes in Inverted Polymer Solar Cells," *Advanced Functional Materials,* vol. 22, pp. 1531-1538, 2012.

[27] J.-C. Wang, W.-T. Weng, M.-Y. Tsai, M.-K. Lee, S.-F. Horng, T.-P. Perng, C.-C. Kei, C.-C. Yu, and H.-F. Meng, "Highly efficient flexible inverted organic solar cells using atomic layer deposited ZnO as electron selective layer," *Journal of Materials Chemistry,* vol. 20, p. 862, 2010.

[28] J. Zhou, N. S. Xu, and Z. L. Wang, "Dissolving behavior and stability of ZnO wires in biofluids: a study on biodegradability and biocompatibility of ZnO nanostructures," *Advanced Materials -Deerfield Beach then Weinheim-,* vol. 18, p. 2432, 2006.

[29] M.-h. Wang, K.-a. Hu, B.-y. Zhao, and N.-f. Zhang, "Degradation phenomena due to humidity in low voltage ZnO varistors," *Ceramics International,* vol. 33, pp. 151-154, 2007.

[30] E. Ando and M. Miyazaki, "Durability of doped zinc oxide/silver/doped zinc oxide low emissivity coatings in humid environment," *Thin Solid Films,* vol. 516, pp. 4574-4577, 2008.

[31] B. A. MacLeod, B. J. T. d. Villers, P. Schulz, P. F. Ndione, H. Kim, A. J. Giordano, K. Zhu, S. R. Marder, S. Graham, J. J. Berry, A. Kahn, and D. C. Olson, "Stability of inverted organic solar cells with ZnO contact layers deposited from sol-gel precursors," *Energy & Environmental Science,* vol. 8, pp. 592-601, 2015.

[32] K. Norrman, M. V. Madsen, S. A. Gevorgyan, and F. C. Krebs, "Degradation Patterns in Water and Oxygen of an Inverted Polymer Solar Cell," *Journal of the American Chemical Society,* vol. 132, pp. 16883-16892, 2010.

[33] S. A. Paniagua, P. J. Hotchkiss, S. C. Jones, S. R. Marder, A. Mudalige, F. S. Marrikar, J. E. Pemberton, and N. R. Armstrong, "Phosphonic acid modification of indium-tin oxide electrodes: Combined XPS/UPS/contact angle studies," *Journal of Physical Chemistry C,* vol. 112, pp. 7809-7817, 2008.

[34] S. Shaheen, "Inverted bulk-heterojunction plastic solar cells," *SPIE Newsroom,* 2007.

[35] D. H. Kim, M. Woodroof, K. Lee, and G. N. Parsons, "Atomic Layer Deposition of High Performance Ultrathin TiO_2 Blocking Layers for Dye-Sensitized Solar Cells," *Chemsuschem,* vol. 6, pp. 1014-1020, 2013.

[36] V. Baglio, M. Girolamo, V. Antonucci, and A. Aricò, "Influence of TiO_2 film thickness on the electrochemical behaviour of dye-sensitized solar cells," *Int. J. Electrochem. Sci,* vol. 6, pp. 3375-3384, 2011.

[37] S. M. George, "Atomic Layer Deposition: An Overview," *Chemical Reviews,* vol. 110, pp. 111-131, 2009.

[38] T. Suntola, "Atomic Layer Epitaxy," in *Handbook of Crystal Growth. 3: Thin Films and Epitaxy. - Part B: Growth Mechanisms and Dynamics*, D. T. J. Hurle, Ed., ed Amsterdam: Elsevier, 1994.

[39] R. L. Z. Hoye, K. P. Musselman, and J. L. MacManus-Driscoll, "Research Update: Doping ZnO and TiO_2 for solar cells," *Apl Materials,* vol. 1, 2013.

[40] A. K. Chandiran, M. Abdi-Jalebi, M. K. Nazeeruddin, and M. Grätzel, "Analysis of Electron Transfer Properties of ZnO and TiO_2 Photoanodes for Dye-Sensitized Solar Cells," *ACS Nano,* vol. 8, pp. 2261-2268, 2014.

[41] S. E. Potts, L. Schmalz, M. Fenker, B. Díaz, J. Światowska, V. Maurice, A. Seyeux, P. Marcus, G. Radnóczi, L. Tóth, and W. M. M. Kessels, "Ultra-Thin Aluminium Oxide Films Deposited by Plasma-Enhanced Atomic Layer Deposition for Corrosion Protection," *Journal of The Electrochemical Society,* vol. 158, pp. C132-C138, 2011.

[42] M. Leskelä and M. Ritala, "Atomic layer deposition (ALD): from precursors to thin film structures," *Thin Solid Films,* vol. 409, pp. 138-146, 2002.

[43] H. Behm, K. Kusters, K. Bahroun, H. Bahre, S. Steves, C. Hopmann, J. Winter, and P. Awakowicz, "Influence of Plasma Pre-treatment on Oxygen Barrier Properties of SiOx CVD-coatings on PET-films Containing Anti-block Particles," in *Polymer Processing Society 28th Annual Meeting*, Pattaya (Thailand), 2012.

[44] A. S. da Silva Sobrinho, G. Czeremuszkin, M. Latrèche, G. Dennler, and M. R. Wertheimer, "A study of defects in ultra-thin transparent coatings on polymers," *Surface and Coatings Technology,* vol. 116–119, pp. 1204-1210, 1999.

[45] R. Paetzold, A. Winnacker, D. Henseler, V. Cesari, and K. Heuser, "Permeation rate measurements by electrical analysis of calcium corrosion," *Review of Scientific Instruments,* vol. 74, pp. 5147-5150, 2003.

[46] A. Dameron, M. Reese, T. Moricone, and M. Kempe, "Methods for Measuring Moisture Ingress," in *Photovoltaic Module Reliability Workshop*, Denver, Colorado, USA, 2010.

[47] J. Meyer, P. Görrn, F. Bertram, S. Hamwi, T. Winkler, H.-H. Johannes, T. Weimann, P. Hinze, T. Riedl, and W. Kowalsky, "Al_2O_3/ZrO_2 Nanolaminates as Ultrahigh Gas-Diffusion Barriers-A Strategy for Reliable Encapsulation of Organic Electronics," *Advanced Materials,* vol. 21, pp. 1845-1849, 2009.

[48] V. Coropceanu, J. Cornil, D. A. da Silva Filho, Y. Olivier, R. Silbey, and J.-L. Brédas, "Charge Transport in Organic Semiconductors," *Chemical Reviews,* vol. 107, pp. 926-952, 2007.

[49] H. Shirakawa, E. J. Louis, A. G. MacDiarmid, C. K. Chiang, and A. J. Heeger, "Synthesis of electrically conducting organic polymers: halogen derivatives of polyacetylene, (CH)," *Journal of the Chemical Society, Chemical Communications,* pp. 578-580, 1977.

[50] K. M. Coakley and M. D. McGehee, "Conjugated Polymer Photovoltaic Cells," *Chemistry of Materials,* vol. 16, pp. 4533-4542, 2004.

[51] B. Kippelen and J. L. Bredas, "Organic photovoltaics," *Energy & Environmental Science,* vol. 2, pp. 251-261, 2009.

[52] D. Carsten and D. Vladimir, "Polymer–fullerene bulk heterojunction solar cells," *Reports on Progress in Physics,* vol. 73, p. 096401, 2010.

[53] J. Shim, "study of charge-collecting interlayers for single-junction and tandem organic solar cells study of charge-collecting interlayers for single-junction and tandem organic solar cells," Doctoral dissertation, Georgia Institute of Technology, 2014.

[54] M. T. Lloyd, D. C. Olson, P. Lu, E. Fang, D. L. Moore, M. S. White, M. O. Reese, D. S. Ginley, and J. W. P. Hsu, "Impact of contact evolution on the shelf life of organic solar cells," *Journal of Materials Chemistry,* vol. 19, pp. 7638-7642, 2009.

[55] M. Jorgensen, K. Norrman, S. A. Gevorgyan, T. Tromholt, B. Andreasen, and F. C. Krebs, "Stability of polymer solar cells," *Adv Mater,* vol. 24, pp. 580-612, 2012.

[56] M. Manceau, S. Chambon, A. Rivaton, J.-L. Gardette, S. Guillerez, and N. Lemaître, "Effects of long-term UV–visible light irradiation in the absence of

oxygen on P3HT and P3HT:PCBM blend," *Solar Energy Materials and Solar Cells,* vol. 94, pp. 1572-1577, 2010.

[57] J.-S. Park, H. Chae, H. K. Chung, and S. I. Lee, "Thin film encapsulation for flexible AM-OLED: a review," *Semiconductor Science and Technology,* vol. 26, p. 034001, 2011.

[58] N. Kim, W. J. Potscavage, B. Domercq, B. Kippelen, and S. Graham, "A hybrid encapsulation method for organic electronics," *Applied Physics Letters,* vol. 94, p. 163308, 2009.

[59] Y. Kim, H. Kim, S. Graham, A. Dyer, and J. R. Reynolds, "Durable polyisobutylene edge sealants for organic electronics and electrochemical devices," *Solar Energy Materials and Solar Cells,* vol. 100, pp. 120-125, 2012.

[60] J. Ahmad, K. Bazaka, L. J. Anderson, R. D. White, and M. V. Jacob, "Materials and methods for encapsulation of OPV: A review," *Renewable and Sustainable Energy Reviews,* vol. 27, pp. 104-117, 2013.

[61] D. K. Hwang, C. Fuentes-Hernandez, M. Fenoll, M. Yun, J. Park, J. W. Shim, K. A. Knauer, A. Dindar, H. Kim, Y. Kim, J. Kim, H. Cheun, M. M. Payne, S. Graham, S. Im, J. E. Anthony, and B. Kippelen, "Systematic Reliability Study of Top-Gate p- and n-Channel Organic Field-Effect Transistors," *ACS Applied Materials & Interfaces,* vol. 6, pp. 3378-3386, 2014.

[62] L. J. Simpson, A. Dameron, S. Christensen, T. Gennett, M. Reese, J. Berry, J. Perkins, and D. Ginley, "Novel transparent conducting barriers for photovoltaics," in *Photovoltaic Specialists Conference (PVSC), 2010 35th IEEE*, 2010, pp. 001052-001056.

[63] A. A. Dameron, D. C. Miller, N. George, B. To, D. S. Ginley, and L. Simpson, "Tensile strain and water vapor transport testing of flexible, conductive and transparent indium–zinc-oxide/silver/indium–zinc-oxide thin films," *Thin Solid Films,* vol. 519, pp. 3177-3184, 2011.

[64] J. S. Lewis and M. S. Weaver, "Thin-film permeation-barrier technology for flexible organic light-emitting devices," *Ieee Journal of Selected Topics in Quantum Electronics,* vol. 10, pp. 45-57, 2004.

[65] G. Dennler, C. Lungenschmied, H. Neugebauer, N. S. Sariciftci, M. Latreche, G. Czeremuszkin, and M. R. Wertheimer, "A new encapsulation solution for flexible organic solar cells," *Thin Solid Films,* vol. 511, pp. 349-353, 2006.

[66] D. M. Tanenbaum, M. Hermenau, E. Voroshazi, M. T. Lloyd, Y. Galagan, B. Zimmermann, M. Hosel, H. F. Dam, M. Jorgensen, S. A. Gevorgyan, S. Kudret, W. Maes, L. Lutsen, D. Vanderzande, U. Wurfel, R. Andriessen, R. Rosch, H. Hoppe, G. Teran-Escobar, M. Lira-Cantu, A. Rivaton, G. Y. Uzunoglu, D. Germack, B. Andreasen, M. V. Madsen, K. Norrman, and F. C. Krebs, "The

ISOS-3 inter-laboratory collaboration focused on the stability of a variety of organic photovoltaic devices," *RSC Advances,* vol. 2, pp. 882-893, 2012.

[67] M. O. Reese, A. J. Morfa, M. S. White, N. Kopidakis, S. E. Shaheen, G. Rumbles, and D. S. Ginley, "Pathways for the degradation of organic photovoltaic P3HT : PCBM based devices," *Solar Energy Materials and Solar Cells,* vol. 92, pp. 746-752, 2008.

[68] L. Ke, R. S. Kumar, S. J. Chua, and A. P. Burden, "Degradation study in flexible substrate organic light-emitting diodes," *Applied Physics a-Materials Science & Processing,* vol. 81, pp. 969-974, 2005.

[69] A. M. Nardes, M. Kemerink, M. De Kok, E. Vinken, K. Maturova, and R. Janssen, "Conductivity, work function, and environmental stability of PEDOT: PSS thin films treated with sorbitol," *Organic Electronics,* vol. 9, pp. 727-734, 2008.

[70] M. Schaer, F. Nüesch, D. Berner, W. Leo, and L. Zuppiroli, "Water Vapor and Oxygen Degradation Mechanisms in Organic Light Emitting Diodes," *Advanced Functional Materials,* vol. 11, pp. 116-121, 2001.

[71] J. McElvain, H. Antoniadis, M. R. Hueschen, J. N. Miller, D. M. Roitman, J. R. Sheats, and R. L. Moon, "Formation and growth of black spots in organic light-emitting diodes," *Journal of Applied Physics,* vol. 80, pp. 6002-6007, 1996.

[72] R. Steim, F. R. Kogler, and C. J. Brabec, "Interface materials for organic solar cells," *Journal of Materials Chemistry,* vol. 20, p. 2499, 2010.

[73] S. E. Shaheen, C. J. Brabec, N. S. Sariciftci, F. Padinger, T. Fromherz, and J. C. Hummelen, "2.5% Efficient Organic Plastic Solar Cells," *Applied Physics Letters,* vol. 78, p. 841, 2001.

[74] S. C. Price, A. C. Stuart, L. Yang, H. Zhou, and W. You, "Fluorine Substituted Conjugated Polymer of Medium Band Gap Yields 7% Efficiency in Polymer–Fullerene Solar Cells," *Journal of the American Chemical Society,* vol. 133, pp. 4625-4631, 2011.

[75] C. Waldauf, M. Morana, P. Denk, P. Schilinsky, K. Coakley, S. a. Choulis, and C. J. Brabec, "Highly efficient inverted organic photovoltaics using solution based titanium oxide as electron selective contact," *Applied Physics Letters,* vol. 89, pp. 233517-233517, 2006.

[76] A. K. K. Kyaw, X. W. Sun, C. Y. Jiang, G. Q. Lo, D. W. Zhao, and D. L. Kwong, "An inverted organic solar cell employing a sol-gel derived ZnO electron selective layer and thermal evaporated MoO_3 hole selective layer," *Applied Physics Letters,* vol. 93, p. 221107, 2008.

[77] T. Stubhan, M. Salinas, A. Ebel, F. C. Krebs, A. Hirsch, M. Halik, and C. J. Brabec, "Increasing the Fill Factor of Inverted P3HT:PCBM Solar Cells Through Surface Modification of Al-Doped ZnO via Phosphonic Acid-Anchored C60 SAMs," *Advanced Energy Materials,* vol. 2, pp. 532-535, 2012.

[78] Z. Hu, J. Zhang, Y. Liu, Z. Hao, X. Zhang, and Y. Zhao, "Influence of ZnO interlayer on the performance of inverted organic photovoltaic device," *Solar Energy Materials and Solar Cells,* vol. 95, pp. 2126-2130, 2011.

[79] S.-Y. Park, H. O. Seo, K.-D. Kim, J. E. Lee, J.-D. Kwon, Y. D. Kim, and D. C. Lim, "Organic photovoltaics with high stability sustained for 100 days without encapsulation fabricated using atomic layer deposition," *physica status solidi (RRL) - Rapid Research Letters,* vol. 6, pp. 196-198, 2012.

[80] G. Xiong, "Towards high performance inverted polymer solar cells through interfacial reengineering," in *Organic Photovoltaics XIV, 27-29 Aug. 2013*, USA, 2013, p. 88300G (16 pp.).

[81] K.-L. Ou, D. Tadytin, K. Xerxes Steirer, D. Placencia, M. Nguyen, P. Lee, N. R. Armstrong, and K. X. Steirer, "Titanium dioxide electron-selective interlayers created by chemical vapor deposition for inverted configuration organic solar cells," *Journal of Materials Chemistry A,* vol. 1, pp. 6794-6794, 2013.

[82] T. Kuwabara, T. Nakayama, K. Uozumi, T. Yamaguchi, and K. Takahashi, "Highly durable inverted-type organic solar cell using amorphous titanium oxide as electron collection electrode inserted between ITO and organic layer," *Solar Energy Materials and Solar Cells,* vol. 92, pp. 1476-1482, 2008.

[83] T. Kuwabara, H. Sugiyama, M. Kuzuba, T. Yamaguchi, and K. Takahashi, "Inverted bulk-heterojunction organic solar cell using chemical bath deposited titanium oxide as electron collection layer," *Organic Electronics,* vol. 11, pp. 1136-1140, 2010.

[84] I. Sasajima, S. Uesaka, T. Kuwabara, T. Yamaguchi, and K. Takahashi, "Flexible inverted polymer solar cells containing an amorphous titanium oxide electron collection electrode," *Organic Electronics,* vol. 12, pp. 113-118, 2011.

[85] C. Y. Chang and F. Y. Tsai, "Efficient and air-stable plastics-based polymer solar cells enabled by atomic layer deposition," *Journal of Materials Chemistry,* vol. 21, pp. 5710-5715, 2011.

[86] S. K. Hau, H.-L. Yip, N. S. Baek, J. Zou, K. O'Malley, and A. K.-Y. Jen, "Air-stable inverted flexible polymer solar cells using zinc oxide nanoparticles as an electron selective layer," *Applied Physics Letters,* vol. 92, p. 253301, 2008.

[87] J.-Y. Sun, W.-H. Tseng, S. Lan, S.-H. Lin, P.-C. Yang, C.-I. Wu, and C.-F. Lin, "Performance enhancement in inverted polymer photovoltaics with solution-

processed MoO_x and air-plasma treatment for anode modification," *Solar Energy Materials and Solar Cells,* vol. 109, pp. 178-184, 2013.

[88] A. Bulusu, H. Kim, D. Samet, and S. Graham, "Improving the stability of atomic layer deposited alumina films in aqueous environments with metal oxide capping layers," *Journal of Physics D: Applied Physics,* vol. 46, p. 084014, 2013.

[89] A. Klein, C. Korber, A. Wachau, F. Sauberlich, Y. Gassenbauer, S. P. Harvey, D. E. Proffit, and T. O. Mason, "Transparent Conducting Oxides for Photovoltaics: Manipulation of Fermi Level, Work Function and Energy Band Alignment," *Materials,* vol. 3, pp. 4892-4914, 2010.

[90] C. Trinh, J. R. Bakke, T. P. Brennan, S. F. Bent, F. Navarro, A. Bartynski, and M. E. Thompson, "Power losses in bilayer inverted small molecule organic solar cells," *Applied Physics Letters,* vol. 101, 2012.

[91] A. Wagenpfahl, D. Rauh, M. Binder, C. Deibel, and V. Dyakonov, "S-shaped current-voltage characteristics of organic solar devices," *Physical Review B,* vol. 82, p. 115306, 2010.

[92] M. Gruenewald, L. K. Schirra, P. Winget, M. Kozlik, P. F. Ndione, A. K. Sigdel, J. J. Berry, R. Forker, J.-L. Brédas, T. Fritz, and O. L. A. Monti, "Integer Charge Transfer and Hybridization at an Organic Semiconductor/Conductive Oxide Interface," *The Journal of Physical Chemistry C,* vol. 119, pp. 4865-4873, 2015.

[93] H. Li, L. K. Schirra, J. Shim, H. Cheun, B. Kippelen, O. L. A. Monti, and J. L. Bredas, "Zinc Oxide as a Model Transparent Conducting Oxide: A Theoretical and Experimental Study of the Impact of Hydroxylation, Vacancies, Interstitials, and Extrinsic Doping on the Electronic Properties of the Polar ZnO (0002) Surface," *Chemistry of Materials,* vol. 24, pp. 3044-3055, 2012.

[94] G. Li, C. Chu, V. Shrotriya, J. Huang, and Y. Yang, "Efficient inverted polymer solar cells," *Applied Physics Letters,* vol. 88, pp. 253503-253503, 2006.

[95] O. Wiranwetchayan, Z. Liang, Q. Zhang, G. Cao, and P. Singjai, "The role of oxide thin layer in inverted structure polymer solar cells," *Materials Sciences and Applications,* vol. 2, p. 1697, 2011.

[96] B. Ehrler, K. P. Musselman, M. L. Bohm, F. S. F. Morgenstern, Y. Vaynzof, B. J. Walker, J. L. MacManus-Driscoll, and N. C. Greenham, "Preventing Interfacial Recombination in Colloidal Quantum Dot Solar Cells by Doping the Metal Oxide," *Acs Nano,* vol. 7, pp. 4210-4220, 2013.

[97] P. E. Burrows, G. L. Graff, M. E. Gross, P. M. Martin, M. Hall, E. Mast, C. C. Bonham, W. D. Bennett, L. A. Michalski, M. S. Weaver, J. J. Brown, D. Fogarty, and L. S. Sapochak, "Gas Permeation and Lifetime Tests On Polymer-Based Barrier Coatings," in *SPIE*, 2001, pp. 75-83.

[98] E. L. Cussler, *Diffusion: mass transfer in fluid systems*: Cambridge university press, 2009.

[99] A. P. Roberts, B. M. Henry, A. P. Sutton, C. R. M. Grovenor, G. A. D. Briggs, T. Miyamoto, A. Kano, Y. Tsukahara, and M. Yanaka, "Gas permeation in silicon-oxide/polymer (SiO_x/PET) barrier films: role of the oxide lattice, nano-defects and macro-defects," *Journal of Membrane Science,* vol. 208, pp. 75-88, 2002.

[100] G. L. Graff, R. E. Williford, and P. E. Burrows, "Mechanisms of vapor permeation through multilayer barrier films: Lag time versus equilibrium permeation," *Journal of Applied Physics,* vol. 96, pp. 1840-1849, 2004.

[101] A. G. Erlat, R. J. Spontak, R. P. Clarke, T. C. Robinson, P. D. Haaland, Y. Tropsha, N. G. Harvey, and E. A. Vogler, "SiO_x gas barrier coatings on polymer substrates: Morphology and gas transport considerations," *Journal of Physical Chemistry B,* vol. 103, pp. 6047-6055, 1999.

[102] G. Dennler, C. Lungenschmied, H. Neugebauer, N. S. Sariciftci, and A. Labouret, "Flexible, conjugated polymer-fullerene-based bulk-heterojunction solar cells: Basics, encapsulation, and integration," *Journal of Materials Research,* vol. 20, pp. 3224-3233, 2005.

[103] N. Kim, "Fabrication and Characterization of Thin-film Encapsulation for Organic Electronics " Doctoral dissertation, Georgia Institute of Technology, 2009.

[104] J. Meyer, D. Schneidenbach, T. Winkler, S. Hamwi, T. Weimann, P. Hinze, S. Ammermann, H. H. Johannes, T. Riedl, and W. Kowalsky, "Reliable thin film encapsulation for organic light emitting diodes grown by low-temperature atomic layer deposition," *Applied Physics Letters,* vol. 94, p. 233305, 2009.

[105] G. Choudalakis and A. D. Gotsis, "Permeability of polymer/clay nanocomposites: A review," *European Polymer Journal,* vol. 45, pp. 967-984, 2009.

[106] J. Greener, K. C. Ng, K. M. Vaeth, and T. M. Smith, "Moisture permeability through multilayered barrier films as applied to flexible OLED display," *Journal of Applied Polymer Science,* vol. 106, pp. 3534-3542, 2007.

[107] A. da Silva Sobrinho, G. Czeremuszkin, M. Latreche, G. Dennler, and M. Wertheimer, "A study of defects in ultra-thin transparent coatings on polymers," *Surface and Coatings Technology,* vol. 116, pp. 1204-1210, 1999.

[108] D. J. Gaspar and E. Polikarpov, *OLED fundamentals : materials, devices, and processing of organic light-emitting diodes*. Boca Raton, FL: CRC Press, Taylor & Francis Group, 2015.

[109] M. Schaepkens, T. W. Kim, A. Gün Erlat, M. Yan, K. W. Flanagan, C. M. Heller, and P. A. McConnelee, "Ultrahigh barrier coating deposition on polycarbonate

substrates," *Journal of Vacuum Science & Technology A,* vol. 22, pp. 1716-1722, 2004.

[110] T. N. Chen, D. S. Wuu, C. C. Wu, C. C. Chiang, Y. P. Chen, and R. H. Horng, "Improvements of permeation barrier coatings using encapsulated parylene interlayers for flexible electronic applications," *Plasma Processes and Polymers,* vol. 4, pp. 180-185, 2007.

[111] L. Zambov, K. Weidner, V. Shamamian, R. Camilletti, U. Pernisz, M. Loboda, G. Cerny, D. Gidley, H.-G. Peng, and R. Vallery, "Advanced chemical vapor deposition silicon carbide barrier technology for ultralow permeability applications," *Journal of Vacuum Science & Technology A,* vol. 24, pp. 1706-1713, 2006.

[112] P. Mandlik, J. Gartside, L. Han, I. C. Cheng, S. Wagner, J. A. Silvernail, R. Q. Ma, M. Hack, and J. J. Brown, "A single-layer permeation barrier for organic light-emitting displays," *Applied Physics Letters,* vol. 92, p. 103309, 2008.

[113] F. J. H. Van Assche, R. T. Vangheluwe, J. W. C. Maes, W. S. Mischke, M. D. Bijker, F. C. Dings, M. F. J. Evers, W. M. M. Kessels, and M. C. M. Van de Sanden, "P-111: A Thin Film Encapsulation Stack for PLED and OLED Displays," *SID Symposium Digest of Technical Papers,* vol. 35, pp. 695-697, 2004.

[114] J. J. W. M. Rosink, H. Lifka, G. H. Rietjens, and A. Pierik, "34.1: Ultra-Thin Encapsulation for Large-Area OLED Displays," *SID Symposium Digest of Technical Papers,* vol. 36, pp. 1272-1275, 2005.

[115] P. F. Carcia, R. S. McLean, M. H. Reilly, M. D. Groner, and S. M. George, "Ca test of Al_2O_3 gas diffusion barriers grown by atomic layer deposition on polymers," *Applied Physics Letters,* vol. 89, p. 031915, 2006.

[116] M. Groner, S. George, R. McLean, and P. Carcia, "Gas diffusion barriers on polymers using Al_2O_3 atomic layer deposition," *Applied Physics Letters,* vol. 88, p. 051907, 2006.

[117] E. Langereis, M. Creatore, S. B. S. Heil, M. C. M. van de Sanden, and W. M. M. Kessels, "Plasma-assisted atomic layer deposition of Al_2O_3 moisture permeation barriers on polymers," *Applied Physics Letters,* vol. 89, p. 081915, 2006.

[118] J. Meyer, H. Schmidt, W. Kowalsky, T. Riedl, and A. Kahn, "The origin of low water vapor transmission rates through Al_2O_3/ZrO_2 nanolaminate gas-diffusion barriers grown by atomic layer deposition," *Applied Physics Letters,* vol. 96, p. 243308, 2010.

[119] A. A. Dameron, S. D. Davidson, B. B. Burton, P. F. Carcia, R. S. McLean, and S. M. George, "Gas diffusion barriers on polymers using multilayers fabricated by

Al_2O_3 and rapid SiO_2 atomic layer deposition," *Journal of Physical Chemistry C,* vol. 112, pp. 4573-4580, 2008.

[120] ASTM Standard E96, "Standard Test Methods for Water Vapor Transmission of Materials," ed: ASTM International, West Conshohoken, PA.

[121] ASTM Standard F1249, "Standard Test Method for Water Vapor Transmission Rate Through Plastic Film and Sheeting Using a Modulated Infrared Sensor," ed: ASTM International, West Conshohoken, PA.

[122] MOCON Inc., *Instruments: Permeation and Barrier Measurement*, Available: http://www.mocon.com/permeation.php, (Accessed 2015).

[123] A. Ranade, N. A. D'Souza, R. M. Wallace, and B. E. Gnade, "High sensitivity gas permeability measurement system for thin plastic films," *Review of Scientific Instruments,* vol. 76, p. 013902, 2005.

[124] P. F. Carcia, R. S. McLean, and M. H. Reilly, "Permeation measurements and modeling of highly defective Al_2O_3 thin films grown by atomic layer deposition on polymers," *Applied Physics Letters,* vol. 97, p. 221901, 2010.

[125] R. Dunkel, R. Bujas, A. Klein, and V. Horndt, "A new method for measuring ultra-low water-vapor permeation for OLED displays," *Journal of the Society for Information Display,* vol. 13, pp. 569-573, 2005.

[126] X. D. Zhang, J. S. Lewis, S. D. Wolter, C. B. Parker, and J. T. Glass, "High sensitivity permeation measurement system for "ultrabarrier" thin films," *Journal of Vacuum Science & Technology A: Vacuum, Surfaces, and Films,* vol. 25, p. 1587, 2007.

[127] G. Nisato, P. C. P. Bouten, P. J. Slikkerveer, W. Bennett, G. Graff, N. Rutherford, and L. Wiese, "Evaluating High Performance Diffusion Barriers: The Calcium Test," in *Proceedings Asia Display/IDW'01*, 2001, pp. 1435-1438.

[128] M. O. Reese, A. A. Dameron, and M. D. Kempe, "Quantitative calcium resistivity based method for accurate and scalable water vapor transmission rate measurement," *The Review of scientific instruments,* vol. 82, p. 085101, 2011.

[129] Y. Leterrier, "Durability of nanosized oxygen-barrier coatings on polymers," *Progress in Materials Science,* vol. 48, pp. 1-55, 2003.

[130] S.-H. Jen, J. A. Bertrand, and S. M. George, "Critical tensile and compressive strains for cracking of Al_2O_3 films grown by atomic layer deposition," *Journal of Applied Physics,* vol. 109, p. 084305, 2011.

[131] J. A. van Delft, D. Garcia-Alonso, and W. M. M. Kessels, "Atomic layer deposition for photovoltaics: applications and prospects for solar cell

manufacturing," *Semiconductor Science and Technology,* vol. 27, p. 074002, 2012.

[132] P. F. Carcia, R. S. McLean, Z. G. Li, M. H. Reilly, and W. J. Marshall, "Permeability and corrosion in ZrO_2/Al_2O_3 nanolaminate and Al_2O_3 thin films grown by atomic layer deposition on polymers," *Journal of Vacuum Science & Technology A: Vacuum, Surfaces, and Films,* vol. 30, p. 041515, 2012.

[133] A. I. Abdulagatov, Y. Yan, J. R. Cooper, Y. Zhang, Z. M. Gibbs, A. S. Cavanagh, R. G. Yang, Y. C. Lee, and S. M. George, "Al_2O_3 and TiO_2 atomic layer deposition on copper for water corrosion resistance," *ACS applied materials & interfaces,* vol. 3, pp. 4593-601, 2011.

[134] W. M. M. Kessels and M. Putkonen, "Advanced process technologies: Plasma, direct-write, atmospheric pressure, and roll-to-roll ALD," *MRS Bulletin,* vol. 36, pp. 907-913, 2011.

[135] M. Leskelä, M. Ritala, and O. Nilsen, "Novel materials by atomic layer deposition and molecular layer deposition," *MRS Bulletin,* vol. 36, pp. 877-884, 2011.

[136] A. W. Ott, K. C. McCarley, J. W. Klaus, J. D. Way, and S. M. George, "Atomic layer controlled deposition of Al_2O_3 films using binary reaction sequence chemistry," *Applied Surface Science,* vol. 107, pp. 128-136, 1996.

[137] H. B. Profijt, S. E. Potts, M. C. M. van de Sanden, and W. M. M. Kessels, "Plasma-Assisted Atomic Layer Deposition: Basics, Opportunities, and Challenges," *Journal of Vacuum Science & Technology A,* vol. 29, p. 050801, 2011.

[138] C. Detavernier, J. Dendooven, D. Deduytsche, and J. Musschoot, "Thermal versus plasma-enhanced ALD: growth kinetics and conformality," *Atomic Layer Deposition Applications 4,* vol. 16, pp. 239-246, 2008.

[139] Beneq Corp., *nSILVER® Anti-tarnish Coating*, Available: http://www.beneq.com/nsilver-anti-tarnish-coating.html, (Accessed 2015).

[140] S.-H. K. Park, C.-S. Hwang, H.-S. Kwack, J.-H. Lee, and H. Y. Chu, "Characteristics of ZnO Thin Films by Means of Plasma-Enhanced Atomic Layer Deposition," *Electrochemical and Solid-State Letters,* vol. 9, pp. G299-G301, 2006.

[141] N. Huby, S. Ferrari, E. Guziewicz, M. Godlewski, and V. Osinniy, "Electrical behavior of zinc oxide layers grown by low temperature atomic layer deposition," *Applied Physics Letters,* vol. 92, p. 023502, 2008.

[142] Renishaw, *Photoluminescence explained*, Available: http://www.renishaw.com/en/photoluminescence-explained--25809, (Accessed 2015).

[143] F. A. Jenkins and H. E. White, *Fundamentals of Optics*: McGraw-Hill, 1976.

[144] E. Guziewicz, M. Godlewski, T. Krajewski, L. Wachnicki, A. Szczepanik, K. Kopalko, A. Wojcik-Glodowska, E. Przezdziecka, W. Paszkowicz, E. Lusakowska, P. Kruszewski, N. Huby, G. Tallarida, and S. Ferrari, "ZnO grown by atomic layer deposition: A material for transparent electronics and organic heterojunctions," *Journal of Applied Physics,* vol. 105, p. 122413, 2009.

[145] S. Yamabi and H. Imai, "Growth conditions for wurtzite zinc oxide films in aqueous solutions," *Journal of Materials Chemistry,* vol. 12, pp. 3773-3778, 2002.

[146] S. B. Darling and F. You, "The case for organic photovoltaics," *RSC Advances,* vol. 3, pp. 17633-17648, 2013.

[147] D. Munoz-Rojas, S. Haiyan, D. C. Iza, J. Weickert, C. Li, W. Haiyan, L. Schmidt-Mende, and J. L. MacManus-Driscoll, "High-speed atmospheric atomic layer deposition of ultra thin amorphous TiO_2 blocking layers at 100 C for inverted bulk heterojunction solar cells," *Progress in Photovoltaics: Research and Applications,* vol. 21, pp. 393-400, 2013.

[148] a. Hadipour, R. Müller, P. Heremans, and R. Muller, "Room temperature solution-processed electron transport layer for organic solar cells," *Organic Electronics: physics, materials, applications,* vol. 14, pp. 2379-2386, 2013.

[149] E. Itoh, Y. Maruyama, and K. Fukuda, "Photovoltaic Properties of Bulk-Heterojunction Organic Solar Cell with Ultrathin Titanium Oxide Nanosheet as Electron Selective Layer," *Japanese Journal of Applied Physics,* vol. 52, pp. 04OK05 (4 pp.)-04OK05 (4 pp.), 2013.

[150] H. Schmidt, H. Flügge, T. Winkler, T. Bülow, T. Riedl, and W. Kowalsky, "Efficient semitransparent inverted organic solar cells with indium tin oxide top electrode," *Applied Physics Letters,* vol. 94, pp. 243302-243302, 2009.

[151] E. L. Ratcliff, B. Zacher, and N. R. Armstrong, "Selective Interlayers and Contacts in Organic Photovoltaic Cells," *The Journal of Physical Chemistry Letters,* vol. 2, pp. 1337-1350, 2011.

[152] J. D. Servaites, M. A. Ratner, and T. J. Marks, "Organic solar cells: A new look at traditional models," *Energy & Environmental Science,* vol. 4, pp. 4410-4422, 2011.

[153] J. Robertson and B. Falabretti, "Band offsets of high K gate oxides on III-V semiconductors," *Journal of Applied Physics,* vol. 100, p. 014111, 2006.

[154] C. S. Kim and H. D. Jeong, "Band Gap Tuning in Nanoporous TiO_2-ZrO_2 Hybrid Thin Films," *Bulletin of the Korean Chemical Society,* vol. 28, p. 2333, 2007.

[155] H. O. Seo, S.-Y. Park, W. H. Shim, K.-D. Kim, K. H. Lee, M. Y. Jo, J. H. Kim, E. Lee, D.-W. Kim, Y. D. Kim, and D. C. Lim, "Ultrathin TiO_2 Films on ZnO Electron-Collecting Layers of Inverted Organic Solar Cell," *The Journal of Physical Chemistry C,* vol. 115, pp. 21517-21520, 2011.

[156] U. Diebold, "The surface science of titanium dioxide," *Surface Science Reports,* vol. 48, pp. 53-229, 2003.

[157] R. F. Bartholomew and D. R. Frankl, "Electrical Properties of Some Titanium Oxides," *Physical Review,* vol. 187, pp. 828-833, 1969.

[158] D. Manno, G. Micocci, R. Rella, A. Serra, A. Taurino, and A. Tepore, "Titanium oxide thin films for NH_3 monitoring: Structural and physical characterizations," *Journal of Applied Physics,* vol. 82, pp. 54-59, 1997.

[159] V.-S. Dang, H. Parala, J. H. Kim, K. Xu, N. B. Srinivasan, E. Edengeiser, M. Havenith, A. D. Wieck, T. de los Arcos, R. A. Fischer, and A. Devi, "Electrical and optical properties of TiO_2 thin films prepared by plasma-enhanced atomic layer deposition," *physica status solidi (a),* vol. 211, pp. 416-424, 2014.

[160] D. Mardare, C. Baban, R. Gavrila, M. Modreanu, and G. I. Rusu, "On the structure, morphology and electrical conductivities of titanium oxide thin films," *Surface Science,* vol. 507–510, pp. 468-472, 2002.

[161] J. A. Venables, G. D. T. Spiller, and M. Hanbucken, "Nucleation and Growth of Thin-Films," *Reports on Progress in Physics,* vol. 47, pp. 399-459, 1984.

[162] N. Kaiser, "Review of the fundamentals of thin-film growth," *Applied Optics,* vol. 41, pp. 3053-3060, 2002.

[163] L. Aarik, T. Arroval, R. Rammula, H. Mändar, V. Sammelselg, and J. Aarik, "Atomic layer deposition of TiO_2 from $TiCl_4$ and O_3," *Thin Solid Films,* vol. 542, pp. 100-107, 2013.

[164] J. Aarik, J. Karlis, H. Mändar, T. Uustare, and V. Sammelselg, "Influence of structure development on atomic layer deposition of TiO_2 thin films," *Applied Surface Science,* vol. 181, pp. 339-348, 2001.

[165] D. R. G. Mitchell, D. J. Attard, and G. Triani, "Transmission electron microscopy studies of atomic layer deposition TiO_2 films grown on silicon," *Thin Solid Films,* vol. 441, pp. 85-95, 2003.

[166] D. R. G. Mitchell, G. Triani, D. J. Attard, K. S. Finnie, P. J. Evans, C. J. Barbé, and J. R. Bartlett, "Atomic layer deposition of TiO_2 and Al_2O_3 thin films and nanolaminates," *Smart Materials and Structures,* vol. 15, p. S57, 2006.

[167] Y. W. Chen, J. D. Prange, S. Duhnen, Y. Park, M. Gunji, C. E. D. Chidsey, and P. C. McIntyre, "Atomic layer-deposited tunnel oxide stabilizes silicon photoanodes for water oxidation," *Nature Materials,* vol. 10, pp. 539-544, 2011.

[168] L. Alibabaei, B. D. Sherman, M. R. Norris, M. K. Brennaman, and T. J. Meyer, "Visible photoelectrochemical water splitting into H_2 and O_2 in a dye-sensitized photoelectrosynthesis cell," *Proceedings of the National Academy of Sciences,* vol. 112, pp. 5899-5902, 2015.

[169] C. N. Berglund and W. E. Spicer, "Photoemission Studies of Copper and Silver: Theory," *Physical Review,* vol. 136, pp. A1030-A1044, 1964.

[170] R. S. Nicholson and I. Shain, "Theory of Stationary Electrode Polarography. Single Scan and Cyclic Methods Applied to Reversible, Irreversible, and Kinetic Systems," *Analytical Chemistry,* vol. 36, pp. 706-723, 1964.

[171] P. T. Kissinger and W. R. Heineman, "Cyclic voltammetry," *Journal of Chemical Education,* vol. 60, p. 702, 1983.

[172] S. Avasthi, W. E. McClain, G. Man, A. Kahn, J. Schwartz, and J. C. Sturm, "Hole-blocking titanium-oxide/silicon heterojunction and its application to photovoltaics," *Applied Physics Letters,* vol. 102, p. 203901, 2013.

[173] D. Placencia, W. Wang, J. Gantz, J. L. Jenkins, and N. R. Armstrong, "Highly Photoactive Titanyl Phthalocyanine Polymorphs as Textured Donor Layers in Organic Solar Cells," *The Journal of Physical Chemistry C,* vol. 115, pp. 18873-18884, 2011.

[174] J. F. Moulder, W. F. Stickle, P. E. Sobol, and K. D. Bomben, *Handbook of X-ray Photoelectron Spectroscopy: A Reference Book of Standard Spectra for Identification and Interpretation of XPS Data*. MN, USA: Physical Electronics, 1995.

[175] E. Carrasco, M. A. Brown, M. Sterrer, H.-J. Freund, K. Kwapien, M. Sierka, and J. Sauer, "Thickness-Dependent Hydroxylation of MgO(001) Thin Films," *The Journal of Physical Chemistry C,* vol. 114, pp. 18207-18214, 2010.

[176] H. Ishii, K. Sugiyama, E. Ito, and K. Seki, "Energy Level Alignment and Interfacial Electronic Structures at Organic/Metal and Organic/Organic Interfaces," *Advanced Materials,* vol. 11, pp. 605-625, 1999.

[177] D. Cahen and A. Kahn, "Electron Energetics at Surfaces and Interfaces: Concepts and Experiments," *Advanced Materials,* vol. 15, pp. 271-277, 2003.

[178] S. Hüfner, *Photoelectron spectroscopy: principles and applications*: Springer-Verlag Berlin Heidelberg, 2003.

[179] I. Lindau and W. E. Spicer, "The probing depth in photoemission and auger-electron spectroscopy," *Journal of Electron Spectroscopy and Related Phenomena,* vol. 3, pp. 409-413, 1974.

[180] H. Shin, M. R. De Guire, and A. H. Heuer, "Electrical properties of TiO_2 thin films formed on self-assembled organic monolayers on silicon," *Journal of Applied Physics,* vol. 83, pp. 3311-3317, 1998.

[181] A. K. Satpati, N. Arroyo-Curras, L. Ji, E. T. Yu, and A. J. Bard, "Electrochemical Monitoring of TiO_2 Atomic Layer Deposition by Chronoamperometry and Scanning Electrochemical Microscopy," *Chemistry of Materials,* vol. 25, pp. 4165-4172, 2013.

[182] I. Streeter, G. G. Wildgoose, L. Shao, and R. G. Compton, "Cyclic voltammetry on electrode surfaces covered with porous layers: An analysis of electron transfer kinetics at single-walled carbon nanotube modified electrodes," *Sensors and Actuators B: Chemical,* vol. 133, pp. 462-466, 2008.

[183] K. Takao, O. Kaoru, M. Takuya, and K. Tomoji, "Tunnelling charge injection into a pentacene layer using dynamic-mode scanning force microscopy," *Nanotechnology,* vol. 18, p. 095503, 2007.

[184] K. B. Holt, A. J. Bard, Y. Show, and G. M. Swain, "Scanning Electrochemical Microscopy and Conductive Probe Atomic Force Microscopy Studies of Hydrogen-Terminated Boron-Doped Diamond Electrodes with Different Doping Levels," *The Journal of Physical Chemistry B,* vol. 108, pp. 15117-15127, 2004.

[185] M. Brumbach, P. A. Veneman, F. S. Marrikar, T. Schulmeyer, A. Simmonds, W. Xia, P. Lee, and N. R. Armstrong, "Surface Composition and Electrical and Electrochemical Properties of Freshly Deposited and Acid-Etched Indium Tin Oxide Electrodes," *Langmuir,* vol. 23, pp. 11089-11099, 2007.

[186] Y. Sun, J. H. Seo, C. J. Takacs, J. Seifter, and A. J. Heeger, "Inverted Polymer Solar Cells Integrated with a Low-Temperature-Annealed Sol-Gel-Derived ZnO Film as an Electron Transport Layer," *Advanced Materials,* vol. 23, pp. 1679-1683, 2011.

[187] S. Sankar and K. G. Gopchandran, "Effect of annealing on the structural, electrical and optical properties of nanostructured TiO_2 thin films," *Crystal Research and Technology,* vol. 44, pp. 989-994, 2009.

[188] Q. Ye, P. Y. Liu, Z. F. Tang, and L. Zhai, "Hydrophilic properties of nano-TiO_2 thin films deposited by RF magnetron sputtering," *Vacuum,* vol. 81, pp. 627-631, 2007.

[189] H. Lu, B. Akgun, and T. P. Russell, "Morphological Characterization of a Low-Bandgap Crystalline Polymer:PCBM Bulk Heterojunction Solar Cells," *Advanced Energy Materials,* vol. 1, pp. 870-878, 2011.

[190] P. F. Carcia, R. S. McLean, M. D. Groner, A. A. Dameron, and S. M. George, "Gas diffusion ultrabarriers on polymer substrates using Al_2O_3 atomic layer deposition and SiN plasma-enhanced chemical vapor deposition," *Journal of Applied Physics,* vol. 106, p. 023533, 2009.

[191] T. N. Chen, D. S. Wuu, C. C. Wu, R. H. Horng, H. F. Wei, L. Y. Jiang, H. U. Lee, and Y. Y. Chang, "Deposition and characterization of ultra-high barrier coatings for flexible electronic applications," *Vacuum,* vol. 84, pp. 1444-1447, 2010.

[192] A. B. Chwang, M. A. Rothman, S. Y. Mao, R. H. Hewitt, M. S. Weaver, J. A. Silvernail, K. Rajan, M. Hack, J. J. Brown, X. Chu, L. Moro, T. Krajewski, and N. Rutherford, "Thin film encapsulated flexible organic electroluminescent displays," *Applied Physics Letters,* vol. 83, pp. 413-415, 2003.

[193] A. P. Ghosh, L. J. Gerenser, C. M. Jarman, and J. E. Fornalik, "Thin-film encapsulation of organic light-emitting devices," *Applied Physics Letters,* vol. 86, p. 223503, 2005.

[194] K. Jung, J. Y. Bae, S. J. Park, S. Yoo, and B. S. Bae, "High performance organic-inorganic hybrid barrier coating for encapsulation of OLEDs," *Journal of Materials Chemistry,* vol. 21, pp. 1977-1983, 2011.

[195] H. N. Lee, H. J. Kim, and Y. M. Yoon, "Thin-film barriers using transparent conducting oxides for organic light-emitting diodes," *Journal of the Society for Information Display,* vol. 17, pp. 739-744, 2009.

[196] Y.-Q. Yang, Y. Duan, P. Chen, F.-B. Sun, Y.-H. Duan, X. Wang, and D. Yang, "Realization of Thin Film Encapsulation by Atomic Layer Deposition of Al_2O_3 at Low Temperature," *The Journal of Physical Chemistry C,* vol. 117, pp. 20308-20312, 2013.

[197] S. E. Potts, W. Keuning, E. Langereis, G. Dingemans, M. C. M. van de Sanden, and W. M. M. Kessels, "Low Temperature Plasma-Enhanced Atomic Layer Deposition of Metal Oxide Thin Films," *Journal of The Electrochemical Society,* vol. 157, pp. P66-P66, 2010.

[198] S.-W. Seo, E. Jung, C. Lim, H. Chae, and S. M. Cho, "Moisture Permeation through Ultrathin TiO_2 Films Grown by Atomic Layer Deposition," *Applied Physics Express,* vol. 5, p. 035701, 2012.

[199] S.-H. K. Park, J. Oh, C.-S. Hwang, J.-I. Lee, Y. S. Yang, and H. Y. Chu "Ultrathin Film Encapsulation of an OLED by ALD," *Electrochemical and Solid-State Letters,* vol. 8, pp. H21-H23, 2005.

[200] W. Keuning, P. van de Weijer, H. Lifka, W. M. M. Kessels, and M. Creatore, "Cathode encapsulation of organic light emitting diodes by atomic layer deposited Al_2O_3 films and Al_2O_3/a-SiN_x:H stacks," *Journal of Vacuum Science & Technology A,* vol. 30, p. 01A131, 2012.

[201] S.-W. Seo, E. Jung, C. Lim, H. Chae, and S. M. Cho, "Water permeation through organic–inorganic multilayer thin films," *Thin Solid Films,* vol. 520, pp. 6690-6694, 2012.

[202] P. E. Burrows, V. Bulovic, S. R. Forrest, L. S. Sapochak, D. M. McCarty, and M. E. Thompson, "Reliability and degradation of organic light emitting devices," *Applied Physics Letters,* vol. 65, pp. 2922-2924, 1994.

[203] T. v. M. P. van de Weijer, "White paper on the characterisation of thin-film barrier layers for protection of organic Light-Emitting Diodes," in *ICT-216641 Fast2light*, 2009, pp. 1-17.

[204] S. M. J. Fahlteich, T. Wanski, N. Schiller, S. A. Schwab, U. Weber, O. Miesbauer, E. K. Niarchos, K. Noller, C. Boeffel, "The Role of Defects in Single- and Multi- Layer Barriers for Flexible Electronics," presented at the Society of Vacuum Coaters 57th Annual Technical Conference, Chicago, IL, USA, 2014.

[205] T.-N. Chen, D.-S. Wuu, C.-C. Wu, C.-C. Chiang, Y.-P. Chen, and R.-H. Horng, "High-Performance Transparent Barrier Films of SiO_x/SiN_x Stacks on Flexible Polymer Substrates," *J. Electrochem. Soc.,* vol. 150, 2006.

[206] N. Cordero, J. Yoon, and Z. Suo, "Channel cracks in a hermetic coating consisting of organic and inorganic layers," *Applied Physics Letters,* vol. 90, p. 111910, 2007.

[207] G. Azimi, R. Dhiman, H.-M. Kwon, A. T. Paxson, and K. K. Varanasi, "Hydrophobicity of rare-earth oxide ceramics," *Nat Mater,* vol. 12, pp. 315-320, 2013.

[208] A. Bulusu, S. Graham, H. Bahre, H. Behm, M. Böke, R. Dahlmann, C. Hopmann, and J. Winter, "The Mechanical Behavior of ALD-Polymer Hybrid Films Under Tensile Strain," *Advanced Engineering Materials,* vol. 17, pp. 1057-1067, 2015.

[209] N. Otsu, "A Threshold Selection Method from Gray-Level Histograms," *Systems, Man and Cybernetics, IEEE Transactions on,* vol. 9, pp. 62-66, 1979.

[210] G. G. Stoney, "The Tension of Metallic Films Deposited by Electrolysis," in *Proceedings of the Royal Society of London. Series A, Containing Papers of a Mathematical and Physical Character* vol. 82, ed, 1909, pp. 172-175.

[211] L. B. Freund and S. Suresh, *Thin film materials : stress, defect formation, and surface evolution*. Cambridge, England ; New York: Cambridge University Press, 2003.

[212] R. Huang, J. H. Prevost, Z. Y. Huang, and Z. Suo, "Channel-cracking of thin films with the extended finite element method," *Engineering Fracture Mechanics,* vol. 70, pp. 2513-2526, 2003.

[213] D. C. Miller, R. R. Foster, Y. D. Zhang, S. H. Jen, J. A. Bertrand, Z. X. Lu, D. Seghete, J. L. O'Patchen, R. G. Yang, Y. C. Lee, S. M. George, and M. L. Dunn, "The mechanical robustness of atomic-layer- and molecular-layer-deposited coatings on polymer substrates," *Journal of Applied Physics,* vol. 105, p. 12, 2009.

[214] N. Fong, P. Berini, and R. N. Tait, "Fabrication and mechanical properties of surface plasmon waveguide biosensors on thin CYTOP membranes," in *Photonics North 2010, June 1, 2010 - June 3, 2010*, Niagara Falls, ON, Canada, 2010, pp. Ontario Photonics Industry Network (OPIN); Quebec Photonic Network; Institut National d'Optique(INO); Canadian Photonics Consortium (CPC); Universite Laval, Centre d'Optique, Photonique et Laser.

[215] M. K. Tripp, C. Stampfer, D. C. Miller, T. Helbling, C. F. Herrmann, C. Hierold, K. Gall, S. M. George, and V. M. Bright, "The mechanical properties of atomic layer deposited alumina for use in micro- and nano-electromechanical systems," *Sensors and Actuators, A: Physical,* vol. 130-131, pp. 419-429, 2006.

[216] K. Tapily, J. E. Jakes, D. S. Stone, P. Shrestha, D. Gu, H. Baumgart, and A. A. Elmustafa, "Nanoindentation Investigation of HfO_2 and Al_2O_3 Films Grown by Atomic Layer Deposition," *Journal of The Electrochemical Society,* vol. 155, pp. H545-H551, 2008.

[217] D. C. Miller, R. R. Foster, S. H. Jen, J. A. Bertrand, S. J. Cunningham, A. S. Morris, Y. C. Lee, S. M. George, and M. L. Dunn, "Thermo-mechanical properties of alumina films created using the atomic layer deposition technique," *Sensors and Actuators a-Physical,* vol. 164, pp. 58-67, 2010.

[218] D. S. Wuu, W. C. Lo, C. C. Chiang, H. B. Lin, L. S. Chang, R. H. Horng, C. L. Huang, and Y. J. Gao, "Plasma-deposited silicon oxide barrier films on polyethersulfone substrates: temperature and thickness effects," *Surface and Coatings Technology,* vol. 197, pp. 253-259, 2005.

[219] H. Huang, K. J. Winchester, A. Suvorova, B. R. Lawn, Y. Liu, X. Z. Hu, J. M. Dell, and L. Faraone, "Effect of deposition conditions on mechanical properties of low-temperature PECVD silicon nitride films," *Materials Science and Engineering: A,* vol. 435–436, pp. 453-459, 2006.

[220] A. S. da Silva Sobrinho, G. Czeremuszkin, M. Latrèche, and M. R. Wertheimer, "Defect-permeation correlation for ultrathin transparent barrier coatings on polymers," *Journal of Vacuum Science & Technology A,* vol. 18, pp. 149-157, 2000.

[221] G. Nisato, M. Kuilder, P. Bouten, L. Moro, O. Philips, and N. Rutherford, "P-88: Thin Film Encapsulation for OLEDs: Evaluation of Multi-layer Barriers using the Ca Test," *SID Symposium Digest of Technical Papers,* vol. 34, pp. 550-553, 2003.

[222] M. Subimal, C. Maria Fátima, T. Denis, G. Bernard, B. Yvan, A. Pedro, and B. Jean Eric, "Influence of low energy argon plasma treatment on the moisture barrier performance of hot wire-CVD grown SiN_x multilayers," *Japanese Journal of Applied Physics,* vol. 53, p. 05FM05, 2014.

[223] J. Bertrand, D. Higgs, M. Young, and S. George, "H_2O vapor transmission rate through polyethylene naphthalate polymer using the electrical Ca test," *The Journal of Physical Chemistry A,* vol. 117, pp. 12026-12034, 2013.

[224] G. Nisato, H. Klumbies, J. Fahlteich, L. Müller-Meskamp, P. van de Weijer, P. Bouten, C. Boeffel, D. Leunberger, W. Graehlert, and S. Edge, "Experimental comparison of high-performance water vapor permeation measurement methods," *Organic Electronics,* vol. 15, pp. 3746-3755, 2014.

[225] B. J. Kim, D. H. Kim, S. Y. Kang, S. D. Ahn, and S. G. Im, "A thin film encapsulation layer fabricated via initiated chemical vapor deposition and atomic layer deposition," *Journal of Applied Polymer Science,* vol. 131, p. 40974, 2014.

[226] J. Affinito and D. Hilliard, "A New Class of Ultra-Barrier Materials," in *Society of Vacuum Coaters 47 th Annual Technical Conference Proceedings*, 2004, pp. 563-593.

[227] M. D. Kempe, M. O. Reese, and A. A. Dameron, "Evaluation of the sensitivity limits of water vapor transmission rate measurements using electrical calcium test," *Review of Scientific Instruments,* vol. 84, p. 025109, 2013.

[228] A. Bulusu, A. Singh, C.-Y. Wang, A. Dindar, C. F. Hernandez, H. Kim, D. Cullen, B. Kippelen, and S. Graham, "Engineering the Mechanical Properties of Ultrabarrier Films Grown by Atomic Layer Deposition for the Encapsulation of Printed Electronics," *Manuscript submitted for publication,* 2015.

[229] A. D. McNaught and A. Wilkinson, *Compendium of chemical terminology* vol. 1669. Oxford: Blackwell Science, 1997.

[230] P. Klobes, K. Meyer, R. G. Munro, N. I. o. Standards, and Technology, *Porosity and Specific Surface Area Measurements for Solid Materials*: U.S. Department of Commerce, Technology Administration, National Institute of Standards and Technology, 2006.

[231] J. Crank, *The Mathematics of Diffusion*, 2nd ed. Oxford: Oxford University Press, 1979.

[232] M. Kempe, A. Dameron, and M. Reese, "Calcium Based Test Method for Evaluation of Photovoltaic Edge-Seal Materials," in *2011 NREL PV Module Reliability Workshop*, 2011.

[233] K. Yongjin, K. Namsu, K. Hyungchul, and S. Graham, "The development of thin film barriers for encapsulating organic electronics," in *Electronic Components and Technology Conference (ECTC), 2011 IEEE 61st*, 2011, pp. 2101-2106.

[234] L. Hu, H. S. Kim, J.-Y. Lee, P. Peumans, and Y. Cui, "Scalable Coating and Properties of Transparent, Flexible, Silver Nanowire Electrodes," *ACS Nano,* vol. 4, pp. 2955-2963, 2010.

[235] P. P. Boix, K. Nonomura, N. Mathews, and S. G. Mhaisalkar, "Current progress and future perspectives for organic/inorganic perovskite solar cells," *Materials Today,* vol. 17, pp. 16-23, 2014.

[236] H. S. Jung and N.-G. Park, "Perovskite Solar Cells: From Materials to Devices," *Small,* vol. 11, pp. 10-25, 2015.

[237] N.-G. Park, "Perovskite solar cells: an emerging photovoltaic technology," *Materials Today,* vol. 18, pp. 65-72, 2015.

[238] G. C. Papavassiliou, G. A. Mousdis, and I. B. Koutselas, "Some new organic–inorganic hybrid semiconductors based on metal halide units: structural, optical and related properties," *Advanced Materials for Optics and Electronics,* vol. 9, pp. 265-271, 1999.

[239] J. Burschka, N. Pellet, S.-J. Moon, R. Humphry-Baker, P. Gao, M. K. Nazeeruddin, and M. Gratzel, "Sequential deposition as a route to high-performance perovskite-sensitized solar cells," *Nature,* vol. 499, pp. 316-319, 2013.

VITA

HYUNG CHUL KIM

Hyungchul Kim received his B.S. degree with a double major in mechanical engineering and electrical engineering at Seoul National University in Korea. After earning his B.S. degree, he studied micro electromechanical systems and received his M.S. degree at Seoul National University. Currently, he is a graduate research assistant working on his doctoral degree in mechanical engineering at the Georgia Institute of Technology. His research interests lie in improving the reliability of flexible electronics using atomic layer deposition films. He is involved in a project of organic photovoltaic cells for the Center for Interface Science: Solar Electric Materials, funded by the Department of Energy.